CVR JOURNAL OF SCIENCE AND TECHNOLOGY

Vol.No. 21, December 2021
P-ISSN 2277 - 3916

DOI 10.32377/CVRJST21
E-ISSN 2581 - 7957

CVR COLLEGE OF ENGINEERING

In Pursuit of Excellence

PATRONS

Dr. Raghava V. Cherabuddi, President & Chairman

Dr. K. Rama Sastri, Director

Dr. K.S. Nayanathara, Principal

Editor : **Dr. K. Lal Kishore, Professor and Dean - Research, CVRCE**

Associate Editor : **Dr. S. Venkateshwarlu, Professor & Head, Dept. of EEE, CVRCE**

Technical support : **Mr. K. Veeranjaneyulu, Asst. Prof., Dept. of CSE, CVRCE**

Editorial Board :

Dr. M.V. Seshagiri Rao	Professor & Dean-Planning & Coordination, CVRCE
Prof. L.C. Siva Reddy	Professor & Vice-Principal, CVRCE
Dr. Rameshwar Rao	Professor & Dean- Projects & Consultancy, CVRCE
Dr. N.V. Rao	Professor & Dean-Academics, CVRCE
Dr. T. Muralidhara Rao	Professor & Head, Dept. of Civil Engg., CVRCE
Dr. A. Vani Vathsala	Professor & Head, Dept. of CSE, CVRCE
Dr. K. Lalithendra	Professor & Head, Dept. of ECE, CVRCE
Dr. S. Harivardhagini	Professor & Head, Dept. of EIE, CVRCE
Dr. Bipin Bihari Jayasingh	Professor & Head, Dept. of IT, CVRCE
Dr. M. Venkata Ramana	Professor & Head, Dept. of Mech. Engg., CVRCE
Dr. H.N. Lakshmi	Professor & Head, Dept. of CSIT, CVRCE
Dr. G. Bikshamaiah	Professor & Head, Dept. of H&S, CVRCE

International Review Board:

Prof. Tzung-Pei Hong	Chair Professor, Dept. of CSI Engg., AI Research Center National University of Kaohsiung 811, Taiwan
Dr. Tomonobu Senjyu	Professor, Department of Electrical Engineering, University of the Ryukyus, Nishihara-cho, Nakagami Okinawa, Japan
Dr. Masoud Mohammadian	Assoc. Professor, Faculty of Science and Technology, University of Canberra, Australia
Dr. Rubén Ruiz García	Full Professor, Head of the Applied Optimization Systems Group, Department of Applied Statistics, Universitat Politècnica de València, Camino de Vera, Spain
Dr. Ray-Hwa Wong	Professor, Department of Mech. Engg., Hwa-Hsia University of Technology, Taipei, Taiwan
Dr. Stefan Talu	Faculty of Mech. Engineering, DMCDI, The Technical University of Cluj-Napoca, B-dul Muncii Street, No. 103-105, Cluj-Napoca, 400641, Romania
Assoc. Prof. Ir. Dr. Norhaliza Abdul Wahab	Director, Control & Mechatronics Engg. Dept., Faculty of Electrical Engineering, UTM Skudai 81310 Johor
Dr. R. Venkata Rao	Professor, Department of Mech Engg., Sardar Vallabhbhai National Institute of Technology (SVNIT), Surat, Gujarat State – 395 007, India
Dr. Vijay Janyani	Professor Dept. of ECE, Malaviya National Institute of Technology (MNIT), Jaipur - 302017 (Rajasthan)
Dr. V. Prasanna Venkatesan	Prof. & Head, Department of Banking Technology, School of Management, R.V.Nagar, Kalapet, Pondicherry University, Puducherry

CVR JOURNAL OF SCIENCE AND TECHNOLOGY

Indexed by

- Google Scholar
- Directory of Research Journals Indexing (DRJI)
- Scientific Indexing Services (SIS)
- International Institute of Organised Research (I2OR)
- Scholar Impact - Journal Index
- Citefactor
- Member Crossref / DOI

Accredited by NAAC with 'A' GRADE

CVR COLLEGE OF ENGINEERING

(UGC Autonomous - Affiliated to JNTU Hyderabad)
Mangalpalli (V), Ibrahimpatnam (M),
R.R. District, Telangana. – 501510
http://cvr.ac.in

EDITORIAL

The Editorial Team is delighted to bring out Volume – 21 of the Bi-annual CVR Journal of Science and Technology due in December 2021, in time, despite partial closure of educational institutions due to COVID-19 Pandemic. We are still working in hybrid mode and expecting normalcy to be restored soon. But emergence of another variant Omicron is threatening every country. Hope in the new year 2022, the humanity will be much safer. It takes almost 6 months to bring out a Volume. Thanks to all the authors, reviewers, and Team CVR Journal, for enabling us to complete the task in time.

The Pandemic has thrown many challenges to researchers. In this Volume two research articles related to COVOD Pandemic are published similar to the last issue. This shows the interest of the researchers to bring out solutions to the problems being faced by the society, though scientific research, and not with mere academic interest.

This Volume covers research articles in the following disciplines:

CIVIL – 3, CSE – 3, CSIT – 1, ECE – 3, EEE – 2, EIE – 3, IT – 4, MECH – 5, H & S – 1.

To maintain quality, blind review of the research articles is being done. Based on the remarks of the reviewer, if the improvements in the articles are done to the satisfaction of the reviewer, then only articles are being accepted for publication. The dates of receipt of the articles, revision done, and date of acceptance are also being printed, to follow the standard practice. Plagiarism check and English language corrections are also being carried out scrupulously.

This Volume has DOI number and e-ISSN number along with print ISSN number on the cover page. Every research article published is given DOI number and they can be accessed on-line. On-line portal is also created for the Journal. This Volume is also brought out in time, with the co-operation ofall the authors and editorial team. We are thankful to the Management for supporting this activity, and permitting to publish the journal in color print, using quality printing paper.

In this issue, COVID related article on “Future Forecasting using Machine Learning Models” might be useful for COVID applications. Another related article on “Classify Covid-19 from Lung Images using Deep Learning Models” must also be useful for research work. The article “A Novel Approach to Vocalize the Hand Gesture Movement for Speech Disabled” must be useful for that type of challenged persons. Article on IOT applications, “Speech Enabled Smart Home Automation” must also make interest reading. We are encouraging P.G. Scholars to publish research papers, based on their project work. The article on “Touch-less Disinfecting Contraption using UV-C light” can find practical applications.

I am thankful to all the members of the Editorial Board for their help in reviewing and short listing the research papers for inclusion in the current Volume of the journal. I wish to thank **Dr. S. Venkateshwarlu, HOD, EEE** for the effort made in bringing out this Volume. Thanks are due to **HOD, H & S, Dr. G. Bhikshamaiah** and the staff of English Department for reviewing the papers. I am also thankful to **Smt. A. Sreedevi, DTP Operator** in the Office of Dean Research for the preparation of research papers in Camera - Ready form.

For further clarity on waveforms, graphs, circuit diagrams and figures, readers are requested to browse the soft copy of the journal, available on the college website www.cvr.ac.in wherein a link is provided. Authors can also submit their papers through our online open journal system (OJS) www.ojs.cvr.ac.in or www.cvr.ac.in/ojs

Prof. K. Lal Kishore
Editor

Patrons:

Dr. Raghava V. Cherabuddi
President & Chairman
CVR College of Engineering,
Vastunagar, Mangalpalli (V),
Ibrahimpatnam (M)
Rangareddy (D),
Telangana 501 510.
E-mail: drcvraghava@gmail.com
Phone: 040-42204001, 02,03

Dr. K. Rama Sastri
Director
CVR College of Engineering,
Vastunagar, Mangalpalli (V),
Ibrahimpatnam (M)
Rangareddy (D), Telangana 501 510.
E-mail: director@cvr.ac.in
Phone: 08414-661666, 661601,661675

Dr. K.S. Nayanathara
Principal
CVR College of Engineering,
Vastunagar, Mangalpalli (V), Ibrahimpatnam (M)
Rangareddy (D), Telangana 501 510.
E-mail: principal@cvr.ac.in
Phone: 08414-6616602, 661601,661675

Editor:

Dr. K. Lal Kishore
Professor and Dean Research
CVR College of Engineering
Vastunagar, Mangalpalli (V),
Ibrahimpatnam (M)
Rangareddy (D), Telangana 501 510.
E-mail: lalkishorek@gmail.com
lalkishore@cvr.ac.in
Mobile: +91 8309105423 , +91 9618023478
Phone: 08414-661658, 661601,661675

Associate Editor:

Dr. S. Venkateshwarlu
Professor & Head
Dept of Electrical and Electronics Engineering
CVR College of Engineering
Vastunagar, Mangalpalli (V),
Ibrahimpatnam (M)
Rangareddy (D), Telangana 501 510.
E-mail: svip123@gmail.com
hod.eee@cvr.ac.in
Mobile: +91 9490749568
Phone: 08414-661661

Technical support:

Mr. K. Veeranjaneyulu
Asst. Prof.
Dept. of Computer Science & Engineering
CVR College of Engineering
Vastunagar, Mangalpalli (V), Ibrahimpatnam (M)
Rangareddy (D),
Telangana 501 510.
E-mail: kveeru876@gmail.com
Mobile: +91 9177462507

Editorial Board:

Dr. M.V. Seshagiri Rao
Professor & Dean-Planning & Coordination
CVR College of Engineering
Vastunagar, Mangalpalli (V),
Ibrahimpatnam (M)
Rangareddy (D),
Telangana 501 510.
E-mail:
rao_vs_meduri@yahoo.com
sheshagiri.rao@cvr.ac.in
Mobile: +91 9440361817
Phone:08414-661617

Prof. L.C. Siva Reddy
Professor & Vice-Principal
CVR College of Engineering
Vastunagar, Mangalpalli (V),
Ibrahimpatnam (M)
Rangareddy (D),
Telangana 501 510.
E-mail: siva_reddy@cvr.ac.in
Mobile: +91 9885806151
Phone:08414-661656

Dr. Rameshwar Rao
Professor & Dean- Projects & Consultancy
CVR College of Engineering
Vastunagar, Mangalpalli (V),
Ibrahimpatnam (M)
Rangareddy (D),
Telangana 501 510.
E-mail:
Rameshwar_rao@hotmail.com
rameshwar_rao@cvr.ac.in
Mobile: +91 9394483591
Phone:08414-661659

Dr. N.V. Rao
Professor & Dean-Academics
CVR College of Engineering
Vastunagar, Mangalpalli (V),
Ibrahimpatnam (M)
Rangareddy (D),
Telangana 501 510.
E-mail:
nvyaghresh@gmail.com
nv.rao@cvr.ac.in
Mobile: +91 9440506701
Phone:08414-661667

Dr. T. Muralidhara Rao
Professor & Head
Dept. of Civil Engineering
CVR College of Engineering
Vastunagar, Mangalpalli (V),
Ibrahimpatnam (M)
Rangareddy (D),
Telangana 501 510.
E-mail:
tmuralidhararao@gmail.com
tmuralidhararao@cvr.ac.in
Mobile: +91 9989214274
Phone:08414-661653

Dr. A. Vani Vathsala
Professor & Head
Dept. of Computer Science & Engineering
CVR College of Engineering
Vastunagar, Mangalpalli (V),
Ibrahimpatnam (M)
Rangareddy (D),
Telangana 501 510.
E-mail: atlurivv@yahoo.com
vani_vathsala@cvr.ac.in
Mobile: +91 9866586106
Phone:08414-661655

Dr. K. Lalithendra
Professor & Head
Dept. of Electronics and Communication Engineering
CVR College of Engineering
Vastunagar, Mangalpalli (V),
Ibrahimpatnam (M)
Rangareddy (D),
Telangana 501 510.
E-mail: lkurra@gmail.com
lalithendra@cvr.ac.in
Mobile: +91 9871483379
Phone:08414-661660

Dr. S. Harivardhagini
Professor & Head
Dept of Electronics and Instrumentation Engineering
CVR College of Engineering
Vastunagar, Mangalpalli (V),
Ibrahimpatnam (M)
Rangareddy (D),
Telangana 501 510.
E-mail:
Harivardhagini@gmail.com
Mobile: +91 9985147962
Phone:08414-661653

Dr. Bipin Bihari Jayasingh
Professor & Head
Dept. of Information Technology
CVR College of Engineering
Vastunagar, Mangalpalli (V),
Ibrahimpatnam (M)
Rangareddy (D),
Telangana 501 510.
E-mail:
bipinbjayasingh@cvr.ac.in
Mobile: +91 9440476544
Phone:08414-661664

Dr. M. Venkata Ramana
Professor & Head
Dept. of Mechanical Engg
CVR College of Engineering
Vastunagar, Mangalpalli (V),
Ibrahimpatnam (M)
Rangareddy (D),
Telangana 501 510.
E-mail:
vramanamaringanti@cvr.ac.in
Mobile: +91 9948084192
Phone:08414-661689

Dr. H. N. Lakshmi
Professor & Head
Dept. of Computer Science & Information Technology
CVR College of Engineering
Vastunagar, Mangalpalli (V),
Ibrahimpatnam (M)
Rangareddy (D),
Telangana 501 510.
E-mail: hn.lakshmi@cvr.ac.in
Mobile: +91 9849698045

Dr. G. Bikshamaiah
Professor & Head
Dept. of Humanities and Science
CVR College of Engineering
Vastunagar, Mangalpalli (V),
Ibrahimpatnam (M)
Rangareddy (D),
Telangana 501 510
E-mail: gbcvr17@gmail.com
hod.hns@cvr.ac.in
Mobile: +91 9949565350
Phone:08414-661631

International Review Board:

Prof. Tzung-Pei Hong
Chair Professor
Department of Computer Science and Information Engineering
AI Research Center
National University of Kaohsiung
No. 700, Kaohsiung University Road, Nan-Tzu District
Kaohsiung 811, Taiwan
Tel:(07)5919191, 5919398
Fax:(07)5919049
Email: tphong@nuk.edu.tw
Website: tphong.nuk.edu.tw

Dr. Tomonobu Senjyu
Professor
Department of Electrical Engineering
University of the Ryukyus,
Nishihara-cho,
Nakagami Okinawa, Japan
Tel:(+81-98-895-8686)
Email: b985542@tec.u-ryukyu.ac.jp

Dr. Masoud Mohammadian
Associate Professor
Faculty of Science and Technology
University of Canberra ACT 2601
Phone: +61 (0)2 6201 2917
Fax: +61 (0)2 6201 5231
Email:masoud.mohammadian@canberra.edu.au
Website:https://research profiles.canberra.edu.au/en/persons/masoud-mohammadian

Dr. Rubén Ruiz García
Full Professor. Head of the Applied Optimization Systems Group
Department of Applied Statistics, Operations Research and Quality
Universitat Politècnica de València
Camino de Vera s/n, Edificio 7A, 46022, Valencia, Spain
rruiz@eio.upv.es
http://soa.iti.es/rruiz

Dr. Ray-Hwa Wong
Professor
Department of Mechanical Eng.,
Hwa-Hsia University of Technology, Taiwan,
111 Gong Jhuan Rd., Chung Ho,
Taipei, Taiwan, R.O.C.
E-mail : rhwong@cc.hwh.edu.tw
Phone / Mobile Number : +886-2-8941-5129 ex 2108/+886-918-706-985

Dr. Stefan Talu
DMCDI
The Technical University of Cluj-Napoca
Faculty of Mechanical Engineering,
B-dul Muncii Street, No. 103-105, Cluj-Napoca, 400641,
Romania
http://research.utcluj.ro.
E-mail(uri) stefanta@mail.utcluj.ro, stefan_ta@yahoo.com
Telephone(s) Fixed line phone:
004 0264 401 200.
Mobile phone: 004 0744263660

Assoc. Prof. Ir. Dr Norhaliza Abdul Wahab
Director,
Control & Mechatronics Engineering Department
Faculty of Electrical Engineering
UTM Skudai 81310 Johor
Malaysia
Phone: +607-5557023, 012-5444297 (HP)
Email: aliza@fke.utm.my
URL: http://norhaliza.fke.utm.my/

Dr. R. Venkata Rao
Professor, Department of Mechanical Engineering
Sardar Vallabhbhai National Institute of Technology (SVNIT), Surat
Ichchanath, Surat, Gujarat State – 395 007, India,
Contact Nos.: 02612201982(O), 02612201661(R), 9925207027(M)
Email ID: ravipudirao@gmail.com, rvr@med.svnit.ac.in
Website: http://svnit.ac.in/facup/5274Rao-Resume.pdf

Dr. Vijay Janyani
Professor
Dept. of Electronics and Communication Engineering
Malaviya National Institute of Technology (MNIT)
Jaipur - 302017 (Rajasthan)
India.
www.mnit.ac.in
Email ID: vijay.janyani@ieee.org

Dr. V. Prasanna Venkatesan
Prof. & Head
Department of Banking Technology,
School of Management, R.V.Nagar,
Kalapet, Pondicherry University,
Puducherry – 605014,
India.Telephone No: 0413 - 2654 652
Mobile No: 0091-9486199939
Email: prasanna.btm@pondiuni.edu.in, prasanna_v@yahoo.com

CONTENTS

E-ISSN 2581 – 7957
P-ISSN 2277 – 3916

CVR Journal of Science and Technology, Volume 21, December 2021
DOI: 10.32377/cvrjst2101

Experimental Investigation on Non-Linear Flow in Porous Media Through Converging Boundaries

B. N. Malleswara Rao
Professor, CVR College of Engineering/Civil Engg. Department, Hyderabad, India
Email: bnmrao@gmail.com

***Abstract*: Water movement through the soil layers iscomplex in nature. But its contribution to the well-being of the human kind as a whole is significant. The subject of seepage flow is one, which appears initially simple, after in depth and detailed study, however, the character of flow of a fluid particle through the tortuous passages of a granular medium assumes an almost incomprehensible complicacy. Most of the practical cases, in addition to size, shape, and angularity of the porous media, convergence of the flow may be expected to playan important role in influencing the flow behavior. The present work envisages carrying out analysis of the data systematically based on the drag on the individual particle, regime wise. In order to meet the objectives of the present investigation, aradial flow permeameters with different angles are fabricated and crushed rock and marbles are used as porous media. Water and diesel are used as the fluid media to develop curves relating friction factor and Reynolds number for different radial flow lines with different ratios of radii of the test section of the permeameter. Analysis is carried out in two phases. In the first phase 'volume diameter' is used as characteristic length to compute coefficient of resistance and Reynolds number as defined by Kovacs. In the second phase of analysis 'Hydraulic radius' is used as characteristic length while defining coefficient of resistance and Reynolds number.**

***Index Terms:* Permeameter, Reynold's number, radial flow,porous media, volume diameter, hydraulic radius, characteristic length,**

I. Introduction

The process of flow through permeable media is of interest to various fields of engineers, scientists and economists who identify the importance of groundwater flows and in the field of oil retrieval processes. The one- dimensional empirical equation suggested by Darcy in 1856 is the starting point for number of practical applications and as a constant challenge for researchers. The original conditions studied by Darcy can be found in many practical cases, it is the extensions to more general cases that are in need of theoretical analysis where experiments are difficult to perform. The first such situation is the fully three- dimensional flows which applicable for groundwater flows and oil recovery methods. While this form of Darcy's law is applied frequently, it appears to be no experimental validation obvious tonsorial depiction of Darcy's philosophy.

A porous media is stated as a solid body containing void spaces, distributed more or less frequently all over the medium in either regular pattern or at random. In porous media pores may be interconnected or indiscriminate, but at least a part of the pore system must be interconnected to make the fluid pass through the medium. This interconnected pore space is called "effective pore space of the medium". Pores may vary in shape, size and magnitude therefore it provides curvilinear paths for the fluid to flow. A matter exists in either the solid state or the fluid state. The fluid state is further divided into liquid and gaseous states. Theoretically fluid is as a substance, capable of flowing. It has no definite shape of its own but conforms to the shape of the containing vessel. The fluids are classified into ideal and real fluids. Fluids having no viscosity and surface tension are called Ideal fluids and are incompressible. Real or Practical fluids are those which are available in nature. Real fluids having the properties such as viscosity, surface tension and compressibility.

II. Literature Review

From the pioneering experiments of Darcy on flow of water through filter beds, a significant amount of theoretical and experimental investigations taken place on seepage flow Hubbert, M.K [4]. A survey of past work indicates that the aim of all the researchers had to connect flow resistance to its behavior in terms of quantifiable properties of the fluid and the medium. Forchheimer conducted experiments on a sandbox model and suggested a quadratic equation. Irmay.S. [5]. But this equation does not take care of transitional regime. While a number of authors Ahmed and Sunada [1] and Anadakrishnan and Varadarajulu [2] have used Darcy's equation to analyse their experimental data. Rose [10] and Rizk [11] conducted dimensional analysis and present a quadratic equation by correlating coefficient of resistance and Reynolds number. But when the data of Dudgeon [3], Niranjan [8] and Pradip Kumar [9] are plotted using the equation suggested by Rose and Rizk, it is found that Reynolds no. attains a low value as 9. Wright [12] and Kovacs [6] have done considerable work on the conditions of limits. Wright [12] published the results of research on a vertical converging permeameter. Moccorquodale [7] analysed the effect of convergence in a horizontal permeameter by applying finite element method.

III. Experimental Setup

Figure 1 depicts the details of the converging flow permeameter used in the present study. The set-up consists of a vertical converging section of 1000 mm height and width varying from 750mm at top to 150mm at bottom. The angle of convergence is 50^0 to 70^0. The radii of convergence

Received on 22-09-2021, Revised on 28-10-2021, Accepted on 29-11-2021.

CVR Journal of Science and Technology, Volume 21, December 2021
DOI: 10.32377/cvrjst2101

at the top and bottom piezometers are 111cm and 26cm respectively. A row of piezometric holes were drilled along the centre line of the permeameter. The piezometric Tapping points are provided at 50mm centre to centre spacing along the centre line of the front face of the permeameter. The short copper tubes attached to these holes are connected to a manometer board by tubes. The piezometric heads are measured to an accuracy of ±0.5 mm. At the bottom of the permeameter, 3.5 mm thick perforated aluminum screen, with more than 85% of the area perforated, was kept retaining the material. A similar screen was kept at the top also, to ensure uniform flow throughout the cross section of the permeameter and to help in producing radial flow entry into the test sample.

In the present study a closed circuit system of supply of fluid was adopted. Fluid collecting tank is pumped to the header tank which is discharged to the collecting tank with the help of a connecting pipe. A perforated horizontal pipe fixed at the end of the delivery pipe dampened turbulence. Further, this arrangement does not allow the fluid to fall in the form of a thick jet at one point near the inlet of the fluid in the tank during each run.

Figure1. 50° Convergent Permeameter

Figure 2. Marble

Figure 3. Gravel

IV. Methodology

A converging permeameter is designed and experimented to accomplish the objective of the study. Series of experiments were conducted on porous medium in converging flow permeameter for all regimes of flow. Flow discharge, velocity and hydraulic gradient are calculatedfrom the test data of converging boundary set up.

Test material is filled up to the top of the experimental set up and the porosity of the medium is calculated. Fluid (Water/Diesel) is pumped from bottom tank to inlet of the permeameter and it is allowed to flow through test material. At the starting of test, flow is passed about 1 to 2 hours to get steady state of flow. The liquid is collected in the measuring tank. From the discharge, velocities are calculated at every pressure taping section of the setup. Simultaneously, pressure heads are measured in the manometer board. The area of the flow was calculated by multiplying the observed pressure head with width of the permeameter at that section. Flow velocities are also calculated at every piezometric taping. Temperatures are measured at the outlet of the setup, for calculation of kinematic viscosity. Tests are repeated for different discharges to cover all states of flow. From the test observations, hydraulic gradient, bulk velocity, radius of piezometric location, width of instrument at that piezometric section, bottom level, cross section area, kinematic viscosity, porosity, void ratio, seepage velocity, volume diameter, discharge is estimated.

A. Experimental Step:

i. The test setup is filled with the solid medium, under gravity, to get even packing.

ii. The flow is allowed through the permeameter such that

CVR Journal of Science and Technology, Volume 21, December 2021
DOI: 10.32377/cvrjst2101

a constant head is maintained in the header tank.

iii. A time log of about 15 to 30 minutes is allowed before the readings of piezometric heads are noted, to ensure that no further reorientation of the particles occurs.

iv. Once the flow is stabilized and air bubbles are removed, the time taken for collecting 10 cm depth of fluid in the measuring tank is noted for discharge measurement.

v. Fluid level readings in piezometers are noted. It is used todetermine the head loss through the medium.

vi. The above procedure is repeated for several discharges, for a prescribed size of medium. During every run temperature of outflow is noted.

vii. The test material is removed and the permeameter is filled with another size of test material.

The above steps are repeated for all sizes of the solid media.The observations are tabulated.

V. Results of the Experiment

This section presents the test results in a radial flow setup covering laminar, non-linear laminar, turbulent, transitional regimes of flow through both crushed rock and glass spheres. The analysis is carried out in two stages. While in the first stage volume diameter is used as characteristic length to explain resistance coefficient and Reynolds number, in second stage hydraulic radius is used as characteristic length to explain these two parameters. The following paragraphs enunciate briefly the special features of all the regimes. In laminar regime, viscous forces are very high as compared to inertial fore. The seepage velocity is constant and head loss is proportional to the velocity of flow. Darcy's law is governing equation.

The viscous and inertial force influence the motion in non-linear laminar regime, but due to gradual increase of inertial force, the flow deviates from the linear relationship as suggested by Darcy's law. The seepage velocity is constant, and the state of flow is still laminar phase. Stationary vertices are formed at the top end of the regime. In the turbulent, transitional stage of flow the seepage velocityoscillates with the regular frequency and loss of head dependents more on the velocity square. Inertial actions dominate and vertices are shed at regular intervals from individual particles. Turbulence may begin in phases as the flow velocity is increased. In the fully turbulent phase, the viscous forces practically disappear and only these inertial forces g overn the flow. The seepag e velocity oscillates haphazardly about an average value. The loss of head may be assumed to vary with the square of the velocity. Since fully developed turbulent flow regime had been extensively investigated the same is excluded from the present investigation.

A. Stage – I experimentation:

In the first stage particle volume diameter is used as the characteristic length.

The values of λ_k and Re_k are computed. No difficulty was faced in obtaining lower values of Reynolds (Re_k) number as diesel was one of the fluids used. Further, small size media of sizes 1.65 cm, 1.162 cm are also used.

It facilitates comparison of fitness and trend of the present work. The variation of coefficient of resistance (λ_k) with Reynolds number (Re_k) is less than 10 is depicted in figure 4 gravel diesel.

The values of Reynolds number (Re_k) thus computed for both diesel and water for all sizes of media are segregated into 3 ranges as (i) Less than 10 (ii) Between 10 and l00 and

(iii) Between 100 and 100. By doing so, two objectives are achieved. It adds to the existing literature on low regime flows where there is no much of the work reported with volume diameter as characteristic length in case of high regime flows.

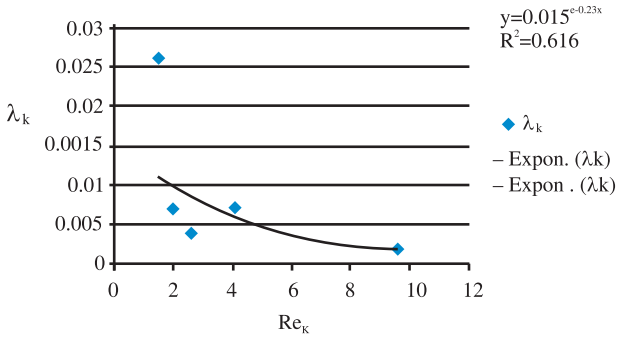

Figure 4. Variation of coefficient of resistance with Reynolds number Re_k less than 10

The data corresponding to present work are seen to lie along a line using method of least squares; an equation is fit to the line which is expressed as

$$\lambda_k = 0.015\ Re^{-.23x} \quad (1)$$

It may be noted that the Reynolds number Re_k in equation is -.23 it indicates that as Reynolds number increases the coefficient of resistance decreases. Theabsolute value of the indexes is 0.015. This infers the coefficient of resistance varies linearly (inversely) with Reynolds number. Comparison of equations shows that in the case of radial laminar flow the numerical constant is 0.015 while in the pipe flow is 64. Therefore, it indicates that the resistance is higher in radial seepage flow comparedto pipe flow, for a given Reynolds number lying in the laminar regime. The tortuous nature of flow channels in a porous medium may be main reason for this observation. The variation of coefficient of resistance with Reynolds number for non-linear regime is shown in figure 4. An equation relating these two parameters is obtained from the method of least squares.

$$\lambda_k = 0.051 Re_k^{-.06x} \quad (2)$$

Equation (2) can however be simplified as

$$\lambda_k = 0.051 Re_k^{-0.6x} \quad (3)$$

Summing up all the above observations, theequations proposed for different regimes are

$$\lambda_k = 0.015 Re_k^{-.23x} \quad (4)$$

$$\lambda_k = 0.05\ Re_k^{-0.6x} \quad (5)$$

Therefore, once the values of Reynolds number for a given

CVR Journal of Science and Technology, Volume 21, December 2021
DOI: 10.32377/cvrjst2101

discharge through medium of known size, is determined from experimental data, then using the corresponding equation the value of coefficient of resistance (λ_k) can be computed.

TABLE I.
STAGE - I (COEFFICIENT OF RESISTANCE AND REYNOLDS NUMBER ARE COMPUTED USING "VOLUME DIAMETER" AS CHARACTERISTIC LENGTH)
Fluid: Water

Material	Parameter	Average values for different permeameter angle			For parallel flow
		70°	60°	50°	
Marble	Re_r	0.0658	0.106	0.134	64
	Λ_r	0.0006	0.00034	0.000222	64
Crushed rock	Re_r	0.116	0.1	0.11	64
	Λ_r	0.0003	0.00055	0.00025	64

TABLE II.
STAGE - II (COEFFICIENT OF RESISTANCE AND REYNOLDS NUMBER ARE COMPUTED USING "HYDRAULIC RADIUS" AS CHARACTERISTIC LENGTH)
Fluid: Diesel

Material	Parameter	Average values for different permeameter angles			For parallel flow
		70°	60°	50°	
Marble	Re_k	10.204	16.888	21.069	64
	λ_k	0.0335	0.00781	0.00595	64
Crushedrock	Re_k	15.66	19.999	23.5	64
	λ_k	0.0809	0.03453	0.02685	64

TABLE III.
COMPARISON OF RE_K AND Λ_K VALUES BETWEEN WATER AND DIESEL
(STAGE–I)

Material	Parameter	Avg. value for different permeameter angles		Avg. value for different permeameter angles		Observed % of variation	
		70^0	60^0	70^0	60^0	70^0	60^0
Marble	Re_k	10.2	16.89	2.25	3.75	78	77.81
	λ_k	0.036	0.008	0.021	0.012	37.91	35.98
Crushed Rock	Re_k	15.66	20.0	4.78	4.28	69.46	78.6
	λ_k	0.081	0.035	0.014	0.022	82.58	37.45

TABLE IV.
COMPARISON OF RE_K AND Λ_K VALUES BETWEEN WATER AND DIESEL
(STAGE–II)

Material	Parameter	Avg. value for different permeameter angles		Avg. value for different permeameter angles		Observed % of variation	
		70^0	60^0	70^0	60^0	70^0	60^0
Marble	Re_k	0.23	0.495	0.066	0.106	77.9	78.56
	λ_k	0.001	0.0002	0.001	0.0003	32.14	33.43
Crushed Rock	Re_k	0.378	0.483	0.116	0.1	69.39	79.3
	λ_k	0.002	0.001	0.0003	0.001	83.83	33.97

VI. CONCLUSIONS

A. *Stage I (Marble):*

- Observed percentage variation of Re_k with 70^0 converging permeameter is 78.
- Percentage variation of 77.81 has been observed in Re_k value with 60^0 converging permeameter.

B. *Stage I (Crushed Rock):*

- Percentage variation of 69.46 has been observed in Re_k value with 70^0 converging permeameter.
- Observed percentage variation of Re_k with 60^0 converging permeameter is 78.6.

C. *Stage II (Marble):*

- Observed percentage variation of Re_r with 70^0 converging permeameter is 77.9.
- Percentage variation of 78.56 has been observed in Re_r value with 60^0 converging permeameter.

D. *Stage II (Crushed Rock):*

- Percentage variation of 69.39 has been observed in Re_r value with 70^0 converging permeameter.
- Observed percentage variation of Re_r with 60^0 converging permeameter is 79.3.

REFERENCES

[1]. Ahmed.N and Sunada D.K "Non-linear flow in porous media", Jr. of Hyd. Div., Proc. ASCE, Hyd, Vol. 96 November, 1969, pp. 1847-1857
[2]. Anandakrishnan.M and Varadarajulu.G, "Laminar and Turbulent flow of water through sand", Jr. of Soil Mech. and Foundation Div. Proc. ASCE, Sept 1963
[3]. Dudgeon.C.R, "An experimental study of flow of water through coarse granular media", La Houllie Blanche,
[4]. Vol. 21, No .7, 1966, p .785
[5]. Hubbert. M.K, "Darcy's law and the field equations of the flow underground fluids", Jr. Petrol. Tech., T.P. 4352, 1956, pp.222.
[6]. Irmay. S, "Theoretical Derivation of Darcy and Forchheimer Formulae", Jr. of Geophysical Research, 1959, Vol.64, N0.4, pp.486.
[7]. Kovacs.G "Seepage Hydraulics of Development in Water Science", ESPC New York, 1981
[8]. Mc Corquodale, J.A, "Finite Element Analysis of Non-Darcy Flow", A Ph.D. thesis presented to the University of Windsor, Canada, 1970
[9]. Niranjan, H.S, "Non-Darcy flow through porous media", M.Tech. Thesis, Civil Engineering Department, IIT, Kanpur, July 1973.
[10]. Pradip Kumar.G.N, "Radial Non-Darcy flow through coarse granular media, a thesis submitted to Sri Venkateswara University, Tirupati, 1994 for the award of degree of Doctor of Philosophy in Civil Engineering.
[11]. Rose.H.E and Rizk.A.M, "Further researches in fluid flow through beds of granular material", Proc. Intuition of Mechanical Engineers, London, No.160, 1949, p.493.
[12]. Rizk, A.M. and Rose, H.E, "Further researches of fluid through beds of granular material", Proc. Institution. Mechanical Engineers, London, No.160, 949, pp.493.
[13]. Wright, D.E. "Non-linear flow through granular media", Jr. of Hyd. Div. ASCE Vol.94, No. HY4, July 1968.

E-ISSN 2581 – 7957
P-ISSN 2277 – 3916
CVR Journal of Science and Technology, Volume 21, December 2021
DOI:10.32377/cvrjst2102

Effect of Egg Shell Powder on Index and Engineering Properties of Clayey Soil

M. Ashok Kumar[1] and Batchu Ramanjaneyulu[2]
[1]Asst. Professor, CVR College of Engineering/Civil Engg. Department, Hyderabad, India
Email: ashokdilip2012@gmail.com
[2]Asst. Professor, CVR College of Engineering/Civil Engg. Department, Hyderabad, India
Email: ramanji139@gmail.com

Abstract: **Eggshell powder is used as an additive to combine with clayey soil so that properties like compaction and shear strength of clayey soil are investigated at 0%,3%,5%& 10% to the weight of soil. It is more efficient & economical both in terms of cost and energy to increase the bearing capacity of the soil rather than going for different deep foundations.**

Index Terms: **Egg shell powder-ESP, Clayey soil, Index properties, Engineering properties, Optimum Moisture content-OMC, Maximum dry density-MDD.**

I. Introduction

Construction on Clayey Soil Appears to be difficult, as it possesses low strength and high compressibility when water content increases with the advancement of science, materials, and equipment, soil stabilisation has begun to take on a new form, where egg shell powder is one among them. It is becoming a common and cost-effective soil improvement technique. "Ref. [1]" To investigate the properties of the soil in terms of liquid limit, plastic limit, optimal moisture content, maximum dry density, and direct shear strength, as well as to see how eggshell powder in different percentages affects these properties such as Liquid limit, Plastic limit, Optimum moisture content, maximum dry density, direct shear strength.

II. Materials used and Methodology Adopted

A. Black Cotton Soil

Black cotton soils are inorganic clays of medium to high compressibility and form a major soil group in India. They are characterized by high shrinkage and swelling properties. Most of the expansive soils are rich in montmorillonite and a few amounts in illite. The black cotton soil is collected from Ibrahimpatanam, Ranga Reddy, Hyderabad.

B. Egg Shell Powder

"Ref. [3]" Eggshell powder primarily contains CaO (99.83%) and the remaining consists of Al2O3, SiO2, Cl, Cr2O3, MnO andCuO. ESP has not been used as stabilizing material, but it could be a good replacement for industrial lime. Egg shell waste was washed and dried before grinding. Egg shell powder was sieved using IS Sieve No.200 (75µ), and the powder passing the sieve 75µis used.

Egg shell powder

C. Methodology Adopted

Different tests are conducted on virgin soil to determine its index & Engineering properties. "Ref. [5]" Then after, tests are done by adding Egg shell powder at 3%, 5% and 10% to the dry weight of soil. Results from the above-mentioned tests are compared and analyzed the effect of ESP on soil.

D. Tests Performed on Soil Samples

1)Atterberg'sLimits

"Ref. [4]" The measure of essential water contents of a fine-grained soil is described by Atterberg's limits. Soil can appear in a variety of forms depending on its water content. They are solid, semi-solid, plastic and liquid.

a) *Liquid Limit:*

Liquid Limit is the water content at which soil changes from a plastic to a liquid state when the soil specimen is just fluid enough for a groove to close when jarred in a specified manner.

b) *Plastic Limit:*

The moisture content of a soil at the boundary between the plastic and semi-solid states of consistency is expressed as a percentage of the weight of the oven-dry soil. When rolled into a thread, it's the moisture content at which a soil starts to crumble.

2) Standard Proctor Test

The Proctor compaction test is a laboratory method for determining the optimum moisture content at which a particular soil type will become most dense and reach its maximum dry density.

Calculations:

Bulk density of soil: $\Upsilon = (W_2-W_1)/ 1000$

Dry density of soil: $\Upsilon_d = \Upsilon / (1+w)$

Where w = moisture content present in soil.

Received on 23-02-2021, Revised on 23-03-2021, Accepted on 10-05-2021.

E-ISSN 2581 – 7957
P-ISSN 2277 – 3916

DOI:10.32377/cvrjst2102

III. Experimental Results of Samples

A. Atterberg's Limits

(1) Liquid Limit:

Table 1 show the Liquid limits values for natural soils which is done in four trials.

TABLE I.
LIQUID LIMIT VALUES FOR NATURAL SOILS

Trials	1	2	3	4
W1(g.)	38.97	38.19	37.6	28.18
W2(g.)	47.11	48.58	47.73	38.11
W3(g.)	43.55	44.3	43.65	34.18
(W2-W3) (g.)	3.46	4.28	4.08	3.93
(W3-W1) (g.)	4.68	6.11	6.05	6.0
W(%)	73.93	70	67.4	65.5
N	16	20	26	32

Where
W1=Weight of container
W2=Weight of container+Wet soil
W3=Weight of container+Dry soil
(W2-W3)=Weight of water
(W3-W1)=Weight of dry soil
w(%)=Moisture content
N=Number of blows

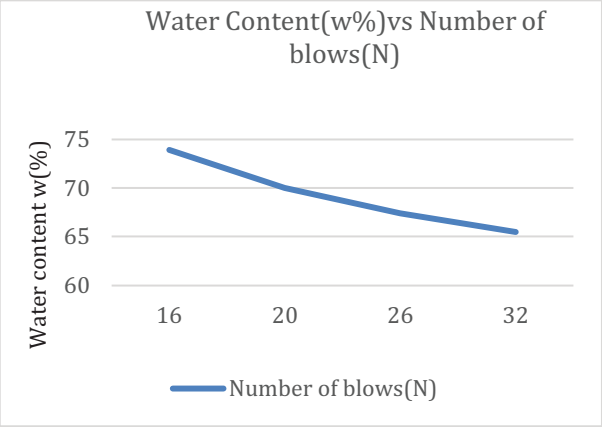

Figure 1. Liquid limit graph for natural soils

The variation of liquid limit can be observed from figure 1 which shows the variation of blows with water content.

Values of Liquid limit for soil with addition of 3% Egg Shell powder is shown in table II.

TABLE II.
LIQUID LIMIT VALUE OF SOIL ADDED WITH 3% OF ESP

Trials	1	2	3	4
W1(g.)	27	28	37.8	27
W2(g.)	63	57	77	38.9
W3(g.)	48.56	45.72	61.64	34.29
(W2-W3) (g.)	14.44	11.28	15.36	4.61
(W3-W1)	21.56	17.72	23.84	7.29
w(%)	66.9	63.48	64.4	63.23
N	10	23	30	41

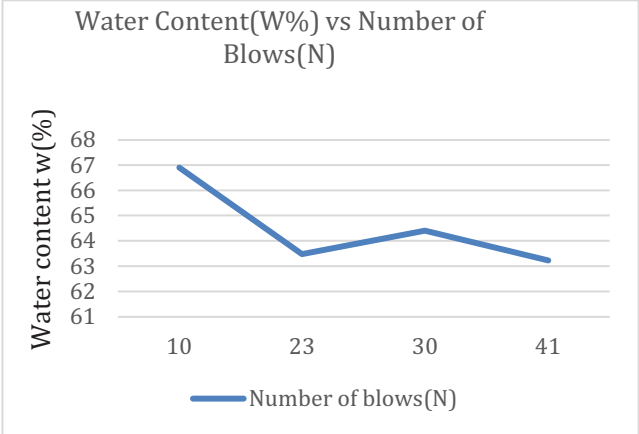

Figure 2. Liquid limit variation for soil with 3% of ESP

Figure 2 shows the variation of blows with water content by the addition of ESP at 3%.

TABLE III.
LIQUID LIMIT VALUE OF SOIL ADDED WITH 5% OF ESP

Trials	1	2	3	4
W1(g.)	39.06	38.5	33.1	27.2
W2(g.)	61.09	60.53	55.3	48
W3(g.)	53.75	53.1	47.8	41
(W2-W3) (g.)	7.34	7.43	7.5	7
(W3-W1) (g.)	14.69	14.6	14.7	13.8
w(%)	50.1	50.8	51.02	50.7
N	15	21	35	42

CVR Journal of Science and Technology, Volume 21, December 2021
DOI:10.32377/cvrjst2102

Table III shows the Liquid limits values for soil added with 5% ESP done in four trials. We can observe the reduction in Liquid limit value with increase in ESP.

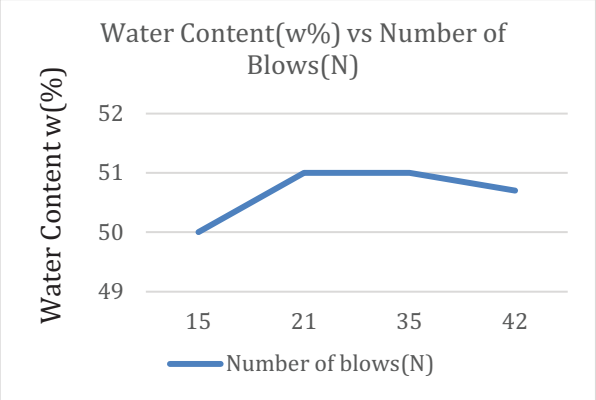

Figure 3. Liquid Limit Variation for Soil With 5% Of ESP

The variation of blows with water content can be seen from fig 3. Reduction of blows can be seen with increase in ESP.
Variation of Liquid limit with addition of 10% ESP can be seen from table IV.

TABLE IV.

LIQUID LIMIT VALUE OF SOIL WITH 10% OF ESP

Trials	**1**	**2**	**3**	**4**
W1(g.)	13.24	12.56	13.53	13.26
W2(g.)	54.92	53.02	53.06	45.12
W3(g.)	42.00	40.68	41.28	35.74
(W2-W3) g.)	28.76	28.12	27.75	22.53
(W3-W1) g.)	12.92	12.34	11.78	9.33
w(%)	44.95	43.91	42.45	41.40
N	18	23	30	35

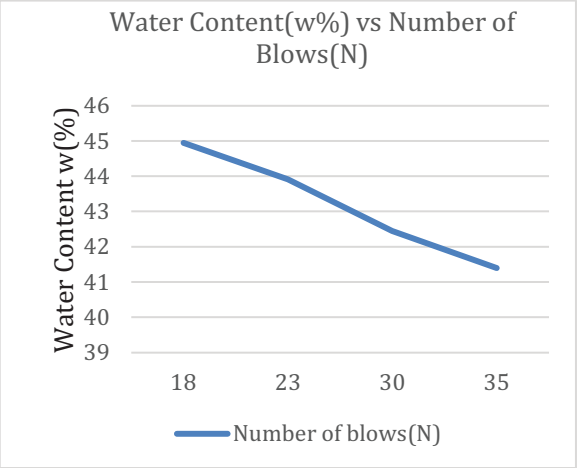

Figure 4. Liquid limit variation for soil with 10% of ESP

Figure 4 shows the variation of blows with water content and we can see the reduction of blows with the addition of ESP.

(2) Plastic Limit:

Plastic limit values for natural soil

W1(g)	**W2(g)**	**W3(g)**	**w(%)**
25.54	29.4	28.7	22.38

Plastic limit values of soil with 3% ESP

W1(g)	**W2(g)**	**W3(g)**	**w(%)**
37.9	40.7	40.1	27.27

Plastic limit values of soil with 5% ESP

W1(g)	**W2(g)**	**W3(g)**	**w(%)**
38.8	43.2	42.14	31.73

Plastic limit values of soil with 10% ESP

W1(g)	**W2(g)**	**W3(g)**	**w(%)**
26.6	28.6	28.1	33.33

(3)Plasticity Index:

Plasticity index values for natural soils

PI = LL-PL
=67.61%-22.38%
=45.23%

Where PI=Plasticity index
LL=Liquid limit
PL=Plastic limit

Plasticity index of soil added 3% ESP

PI = LL-PL
=63.8%-27.27%
=36.53%

Plasticity index of soil added 5% ESP

PI = LL-PL
=51%-31.73%
=19.27%

Plasticity index of soil added 10% ESP

PI = LL-PL
=43.2%-33.33%
=9.87%

B. Standard Proctor Test

The soil to be tested is oven dried to remove the natural moisture content in the soil. To the oven dried sample fixed ESP and water content ranging from 12% to 21% (i.e,12%,15%,18%,21%)are added to the dry weight of soil.

Table V shows the values of optimum moisture content(OMC) and maximum dry density for natural soils. Four trails are done to get the average valuesw of OMC and max. dry density.

CVR Journal of Science and Technology, Volume 21, December 2021
DOI:10.32377/cvrjst2102

TABLE V.
VARIATION OF DRY DENSITY FOR NATURAL SOIL

Details	1	2	3	4
Water to be added(%)	20	23	26	29
Weight of water (g)	500	575	725	800
Weight of compacted soil(g)	1655	1672	1744	1765
Water content(%)	24.9	27.2	30.06	32.4
Wet density(g/cc)	1.655	1.744	1.806	1.827
Dry density(g/cc)	1.325	1.360	1.388	1.379

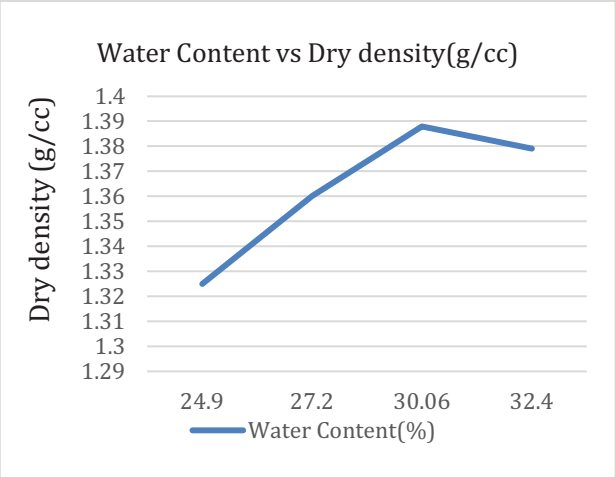

Figure5. Variation of Dry density with water content for natural soil

The variation of dry density and OMC can be seen from the figure 5. Dry density goes on increasing with increase in water content up to 30.06% and it falls gradually with further increase in water content.

TABLE VI.
VARIATION OF DRY DENSITY FOR SOIL WITH 3% ESP

Details	1	2	3	4
Water to be added(%)	18	21	24	27
Weight of water (g)	450	525	600	675
Weight of compacted soil(g)	1595	1619	1745	1735
Water content(%)	23	24.2	28.6	31.4
Wet density(g/cc)	1.65	1.67	1.807	1.796
Dry density(g/cc)	1.347	1.348	1.404	1.369

The variation of dry density and OMC with addition of 3% ESP can be seen from Table 6. The value of OMC is increased with decrease in water content and can be seen from figure 6.

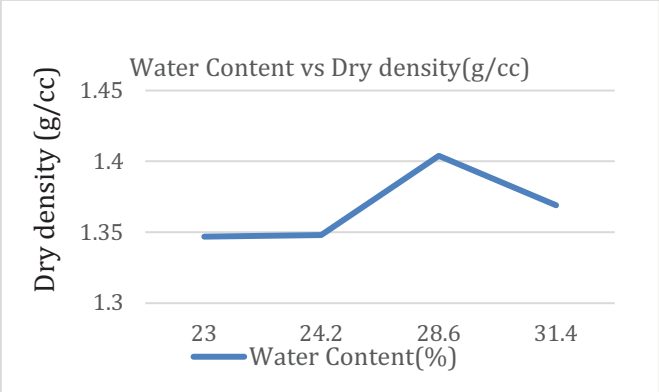

Figure 6. Variation of Dry density with water content for soil with 3% of ESP

TABLE VII.
VARIATION OF DRY DENSITY FOR SOIL WITH 5% ESP

Details	1	2	3	4
Water to be added(%)	15	18	21	24
Weight of water (gm)	375	450	525	600
Weight of compacted soil(gm)	1477	1619	1745	1735
Water content %)	19.2	22.19	25.6	28.6
Wet density(g/cc)	1.501	1.688	1.829	1.796
Dry density(g/cc)	1.282	1.256	1.456	1.43

Table 7 shows the values of water content and dry density after the addition of 5% ESP to the soil.

The variation of dry density and OMC with addition of 5% ESP can be seen from the figure 7.

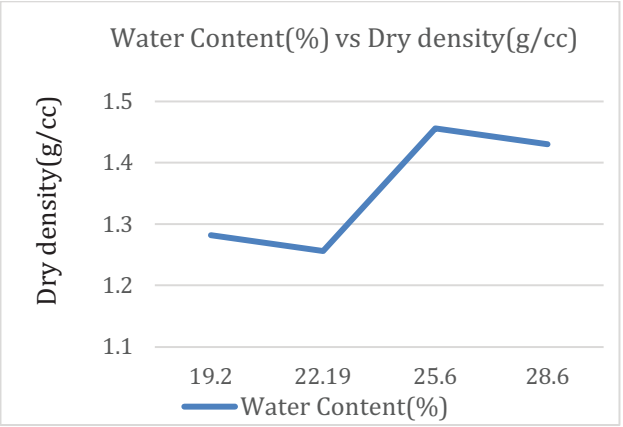

Figure 7. Variation of Dry density with water content for soil with 5% of ESP

CVR Journal of Science and Technology, Volume 21, December 2021
DOI:10.32377/cvrjst2102

TABLE VIII.

VARIATION OF DRY DENSITY FOR SOIL WITH 10% ESP

Details	1	2	3	4
Water to be added(%)	12	15	18	21
Weight of water (g)	300	375	450	525
Weight of compacted soil(g)	1500	1713	1542	1520
Water content (%)	17.24	19.95	21.6	23.39
Wet density(g/cc)	1.48	1.691	1.522	1.501
Dry density(g/cc)	1.26	1.41	1.33	1.217

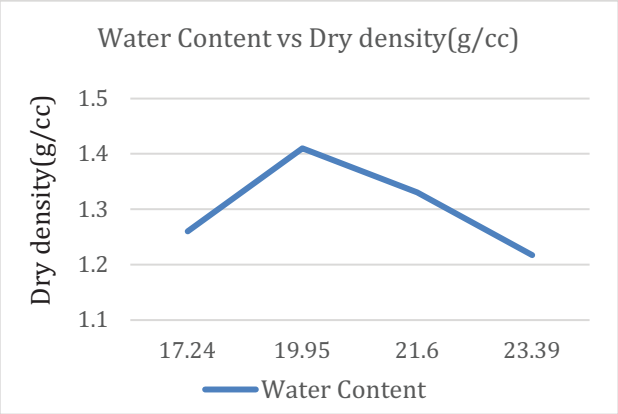

Figure 8. Variation of Dry density with water content for soil with 10% of ESP

IV. EXPERIMENTAL ANALYSIS OF SAMPLES

A. *Influence of ESP on Atterberg's limits*

Atterberg limits got altered after the addition of ESP at various percentages. The variation of Atterberg limits with different percentages of ESP is shown in Table IX. Noticeable reduction in Liquid limit, Plastic limit & Plasticity index can be seen from Figure 9.

TABLE IX.

VARIATION OF ATTERBERG'S LIMITS OF SOIL WITH DIFFERENT ESP %

ESP(%)	**Liquid limit(%)**	**Plastic limit(%)**	**Plasticity index(%)**
0	67.6	22.38	45.23
3	63.8	27.27	36.53
5	51	31.73	19.27
10	43.2	33.33	9.87

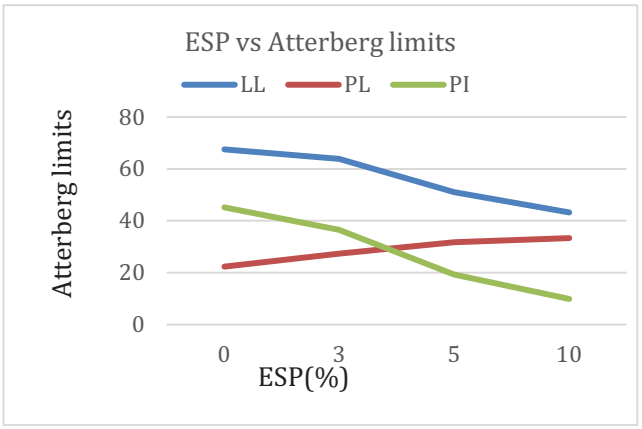

Figure 9. Variation of Atterberg limits with 0%,3%,5%,10% of ESP to the soil

Table X shows the variation of OMC and MDD with the variation of ESP in percentages and the considerable rise in MDD with reduction in OMC can be observed.

TABLE X.

VARIATION MOISTURE CONTENT AND MAXIMUM DENSITY AT DIFFERENT PERCENTAGES OF ESP

ESP(%)	Optimum moisture content (%)	Maximum dry density(g/cc)
0	30.6	1.383
3	28.6	1.404
5	25.6	1.376
10	19.95	1.41

It can be clearly seen from Figure 10 that OMC of soil is decreased with increase in ESP.

Figure 11 shows the variation of MDD with increment in ESP. An initial rise in MDD is observed with addition of ESP. It started to fall with the increment of ESP and reached the maximum value at 10% of ESP.

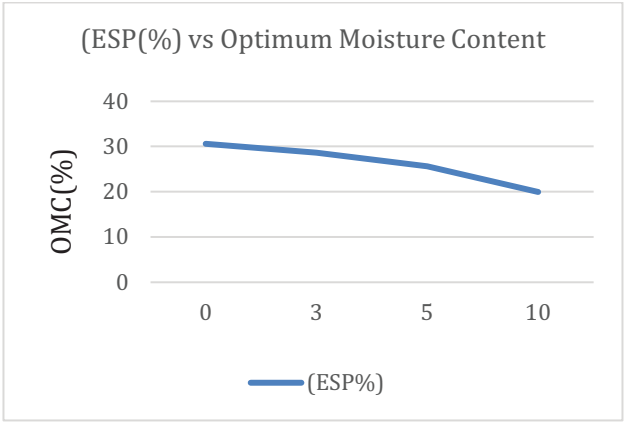

Figure 10. Variation of Optimum moisture content in soil with different percentages of ESP

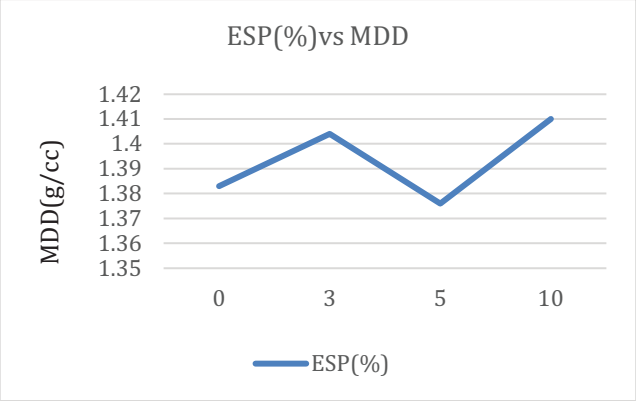

Figure11. Variation of Maximum dry density in soil with different percentages of ESP

V. Conclusions

- The liquid limit value decreased gradually due to the increase in the porous property of eggshell powder when the eggshell powder is added. The plastic limit value increased gradually when the eggshell powder is added to the soil that consequently resulted in the reduction of plasticity index, which is an indication of improvement of soil property.
- The initial increase in the dry density indicates the improvements in the soil properties and further resulted in the enhancement of soil properties with the application of eggshell powder.
- The initial decrease in OMC is due to the absorption capacity of the eggshell powder due to its porous properties. The subsequent increase is a result of the pozzolanic action of eggshell powder with addition of varying percentages of ESP.
- Thus, the use of ESP can improve both index & engineering properties of soil.

References

[1] Amu O. O, Fajobi A. B, and Oke B.O (2005). "Effect of Eggshell Powder on the Stabilizing Potential of Lime on an Expansive Clay Soil." Research Journal of Agriculture and Biological Sciences, 1(1), pp 80-84.

[2] Amu O.O and Salamy B.A, (2010)." Effectof Common Salt on Some Engineering Properties of Eggshell Stabilized Lateritic Soil." ARPN Journal of Engineering and Applied Sciences, 5(9), pp 64-73.

[3] CroftC.P.,McGeoryandD.HCarlson(1999)."Physical Geology". McGraw Hill companies Inc. New York,8, pp 48-56.

[4] J.Olarewaju,M.O.BalogunandS.O.Akinlolu(2011). "Suitability of Eggshell Stabilized Lateritic Soil as Subgrade Material for Road Construction." Civil Engineering Programme, 16(2011), pp 899-908.

[5] E. Nyankson1, 2, B. Agyei-Tuffour1, 3, E. Annan1, 3, D. Dodoo-Arhin1, A. Yaya1, L. D. Brefo1, E. S. Okpoti1 & E.Odan (2013)." Characteristics of Stabilized ShrinkSwell Deposits Using Eggshell Powder." Global Journal of Engineering Design and Technology 2(3), pp 1-7.

[6] KarthikaPrasad,NissyMathachan,(2016) "Effectof Curing on Soil Stabilized with egg shell"IJRSTvol2, Issue 12.

[7] Amer Ali Al-Rawas(2005) "Effect of lime, cement and Sarooj (artificial pozzolan) on the swelling potential of an expansive soil from Oman" Building and Environment Vol 40, Issue 5.

[8] E. Nyankson1, 2, B. Agyei-Tuffour1, 3, E. Annan1, 3, D. Dodoo-Arhin1(2013) "Characteristicsof Stabilized soil"

[9] Shrink-Swell Deposits Using Eggshell Powder" G.J. E.D.T., Vol. 2(3).

E-ISSN 2581 – 7957
P-ISSN 2277 – 3916

CVR Journal of Science and Technology, Volume 21, December 2021
DOI: 10.32377/cvrjst2103

Seismic Analysis of Underground Reinforced Concrete Highway Tunnels with Different Shape Openings using Curved Arch Concept

Nalamadha. Mahesh Yadav[1] and J. Sandhya Rani[2]
[1]PG Scholar, CVR College of Engineering/Civil Engg. Department, Hyderabad, India
Email: nalamadhamahesh@gmail.com
[2]Asst. Professor, CVR College of Engineering/Civil Engg. Department, Hyderabad, India
Email: Sandhyajaligama25@gmail.com

Abstract: **A tunnel is an underground passageway, dug through the surrounding soil/earth/rock and enclosed except for entrance and exit, commonly at each end. Now-a-days, tunnels are being used for many purposes like roadway, railway tracks, for canal etc. Tunnels help in reducing the distance between any two places. In this research work, Seismic analysis of tunnel was carried out for different shape openings of tunnel using curved arch concept. The design and analysis work has been carried out using SAP-2000 package. Analysis of different type of tunnels for seismic loading is done for the variation of the stresses, moments and displacements. Same process was followed for the tunnel shapes and based on results; the best and stronger tunnel is specified. This paper mainly concentrates on the variation of displacements and stresses under static loading conditions and efficiency under static loads.**

Index Terms: **Underground tunnels, response of structure, design and analysis, displacements, stresses, SAP-2000**

I. Introduction

Seismic analysis of tunnels is important for safety evaluation of the tunnel structure during earthquakes. Simplified models of tunnels are commonly adopted in seismic design by practitioners, in which the tunnel is usually assumed as a beam supported by the ground. These models are made to run in real time to give a virtual response close to the actual system. However, simplified methods are limited due to the assumptions that need to be made to reach the solution, e.g., shield tunnels are assembled with segments and bolts to make a lining ring and such structural details might not be included within the simplified model.

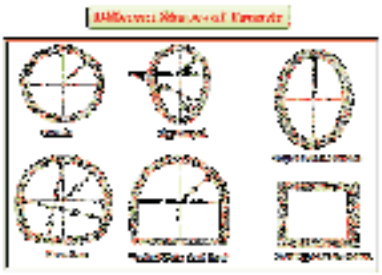

Figure 1. Different shapes of tunnel

A reliable evaluation of the seismic response of tunnel structures is crucial in civil and earthquake engineering. As the structural design has shifted to the performance design in recent years, the seismic design, accounting for the soil–structure interaction (SSI) effects, becomes more important. The presence of a tunnel structure considerably modifies the free field ground motion leading to a different seismic response of the tunnel lining. This phenomenon is related to the combined effects of the kinematic interaction and the dynamic (inertial) interaction. The kinematic interaction is influenced by the inability of a structure to match the free field deformation. The dynamic interaction is caused by the existence of a structural mass making the effect of inertial force on the response of the surrounding environment, in which case dynamic forces in the tunnel's structure cause the tunnel to deform the soil, thus producing stress waves that travel away from the structure (radiation damping).

Figure 2. Cross-sectional view of a general tunnel

A. Objectives:

- To study the variation of stresses, moments and displacements of the tunnel.
- To compare the variations of structure parameters analyzed using SAP-2000.
- To verify that which cross section is more efficient and strongest.
- To suggest the improvements and remedies.

B. Scope:

In the static analysis of tunnel pore water pressure can also be considered and carry the analysis by applying the pore water pressure all over the tunnel slab.

II. Literature Review

Seismic Damage Analysis of Box Metro Tunnels Accounting for Aspect Ratio and Shear failure by Duy-Duan Nguyen, Tae-Hyung Lee, Van-Quang Nguyen and Duhee Park**.** In this paper they performed a series of inelastic frame analysis for single, double and triple concrete

Received on 28-08-2021, Revised on 23-10-2021, Accepted on 22-11-2021.

CVR Journal of Science and Technology, Volume 21, December 2021
DOI: 10.32377/cvrjst2103

reinforced box tunnel focus mainly on the influence of aspect ratio of box tunnels and shear structural failure. Here, flexural failure is considered with an aspect ratio of 1 for the damage analysis of box tunnels. As per their analysis only flexural failures occurs in single box tunnels, whereas for double and triple box tunnels shear structural failures occurs at the inner column. structural collapse is not found for single box tunnels. It is also proved that the increase in the aspect ratio leads to increase in the seismic resistance. It is also proposed revised damage indices (DIs) corresponding to three damage states for single box tunnels. Here, DI is the ratio of elastic moment to yield moment.[1]

Finite Element Seismic Analysis of Cylindrical Tunnel in Sandy Soils with Consideration of Soil-Tunnel Interaction by M. Saleh Asheghabadi and H. Matinmanesh, Department of civil engineering, Islamic Azad University, Njafabad branch, Isfahan, Iran. Distribution of Seismic waves from the bedrock through the soil layers can cause severe damages to the structures not only on the soil surface but also to subsurface structures. This paper presents an idealized two-dimensional plain strain finite element seismic soil-tunnel interaction analysis using ABAQUS v.6.8 program. The analysis performed by considering three actual ground motion records representing seismic motions with low, intermediate, and high frequency content. Two different sandy soils i,e. dense and loose sand have been modelled. In order to consider the effect of soil-tunnel interaction, all of the analysis was performed for without tunnel condition and compared with models including tunnel. Influence of different subsoil's dense and loose sand in each actual ground motion record has been investigated on amplification, acceleration response and stress and strain propagation on the soil-tunnel interface. Results illustrate that existence of tunnel amplifies the seismic waves on the soil surface and the maximum amplification occurs on the interface of the tunnel and soil.[2]

Seismic analysis of dynamic structure-soil-tunnel interaction for a case of the Thessaloniki Metro by D. Lončarević, E. Bilotta & F. Silvestri, University of Naples Federico II, Naples, Italy; G. Tsinidis University of Sannio, Benevento, Italy. This paper studies the dynamic interaction between an underground metro station and a building with basement which are at a distance. This paper studies, the effect of building on the metro station when subjected to seismic excitation in the transversal direction. They have considered a real case study of metro station in Thessaloniki, Greece. This metro structure is analyzed under plain strain conditions using ABAQUS software and the building is simulated as an equivalent single degree of freedom oscillator. The results obtained by this analysis are compared with the results obtained by the analysis of underground structure without considering the building aside. By this comparison, we can identify and quantify the effects of the dynamic interaction between the structures on the racking response of the station. The analytical result indicates a general increase of seismic response of the station due to the presence of the building.[3]

Numerical Modeling of the transverse dynamic behavior of circular tunnels in clayey soils by A. Amorosi, D. Boldini. In this paper, they went with different approaches aimed at investigating the dynamic behavior of circular tunnels in transverse direction. Cases referring to a shallow tunnel built in two different clayey soils are analyzed. The adopted approach includes 1D numerical analysis performed modelling the soil as a single phase visco-elastic non-linear medium, the results of which were then used to evaluate the input data for selected analytical solutions proposed in the literature, and 2D fully coupled FE simulations adopting visco-elastic and visco-elasto-plastic effective stress models for the soil. The results were proposed in terms of seismic-induced loads in the transverse direction of the tunnel lining. Particularly the plasticity-based analysis indicates that a seismic event can produce a substantial modification of loads acting on the lining, leading to permanent increments of both hoop pressure/force and bending moment.[4].

III. Methodology

1) In this study analysis of tunnels with different shape openings was carried out using SAP-2000.
2) Some dimensions for tunnel shapes with the reference of some standard journals are taken into consideration.
3) And also, the specifications for seismic load application.
4) A grid is created with required dimensions.
5) With that grid and dimensions, tunnel shapes in SAP-2000 are modelled.
6) After the shapes were modeled, define materials i.e., soil details which is to be applied on the tunnel.
7) Now define the load cases i.e., soil and earthquake load in X-direction.
8) Fix the joints which are at the bottom of the tunnel and in contact with the soil.
9) The load coming on to the tunnel from above is soil pressure.
10) Loads coming from sides are known as active earth pressure.
11) Calculate the soil loads from top and active earth pressures.
12) Apply the loads calculated at the respective joints.
13) Define a diaphragm in the joint constraints.
14) Now all set to go for seismic analysis of tunnel.
15) Now run the analysis program and note down the results.
16) Take out the displacement values of the tunnels, stresses and moments also.
17) Study the obtained results and make a conclusion.
18) Suggest remedy measures needed.

IV. Calculation of Loads Acting on the Tunnel

In this research I considered a 3m soil layer on the tunnel. And net weight of soil is 20KN/m^2. Tunnel is covered with soil on all sides which act as a backfill of a retaining wall. So, here active earth pressure is also acting on the tunnel, and on the slab total soil load will act. Below is the clear picture of loads acting on the tunnel.

Active earth pressure coefficient, K_a = 1/3

Passive earth pressure coefficient, K_p= 3

Forces coming onto the tunnel by the soil layer can be calculated as below.

Earth pressure acting on slab, $\sigma = \rho gH = \gamma H$ (KN/m^2)

Active earth pressure acting on retaining wall,

$\sigma_a = K_a \rho gH = K_a \gamma H$ (KN/m^2)

Load acting on the slab, $\sigma = 20*3 = 60$ KN/m^2

So, the total load acting on the slab = 60*(8*30) = 14,400 KN

Now coming to the loads on the side slabs or retaining walls, as we go down or deeper from the top of the soil surface the active earth pressure acting on the walls get increasing. That variation of loads is as shown below. And variation of loads is same on both sides as the tunnel is symmetric. Depth "**H**'' is from top of the soil layer.

At 3m, $\sigma_a = 1/3*20*3 = 20$ KN/m^2
At 4m, $\sigma_a = 1/3*20*4 = 26.67$ KN/m^2
At 5m, $\sigma_a = 1/3*20*5 = 33.33$ KN/m^2
At 6m, $\sigma_a = 1/3*20*6 = 40$ KN/m^2
At 7m, $\sigma_a = 1/3*20*7 = 46.67$ KN/m^2
At 8m, $\sigma_a = 1/3*20*8 = 53.33$ KN/m^2
At 9m, $\sigma_a = 1/3*20*9 = 60$ KN/m^2
At 10m, $\sigma_a = 1/3*20*10 = 66.67$ KN/m^2
At 11m, $\sigma_a = 1/3*20*11 = 73.33$ KN/m^2

V. Analytical Study

To achieve same height for all the tunnels, base width must vary from tunnel to tunnel. Make sure that height of all tunnels is same. Then, modeling of tunnel shapes using the finite element software can be done. Use SAP-2000 for modeling and analysis. Dimensions are mentioned as below,

Height of the tunnel - 8m
Length of the tunnel - 30m
Width of the tunnel - varies from shape to shape

After taking the dimensions, note concrete grade, steel specifications and also tunnel lining thickness.

Thickness of tunnel lining – 0.3m
Grade of concrete – M50
Grade of steel – HYSD 415
No of layers of reinforcement – 2
Diameter of steel – 20d
Clear cover – 50mm

After completing the modeling part soil data from some journals is collected.

Thickness of soil layer above the tunnel – 3m
Type of soil – type II (medium hard clay soil)

Soil properties:

Weight per unit volume of soil=20 KN/m^3
Poisson ratio = 0.3
Modulus of elasticity, E = 65000 N/m^2
Cohesion, C = 3
Friction angle, $\phi = 30^0$

From the above the tunnel, the load is soil load which directly acts vertically downwards on the tunnel. And the soil load coming from sides is Active earth pressure (P_a). Calculate the earth pressures at every joint corresponding to their height from the top of the soil surface.

Soil pressure of soil on the slab of tunnel, $P = \gamma*H$

Active earth pressure, $P_a = 1/3 *\gamma*H$

Here, γ = unit weight of soil

H = depth of the respected joint from the soil layer surface above the tunnel

Calculate the loads at the points considered. Now follow the procedure for specifying soil data, fixing the bottom joints with the soil, defining load cases, load application and applying diaphragm.

- ➔ Define – Materials – Add new material – Reg ion & material type – give soil details – ok (material defined)

After defining the material properties, we need to define the load patterns.

- ➔ Define – load patterns – define soil & earthquake loads – give earthquake load specifications – ok (load patterns are defined)
- ➔ For the application of earthquake load the specifications considered for this study are:
- ➔ IS code 1893-2002 (part 1)
- ➔ Seismic zone – II
- ➔ Seismic zone factor, Z – 0.1(Hyderabad)
- ➔ Importance factor, I – 1.5
- ➔ Soil type – II
- ➔ Select joints to be fixed – go to Assign – joints – Restraints - Fixed – ok.
- ➔ Select joints on which loads to be applied – Assign – joint load – forces – select Soil load – give loads – ok.
- ➔ Select area of loading – Assign – Area loads – Uniform (shell) – Soil load – enter load amount – ok.
- ➔ Select all the joints – Assign – Joint – Constraints – Define joint constraint – Diaphragm – ok.

Now it's all set for analysis of tunnel structure. Confirm all the loads, diaphragms etc., once again. Then Run the analysis. The deformed shape of the structure will show up. Go to display command and set deformed shape with contours, moment diagrams with values, stress diagrams with contours and values, displacement contour and axial force variation with values.

Using the above data, the tunnel modeling in SAP-2000 is done. And those models are as shown below with cross section view and three-dimensional view.

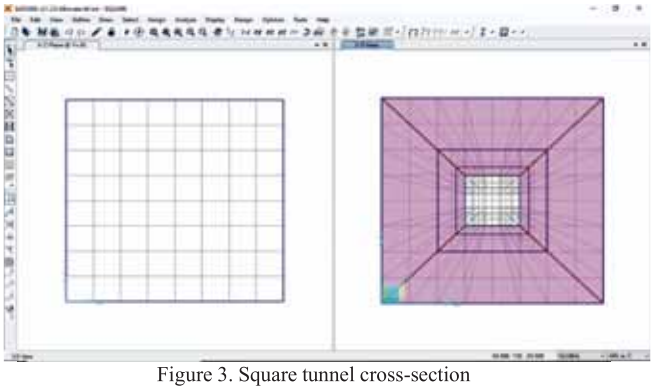

Figure 3. Square tunnel cross-section

CVR Journal of Science and Technology, Volume 21, December 2021
DOI: 10.32377/cvrjst2103

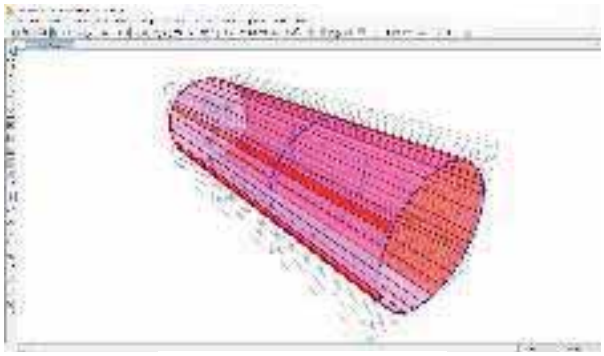

Figure 4. Circular tunnel-3D view

Similarly the Rectangular, Semi-circular, 3/4th circular, Vertical walls-arch roof, Vertical walls-semi circular arch and elliptical tunnel shapes are designed.

VI. Results and Discussions

The analysis carried out was linear static analysis. After running the analysis, the results of deformation, moments and stress variations with their diagrams and contours are obtained as shown below.

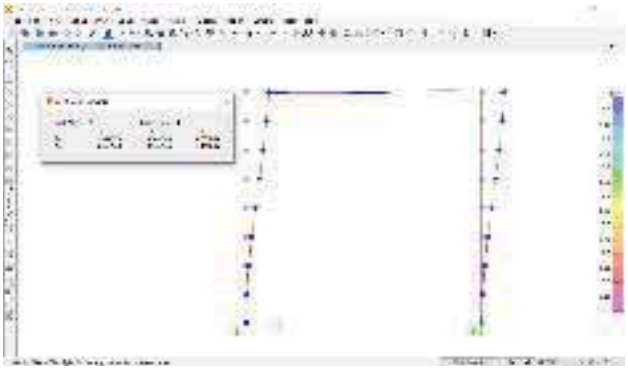

Figure 5. Square Tunnel - Deformed shape

As seen from **Figure 5** the deflection curve of Square tunnel from origin means base point and there is an increment in the deflection of the curve. Consider earthquake wave in X-direction, tunnel lean towards positive X-axis. Deflection at base is 0 and max deflection at the top is 7.8mm.

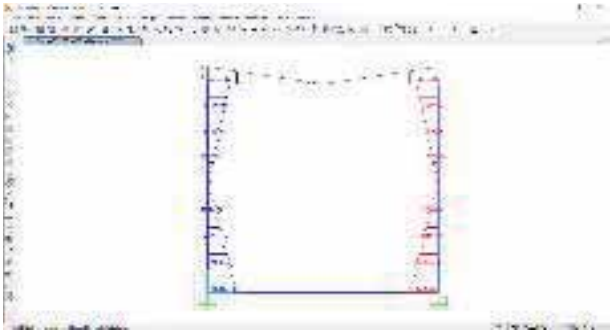

Figure 6. Square Tunnel - Stress variation values

As seen from **Figure 6** stress diagram, on left side stress value is max at the fixed base. We go up stress gets reduced and become min at midpoint and again increasing from there to top. Positive stress indicates tension force. So left half of the tunnel subjected to tension during earthquake load. On the right half of tunnel from bottom to top stresses are negative.

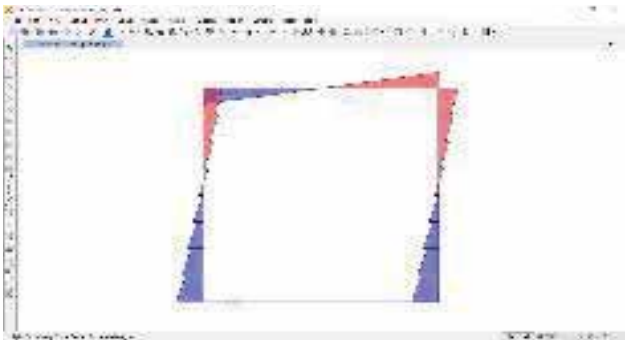

Figure 7. Square Tunnel – moment diagram

Positive (+ve) moment indicates sagging and negative(-ve) moment indicates hogging of the curve. So, from **Figure 7** we can observe, on left side at base moment is max. The moment gets reduced and changes its sign and become –ve in the upper part of the curve. That point is known as point of **contra flexure**. Negative moments are continued up to top and become max. That –ve moments indicates happening of hogging. Coming to the slab part from left to right sagging (+ve moments) and hogging (-ve) can be observed. Right flank is similar to left one, same moment variation can be observed.

TABLE I.
Results Obtained From Analysis– Square Tunnel

Ht. from base(m)	Deformation (mm)	Moment (KN-m)	Stress (KN/m^2)
0	0	15.39	3429
1	3	12.14	2282.38
2	10	8.88	1570.18
3	21	5.63	801.28
4	34	2	135.51
5	47	-2.72	634.77
6	60	-5.6	1301.58
7	70	-8.24	1863
8	78	10.56&985	-2190.26
8	78	-9.85&-10.56	-2203
7	70	-8.24	-1712.86
6	60	-5.6	-908.3
5	47	-2.72	-254.74
4	34	2	-590.89
3	21	5.63	-1277.8
2	10	8.88	-2022.14
1	3	12.14	-2933.29
0	0	15.39	-3429.48

CVR Journal of Science and Technology, Volume 21, December 2021
DOI: 10.32377/cvrjst2103

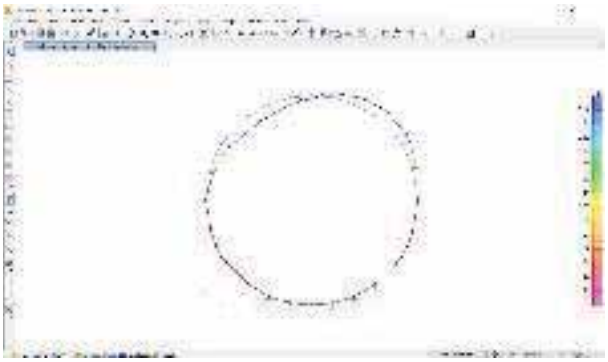

Figure 8. Circular Tunnel – Deformed shape

From **Figure 8**, deflection variation of tunnel can be observed. Some of the base joints are fixed which are having no deflection. After fixed joints deflection increases from the base. The deflection at the top joint is 0. And same deflection variation can be seen on the right half of the tunnel. Max deflection is 0.3mm at 6m from base.

Figure 9 is stress variation diagram of circular tunnel. Coming to stress variation Left half has +ve stresses and it is pure tension. Max stress is at bottom and min stress 90km/m2 is at top. Similarly, on the fright side stresses are – ve from middle to bottom. It indicates compression at the bottom only.

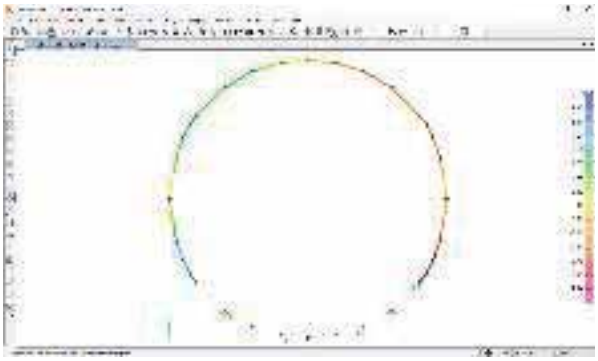

Figure 9. Circular tunnel - Stress contour

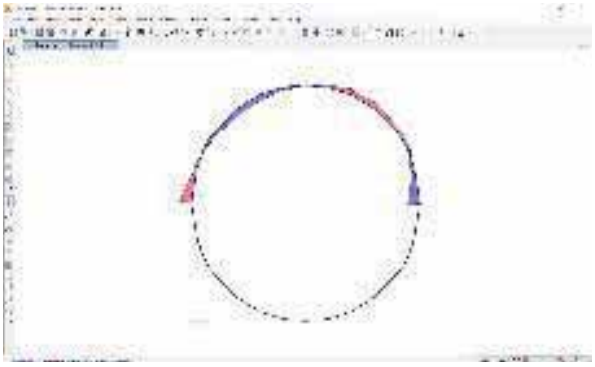

Figure 10. Circular tunnel – moment variation diagram

Figure 10 is moment variation diagram. It is clear that moments are much less at left bottom side after fixed joints. And become 0 at mid height. Again, increases and become max at 3/4th of height from bottom and gets decreased further and becomes 0 at the topmost point. These positive moments show that tunnel undergoes sagging on left. On right half stresses are –ve means tunnel undergoes hogging.

TABLE II.
RESULTS OBTAINED FROM ANALYSIS – CIRCULAR TUNNEL

Ht. from base(m)	Deformation(mm)	Moment (KN-m)		Stress (KN/m^2)	
0	0	5.77	-5.77	1319.95	1313.85
0.3	0	5.16	-5.16	1188	1172.3
0.8	0	4.23	-4.23	959.65	939.76
1.5	0	2.88	-2.88	659.77	635.72
3	1	0.26	-0.26	125	92
4.5	2	1.77	-1.77	412.4	380.82
5.2	2	2.21	-2.21	527.95	495.58
5.7	3	2.39	-2.39	602.63	569.16
6	3	2.35	-2.35	541.44	519.07
7	3	1.9	-1.9	431.88	417.71
7.6	2	1.17	-1.17	289.62	284.96
8	1	0.3	-0.3	90	

Do the same analysis by following the same procedure for the remaining tunnel models that are mentioned earlier and get the results. These results can be analyzed by using graphical representation of the results.

VII. COMPARISON OF PARAMETERS

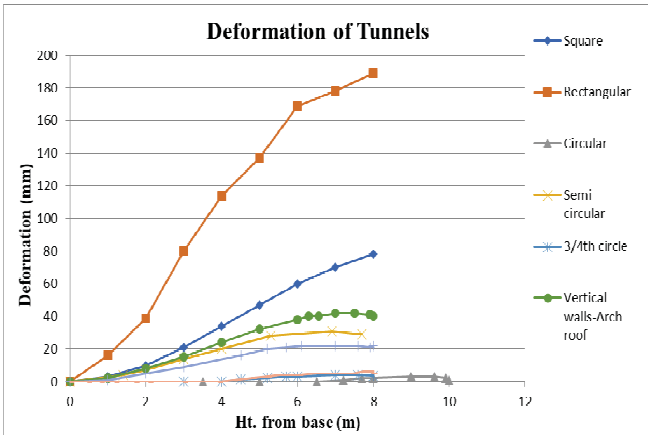

Figure 11. Representation of tunnel deformations

Figure 11 represents the deformation of tunnels analyzed. Observe the max deformation of each tunnel shape. Rectangular tunnel has the maximum deformation among all the tunnels. The smallest value of maximum deformation of tunnel can be observed in circular tunnel. The max deformation of circular tunnel is 0.3mm which is the smallest among all the maximum deformations of tunnels. By this means, it is clear that, for same combination of soil and earthquake loads for the tunnel shapes circular tunnel has shown least deformation among all the tunnel shapes.

CVR Journal of Science and Technology, Volume 21, December 2021
DOI: 10.32377/cvrjst2103

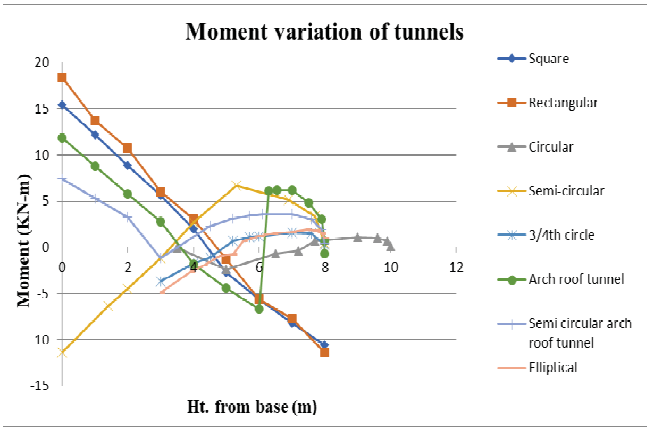

Figure 12. Representation of tunnel moment variation

Figure 12 is drawn to compare the moment distribution of tunnels analyzed. Compare all the moment value of each tunnel model. Rectangular tunnel is having the max moment value at 0m means base. And the moment is positive, so it undergoes sagging up to 4m height. After that –ve moments, means hogging occurs. After rectangular tunnel, semi-circular has the 2nd maximum moment of -11.37KN-m at its base.

Observe the moment graph of circular tunnel. Its values are very nearer to the X-axis. The maximum moment value is -2.43KN-m at 5m height from base. So, it is clear that as the circular shaped tunnel having the least value of maximum moment among the maximum moment values of all the tunnels that are analyzed. Finally, it can be concluded that for same combination loads of soil and earthquake loads for the tunnel shapes circular tunnel has shown least max moment on the structure among all the tunnel shapes.

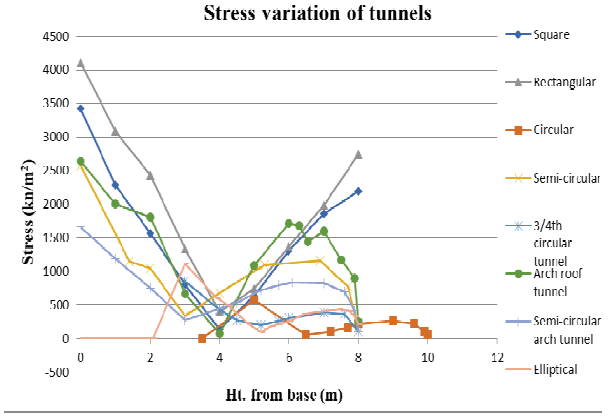

Figure 13. Representation of tunnel stresses

Figure 13 is drawn to compare the stress distribution of the tunnels analyzed. Compare all the stress values of each tunnel model. Rectangular tunnels have more stresses from left half which transfers to the right half which acts as compressive stresses. Among all the tunnels analyzed, it is clear that stress curve of circular tunnel is near to X-axis. And also, the maximum stress value of the circular tunnel is the least among all the max stress values of the other tunnel models. So, it is clear that circular tunnel is strong to resist the shear coming onto it.

VIII. Conclusions

1) Shape is the very important factor to be considered while constructing a tunnel.
2) The circular tunnel exhibits minimum deformations, moments and stresses. Hence, it can be considered as the most efficient shape among the models considered.
3) Soil type also shows an effect on propagation of seismic loads on the tunnel structure.
4) The main advantage is that only linear static analysis is sufficient.
5) Existence of tunnel amplifies the seismic waves on the soil surface and the maximum amplification occurs on the interface of the tunnel and soil.
6) To reduce the deformations, stresses, and moments on the structure, use sand around structure.
7) Sand absorbs seismic waves better than any other soil material.
8) Use high grade concrete, which reduces the deformation of tunnel.

References

[1] https://www.iitk.ac.in/nicee/wcee/article/WCEE2012_1332.pdf
[2] Duy-Duan Nguyen, Tae-Hyung Lee, Van-Quang Nguyen and Duhee Park; Seismic Damage Analysis of Box Metro Tunnels Accounting for Aspect Ratio and Shear Failure
[3] M. Saleh Asheghabadi and H. Matinmanesh, Isfahan, Iran; Finite Element Seismic Analysis of Cylindrical Tunnel in Sandy Soils with Consideration of Soil-Tunnel Interaction
[4] D. Lončarević, E. Bilotta & F. Silvestri, University of Naples Federico II, Naples, Italy ; G. Tsinidis University of Sannio, Benevento, Italy;; Seismic analysis of dynamic structure-soil-tunnel interaction for a case of the Thessaloniki Metro
[5] Amorosi, D. Boldini; Numerical Modelling of the transverse dynamic behaviour of circular tunnels in clayey soils
[6] Duy-Duan Nguyena, Duhee Park, Sadiq Shamsher, Van-Quang Nguyen, Tae-Hyung Lee; Seismic vulnerability assessment of rectangular cut-and-cover subway Tunnels
[7] M. Saleh Asheghabadiand H. Matinmanesh; Finite Element Seismic Analysis of Cylindrical Tunnel in Sandy Soils with Consideration of Soil-Tunnel Interaction
[8] L. M. Gill, E. Hernandez, P. De la Fuente; university of Granada, E.T.S.I. de Caminos, Granada, Spain; Simplified traverse seismic analysis of buried structures
[9] Hassan Sedarat, Alexander Kozak, Youssef M.A. Hashash, Anoosh Shamsabadi, Alex Krimotat; Contact interface in seismic analysis of circular tunnels
[10] George D. Hatzigeorgiou, Dimitri E. Beskos; Soil–structure interaction effects on seismic inelastic analysis of 3-D tunnels
[11] G. Kampasa, J.A. Knappettb, M.J. Brownb, I. Anastasopoulosc, N. Nikitasd, R. Fuentesd; The effect of tunnel lining modeling approaches on the seismic response of sprayed concrete tunnels in coarse-grained soils
[12] Haris Alexakis and Nicos Makris; Structural Stability and Bearing Capacity Analysis of the Tunnel-Entrance to the Stadium of Ancient Nemea
[13] Hashash, Y., Park D., M.A., Yao, Ovaling Deformations of Circular Tunnels Under Seismic Loading

[14] Hashash, Y.M.A., Hook, J.J. Schmidt, B. Yao, 2001. Seismic design and analysis of underground structure, Vol 30, Issue 9, pp 851-861

[15] Konagai K (1998). Diagonal expansion and contraction of a circular tunnel during earthquake, Vol 15, No.1, pp 47-51.

[16] M. Maleki, H. Sereshteh, M. Mousivand, M. Bayat; An equivalent beam model for the analysis of tunnel-building interaction

[17] Mirko Corigliano, Laura Scandella, Carlo G. Lai & Roberto Paolucci; Seismic analysis of deep tunnels in near fault conditions: a case study in Southern Italy, volume 9, pages975–995(2011).

[18] Grigorios Tsinidis, Kyriazis Pitilakis & Christos Anagnostopoulos; Circular tunnels in sand: dynamic response and efficiency of seismic analysis methods at extreme lining flexibilities, volume 14, pages2903–2929(2016)

[19] MilindPatil, DeepankarChoudhury, P.G.Ranjith, JianZhao; Behavior of shallow tunnel in soft soil under seismic conditions, Volume 82, December 2018, Pages 30-38

[20] Ulas Cilingir, S.P. GopalMadabhushi; Effect of Depth on the Seismic Response of Square Tunnels, Volume 51, Issue 3, June 2011, Pages 449-457

[21] QiangqiangSun, Daniel Dias, LuisRibeiro e Sousa; Impact of an underlying soft soil layer on tunnel lining in seismic conditions, Volume 90, August 2019, Pages 293-308

E-ISSN 2581 – 7957
P-ISSN 2277 – 3916

CVR Journal of Science and Technology, Volume 21, December 2021
DOI: 10.32377/cvrjst2004

An Efficient Selection of Initial Centroids for K-Means Clustering

S. Bhavani[1] and N. Subhash Chandra[2]
[1]Research Scholar, CVR College of Engineering/CSE Department, Hyderabad, India.
E-mail: bhavanisrirangam122@gmail.com
[2]Professor, CVR College of Engineering/CSE Department, Hyderabad, India.
E-mail: subhashchandra.n.cse@gmail.com

Abstract: **One of the most popular unsupervised clustering algorithms is the K-Means clustering algorithm which can be used for segmentation to analyse the data. It is a centroid-based algorithm, where it calculates the distances to assign a point to a cluster. Each cluster is associated with a centroid. The selection of initial centroids and the number of clusters play a major role to decide the performance of the algorithm. In this context, many researchers worked on, but they may not reach a goal to cluster the images in minimum runtime. Existing histogram based initial centroid selection methods are used on grayscale images only. Two methods, i.e., Histogram based initial centroids selection and Equalized Histogram based initial centroids selection to cluster colour images have been proposed in this paper.**

The colour image has been divided into R, G, B, three channels and calculated histogram to select initial centroids for clustering algorithm. This method validated on three benchmark images and compared to the existing K-Means algorithm and K-Means++ algorithms. The proposed methods give an efficient result compared to the existing algorithms in terms of runtime.

Index Terms: **Histogram, Equalized Histogram, Initial Centroids, K-clusters, K-Means clustering, K-Means++ clustering.**

I. Introduction

In computer vision, image segmentation is the process of partitioning an image into multiple segments. The goal of segmenting an image is to change the representation of an image into something that is more meaningful and easier to analyse. This paper presents segmentation of images using clustering techniques. A cluster refers to a collection of data points aggregated together because of certain similarities. K-Means clustering is one of the simplest and popular unsupervised machine learning algorithms. Assuming the number of clusters k and selecting initial centroids play an important role for clustering in K-Means clustering. For the choice of k, that is, number of clusters, a popular method called "Elbow Method" gives optimum value, but the algorithm has to run several times and then only k value can be decided. There are many methods for initial cluster centre choice like "random data points", "K-Means++". The general procedure to determine the best partition and optimal number of clusters is by validation measures like Sum of Squared Error (SSE) [11], Silhouette Score [10], Calinski_Harabasz_Score [12], Davies_Bouldin_Score [2], Clustering Fitness and Run Time [10].

The aim of this paper is to propose an efficient centroids selection for K-Means clustering based on the histogram peaks that are high density data points to be clustered within a single cluster initially, later the next level density etc. The selection of the centroids is chosen by sorting the histogram. After the selection of centroids, the rest of the process is like a random centroids method.

II. Related Works

In K-Means with random initial centroids method k number of random centroids or initial seeds is selected initially for k number of clusters. The algorithms start calculating the distance between a pixel point and all the centroids, and the pixel will be assigned to the cluster with a minimum distance. Once a new point is assigned, then a new centroid is obtained by taking the mean of all data points of that cluster. This will be continued for all the data points. This procedure will be continued until there is no change in the previous centroid and new centroid for all the clusters [4].

D. T. Pham et. al. [9] says, instead of using a single predefined K, a set of values might be adopted. It is important for the number of values considered to be reasonably large to reflect the specific characteristics of the data sets. At the same time, the selected values have to be significantly smaller than the number of objects in the data sets, which is the main motivation for performing data clustering, but this method could be computationally expensive if it is used with large data sets because it requires several applications of the K-Means algorithm before it can suggest a guide value for K.

Haimonti Dutta et. al. [7] presented a semi-supervised K-Means algorithm but the presence of small and noisy clusters in the data made it difficult to find an agreement in the optimal choice of K and says, more sophisticated seeding techniques incorporating machine learning algorithms are required.

Nameirakpam Dhanachandra et. al. [8] proposed subtractive clustering method on medical images to generate centroids based on the potential value of the data points. Here, the author took the number of clusters, k=3.

Zubair Khan et. al. [13] proposed an adaptive histogram-based approach to determine the initial parameters for K-Means on grey images. Here, authors took the initial parameter as a single variable known as grey level is used to assign intensity values to the pixels. It is a 2-step initial parameter estimation procedure to choose proper number of clusters and optimal initial cluster centres will give a better

Received on 04-09-2021, Revised on 30-09-2021, Accepted on 23-11-2021.

CVR Journal of Science and Technology, Volume 21, December 2021
DOI: 10.32377/cvrjst2004

analysis on the data or image from which it can be decided that the K value as well as initial seeding of the algorithm, but the initialization problem of K-Means is used only for grey images. This can be extended for the colour images and the task of grouping the individual peaks in the histograms to represent the true colour and the object boundaries in the image.

Rena Nainggolan et. al. [11] said that, in manual choice of K, the algorithm has to be run many times in order to get efficient clustering results. There are also a few methods like Silhouette Method, Hierarchical clustering method etc., exist for the choice of K.

Raja Kishor Duggirala [7] proposed a fuzzy-based clustering; one can know if data objects fully or partially belong to the clusters based on their membership in different clusters. Hybridization of K-Means with the FCM (Fuzzy C-Means) is implemented for the improvement in performance. Hybrid algorithm of KM and FCM is exhibiting a better performance in terms of execution time of the CPU, Clustering Fitness (CF) and Sum of Squared Error (SSE).

Bernad Jumadi Dehotman Sitompul et. al. [2] proposed the clustering method of determining initial centroid of K-Means algorithm based on minimum Sum of Squared Error, able to improve clustering result and enhance DBI value obtained by simple and determine initial centroid of K-Means algorithm. Here, the authors used numerical data like Seeds Dataset and suggested future work for categorical and image data.D. Arthur, [5] proposed the KMeans++ method, where the centroids to be distant from each other, leading to better results than random initialization. In this method, initially the first cluster centre has been chosen at random from data points, then for the next centre, each data point of the nearest cluster centre is chosen using squared distance method by using the probability formula (1). This step will be repeated until the number of centres has been chosen. The rest of the process is like a random centroids method.

$$C_i = \frac{D(x)^2}{\sum_{x \in X} D(x)^2} \quad (1)$$

Ahmet Esad TOP et. al. [1] proposed K-Means with a method of Naïve Sharding centroid initialization. The algorithm sorts the pixels in ascending order according to their R, G, B value summations and divides them into shards to choose centroids rather than selecting them randomly, which is the case in the traditional K-Means algorithm. The dataset is then horizontally split into k pieces, or shards. Finally, the original attributes of each shard are independently summed, their mean is computed, and the resultant collection of rows of shard attribute mean values becomes the set of centroids to be used for initialization. Sharding initialization is expected to execute quicker than random centroid initialization, especially considering the time needed for randomly initializing centroids for increasingly complex datasets.

Chunhui Yuan et. al. [3] proposed four kinds of K-value selection algorithms, such as Elbow Method, Gap Statistic, Silhouette Coefficient, and Canopy, are used to cluster the Iris data set to obtain the best K value and the clustering result of the data set. For large scale data sets both time and space complexity will be more to run the Gap Statistic algorithm. The computational overhead can be very large; hence the Silhouette Coefficient algorithm is also not used for large-scale data sets. For large and complex data sets, it is obvious that the Canopy algorithm is the best choice. For real-world multidimensional data containing complex fields of information and for experimental verification, there is a necessity to deeply explore the advantages and disadvantages of each algorithm or to improve the performance of the algorithm.

III. The Proposed System

This section presents our approach to find efficient centroids selection with the application of Histogram based K-Means algorithm on 3 different images.

3.1. Pre-Processing of Image:

Downloaded images are resized and each image is converted into a data frame in order to apply the K-Means algorithm.

3.2. K-Means algorithm:

Given a set of observations (x1, x ... xn), where each observation is a d-dimensional real vector, K-Means clustering aims to partition the n observations into k (≤ n) sets S = {S1, S2, ..., Sk}, so, as to minimize the sum of square error (SSE). Formally, the objective is defined with the equation (2).

$$\arg\min S \sum_{i=1}^{k} \sum_{x \in S_i} \|x - \mu_i\|^2 = \arg\min S \sum_{i=1}^{k} |S_i| Var S_i \quad (2)$$

Where, μ_i is the mean of points in S_i, x is any data point and S_i is i^{th} cluster.

3.2.1. Histogram of an image:

An image histogram is a type of histogram that acts as a graphical representation of the intensity distribution in a digital image [6]. It plots the number of pixels for each intensity value. By looking at the histogram for a specific image, a viewer will be able to judge the entire intensity distribution immediately. For pseudocode refer to the Histogram algorithm.

Algorithm: Histogram

Input: Grey image/Single Channel of an Image
Output: Histogram of the given image
Step 1: Declare an n dimensional array of histogram with 256 levels
Step 2: Read the shape of image into a variable
Step 3: For each row
  Step 4: For each column
    Step 5: Increment corresponding histogram level count in an n dimensional array of histogram
Step 6: Return an n dimensional array of histogram

3.2.2. Histogram Based K-Means:

The given colour image split into the R, G, B channels and for each channel a separate histogram is generated. Each histogram is sorted in descending order to get a high density of intensity. Based on the given k value, those many or several centroids selected from the sorted list of histograms. The selected centroids are given as input to the K-Means algorithm as initial centroids. For pseudocode refer to the Histogram Based K-Means algorithm.

TABLE I.
COMPARISON OF RUNTIMES IN SECONDS

K	Lena Image				Baboon Image				Peppers Image			
	K-Means with Random Centroids	K-Means ++	Histogram based K-Means	Equalized Histogram based K-Means	K-Means with Random Centroids	K-Means++	Histogram based K-Means	Equalized Histogram based K-Means	K-Means with Random Centroids	K-Means ++	Histogram based K-Means	Equalized Histogram based K-Means
2	0.273	0.373	0.17	0.339	0.378	0.556	0.176	0.365	0.235	0.322	0.152	0.374
3	0.72	0.811	0.216	0.381	0.599	0.704	0.184	360.	0.335	0.536	0.174	0.357
4	0.655	0.929	0.195	0.35	0.77	1.15	0.213	0.384	0.577	0.866	0.276	0.393
5	0.842	1.1	0.172	0.393	1.147	1.004	0.207	0.393	0.75	0.897	0.205	0.385
6	1.5	1.548	0.26	0.486	1.565	1.804	0.226	0.436	1.022	1.047	0.225	0.404
7	1.716	1.891	0.284	0.486	1.901	2.169	0.294	0.517	1.986	1.29	0.247	0.477
8	2.054	2.036	0.382	0.863	2.591	3.646	0.319	0.561	1.875	2.371	3360.	0.916
9	2.838	2.308	0.427	0.801	4.366	3.458	0.571	0.705	3.269	5.343	0.639	1.448
10	3.804	2.838	0.876	0.986	3.577	3.786	0.685	0.924	3.875	3.865	0.583	0.785

Algorithm: Histogram Based K-Means
Input: Input Image, Number of Clusters
Output: Clustered Image
Step 1: Split Image into B, G, and R channels
Step 2: Call Histogram for each channel
Step 3: Sort histograms of each channel in descending order.
Step 4: Declare an n dimensional array of Initial Centroids
Step 5: for 0 to k clusters
Step 6: Append centroids for each channel from sorted histograms to Initial Centroids
Step 7: Call K-Means with Initial Centroids
Step 8: Output the Clustered Image

3.2.3. Equalized Histogram of an image:

Histogram equalization is a technique for adjusting image intensities to enhance contrast [6]. Let f be given an image represented as an RxC matrix of integer pixel intensities ranging from 0 to L-1. L is the number of possible intensity values, often 256. Let p denote the normalized histogram (probability of intensity) of 'f' with a bin for possible intensity. Hence; 'pn' is defined with the equation (3).

$$p_n = \frac{number\ of\ pixels\ ith\ intensity\ \ n}{total\ number\ of\ pixels} \quad (3)$$

Where n=0, 1 ... L-1.

The equalized histogram image g will be defined by the equation (4).

$$g_{i,j} = floor((L-1)\sum_{n=0}^{n_{i,j}} p_n \quad (4)$$

Where floor () rounds down to the nearest integer. This is equivalent to transforming the pixel intensities, l, of 'f' by the equation (5).

$$T(l) = floor((L-1)\sum_{n=0}^{l} p_n \quad (5)$$

For pseudocode refer algorithm Equalized Histogram.

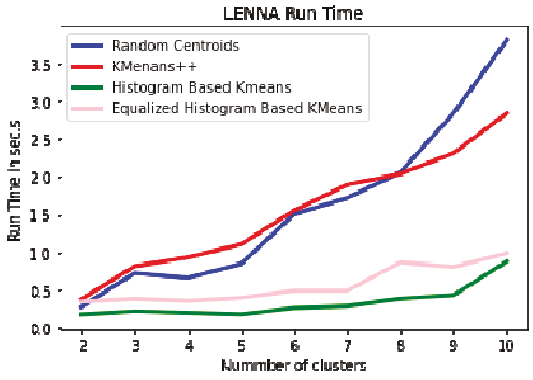

Figure 1. Runtime in Seconds for Lena Image

Figure 2. Original Lena Image

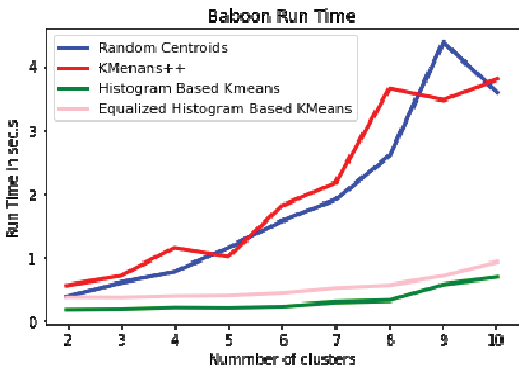

Figure 3. Runtime in Seconds for Baboon Image

Figure 4. Original Baboon Image

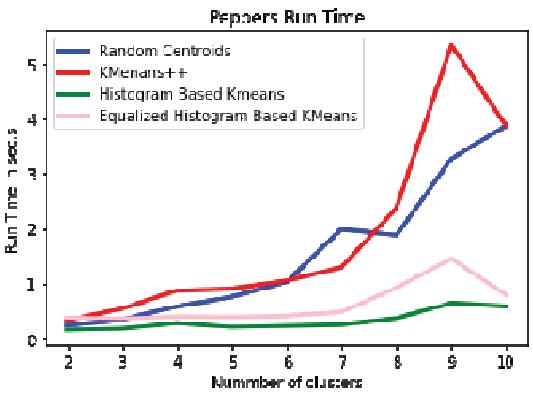

Figure 5. Runtime in Seconds for Peppers Image

Figure 6. Original Peppers Image

TABLE II.
LENA IMAGE RESULTS

K	K-Means with Random Centroids	K-Means++	Histogram based K-Means	Equalized Histogram based K-Means
2	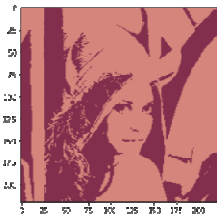	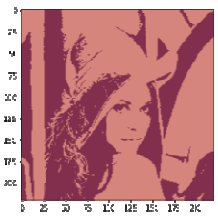	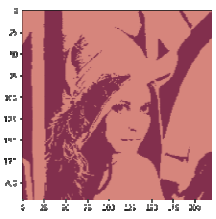	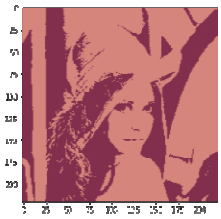
8	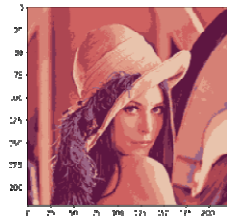	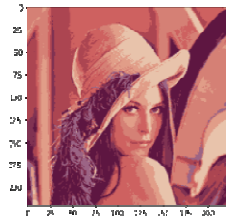	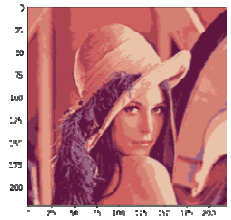	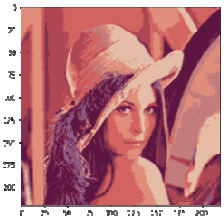

Algorithm: Equalized Histogram

Input: Grey image/Single Channel of an Image
Output: Equalized Histogram of the given image
Step 1: Call Histogram of channel
Step 2: Read the shape of image into a variable
Step 3: Calculate Probability Distribution Function of Histogram
Step 4: Calculate Cumulative Distribution Function of Histogram
Step 5: Define transformation function
Step 6: For each row
Step 7: For each column
Step 8: Apply transformation function and store in resulting an n dimensional array as Equalized Histogram of channel
Step 9: Return Equalized Histogram of channel

3.2.4. Equalized Histogram based K-means:

The given colour image split into the RGB channels and for each channel a separate Equalized Histogram is generated. Each Equalized Histogram is sorted in descending order to get high density and intensity values. Based on the given k value, those several numbers of centroids selected from the

CVR Journal of Science and Technology, Volume 21, December 2021
DOI: 10.32377/cvrjst2004

sorted list of Equalized Histograms. The selected centroids are given as input to the K-Means algorithm as initial centroids. For pseudocode refer Equalized Histogram Based K-Means.

Algorithm: Equalized Histogram Based K-Means

Input: Input Image, Number of Clusters
Output: Clustered Image
Step 1: Split Image into B, G, R channels
Step 2: Call Equalized Histogram for each channel
Step 3: Sort histograms of each channel in descending order.
Step 4: Declare an n dimensional array of Initial Centroids
Step 5: For 0 to k clusters
Step 6: Append centroids for each channel from sorted histograms to Initial Centroids
Step 7: Call K-Means with Initial Centroids
Step 8: Output the Clustered Image.

TABLE III.
BABOON IMAGE RESULTS

K	K-Means with Random Centroids	K-Means++	Histogram based K-Means	Equalized Histogram based K-Means
2	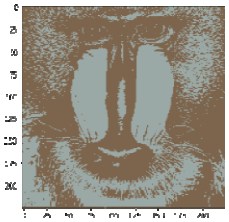	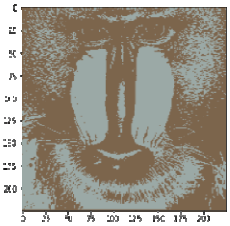	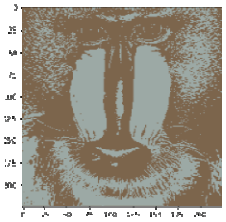	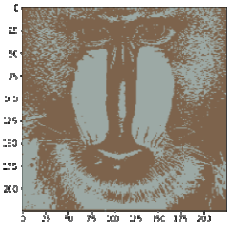
8	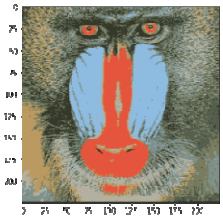	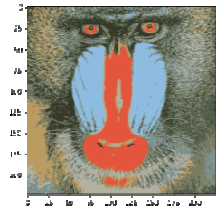	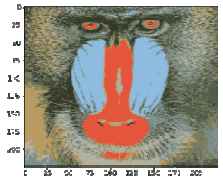	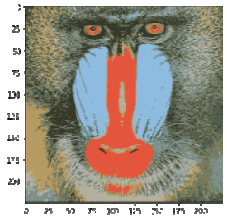

TABLE IV.
PEPPERS IMAGE RESULTS

K	K-Means with Random Centroids	K-Means++	Histogram based K-Means	Equalized Histogram based K-Means
2	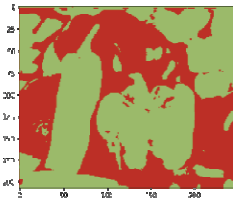	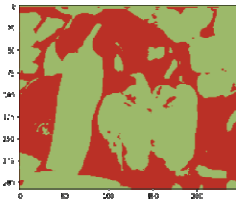	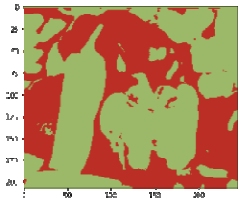	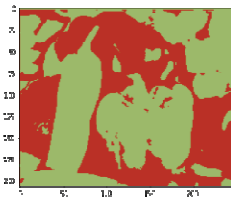
8	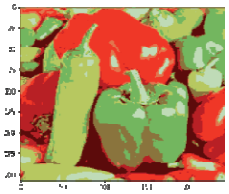	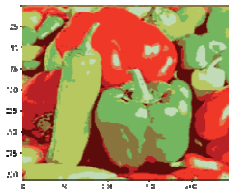	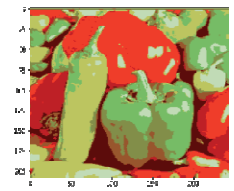	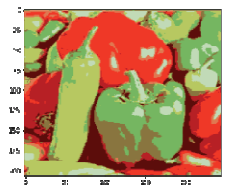

IV. Result and Discussion

The proposed system is experimented using https://colab.research.google.com, an open source for python programming.

Performance Analysis:

The present proposed models are experimented on 3 different images and runtimes of all clustering techniques are measured. Comparison of results of runtime in seconds of each clustering technique is listed in Table 1, the corresponding line graphs are also presented in figure 1, figure 3, and figure 5. Original images are presented in figure 2, figure 4, and figure 6. The clustering results for 'k' values 2 and 8 are presented in tables from 2 to 4.

V. Conclusions

Clustering is playing a vital role in image segmentation which is used in many applications. The most commonly used K-Means clustering which takes randomly generated initial centroids is not reaching the local optima. The proposed Histogram based selection of initial centroids to overcome the above drawback. The present paper also proposed equalized histogram-based selection of initial centroids to improve the performance of the algorithm. But, in the above analysis, the equalized histogram method is not performing appreciated results. This can be enhanced by considering spatial values as another dimension in clustering.

It is observed that Histogram based, and Equalized Histogram based K-Means gives better performance in the view of runtime comparatively with Random centroids K-Means and K-Means++. Histogram based K-Means is taking less runtime as compared to the Equalized Histogram based K-Means, but in future, it can be extended that Equalized Histogram based K-Means may perform better in other kind of parameters like Sum of Squared Error, Silhouette Score etc., with the application of spatial dimensions.

References

[1] Ahmet Esad TOP, F. Şükrü TORUN & Hilal KAYA, PARALLEL K-MEANS CLUSTERING WITH NAÏVE SHARDING FOR UNSUPERVISED IMAGE SEGMENTATION VIA MPI, Mühendislik Bilimleri ve Tasarım Dergisi 8(3), 791 – 798, 2020, e-ISSN: 1308-6693, Journal of Engineering Sciences and Design DOI: 10.21923/jesd.748209.

[2] Bernad Jumadi Dehotman Sitompul, Opim Salim Sitompul and Poltak Sihombing, Enhancement Clustering Evaluation Result of Davies-Bouldin Index with Determining Initial Centroid of K-Means Algorithm, Journal of Physics: Conference Series, Volume 1235, The 3rd International Conference on Computing and Applied Informatics 2018 18–19 September 2018, Medan, Sumatera Utara, Indonesia, 1-6.

[3] Chunhui Yuan & Haitao Yang, "Research on K-Value Selection Method of K-Means Clustering Algorithm", (2019), J. 2. 226-235. 10.3390/j2020016, doi: https://doi.org/10.3390/j2020016.

[4] Data Mining – Concepts and Techniques - Jiawei Han & Micheline Kamber, Morgan Kaufmann Publishers, 3rd Edition, 2012.

[5] David Arthur and Serei Vassilvitskii, 2007, k-means++: The Advantages of Careful Seeding, In Proceedings of the Eighteenth Annual ACM-SIAM Symposium on Discrete Algorithms, New Orleans, SIAM, pp. 1027-1035.

[6] Digital Image Processing, Rafael C. Gonzalez and Richard E. Woods, Fourth edition. Pearson Education, 2018.

[7] Haimonti Dutta, Rebecca J. Passonneau, Austin Lee, Axinia Radeva, Boyi Xie, David Waltz and Barbara Taranto, Learning Parameters of the K-Means Algorithm from Subjective Human Annotation, Proceedings of the Twenty-Fourth International Florida Artificial Intelligence Research Society Conference, 2011, 465-470.

[8] Nameirakpam Dhanachandra, Khumanthem Manglem, Yambem Jina Chanu, Image Segmentation Using K -means Clustering Algorithm and Subtractive Clustering Algorithm, Procedia Computer Science, Volume 54, 2015, ISSN 1877-0509, https://doi.org/10.1016/j.procs.2015.06.090, 764-771.

[9] Pham, D. & Dimov, Stefan & Nguyen, Cuong, Selection of K in K -means clustering, Manufacturing Engineering Centre, Cardiff University, Cardiff, UK 2004, 103-119, https://doi.org/10.1243/095440605X8298.

[10] Raja Kishor Duggirala, Segmenting Images Using Hybridization of K-Means and Fuzzy C-Means Algorithms, Introduction to Data Science and Machine Learning, Keshav Sud, Pakize Erdogmus and Seifedine Kadry, IntechOpen, (July 10th 2019), 1-27, DOI: 10.5772/intechopen.86374. Available from: https://www.intechopen.com/chapters/68050.

[11] Rena Nainggolan, Resianta Perangin-angin, Emma Simarmata, and Feriani Astuti Tarigan, , Improved the Performance of the K-Means Cluster Using the Sum of Squared Error (SSE) optimized by using the Elbow Method, Journal of Physics: Conference Series, 2019, doi: 10.1088/1742-6596/1361/1/012015, 1-6.

[12] Y. Liu, Z. Li, H. Xiong, X. Gao and J. Wu, "Understanding of Internal Clustering Validation Measures," 2010 IEEE International Conference on Data Mining, 2010, pp. 911-916, doi: 10.1109/ICDM.2010.35.

[13] Zubair Khan, Jianjun Ni, Xinnan Fan & Pengfei Shi, An improved K-means clustering algorithm based on an adaptive initial parameter estimation procedure for image segmentation. International Journal of Innovative Computing, Information and Contro, 2017, 1509-1525.

E-ISSN 2581 –7957
P-ISSN 2277 – 3916

CVR Journal of Science and Technology, Volume 21, December 2021
DOI: 10.32377/cvrjst2105

Web Page Genre Identification and Categorization using Single-Label and Multi-Label Corpuses in English and Telugu Languages

K. Pranitha Kumari[1] and K. Srinivasa Reddy[2]
[1]Assoc. Professor, CVR College of Engineering/CSE Department, Hyderabad, India
Email: k.pranithakumari@cvr.ac.in
[2]Assoc. Professor, CVR College of Engineering/CSE Department, Hyderabad, India
Email: k.srinivasareddy@cvr.ac.in

Abstract: **As web is fluid, new web page genres emerge, and these genres are known as emerging genres. Genre based searches can yield better search results than topic based searches for the user. In this paper, Refined Adjustable Centroid Classification (RACC) algorithm is proposed to classify web page genres including emerging genres in multiple languages. Seven Telugu web page genres TELPOETRY, TELENTERTAINMENT, TELFAQ, TELCHILDREN, TELSOCIAL, TELETIQUETTE and TELE-GENRE are identified using the method of annotation by objective sources. Telugu web page genre corpus(10-genre) is developed which contains newly identified seven Telugu web page genres and three existing Telugu web page genres. The 7-genre, 10-genre, 20-genre, 23-genre and newly formed Telugu 10-genre corpuses are classified using RACC algorithm. The classification results obtained show that RACC algorithm gave better results when compared with existing classification techniques on all five corpuses. The experimental results obtained are statistically significant ($p<0.05$).**

Index Terms: **Telugu web page genres, Emerging genres, syllable extraction, genre threshold, web page genre classification, genre corpus, identification of genres**

I. Introduction

As the web is mutable, it is very hard to find required information from web pages retrieved by a search engine. To solve this problem, it is better to classify the web pages based on their genre instead of topic. Genre is a non-topical descriptor. It can be characterized by its type, functionality, content, form, discourse functionality, communicative purpose, layout and social acceptance. Genres normally have established names and are acknowledged by specific discourse communities.

To search the information using genres, it is necessary to collect web page genres. As web is fluid, new genres will come into existence called as emerging genres. Contemporary web page genres are fewer in number and do not include emerging genres [23]. Therefore, it is necessary to identify emerging genres from the web pages. So far, no proper methodology is developed to identify emerging genres.

Web page genre classification is an essential technique that can contribute to the progress of search results. Generally, classification techniques are used to find the correctness of the genre corpora [23]. Currently many classification techniques are available, but not all classification techniques are useful to classify the web page genre corpuses accurately. The accuracy of a classifier depends on the type of genre corpuses. Hence, a scalable technique is required to classify the web page genre corpuses that can accommodate emerging genres.

Usage of the internet in India is increasing day by day. Therefore, information in Indian languages on the web is also growing rapidly. So, there is a need to adopt genre based search for querying Indian language web pages. Until now, no one has identified a web page genre in the Indian language. Most of the Indian languages are syllabic languages in which each syllable is a glyph or a combination of glyphs and each glyph is represented with a unique code called Unicode [22].

This paper proposes a refined adjustable centroid classification technique which distinguishes genres correctly when compared with the well-known state of the art classification techniques on both single-label and multi-label corpuses in multiple languages, and a Telugu web page genre corpus with ten newly identified genres. The new 10-genreTelugu web page corpus is tested using different classification techniques.

The structure of the paper is as follows. Section 2 discusses the related work. Section 3 describes proposed Refined Adjustable Centroid Classification algorithm and experiments on web page genre classification. Section 4 discusses the process of identification of genres in Telugu web pages and classification results. Finally, Section 5 concludes the paper.

II. Related Work

A brief review of the reported work in literature towards the identification and classification of web page genres are presented in this section. With reference to a comprehensive survey of web page genres, there are two important issues in the area of research on web page genres: 1) genre evolution on the web and 2) the application of genre for classification of web pages on the web.

The Orators since Aristotle have initiated genres in the communication by considering subject, form, and purpose. The authors in genre analysis have given various definitions for genre such as: genre as a set of rules of discursive properties [32], genre is a social action [20], genre as a persuasive classifying statement [25], genre as a class of communicative events [31], genre as a typified

Received on 04-09-2021, Revised on 30-09-2021, Accepted on 23-11-2021.

CVR Journal of Science and Technology, Volume 21, December 2021
DOI: 10.32377/cvrjst2105

communicative action [36], genre is related to topic or subject [14]. In [16], genre is stated as a widely acknowledged class of texts determined by communicative purpose. The observations similar to [16] are given in [18] and they observed that most definitions of genre include the notions of document form, expected content, and intended communicative purpose, and the notion of social acceptance.

The study on web page genres is initiated in [4][5] by considering the objectives such as: the development of genres on the web and significant impact of genres on the web. A survey is carried out on genre evolution on the web in [29] and gave a special name to a genre on the web called as cybergenre. Web page genre identification mainly considers four factors such as granularity of web page genres, labels associated with each web page, assignment of genre labels and the characterization of genres. Among all four factors, "the characterization of genres" has more influence on the evolution of genres in various media. Three home page genres such as personal, corporate, and organizational home page genres from a collection of 321 websites are identified in [15]. Online encyclopedias web page genre is identified in [7]. BLOG is identified as an emerging genre in [2]. Corporate blogs is identified as an emerging genre [3] of computer-mediated communication from CBC/Corporati corpus by considering pragmatic aspects and linguistic aspects. Most recently in [17], a specialized genre named as Touristic Websites genre, which is a hybrid genre is identified. Rehm et al. constructed reference benchmark web page genres and are given in [24]. The limitations of existing work on genre identification are, there is no automatic framework for identification of emerging genres in web pages and no researcher focused on Indian language web page genre identification (i.e. genres are available in English, Spanish, German, Italian, Arabic and Russian language web pages, and are also very limited in number).

The classifier performance depends on type of the genre (single-label or multi-label), feature set to represent web page genre, and level of granularity of genre. The necessity of multi-label genre to a web page is described in [9][10][19][34]. In [28], they performed cross-testing experiments in web page genre classification on different web page genre corpuses such as: HGC, I-EN, KI-04, KRYS-I, MGC and 7-genre corpus [27][37][38][39] by considering a variety of features. In [33], a work on web page genre classification is performed on a set of 1539 web pages labeled manually and named as 20-genre corpus. In [27], three small sets of carefully chosen features are used to represent the web pages and introduced a new classification model called as an inferential model for classifying web pages by genre. In [12][13], they investigated cross classification testing on three web page genre corpuses (7-genre, KI-04 and 20-genre corpuses). The usefulness of combinations of content, form, and functionality features in web page genre classification is examined in [6]. As observed from the literature, there is no scalable classification method for emerging genres in web page genre classification which is applicable for both single-label and multi-label. A feature extraction method to extract genre specific features and language-independent features is required.

The features are extracted from Telugu web pages either directly from the text or by using OCR system. To work with machine learning techniques, Telugu web page features can be denoted in English. WX notation specifies a transliteration scheme to symbolize Indian Language scripts in English. As given in [1], the purpose of WX notation is to furnish a unique representation of Indian languages in English alphabets. A transliteration model for Indian languages to convert UTF to WX notation and WX notation to UTF was implemented in [8]. In [8], they conducted a study on Hindi, Telugu, Bengali, Punjabi, Malayalam and Kannada language documents. In [21], to locate and extract Telugu script in a document image, OCR system is built by taking into account the circular nature of Telugu script. In [11], a dictation system for Telugu speech recognition is built. During this process, they considered CIIL Mysore Telugu text corpus of 3 million words of running texts in Telugu for training. They also made rules for syllabification based on the canonical structure of Telugu script using WX notations but not directly from Telugu script.

III. Web Page Genre Classification

A. Refined Adjustable Centroid Classification

Classification is a method used to find the effectiveness of web page genre corpuses. A scalable classification technique is essential to classify web page genres. A Refined Adjustable Centroid Classification(RACC) algorithm is proposed in this paper to classify web page genres. RACC algorithm is the modification of ACC algorithm[23]. RACC algorithm is used to classify both single-label and multi-label web page genre corpuses which better represent a real world environment. The main idea of RACC algorithm is to find the similarity between each web page in test set and each web page genre profile in training set. RACC algorithm is described in Fig. 1 and it consists of two phases. In the training phase, for each web page genre, web page genre profile (centroid) is created. Web page profile contains n-gram features with their corresponding normalized weights. Web page genre profile is created by combining all unique n-gram features of all web page profiles belonging to that particular genre and the weight of each n-gram 'x' is the sum of the weights of 'x' in all the web pages. Genre threshold is also calculated in RACC. In test phase, cosine similarity between each web page and each web page genre profile is calculated and compared with genre threshold.

In case of single-label classification, among all genre similarities which are calculated, if the similarity between web page and web page genre is greater than that particular web page genre threshold among all highest the web page genre threshold then that web page genre is predicted as actual genre for that web page. In case of multi-label classification, if the similarity between web page and web page genre is greater than that particular web page genre threshold then that web page genre is predicted as actual genre for that web page. Here there is a possibility of predicting multiple genres for each web page. Setting genre threshold is important in multi-label classification. In RACC

CVR Journal of Science and Technology, Volume 21, December 2021
DOI: 10.32377/cvrjst2105

Input: Genre corpus

Output: Predicted genres

Notations: G: genre, Gc: genre corpus, exG: existing genre, WP: web page, Th: threshold, Nc: new corpus, Sim: cosine similarity, Tf: n-gram frequency, df: n-gram document frequency, Tw: n-gram weight, SimSum: sum of all the similarities, df: document frequency, MTh: modified threshold.

Training phase:

- For each genre exG ∈ Gc, Create genre profile exG_i
- For each web page WP ∈ exG_i, create web page profile WP_j
- For each n-$gram_{k,i}$ ∈ exG_i
  - $Tf_{k,i} \leftarrow Tf_{k,i} + Tf_{k,j}$
- For each n-$gram_{k,i}$ ∈ exG_i
  - Find $df_{k,i}$
  - if n-$gram_{k,i}$ exists in exG_i
  - $df_{k,i} \leftarrow df_{k,i} + 1$
  - $TW_{k,i} \leftarrow Tf_{k,i} * \log(|G_c|/df_{k,i})$
  - $Sim(WP, G) = \frac{\sum_{i=1}^{n} WP(tw_i) \times G(tw_i)}{\sqrt{\sum_{i=1}^{n} (WP(tw_i))^2} \times \sqrt{\sum_{i=1}^{n} (G(tw_i))^2}}$
  - $SimSum_i = SimSum_i + Sim(WP,G)$
- Find genre threshold

$$Th_i = \frac{Sim(WP_j, exG_i) + SimSum_i}{|G_i|}$$

Test phase:

- For each web page WP ∈ exG_i, create web page profile WP_j
- For each n-$gram_{k,i}$ ∈ exG_i,
  - For each n-$gram_{k,i}$ ∈ WP_j ,
  - Compute $Sim(WP_j, exG_i) \leftarrow \sum$n-gram∈(i∩j) $Tw_{k,i} * Tw_{k,j} / (\| Tw_{k,i} \| * \| Tw_{k,i} \|)$
- if $Sim(WP_j, exG_i) > Th_i$, p≠i (for single-label corpus)
  - WP_j predicted as actual genre exG_i with highest Th_i genre
- if $Sim(WP_j, exG_i) > Th_i$ (for multi-label corpus)
  - WP_j predicted as actual genre

Figure 1. RACC Algorithm

algorithm, the genre thresholds are genre specific thresholds instead of a fixed constant value.

B. Classification Experiments

The classification experiments are carried out on four corpuses: single-label 7-genre corpus and 10-genre corpus, multi-label 20-genre corpus and 23-genre corpus[23]. The performance evaluation measures used for single-label and multi-label classification experiments are described in [35] and [30] respectively. Performance measures such as precision, recall, F-measure and accuracy are used to evaluate the classification results on single-label genre corpuses Tan et al. [41] and Witten and Frank [35]. In this paper, macro-precision, macro-recall and macro F-measure[40] are used to evaluate the multi-label classifiers because macro-averages gives equal weight to each genre, whereas micro-averages gives equal weight to each web page. Binary relevance (BR) approach is followed during the multi-label classification. The advantage of the BR approach is its low computational complexity compared with other multi-label methods. Weka[42] and Meka [43] tools are used in the experimentation and implementations of SVM and Naive Bayes algorithms were developed by Witten and Frank [35]

The 7-genre corpus is classified using RACC, the results obtained are better when compared with ACC in terms of precision, recall and F-measure and are reported in Table 1. ANOVA test results show that the classification performance of RACC algorithm on single label 7-genre corpus is statistically significant in terms of F-measure ($p < 0.05$). The 10-genre corpus is evaluated using RACC, ACC and SVM classification algorithms and the results are reported in Table 2. All the three classification algorithms gave good results on 10-genre corpus but among the three, RACC algorithm performance is better. Based on ANOVA and paired t-test results, the performance of RACC algorithm is statistically significant than that of ACC and SVM in terms of precision, recall and F-measure ($p < 0.05$).

The RACC algorithm is used to classify multi-label 20-genre corpus. This multi-label classification task is performed by using twenty binary classifiers, each for a genre. The classification performance of RACC algorithm on the 20-genre corpus is compared with the existing work done on the same corpus and is shown in Table 3. The results obtained are statistically significant in terms of precision, recall and F-measure ($p < 0.05$).

TABLE I.
COMPARISON OF RACC ALGORITHM PERFORMANCE ON SINGLE-LABEL 7-GENRE CORPUS WITH ACC IN TERMS OF PRECISION, RECALL AND F-MEASURE

Genre	ACC			RACC		
	Precision	Recall	F-Measure	Precision	Recall	F-Measure
BLOG	1.0	0.97	0.9847	1.0	0.98	0.989
ESHOP	0.99	0.99	0.99	0.99	0.99	0.99
FAQS	0.99	1.0	0.9949	0.992	1.0	0.995
FRONTPAGE	1.0	1.0	1.0	1.0	1.0	1.0
LISTING	0.989	0.98	0.9845	0.989	0.99	0.99
PHP	0.966	0.995	0.98	0.97	0.995	0.985
SPAGE	0.985	0.985	0.985	0.989	0.988	0.989
Average	0.988	0.988	0.988	0.99	0.991	0.991

TABLE II.
COMPARISON OF RACC ALGORITHM RESULTS WITH ACC AND SVM CLASSIFIERS ON SINGLE LABEL 10-GENRE CORPUS

Classifiers	A	P	R	FM
RACC	0.966	0.96	0.959	0.96
SVM	0.923	0.924	0.923	0.922
ACC	0.961	0.952	0.966	0.955

A = Accuracy, P = Precision, R = Recall, FM = F-measure.

TABLE III.
COMPARISON OF EXISTING WORK ON 20-GENRE CORPUS WITH RACC ALGORITHM RESULTS

Classifiers	A	P	R	FM
RACC (BR)	0.971	0.97	0.968	0.969
ACC(BR)	0.965	0.968	0.963	0.966
Mason	0.843	0.99	0.754	0.846

A = Accuracy, P = Precision, R = Recall, FM = F-measure.

TABLE IV.
COMPARISON OF RACC ALGORITHM RESULTS WITH ACC (BR) AND SVM (BR) CLASSIFIERS ON MULTI-LABEL 23-GENRE CORPUS

Classifiers	A	P	R	FM
RACC (BR)	0.955	0.969	0.948	0.957
SVM (BR)	0.817	0.871	0.953	0.91
ACC (BR)	0.947	0.964	0.948	0.953

A = Accuracy, P = Precision, R = Recall, FM = F-measure.

The classification experiment is also performed on multi-label 23-genre corpus. This multi-label classification task is performed by using twenty three binary classifiers, each for a genre. The classification performance of RACC algorithm on 23-genre corpus is compared with ACC and SVM (BR) in terms of precision, recall and F-measure and is shown in Table 4. The results obtained are statistically significant in terms of precision, recall and F-measure ($p < 0.05$).

IV. INTRODUCING AND CLASSIFYING GENRES IN TELUGU WEB PAGES

A. Syllable Extraction

The alphabets of different languages have unique codes that are present in the Unicode set. Unicode from 0C00 to 0C7F are allocated for Telugu syllables. Unicode Transformation Format (UTF) is the universal character code standard to represent character sets. UTF-8 is an alternative coded representation and maintains compatibility with ASCII. The web pages in Telugu are transliterated into an orthographic form using one of the standard forms which the machine can understand. WX notation is used to transliterate the Telugu text in UTF-8 to roman script and each Telugu syllable is represented using this notation. Character n-gram method is used to represent web pages. Character n-gram of length 'k' has 'k' syllables. To extract n-gram features of Telugu web pages it is necessary to extract syllables from web pages.

As Telugu is a syllabic language, syllables of Telugu web pages are extracted using Syllable extraction algorithm[22]. A Unicode based syllable extraction method is proposed[22] to extract syllables from Telugu web pages. Unicode sets defined for Telugu letters are used in Syllable extraction algorithm as follows: Vowel Unicode V = {0c05, 0c06, 0c07, 0c08, 0c09, 0c0a, 0c0b, 0c0c, 0c0e, 0c0f, 0c10, 0c12, 0c13, 0c14}. Consonant unicode set C = {0c15, 0c16, 0c17, 0c18, 0c19, 0c1a, 0c1b, 0c1c, 0c1d, 0c1e, 0c1f, 0c20, 0c21, 0c22, 0c23, 0c24, 0c25, 0c26, 0c27, 0c28, 0c2a, 0c2b, 0c2c, 0c2d, 0c2e, 0c2f, 0c30, 0c31, 0c32, 0c33, 0c35, 0c36, 0c37, 0c38, 0c39}. Halant h=0c4d. Special signs S={0c01, 0c02, 0c03}.Vowel signs VS={0C66, 0C67, 0C68, 0C69, 0C6A, 0C6B, 0C6C, 0C6D, 0C6E, 0C6F,0C78, 0C79, 0C7A, 0C7B, 0C7C, 0C7D, 0C7E, 0C7F}.

B. Introducing Telugu Web Page Genres

This paper focused on identifying web page genres in Telugu and introducing Telugu web page genre corpus. Telugu web page genre identification process consists of the following steps:

- If existing Telugu web page genre corpus is available then predict genre labels and apply IEG algorithm[23]to identify new Telugu web page genres.
- If there is no existing Telugu web page genre corpus then predict genre labels, collect web pages and based on the method of annotation by objective sources assign genre labels to the web pages.

During the identification process, a web page collection consisting of 100 web pages was downloaded in the year 2020 from different Telugu web sites. Telugu web page 3-genre corpus[22] is used and applied to IEG algorithm. Web pages are labeled in this corpus with a single-label using annotation by objective sources because it is faster and lesser complex compared to human annotation. Sevn genres TELPOETRY, TELENTERTAINMENT, TELFAQ, TELCHILDREN, TELSOCIAL, TELETIQUETTE and TELE-GENRE are identified from the Telugu web pages by considering the characteristics of web page genres such as communicative purpose and discourse functionality. These characteristics are considered because the users of the internet would share and communicate with each other through web pages. Table 5 shows the characterization of Telugu web page genres identified in this paper. A new Telugu web page genre corpus named as 10-genre corpus is shown in Table 6 is formed with 3-genre corpus and newly identified Telugu web page genres.

E-ISSN 2581 –7957
P-ISSN 2277 – 3916

DOI: 10.32377/cvrjst2105

TABLE V.
CHARACTERIZATION OF TELUGU WEB PAGE GENRES

Genre	Characteristics	References
TELPOETRY	Communicative purpose and discourse functionality	http://en.wikipedia.org/wiki/
TELENTERTAINMENT	Communicative purpose and discourse functionality	http://en.wikipedia.org/wiki/
TELFAQ	Communicative purpose and discourse functionality	http://en.wikipedia.org/wiki/
TELCHILDREN	Communicative purpose and discourse functionality	http://en.wikipedia.org/wiki/
TELSOCIAL	Communicative purpose and discourse functionality	http://en.wikipedia.org/wiki/
TELETIQUETTE	Communicative purpose and discourse functionality	http://en.wikipedia.org/wiki/
TELE-GENRE	Communicative purpose and discourse functionality	http://en.wikipedia.org/wiki/

TABLE VI.
SINGLE-LABEL TELUGU 10-GENRE CORPUS

Genre Name	Total web pages
TELARTICLE	50
TELBLOG	54
TELNEWS	51
TELPOETRY	98
TELENTERTAINMENT	100
TELFAQ	100
TELCHILDREN	100
TELSOCIAL	99
TELETIQUETTE	100
TELE-GENRE	98

C. N-gram Reresentation

Syllable n-grams are used to represent each web page. An example for extraction of syllable n-grams from the Telugu word ఉస్మానియా is shown in Fig. 2. The 3-gram features are extracted from all the web pages of 10-genre corpus. For each n-gram, n-gram weight is calculated and then CFS is applied to reduce the number of features.

E.g.: ఉస్మానియా
- Unicodes
  - 0c09 0c38 0c4d 0c2e 0c3e 0c28 0c3f 0c2f 0c3e
- Syllables
  - 0c09 0c380c4d0c2e0c3e 0c280c3f 0c2f0c3e
- N-grams
  - 0c090c380c4d0c2e0c3e0c280c3f
  - 0c380c4d0c2e0c3e0c280c3f0c2f0c3e
  - 0c280c3f0c2f0c3e0020
- ఉస్మాని
- స్మానియా
- నియా-

Figure 2. Extraction of syllable n-grams from Telugu word

D. Classification Experiments N Telugu Genre Corpus

The newly formed Telugu web page genre corpus is tested using different classification techniques. The classification results obtained in terms of accuracy, precision, recall and F-measure are shown in Table 7. Classification performance of RACC algorithm on Telugu web page genre corpus is tested using ANOVA, and it is observed that there is no statistically significant difference between the RACC, ACC, SVM and Naive Bayes classification techniques ($p < 0.05$). The reason is that most of the n-grams in the Telugu web page genres are unique.

TABLE VII.
COMPARISON OF RACC ALGORITHM RESULTS ON TELUGU 10-GENRE CORPUS WITH EXISTING CLASSIFICATION ALGORITHMS IN TERMS ACCURACY, PRECISION, RECALL AND F-MEASURE

Classifiers	A	P	R	FM
SVM	0.912	0.911	0.912	0.912
Naïve Bayes	0.90	0.93	0.92	0.925
ACC	0.98	0.972	0.978	0.974
RACC	0.987	0.99	0.986	0.985

A = Accuracy, P = Precision, R = Recall, FM = F-measure.

V. CONCLUSIONS

A scalable classification algorithm called Refined Adjustable Centroid Classification (RACC) is proposed for web page genre classification. RACC is the modification of ACC algorithm. The proposed algorithm is scalable because adding new genre to the classification model needs only the creation of a centroid for the new genre in the training phase. The proposed algorithm is used to classify different kinds of web page genre corpuses. On single-label 7-genre corpus, RACC algorithm performance in terms of F-measure is 99.1% when compared with ACC (98.8%). On single-label 10-genre corpus, RACC algorithm performance in terms of F-measure is 96.0% when compared with SVM (92.2%) and ACC (95.5%). On multi-label 20-genre corpus,

RACC algorithm performance in terms of F-measure is 96.9% when compared with ACC (96.6%) and Mason (84.6%). On multi-label 23-genre corpus, RACC algorithm performance in terms of F-measure is 95.7% when compared with SVM (91.0%) and ACC (95.3%). The experimental results suggest that RACC algorithm performance is better when compared with other classification algorithms on all the four corpuses. Statistical analysis is done using both ANOVA and paired t-test. The results obtained are found to be statistically significant ($p < 0.05$).

Syllable extraction algorithm is used to extract n-gram features from Telugu web pages. Seven new Telugu web page genres named as TELPOETRY, TELENTERTAINMENT, TELFAQ, TELCHILDREN, TELSOCIAL, TELETIQUETTE and TELE-GENRE are identified from randomly collected web pages based on annotation by objective sources and applying IEG algorithm with the use of existing 3-genre Telugu web page genre corpus. RACC algorithm performance in terms of F-measure is 98.5% on the newly formed 10-genre Telugu corpus when compared with SVM (91.2%), Naïve Bayes (92.5%) and ACC (97.4%). Statistical analysis results show that there is no statistically significant difference between the results of all the four algorithms. The reason is that the web pages in these genres are having unique 3-gram features. Overall, the ACC algorithm results are better when compared to the remaining three algorithms.

The work presented in this paper provides many directions for future extensions. This paper constructed ten Telugu web page genres, but still many genres are available in Telugu web pages. Constructing genre corpuses for Telugu web pages that contain more genres could be considered as a future work. A further possible extension could be to expand this work of identifying genres to other Indian languages. Future work could also include a study to develop an efficient and effective genre based search engine that supports genres in various orthographic spoken languages.

REFERENCES

[1] Bharati A., Chaitanya V., Sangal R. and Ramakrishnamacharyulu K.V., "Natural Language Processing: A Paninian Perspective", Prentice Hall of India, 1995.

[2] Blood R., "Weblogs: A History and Perspective", Rebecca's Pocket,07September2000.http://www.rebeccablood.net/essays/weblog_history.html.

[3] Cornelius P., "The corporate blog as an emerging genre of computer-mediated communication: features, constraints, discourse situation", Ph.D. thesis, 2010.

[4] Crowston K. and Williams M., "Reproduced and Emergent Genres of Communication on the World-Wide Web", In Proceedings of the 30th Hawaii International Conference on System Sciences (HICSS-30), IEEE Computer Society, pp. 30-39, 1997.

[5] Crowston K. and Williams M., "Reproduced and Emergent Genres of Communication on the World-Wide Web", The Information Society, vol. 16(3), pp. 201-216, 2000.

[6] Dong L., Watters C., Duffy J. and Shepherd M., "An Examination of Genre Attributes for Web Page Classification", In Proceedings of the 41st Hawaii International Conference on System Sciences (HICSS-41), IEEE Computer Society, 2008.

[7] Dott A. E., "An analysis of Wikipedia digital writing", Conference of the European Chapter of the Association for Computational Linguistics, 2006.

[8] Gupta R., Goyal P. and Diwakar S., "Transliteration among Indian Languages using WX Notation", In Proceedings of Semantic Approaches in Natural Language Processing, KONVENS 2010, Germany, September 2010.

[9] Jebari C. and ArifWani A., "A Multi-label and Adapative Genre Classification of Web Pages", In Proceedings of 11th International Conference on Machine Learning and Applications (ICMLA), 2012.

[10] Jebari C., "Enhancing the identification of web genres by combining internal and external structures", Pattern Recognition Letters, vol. 146, pp. 83-89, 2021.

[11] Kalyani N. and Sunitha K.V.N., "Syllable analysis to build a dictation system in Telugu Language", International Journal of Computer Science and Information Security (IJCSIS), vol. 6(3), 2009.

[12] Kanaris I. and Stamatatos E., "Webpage genre identification using variable-length character n-grams", In Proceedings of the 19th IEEE International Conference on Tools with Artificial Intelligence (ICTAI 2007), vol. 2, pp. 3-10, 2007.

[13] Kanaris I. and Stamatatos E., "Learning to Recognize Webpage Genres", Information Processing & Management, vol. 45(5), pp. 499-512, 2009.

[14] Karlgren J. and Cutting D., "Recognizing Text Genre with Simple Metrics Using Discriminant Analysis", Proceedings of the 15th International Conference on Computational Linguistics (COLING), Kyoto, Japan, 1994.

[15] Kennedy A. and Shepherd M., "Automatic Identification of Home Pages on the Web", In Proceedings of the 38th Hawaii International Conference on System Sciences (HICSS-38), IEEE Computer Society, 2005.

[16] Kessler B., Numberg G. and Shutze H., "Automatic Detection of Text Genre". Proceedings of the 35th Annual Meeting of the Association for Computational Linguistics and 8th Conference of the European Chapter of the Association for Computational Linguistics, Madrid, Spain, 1997.

[17] Koskensalo A., "Problems of LSP-Didactics Shown in Case of Specialized Genre of Touristic Websites", US-China Foreign Language, ISSN 1539-8080, Vol. 12, No. 7, 543-550, July 2014.

[18] Kwasnik B.H. and Crowston K., "Introduction to the Special Issue: Genres of Digital Documents", Information Technology & People, vol. 18(2), pp. 76-88, 2005.

[19] Mason J.E., "An n-gram Based Approach to the Automatic Classification of Web Page by Genre", Ph.D. thesis, Dalhousie University, Nova Scotia, 2010.

[20] Miller C., "Genre as Social Action". Quarterly Journal of Speech, vol. 70, pp.151-167, 1984.

[21] Negi A., Shanker K.N. and Chereddi C.K., "Localization, Extraction and Recognition of Text in Telugu Document Images", In Proceedings of the IEEE Seventh International Conference on Document Analysis and Recognition (ICDAR - 2003), 2003.

[22] Pranitha Kumari K., Venugopal Reddy A., "Syllable n-gram approach for Identification and Classification of genres in

Telugu language", in Proceedings of International Conference on Networks & Soft Computing, pp. 141-145, 19-20 August, 2014.

[23] Pranitha Kumari K., Venugopal Reddy A., "Identification and Classification of Emerging Genres in Web Pages", in Proceedings of International Conference on Computing and Communication Technologies, pp. 1-6, 11-13 December, 2014.

[24] Rehm G., Santini M., Mehler A., Braslavski P., Gleim R., Stubbe A., Symonenko S., Tavosanis M., and Vidulin V., "Towards a Reference Corpus of Web Genres for the Evaluation of Genre Identification Systems", In Proceedings of the 6th Language Resources and Evaluation Conference (LREC 2008), 2008.

[25] Rosmarin A., "The Power of Genre", University of Minnesota Press, 1985.

[26] Rosso M., "Using Genre to Improve Web Search", Ph.D. thesis, University of North Carolina, Chapel Hill (USA), 2005.

[27] Santini M., "Automatic Identification of Genre in Web Pages", Ph.D thesis, University of Brighton, 2007.

[28] Sharoff S., Zhili W. and Katja M., "The Web Library of Babel: evaluating genre collections", LREC, 2010.

[29] Shepherd M. and Watters C., "The Evolution of Cybergenres", In Proceedings of the 31st Hawaii International Conference on System Sciences (HICSS-31), IEEE Computer Society, vol. 2, pp. 97-109, Hawaii, USA, 1998.

[30] Sorower M.S., "A Literature Survey on Algorithms for Multi-label Learning", Oregon State University, Corvallis, vol. 18, pp. 1-25, 2010.

[31] Swales J., "Genre analysis", English in Academic and Research Settings. Cambridge University Press, Cambridge, UK, 1990.

[32] Todorov T., "Genres in Discourse", Cambridge University Press, Cambridge (UK) (translated by Catherine Porter from French, Editions du Seuil, 1978), 1990.

[33] Vidulin V., Lustrek M., and Gams M., "Training the Genre Classifier for Automatic Classification of Web Pages", In Proceedings of the 29th International Conference on Information Technology Interfaces, Journal of Computing and Information Technology, vol. 15(4), pp. 305-311, 2007.

[34] A. Onan, ''An ensemble scheme based on language function analysis and feature engineering for text genre classification,'' J. Inf. Sci., vol. 44(1), pp. 28–47, 2018.

[35] Witten I.H. and Frank E., "Data Mining: Practical Machine Learning Tools and Techniques", Morgan Kaufmann Publishers, Amsterdam, The Netherlands, 2nd edition, 2005.

[36] Yates J. and Orlikowski W., "Genres of organizational communication: A structural approach to studying communications and media", Academy of Management Review, vol. 17(2), pp. 229-326, 1992.

[37] K. Pranitha Kumari and A. Venugopal Reddy, "Performance improvement of web page genre classification," International Journal of Computer Applications, vol. 53(10), September 2012.

[38] K. Pranitha Kumari, A. Venugopal Reddy and S. Sameen Fatima, "Web page genre classification: Impact of n-gram lengths," International Journal of Computer Applications, vol. 88(13), February 2014.

[39] M. Wan, A. C. Fang, and C.-R. Huang, ''The discriminativeness of internal syntactic representations in automatic genre classification," Journal of Quantitative Linguistics, vol. 28(2), pp. 138-171, 2021.

[40] Godbole S. and Sarawagi S., "Discriminative Methods for Multi-labeled Classification", In Proceedings of the 8th Pacific-Asia Conference on Knowledge Discovery and Data Mining (PAKDD 2004), Springer, pp. 22-30, 2004.

[41] Tan P.T., Vipin Kumar and Michael S., "Introduction to Data Mining", 2006.

[42] Meka machine learning workbench download site. http://sourceforge.net/projects/meka/.

[43] Weka machine learning workbench download site. www.cs.waikato.ac.nz/ml/weka/downloading.html.

E-ISSN 2581 –7957
P-ISSN 2277 – 3916

CVR Journal of Science and Technology, Volume 21, December 2021
DOI: 10.32377/cvrjst2106

Smart Water Quality Monitoring System using IoT

M. Deva Priya
Assoc. Professor, Sri Krishna College of Technology /CSE Department, Coimbatore, Tamil Nadu, India
Email: m.devapriya@skct.edu.in

Abstract: **The normal method of testing or analyzing water is by collecting water samples manually and sending them to lab tests where they are tested for various chemical compounds consuming much time and manpower. This challenge can be overcome by using Internet of Things (IoT). In the proposed method, Temperature, pH value, Conductivity, Chemical Oxygen Demand (COD) and Total Dissolved Solids (TDS) of water samples are collected using respective sensors. A Microcontroller is interfaced with the sensors and data is forwarded to a Personal Computer (PC) for processing. The data is also stored on the Cloud using IoT based ThingSpeak. The resources involved in water quality monitoring are greatly reduced and the parameters are analyzed in real-time. The information is also sent to a smartphone or laptop/PC. This quick process is beneficial as it aids in analyzing and saving water bodies that are at the verge of becoming completely unusable.**

Index Terms: **Water Quality, PH, Conductivity, Temperature, Turbidity, IoT, Wi-Fi**

I. Introduction

Water is the most important source for the survival of humankind. This resource is greatly polluted by the current urbanization and revolution in other fields [1]. The drastically affected resource is water. Many stations are established by the government to save water from becoming contaminated and unusable. These stations are established and maintained by the Central Pollution Control Board (CPCB). These stations analyze the water body assigned to them for monitoring and a report is generated and shared to the officials through GPRS/3G/4G networks for necessary action [2].

Internet of Things (IoT) is the integration of internet and devices. The idea of automating and meeting daily needs through devices via internet established IoT has become common. This technology is greatly helpful in achieving many useful innovations of current generation needs. A study says that there are more than a Billion “Things” that use IoT [3].

Determining water quality is the need of the hour as contamination leads to various daring diseases. In this Paper, water quality is monitored by collecting, processing data and transferring the result to the rightful person. Data is collected and stored on the cloud for further processing. Nowadays, smartphones are universally used as they have all the inbuilt features. This has led to a dramatic increase in the number of mobile applications. The mobile features support sending and receiving data by enabling the IoT devices to connect and transfer data [4]. In a ubiquitous network, smart things have become a part of the internet. Authorized users can upload data derived from smart things on the cloud. Applications can be created with sensor logging, location tracing and social network of things with status updates using ThingSpeak. Application Programming Interface (API) of ThingSpeak enables handing of numeric data [5, 6]. The ThingSpeak channel provisions inclusion of fields like elevation, latitude, longitude and status. The data collected from the sensors are sent to the cloud, where they are stored as a channel.

Cloud enables easy access of the stored data. Channel data can be examined, envisaged and new data can be computed. It is possible to interact with web sites and social media. This feature enables finding new data and visualizing data in the form of plots, charts etc., using analytical tools. It can access MATLAB to provide sensor data [7]. Tools are employed for communication among devices. Actions can be taken for both raw and new data in a channel. It aids the devices to operate by queuing commands.

The investment depends on the number of parameters that are to be measured. The fluctuations in the water quality have to be rapidly recognized and sent to higher officials. A novel method is proposed for sensing real-time data and sharing it through smart phones or PC/Laptop. The proposed system measures the quality of water using various IoT sensors and sends digital data to the devices eliminating manual intervention. In this Paper, Section 2 discusses about the work done by various researchers in monitoring the water quality while Section 3 discusses on IoT. Section 4 discusses about the implementation of monitoring water quality system and the results obtained are discussed in Section 5. Section 6 gives the conclusion.

II. Related Work

The water resources are getting depleted and deteriorated due to increase in population, demand for water in agriculture, industries and other personal needs of humans. Water quality is also affected greatly due to pesticides and other chemicals that are used in agriculture. Major river bodies are greatly affected by discharges from industries and untreated sewages. To deal with the issues that are associated with manual water monitoring, CPCB planned to establish real-time Water Quality Monitoring (WQM) network across the Ganga basin. Papageorgiou (2003) [8] have dealt with designing localized algorithms and have used direct diffusion as a collection of concepts that define the communication patterns primary to such algorithms. The design characteristics vary from outmoded wireless networks and are data and application based. Le et al (2007) [9] have deployed sensors for monitoring water quality in terms of salinity and level of underground water in northern Australia in real-time.

Qiao & Song (2010) [10] have developed an online system for monitoring water quality based on General Packet Radio Service (GPRS)/ Global System for Mobile

Received on 09-06-2021, Revised on 02-07-2021, Accepted on 27-08-2021.

CVR Journal of Science and Technology, Volume 21, December 2021
DOI: 10.32377/cvrjst2106

Communications (GSM) features. The information is transferred using the GPRS network that helps to remotely analyze the water quality parameters. Silva et al (2011) [11] have presented a web dependent water monitoring system by deploying sensors using ZigBee and WiMAX. The parameters are measured, collected, processed and directed through the ZigBee gateway to the web server using WiMAX. The water quality is analyzed remotely in real-time. Bhardwaj (2011) [12] has clearly stated the route of river Ganga and the amount of waste dumped in it along the path. It is clearly understood that even the most important water resource of our nation is severely affected by pollutants.

He & Zhang (2012) [13] have designed a water quality measuring system based on sensors. The remote sensor is based on ZigBee. The parameters and the data are sent to the Web using GPRS. With the help of the Internet, the information is gathered at the remote server. Amruta & Satish (2013) [14] have designed a solar powered water quality network that utilizes a Remote Sensor Network (RSN). The Base Station (BS) gathers the information from a remote sensor. The BS associated with the ZigBee module is powered by the sunlight baseboard from where the energy for the system is harvested.

Wang et al (2015) [15] have focused on a novel research using IoT. Starting from the viewpoint of correlative technologies depending on time to assess the evolutionary process of IoT, they have dealt with the associations among the correlation methods that are widely absent in the existing literature. They have highly focused on the overview and association of prevailing technologies and less on challenges describing the evolutionary process of IoT. Cloete et al (2016) [16] have focused on designing and developing a water quality monitoring system with an aim of informing the details of the related parameters in real-time. The system is capable of measuring the physicochemical parameters of water quality which include flow, temperature, pH, conductivity, and oxidation reduction potential. Das & Jain (2017) [17] have used Thing speak to store and analyze data collected from sensors related to water quality. This is time efficient and effective in analyzing data.

III. Proposed Smart Water Quality Monitoring System using IoT (SWQMSI)

The proposed system includes 3 phases namely, Pre-processing, Feature Extraction and Classification.

A. Preprocessing

In this phase, it is ensured that the collected data in the right form so it can be further processed. Handling missing data is the greatest challenge. The missing value can be replaced using data loss prevention algorithms that are employed in statistical data. The missing value is substituted with the median of the data available. In a histogram, the data is transformed into a graph. The median is found using the following formula.

$$\text{Median} = L_m + \left(\left(\frac{\frac{N}{2} - F_{m-1} - 1}{F_m} \right) . c \right) \quad (1)$$

Here,

L - Median bar lower limit
N - Total count of observations
F_{m-1} - Cumulative frequency of the bar
f - median bar frequency
c - median bar width

In this approach, IoT sensors are used to obtain the pH level, conductivity, Turbidity and temperature of the water. These data are in the form of analog signals that are converted to digital signals using an Analog to Digital converter. Then the converted digital signals are sent through Wi-Fi to the microcontroller. When data from the sensors is received by the microcontroller, it is further processed and sent to the Smartphone or Laptop/PC. The data flow is from sensors to the webpage that is accessed at the end user device via microcontroller. These processes are carried out by programs that are written using Embedded-C in Arduino IDE.

B. Feature extraction

The most prominent information is extracted from the dataset for analysis. It involves simplifying the amount of information required to represent a large set of data accurately.

C. Classification

The pH value of water should be in the range 6.5 to 8.5. If the value is below 6.5, then it is acidic; If it is greater, then it is alkaline, else neutral. The acceptable temperature range is 28 - 44 degree centigrade. Distilled water can have a conductivity of 0.5 to 3 μmhos/cm, while that of rivers ranges from 50 to 1500 μmhos/cm, and that of inland fresh waters specify that streams with mixed fisheries are between 150 to 500 μmhos/cm. Similarly, the Total Dissolved Solids (TDS) in milligrams per unit (mg/L) for drinking water can have a maximum concentration level of 500 mg/L EPA. As said by WHO recommends, the Chemical Oxygen Demand (COD) of drinking water is 10 ppm. When the values of each parameter exceed the limits, they are confirmed to be contaminated.

IV. System Design

The data collected by the sensors are processed using the LPC2148 microcontroller module and are sent via the ESP8266 Wi-Fi module to the webpage in the end device. The overall collection, processing, analyzing and transfer of data are done in real-time. Fig.1. shows how the components are connected to each other.

The system uses the following sensors namely, pH, temperature, conductivity and ultrasonic [18], microcontroller unit as the predominant processing module and a data communication module (ESP8266 Wi-Fi module). The microcontroller unit plays a predominant role designed for water quality measurement as it consumes less power and is smaller in size. It includes a chip ADC that interprets the analog signals into digital values for investigation. Based on the nature of output, the sensor's analog outputs are connected to the microcontroller's analog pins, and digital outputs are connected to the digital pins. The microcontroller processes the data and sends to the

ThingSpeak server through the Wi-Fi module (NodeMCU) [19].

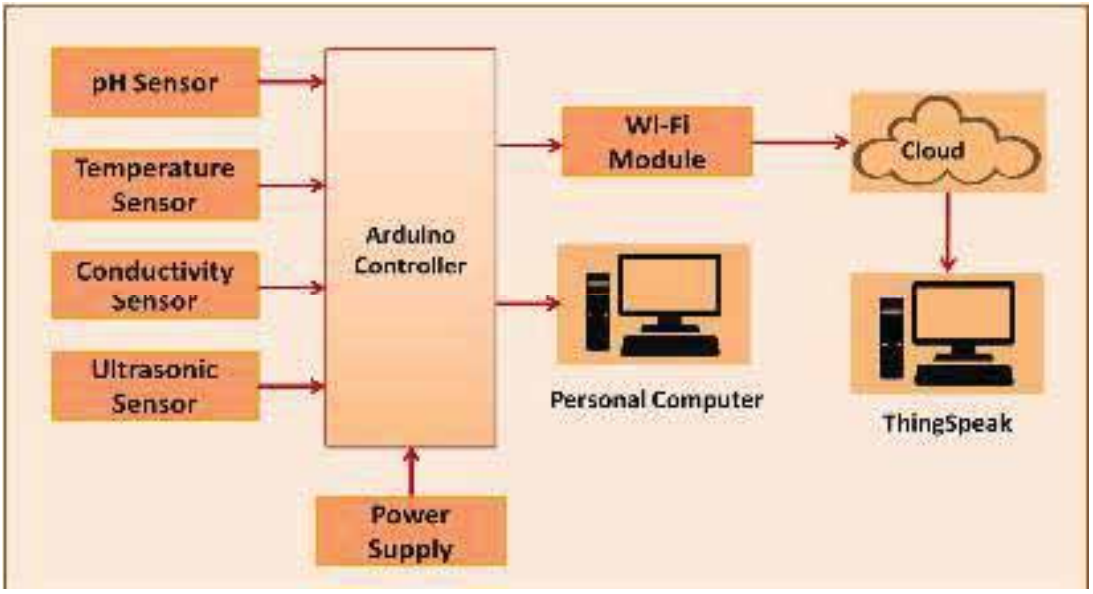

Figure 1. Block diagram of component integration

Arduino UNO microcontroller is used in this system as it has many merits. It has a faster flash memory, consumes less power and is smaller in size. This microcontroller helps in reducing the consumption of power and space. The Wi-Fi module is connected through the [Tx/Rx] pin through which transferring and receiving of data is done. The ESP8266 Wi-Fi provides easy connectivity with any microcontroller, enabling it to be a great Wi-Fi module for IoT devices. This system uses Attention Commands to connect and open the Transmission Control Protocol (TCP) connection through the Wi-Fi network instead of using TCP/IP stack. So communication from the microcontroller to the ESP8266 Wi-Fi module is enough to push the processed data to the web.

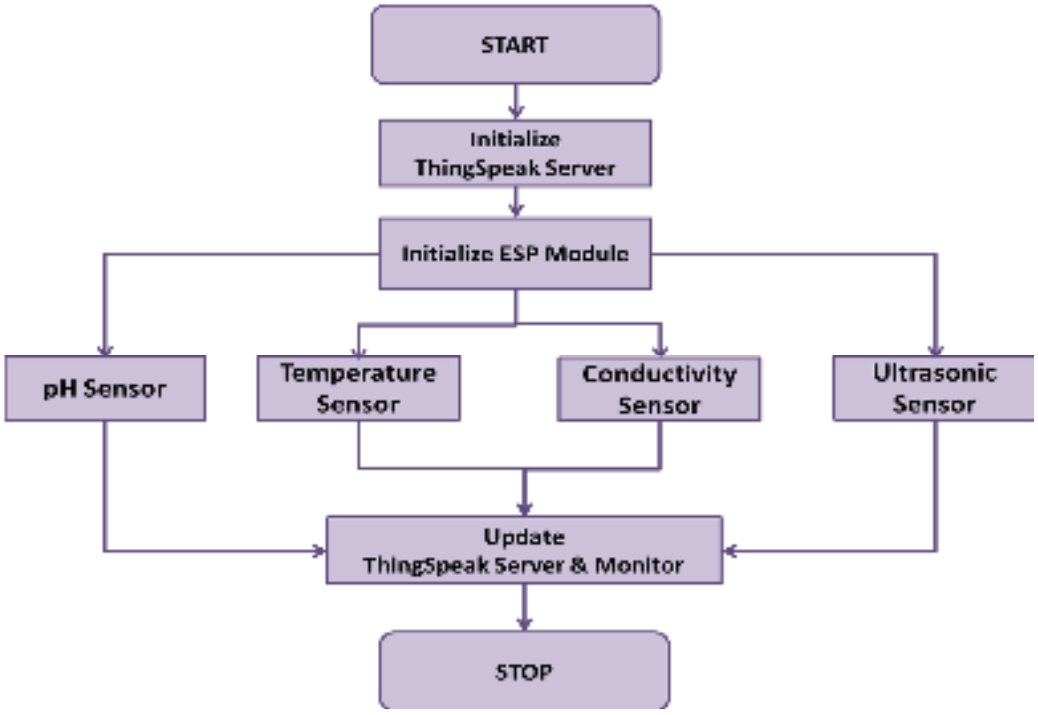

Figure 2. Overall Functioning of the System

The steps are shown in Fig. 2. Primarily, the serial monitor in the Arduino is set to 115200 baud rate, and the Wi-Fi module and the ThingSpeak server are initialized. The values of the sensors are updated on the server. As the ultrasonic sensor deals with digital value, it is taken directly for duration (Seconds). From the duration, distance can be computed as shown in the following equation.

Distance = (Duration) / 58.8 (2)

CVR Journal of Science and Technology, Volume 21, December 2021
DOI: 10.32377/cvrjst2106

The DHT 11 Sensor handles the analog values of both temperature and humidity. In case of pH sensor, the analog values of 10 samples are taken into account. The average value is computed. Similarly, the conductivity is also measured. The microcontroller unit with sensors considers samples every 10s and the parameters are shown on the Arduino IDE serial display. The server is updated every 20s.

Based on the Nernst equation, the pH value of water is directly proportional to water voltage.

$$E = E^{\circ} + \left(\frac{RT}{zF}\right).pH \quad (3)$$

where,

E - Cell potential under the prevailing conditions

E° - Cell potential under standard temperature and pressure conditions

R - Universal gas constant

T - Temperature

z - Number of electric moles

F - Constant Faraday

The Turbidity of water is inversely proportional to the voltage in water.

$$T = -1120.4\,x^2 + 5742.3x - 4352.9 \quad (4)$$

where,

x - Voltage

The sensors used and their purpose are detailed in Table I.

TABLE I.
SENSORS AND THEIR DESCRIPTION

Sensors	Description
pH Sensor	Used to find the pH value which is the level of acidic or alkaline level of the water. If the value is below 7, then it is acidic; If it is greater, then it is alkaline, else neutral.
Electric Conductivity Sensor	Used to measure the electric conductivity. Salts generally have positive and negative ions which are good conductors of electricity. This ability of ions in water with dissolved salt to conduct electricity is called Electric conductivity.
Turbidity Sensor	Used to measure the turbidity which is the measure of particles suspended in the water
Temperature Sensor	Used to measure the temperature which is the measure of heat or chillness around

V. IMPLEMENTATION

The system is designed in Embedded-C and simulated using Arduino IDE. Authorized users have access to the data stored on ThingSpeak server [20]. The data is collected, stored, examined and conveyed in real-time. Users with access to Thingspeak can login as shown below (Fig. 3). The real-time values are shown in the form of graphs [21].

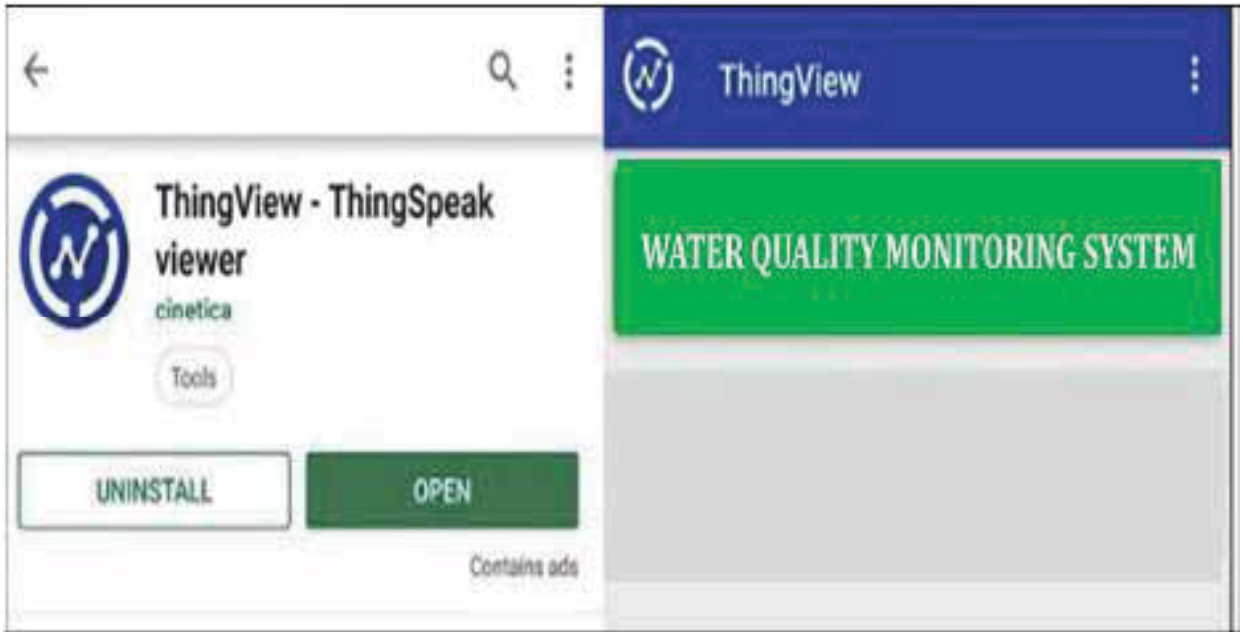

Figure 3. ThingSpeak Application

ThingSpeak supports analysis of IoT data collected from edge node devices [22, 23]. The channel with data and status fields are the primary components. Once a channel is developed, data can be altered, handled and inferred using MATLAB [24, 25]. The following table (Table 2) shows some sample data of raw values collected and the graphs generated from these values for different Stations. Fig. 4 shows the hardware setup of the Project. Figure 5 to Figure 9 show the Temperature, pH value, Conductivity, Chemical Oxygen Demand (COD) and Total Dissolved Solids (TDS) obtained at different stations.

CVR Journal of Science and Technology, Volume 21, December 2021
DOI: 10.32377/cvrjst2106

TABLE 1I.
SENSORS AND THEIR DESCRIPTION

Stations	Temperature (○C)	pH	Conductivity (µS/cm)	COD (ppm)	Total Dissolved Solids (mg/L)
1	28.4	6.6	6.6	7.3	5.7
2	29.2	6.1	6.1	8.1	5.91
3	27.6	5.9	5.9	8.5	4.83
4	28.7	6.7	6.7	7.8	5.27
5	29.3	7.1	7.1	8.2	4.72
6	31.4	6.2	6.2	7.7	5.36

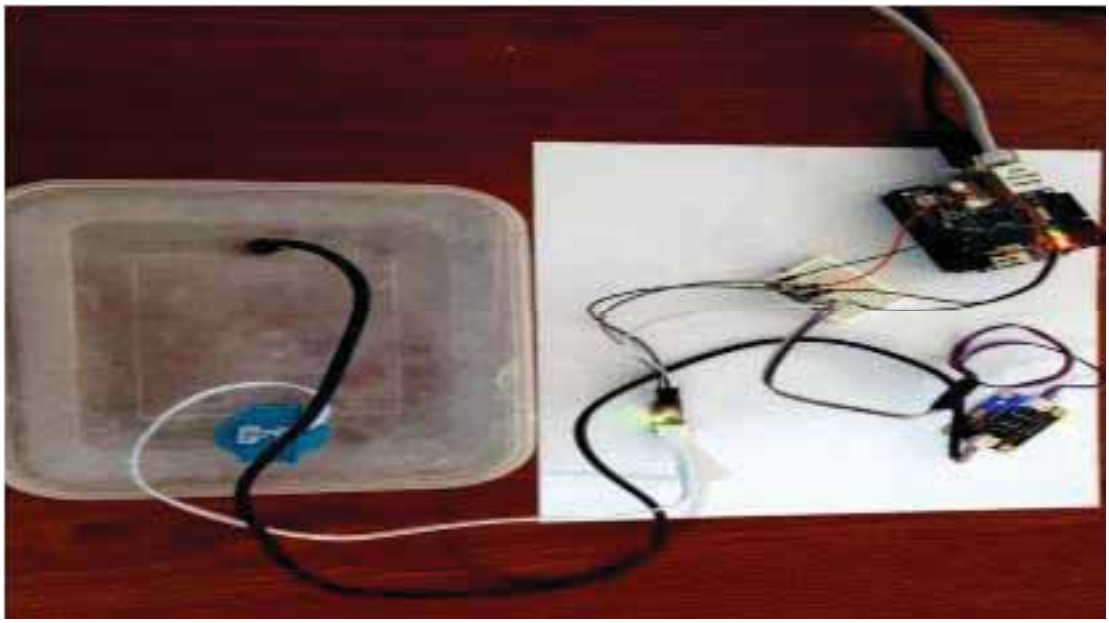

Figure 4. Hardware

B. Working with ThingSpeak

ThingSpeak is an IoT application's open source, wherein data can be stored and retrieved.

Getting started:

- ✓ Sign-up in ThingSpeak
- ✓ Create new channel to store the data obtained from sensors
- ✓ Give the field names as pH, Temperature, conductivity, TDSx
- ✓ If public option is checked, data is available to all

Sending data to Thing Speak:

- ✓ Configure the microcontroller program to the URL that is provided by ThingSpeak
- ✓ Additional data can be added through the link
- ✓ Charts can be generated from data that is sent to the ThingSpeak channel using View Charts option

Both data uploading and graph generation in ThingSpeak takes place in real-time.

E-ISSN 2581 –7957
P-ISSN 2277 – 3916
CVR Journal of Science and Technology, Volume 21, December 2021
DOI: 10.32377/cvrjst2106

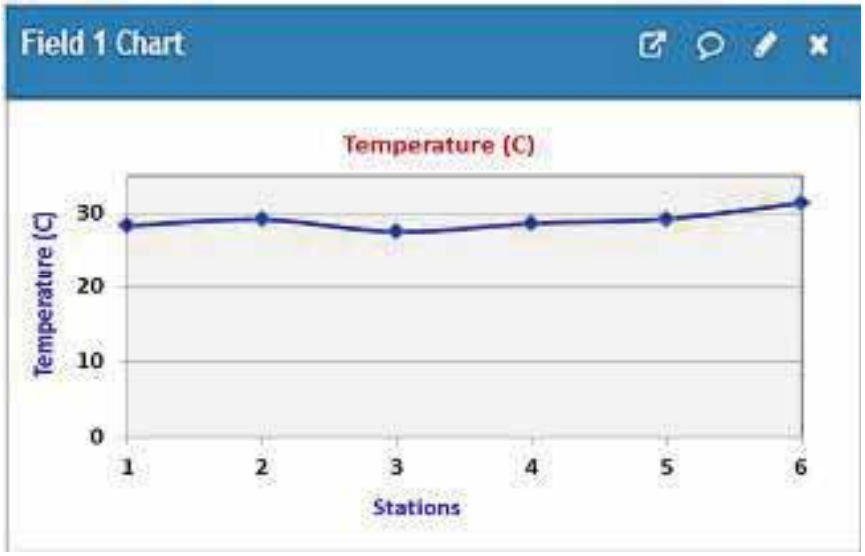

Figure 5. Temperature measured at Different Stations

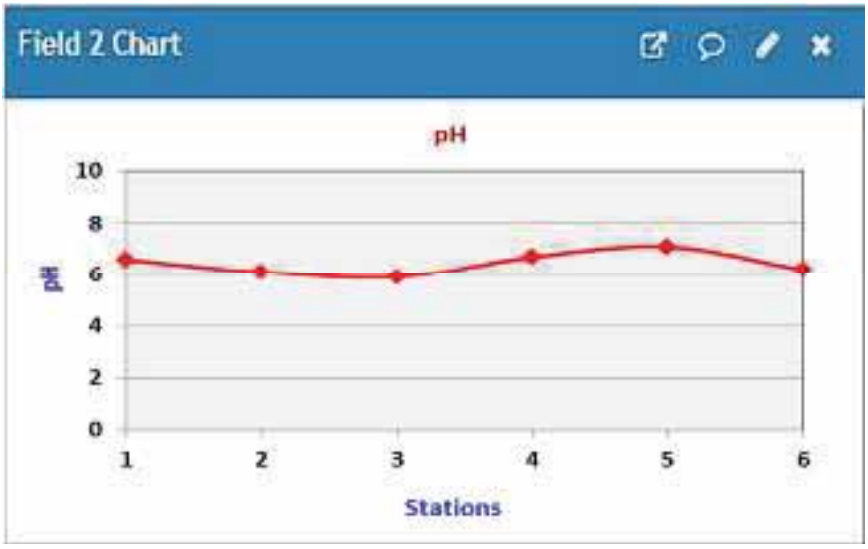

Figure 6. pH Value measured at Different Stations

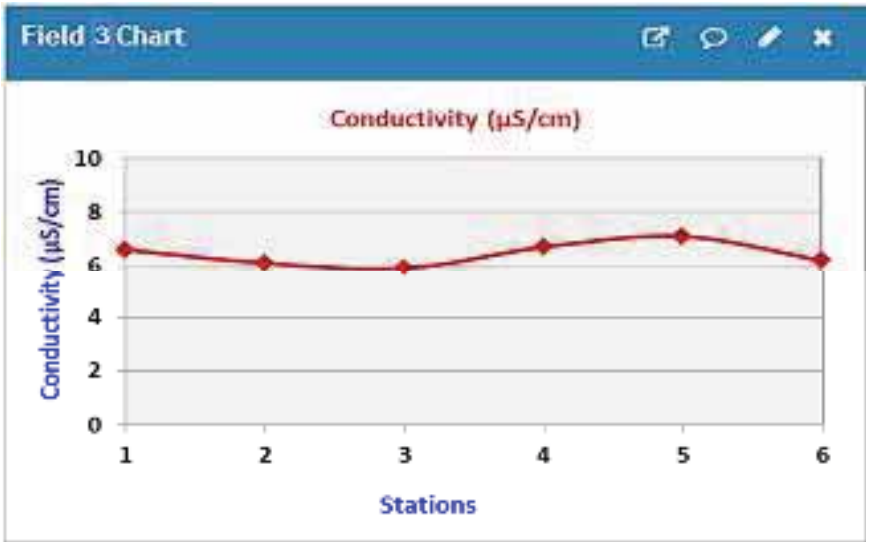

Figure 7. Conductivity measured at Different Stations

Figure 8. Chemical Oxygen Demand (COD) measured at Different Stations

Figure 9. Total Dissolved Solids (TDS) measured at Different Stations

VI. Conclusions

The system propounded for water monitoring is an efficient and low-priced IoT solution for real-time water quality monitoring. The micro controller and sensors are interfaced. An effectual algorithm is designed to track water quality. ThingSpeak is used to observe the Temperature, pH value, Conductivity, Chemical Oxygen Demand (COD) and Total Dissolved Solids (TDS) of water at different stations through the webserver. These parameters are also observed in the ThingSpeak mobile application.

References

[1] Pasika, S., & Gandla, S. T. (2020). Smart water quality monitoring system with cost-effective using IoT. Heliyon, 6(7), e04096.

[2] Jha, B. K., Sivasankari, G. G., & Venugopal, K. R. (2020). Cloud-based smart water quality monitoring system using IoT sensors and machine learning. International Journal, 9(3).

[3] Martínez, R., Vela, N., El Aatik, A., Murray, E., Roche, P., & Navarro, J. M. (2020). On the use of an IoT integrated system for water quality monitoring and management in wastewater treatment plants. Water, 12(4), 1096.

[4] Tarik, M., Malik, M. S., Yadav, P., Muzzaffar, H., & Nagar, G. (2020). Smart Water Quality Monitoring System based on IoT. Journal of Critical Reviews, 7(19), 3447-3452.

[5] Ighalo, J. O., Adeniyi, A. G., & Marques, G. (2021). Internet of things for water quality monitoring and assessment: a comprehensive review. Artificial intelligence for sustainable development: theory, practice and future applications, 245-259.

[6] Pasha, S. (2016). ThingSpeak based sensing and monitoring system for IoT with Matlab Analysis. International Journal of New Technology and Research, 2(6).

[7] Othman, N. A., Damanhuri, N. S., Mazalan, M. A. S., Shamsuddin, S. A., Abbas, M. H., & Meng, B. C. C. (2020). Automated water quality monitoring system development via LabVIEW for aquaculture industry (Tilapia) in Malaysia. Indones. J. Electr. Eng. Comput. Sci, 20(2), 805-812.

[8] Papageorgiou, P. (2003). Literature survey on wireless sensor networks.
[9] Le Dinh, T., Hu, W., Sikka, P., Corke, P., Overs, L., & Brosnan, S. (2007, October). Design and deployment of a remote robust sensor network: Experiences from an outdoor water quality monitoring network. In the 32nd IEEE Conference on Local Computer Networks (LCN 2007) (pp. 799-806). IEEE.
[10] Qiao, T. Z., & Song, L. (2010, October). The design of a multi-parameter online monitoring system of water quality based on GPRS. In the 2010 International Conference on Multimedia Technology (pp. 1-3). IEEE.
[11] Silva, S., Nguyen, H. N., Tiporlini, V., & Alameh, K. (2011, December). Web based water quality monitoring with sensor network: Employing ZigBee and WiMax technologies. In the 8th International Conference on High-capacity Optical Networks and Emerging Technologies (pp. 138-142). IEEE.
[12] Bhardwaj, R. M. (2011). Overview of Ganga River Pollution. Report: Central Pollution Control Board, Delhi.
[13] He, D., & Zhang, L. X. (2012). The Water Quality Monitoring System based on Wireless Sensor Network. Report: Mechanical and Electronic Information Institute, China University of Geo-Science, Wu Hen, China, 7.
[14] Amruta, M. K., & Satish, M. T. (2013, March). Solar powered water quality monitoring system using wireless sensor network. In 2013 International Multi-Conference on Automation, Computing, Communication, Control and Compressed Sensing (iMac4s) (pp. 281-285). IEEE.
[15] Wang, F., Hu, L., Zhou, J., & Zhao, K. (2015). A survey from the perspective of the evolutionary process in the internet of things. International Journal of Distributed Sensor Networks, 11(3), 462752.
[16] Cloete, N. A., Malekian, R., & Nair, L. (2016). Design of smart sensors for real-time water quality monitoring. IEEE access, 4, 3975-3990.
[17] Das, B., & Jain, P. C. (2017, July). Real-time water quality monitoring system using Internet of Things. In 2017 International Conference on Computer, Communications and Electronics (Comptelix) (pp. 78-82). IEEE.
[18] Moparthi, N. R., Mukesh, C., & Sagar, P. V. (2018, February). Water quality monitoring system using IoT. In 2018 Fourth International Conference on Advances in Electrical, Electronics, Information, Communication and Bio-Informatics (AEEICB) (pp. 1-5). IEEE.
[19] Daigavane, V. V., & Gaikwad, M. A. (2017). Water quality monitoring system based on IoT. Advances in wireless and mobile communications, 10(5), 1107-1116.
[20] Hemdan, E. E. D., Essa, Y. M., El-Sayed, A., Shouman, M., & Moustafa, A. N. (2021, July). Smart Water Quality Analysis using IoT and Big Data Analytics: A Review. In 2021 International Conference on Electronic Engineering (ICEEM) (pp. 1-5). IEEE.
[21] Cao, H., Guo, Z., Wang, S., Cheng, H., & Zhan, C. (2020). Intelligent wide-area water quality monitoring and analysis system exploiting unmanned surface vehicles and ensemble learning. Water, 12(3), 681.
[22] Miry, A. H., & Aramice, G. A. (2020). Water monitoring and analytic based ThingSpeak. International Journal of Electrical and Computer Engineering, 10(4), 3588.
[23] Khatri, P., Gupta, K. K., & Gupta, R. K. (2019, February). Smart Water Quality Monitoring System for Distribution Networks. In Proceedings of International Conference on Sustainable Computing in Science, Technology and Management (SUSCOM), Amity University Rajasthan, Jaipur-India.
[24] Saab, C., Shahrour, I., & Chehade, F. H. (2020). Risk Assessmnt of Water Accidental Contamination Using Smart Water Quality Monitoring. Exposure and Health, 12(2), 281-293.
[25] Imran, L. B., Latif, R. M. A., Farhan, M., & Aldabbas, H. (2020). Smart City Based Autonomous Water Quality Monitoring System Using WSN. Wireless Personal Communications, 115(2), 1805-1820.

E-ISSN 2581 – 7957
P-ISSN 2277 – 3916

DOI:10.32377/cvrjst 2107

Ensemble Classifier Model with Crow Search Feature Selection for Recognition of EEG Motor Imagery

V. Gokula Krishnan[1] and V. Divya[2]
[1]Assoc. Professor, CVR College of Engineering/CSIT Department, Hyderabad, India
Email: gokul_kris143@yahoo.com
[2]Research Scholar, Sathyabama Institute of Science and Technology/School of Electrical Engineering, Chennai, India
Email: vdivya6891@gmail.com

Abstract: **The patient with limb dyskinesia can do his daily activities and rehabilitation training with the help of Brain Computer Interaction (BCI) based on Electroencephalography (EEG). But the EEG feature extraction and classification faces the issues of low efficiency and accuracy due to large individual differences and low signal-to-noise ratio. To solve this problem, this paper proposes a recognition method of motor imagery EEG signal based on ensemble classifier. To increase the quality of EEG signal characteristic data, this method initially uses the short-time Fourier transform (STFT) and continuous Morlet wavelet transform (CMWT) by pre-processing the collected experimental datasets, which is based on time series characteristics. In order to achieve high quality features, ensemble classifier effectively recognize the EEG signals. The quality of EEG signal feature acquisition is improved by ensuring the high accuracy and precision of EEG signal recognition. Haralick features are extracted to improve the motor imagery, where Crow Search Algorithm (CSA) is used to select the optimal features. The experiments are carried out on laboratory measured data and BCI competition dataset. The results showed accuracy of this method for EEG signal recognition is better than existing techniques.**

Index Terms: **Brain computer interaction (BCI), short-time Fourier transform (STFT), continuous Morlet wavelet transform (CMWT), Crow search algorithm (CSA), Horlick features and Ensemble classifier.**

I. INTRODUCTION

BCI is a communication control system directly established between the brain and external devices (computers or other electronic devices), using signals generated during brain activity [1]. Instead of relying on the muscles and organs, the system directly builds communication between the brain and the machine. Electroencephalogram (EEG) is one of the most common signals used for building a BCI system because of its cost-effectiveness, non-invasive implementation, and portability. BCIs have shown potential in applying various fields such as communication, control, and rehabilitation [2]. Recent years have witnessed intense research into different types of BCI systems. According to the signal acquisition method, BCI technology can be divided into three types: non-implantable system, semi-implantable system, And an implantable system. Non-implantable BCI systems mainly use EEG to recognize human's intention. According to the signal generation mechanism, BCI systems can be divided into induced BCI systems and spontaneous BCI systems. The induced BCI systems are: steady-state visual evoked potentials (SSVEP) [3-4], slow cortical potentials [5], and the P300 [6-8] and the spontaneous BCI systems are: motor imagery (MI) [9-12].

Derived from this type of data, the curse of dimensionality problem [13] is usually present, as the features vastly outnumber the observations. In the particular case of this work, machine learning algorithms may lose the ability to generalize knowledge. A possible solution is Feature Selection (FS), which brings several benefits: noise and redundancy removal, reduced computational costs, and improved classification accuracy. FS is often highlighted in the existing literature on BCI applications [14], citing its importance in real-time performance or the understanding of the brain, among other benefits. However, FS is an NP-hard problem [15], which renders brute-force approaches unfeasible due to the size of the search space. The three main types of alternative methods are filter, wrapper and embedded [16]. Filter methods measure the relationship between features and the dependent class variable. Wrapper methods evaluate the performance of a classifier using different feature subsets. Embedded methods integrate FS into the classifier. The advantage of filters lies in their lower computational complexity, whereas wrapper and embedded approaches frequently achieve better results. In this paper, a wrapper method based on a Genetic Algorithm (GA) is employed. GAs are popular for BCI tasks, be it for FS [17–19] or other purposes [20].

Neural networks are a promising alternative to address the complexity of BCI data, since they are universal approximators and thus they can represent a wide variety of continuous functions. Besides standard Feed-Forward Neural Networks (FFNNs), which are the simplest kind of neural network in terms of structural design, there is growing interest in architectures that are able to leverage context. Convolutional Neural Networks (CNNs) extract local patterns through the convolution operator and have been successfully applied to EEG signals [21- 22]. Recurrent Neural Networks (RNNs) [23-24], which are not as widespread as CNNs yet, can dynamically store context to improve processing of individual bits of data. In EEG-based Motor Imagery (MI), many machine learning algorithms and feature extraction methods have been studied to try to overcome the limitations of small dataset and poor signal-to-noise ratios. The Support Vector Machine (SVM), despite its age, can still produce promising results when

Received on 16-06-2021, Revised on 22-07-2021, Accepted on 24-08-2021.

CVR Journal of Science and Technology, Volume 21, December 2021
DOI:10.32377/cvrjst 2107

paired with the right features: in [25], mutual information is calculated from Common Spatial Pattern (CSP) features to select optimal frequency bands, and dimensionality is further reduced by means of Linear Discriminant Analysis (LDA) before finally classifying the patterns with SVM; in a later study [26], the same authors use LDA for spatial filtering and a Long Short-Term Memory (LSTM) network for temporal filtering before classifying again with SVM. Alternative approaches to classic machine learning also exist, such as classification by Riemannian geometry [27] or by a residual norm-based strategy [28].

II. Related Works

Saa and Cetin [29] have proposed the Filter Bank Common Spatial Pattern (FBCSP). After filtering the original EEG signal with a set of filters, the CSP method is used to extract features on each filtered frequency band. Finally, the feature selection algorithm is applied on the basis of the extracted features. The above work research has improved the accuracy of some motor imaging tasks to a certain extent. However, since it takes a lot of time to select the characteristics of the experimental data set for each experimental object, it is not universal. Suk and Lee [30] proposed a technique for selecting class and subject specific frequency bands on the basis of the analysis of channel frequency map, which is a channel-frequency matrix. They individually performed spatial filtering, feature extraction and classification for each frequency band. Thus, they considered the cumulated outputs at the end to feed as an input EEG. They found their proposed technique to surpass the performance of common spatial pattern (CSP) in terms of session-to-session transfer rate and cross-validation. For certain subjects, they found increased classification accuracy.

Wei et al., [31] have used EEG emotion data set SEED for emotion recognition research. The abstract features of EEG samples are automatically extracted based on the convolutional neural network in deep learning, eliminating the need for manual feature selection and dimensionality reduction. And with the most advanced methods at present, a considerable accuracy rate has been achieved. Liang et al., [32] have developed an online sequential algorithm called OS- ELM (online sequential extreme learning machine) for SLFNs with additive or radial basis function (RBF) hidden nodes in a consolidated framework. It has been designed to learn data either chunk- by- chunk or one-by-one. A detailed performance comparison of the proposed method was done with other renowned sequential learning algorithms on standard issues related to time series prediction, classification and regression. The experimental results proved OS-ELM to be faster and generated better generalization performance than its counterparts. Zhang et al., [33] an example of this, but the method was not robust to changes in data pre-processing in preliminary experiments conducted by the authors of this manuscript. In particular, their model appears to over fit to data which was overlapping between training and test sets, resulting in astoundingly high accuracies (98%). With clearer separation between the training and testing sets, we found their model to achieve approximately 36% accuracy on the four-class problem.

III. Proposed System

In this section, the explanation of proposed method is given briefly. Initially, the publicly available datasets are considered for this research work. In pre-processing, a filter is used to remove unwanted signals and two transformation models are included. Then, these outputs are given as input to Haralick feature extraction technique for relevant feature extraction. The optimal features are selected by using crow-search algorithm and finally, these optimal features are given as input to ensemble classifier for final classification. Figure 1 describes the working flow of proposed methodology.

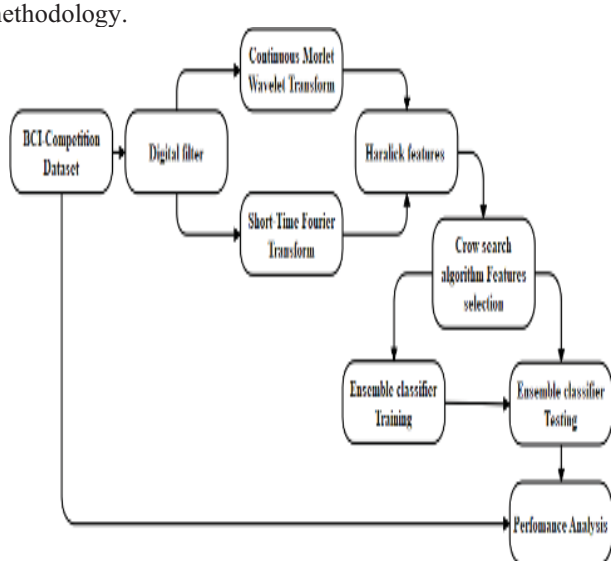

Figure 1. Proposed System model.

A. Dataset Description

Dataset 1: The first dataset was from BCI-Competition-III-IVa and was collected in a cue-based setting. Only cues for the classes "right" and "foot" are provided. This dataset was recorded from five healthy subjects (aa, al, av, aw and ay) at 100 Hz. The subjects sat in a comfortable chair with arms resting on armrests. The raw data were continuous signals of 118 EEG channels and markers that indicate the time points of 280 cues. Each sample was segmented from [0, 2.5] s by marks, then passed a band-pass filter (5-order Butterworth digital filter with cut-off frequencies at [8, 30] Hz) to remove muscle artifacts, line-noise contamination, and DC drifts. Under the condition that the positive sample and the negative sample were balanced, 100 samples were randomly selected as the training pool. The remaining samples were used as the test samples.

Dataset 2: The second dataset was from BCI-Competition-IV-1. The dataset was recorded from seven healthy subjects (a, b, c, d, e, f and g), including four healthy individuals (named "a," "b," "f," "g") and three artificially generated "participants" (named "c," "d," "e"). 59-channel EEG signals were recorded at 100 Hz. Two motor imagery classes were selected for each subject from the three classes: left hand, right hand, and foot. There were two subjects (a, f) whose motor imaging tasks were different from the others,

so they were eliminated. Here we only used the calibration data because of the complete marker information. Each sample was segmented from [0, 2.5] s by marks, then passed a band-pass filter (5-order Butterworth digital filter with cut-off frequencies at [8, 30] Hz) to remove muscle artifacts, line-noise contamination, and DC drifts. After pre-processing, we obtained 200 samples for each subject. In this proposed system subject "g" is not considered. We randomly selected 100 samples as a training pool and the rest as test samples, like dataset 1.

B. Feature Extraction

These two phenomena are an important basis for distinguishing different types of EEG signals. Therefore, the time-frequency domain analysis method combines the two methods as one for the effective analysis methods [34], where the two methods includes Short-Time Fourier Transform and Continuous Morlet Wavelet Transform that are briefly discussed in the below section.

C. Haralick feature extraction

The extraction of distinguishing features from the given EEG data is carried out by Haralick features for better classification. According to the spatial dependencies of gray tone images, the quantifiable textural properties are obtained from the CMWT and STFT, which is utilized as statistical measures of textures. Haralick characteristics produce accurate extraction that is resilient in the various arm and leg movements. The transformation technique bidimensionally represents the spatial gray level distribution. After creating the co-occurrence matrices, the Haralick features may be extracted from the gray level histogram. The final feature vector is produced by the estimated Haralick features.

D. Short-Time Fourier Transform

The short-time Fourier transform first divides the entire time series into several time segments of equal length. Then calculate the frequency spectrum information in each time segment by Fourier transform. Obtain the change of each frequency component with respect to time from the surface. The calculation formula is as follows:

$$s(f,k) = \sum_{n-0}^{N-1} s(n)[W(n-k)e^{\frac{f2\pi fn}{-N}}] \quad (1)$$

Where, $S(n)$ represents the time series of EEG signals. $W(n)$ represents window function. N represents the number of time points recorded. k represents the index of different time windows. f represents the frequency component in the signal. n represents the time point. The length of the time window required to be divided in the formula is the same, which determines that the algorithm performs well when measuring high-frequency components. When measuring low-frequency components, it is often accompanied by distortion.

In order to effectively measure the change trend of the μ rhythm and β rhythm in the signal, this paper selects the time-frequency matrix obtained by the time window of $0.5s$ and the hamming window function. Combine the time-frequency matrices on the two channels C3 and C4. A three-dimensional tensor with a size of $33*35*2$ is obtained as the input of the subsequent convolutional neural network. From the output matrix the 32 features are extracted such as autocorrelation, contrast, correlation, correlation, cluster output, cluster hue, difference, energy entropy, uniformity, uniformity, extreme likelihood, number of cubes, variance, normal sum, sum change, entropy of a sum, difference fluctuation, entropy conversion are highlighted. the evidence of correlation1, the informational proportion of correlation2, the inverse difference, the standardized inverse contrast and the normalized inverse of the change

E. Continuous Morlet Wavelet Transform

The Morlet wavelet transform uses a wavelet of finite length and attenuation as the base to measure the intensity of each rate component in the signal over time. The formula is as follows:

$$W(a,b) = \int_{-\infty}^{\infty} x(x)\frac{1}{\sqrt{a}}\psi(\frac{t-b}{a})dt \quad (2)$$

Where, $x(t)$ represents the signal sequence. $\psi(t)$ represents the wavelet basis.t represents the time point. The parameter a controls the scaling of the wavelet function. When a takes a value from small to large, the wavelet function gradually widens, so the low-frequency components can be better measured. And by adjusting the parameter b, the shift of the wavelet function is controlled to obtain the intensity information of each frequency band at different time domain positions. The calculation formulas of Morlet wavelet center time and time domain span are as follows:

$$\psi(x) = e^{-x^2}\cos\left(\pi\sqrt{\frac{2}{In\,2}}\,x\right) \quad (3)$$

$$t_0 = \frac{\int_{-\infty}^{\infty} t|\psi(t)|^2 dt}{\int_{-\infty}^{\infty}|\psi(t)|^2 dt} \quad (4)$$

$$\Delta t_\psi = \sqrt{\frac{\int_{-\infty}^{\infty}(t-t_0)^2|\psi(t)|^2 dt}{\int_{-\infty}^{\infty}|\psi(t)|^2 dt}} \quad (5)$$

The calculation formula for center frequency and bandwidth is as follows:

$$\omega_0 = \sqrt{\frac{\int_{-\infty}^{\infty}\omega|\psi(\omega)|^2 d\omega}{\int_{-\infty}^{\infty}|\psi(\omega)|^2 d\omega}} \quad (6)$$

$$\Delta\omega_\psi = \sqrt{\frac{\int_{-\infty}^{\infty}(\omega-\omega_0)^2|\psi(\omega)|^2 d\omega}{\int_{-\infty}^{\infty}|\psi(\omega)|^2 d\omega}} \quad (7)$$

Where, $\Psi(\omega)$ is the frequency component information obtained after $\psi(t)$ undergoes Fourier transform. It can be known from the above formula that when the wavelet transform measures high frequency components, because the wavelet used is narrow, a smaller time domain span can be obtained, but the frequency domain span will be enlarged accordingly. Therefore, in the output time-frequency matrix, the resolution of the frequency dimension of the high frequency part is relatively low, and the low frequency part is just the opposite. Similarly, the C3 and C4 channel position information are integrated, and a sample matrix of size 35×1152×2 is obtained as the input of the neural network. From the output matrix the 32 features are extracted. Which is mentioned in the above SIFT section. The extracted SIFT Horlick features and CMWT features are fused and are given to the feature selection.

CVR Journal of Science and Technology, Volume 21, December 2021
DOI:10.32377/cvrjst 2107

F. Feature Selection using Crow search algorithm (CSA)

Naturally, every creature has its own behaviours and character. Each creature would have certain patterns of activities to fulfil its needs like food collection, reproduction and so on. Similarly, observing the characteristics and behaviours of crow reveals notable information [35-38]. Usually, crows live as a group also called flock. The study depicts that the crows [39] are very clever in nature and have strong memory power. A crow would remember the faces of the other crows as well as its hide spots (food sources) for a long period of time. It has its own way of communication techniques to share information with each mate. It also has the habit of learning from mate's by monitoring them. By this way, it identifies the mates hidden food sources and takes the Food when the owner is not present in its spot. The crows involved in this theft activity are always conscious of the other mates, and they often change their locations to avoid being a future sufferer.

The basic terminologies used in CSA are presented in this part. The current iteration is denoted as $k\,(k = 1, 2, 3 \ldots . max\_iteration)$. The maximum number of iterations is denoted as $max\_iteration$. N denotes the flock size. There are two crows i *and* j, and their positions are shown in Fig. 2.

Figure 2. Crow position movement in CSA

The position of the crow i during the iteration k is denoted as $x^{i,k}(k = 1, 2, 3, \ldots, N)$. Each crow maintains the present best location in memory $m^{i,k}$. So, the crow would change its location to find better food spots than it has right now. Let a scenario while crow i decides to change its position, and at the same time a crow j flies be assumed. Crow i decides to follow the crow j to predict the hidden food source of crow j. The new position identification process has two possible cases.

Case 1: If crow j is not aware of the follower crow i, then the new position of the crow i will be obtained using Eq. (8).

$$x^{i,k+1} = x^{i,k} + r_i \times fl^{i,k} \times (m^{j,k} - x^{i,k}) \qquad (8)$$

where r_i is a random value generated between 0 and 1. Based on the flight length (fl), local or global search is performed. If lower value is chosen for $fl\,(< 1)$, then the search will be performed in the local domain. When the higher value is chosen for fl it would lead the search in the global domain.

Case 2: If crow j is identified to be spying the activity of crow i, then, crow j will divert the path. In this way, crow j safeguards its food source. In this case, crow i would take a random position. The above two cases are denoted in Eq. (9)

$$x^{i,k+1} = \begin{cases} x^{i,k} + r_i \times fl^{i,k} \times (m^{j,k} - x^{i,k}) & r_j \geq AP^{i,k} \\ a\ random\ position & otherwise \end{cases} \qquad (9)$$

Awareness probability [39] is denoted as AP which is used to minimize the imbalance between intensification and diversification. The flow chart of the CSA is defined in the below figure 3.

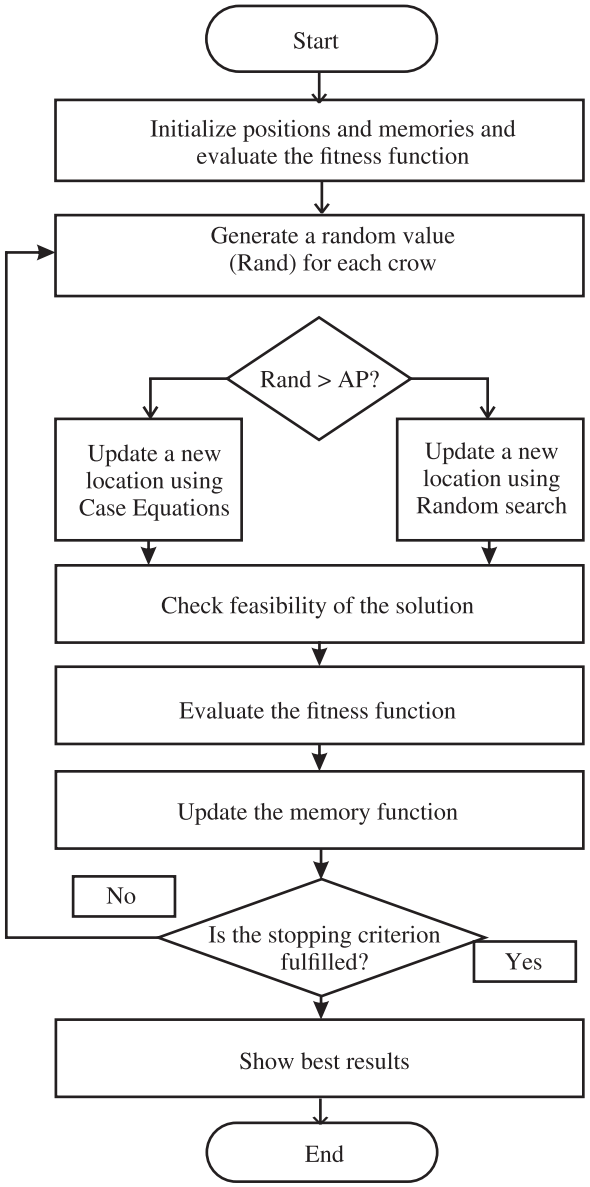

Figure 3. Flow chart of the Crow search algorithm.

IV. CLASSIFICATION

Supervised machine learning approaches are used for the classification of Motor Imagery. There are various steps involved in the supervised learning approaches. For classification purposes, many classifiers have been used in the method. Some commonly used classification methods are Artificial Neural Networks (ANN), Bayesian classification, K-Nearest Neighbor (KNN) classifiers, and Support Vector Machine (SVM).The classification might provide the solution whether the underwater images are consist of metal or not.

A. KNN Algorithm

KNN is a simple algorithm that stores all available cases and classifies new classes based on a similarity measure (e.g. distance functions). KNN has been used in statistical estimation and pattern recognition already in the beginning

CVR Journal of Science and Technology, Volume 21, December 2021
DOI:10.32377/cvrjst 2107

of 1970's as a non-parametric technique. The algorithm works as follows. A case is classified by a majority vote of its neighbors, with the case being assigned to the class most common amongst its K nearest neighbor measured by a distance function. If $K = 1$, then the case is simply assigned to the class of its nearest neighbour. There are three distances used for continuous variables: Euclidean (10), Manhattan (11), Minkowski (12).

$$\sqrt{\sum_{i=1}^{k}(x_i - y_i)^2} \quad (10)$$

$$\sum_{i=1}^{k}|x_i - y_i| \quad (11)$$

$$\left(\sum_{i=1}^{k}(|x_i - y_i|)^2\right)^{1/q} \quad (12)$$

$$D_H = \sum_{i=1}^{k}|x_i - y_i|^2 \quad (13)$$

In instance of categorical variables, Hamming distance (5) must be used. It also brings up the issue of standardization of the numerical variables between 0 and 1 when there is a mixture of numerical and categorical variables in the dataset. Choosing the optimal value for K is best done by first inspecting the data. In general, a large K value is more precise as it reduces the overall noise but there is no guarantee. Cross validation is another way to retrospectively determine a good K between 3-10.

B. SVM Algorithm

SVM is a popular classification technique discovered in 1995. A classification task usually involves separating data into training and testing sets. Each instance in the training set contains one "target value" and several "attributes". The goal of SVM is to produce a model (based on the training data) which predicts the target values of the test data given only the test data attributes.

Given a training set of instance-label pairs$(x_i, y_i), i = 1, \ldots, l$ where $x_i \in R^n$and $y \in \{1 - 1\}^l$, the SVM require the solution of the following optimization problem:

$$\min_{w,b,\xi} \frac{1}{2}w^T w + C\sum_{l=1}^{l}\xi_i$$

$$subject\ to\ {}^{y_i(w^T\phi(x_i)+b)\geq 1-\xi_i}_{\xi_i \geq 0} \quad (14)$$

Here training vectors $x_i$are mapped into a higher (maybe infinite) dimensional space by the function ϕ. SVM finds a linear separating hyperplane with the maximal margin in this higher dimensional space. $C > 0$ is the penalty parameter of the error term. Furthermore, $K(x_i, x_j) \equiv \emptyset(x_i)^T\phi\,(x_i)$is called the kernel function. The following are four basic kernels:

Linear:

$$K(x_i, x_j) = x_i^T x_j \quad (15)$$

The algorithm requires that each data instance is represented as a vector of real numbers. Hence, if there are categorical attributes, it has to be first converted into numeric data. Another thing to do before applying SVM is performing scaling. The main advantage of scaling is to avoid attributes in greater numeric ranges dominating those in smaller numeric ranges. Another advantage is to avoid numerical difficulties during the calculation.

C. ANN Algorithm

Generally speaking, ANN can be considered as an information processing system which is composed of a network of interconnected simple processing elements, i.e. neurons. Determined by the connections between these neurons and the associated parameters, ANN can exhibit complex global behaviour to generate expected outputs via supervised or unsupervised learning. Inspired by the biological nervous system, the learning process is to adjust the connection strength or weights between the neurons. Each neuron forms a node in the whole network and after training each node is assigned with a determined bias or threshold. For each interconnection between two nodes, a weight is also assigned to represent the link-strength between the neurons.

Let $x = (x1, x2, \ldots, xd)^T$ be an input vector and $w = (w1, w2, \ldots, wd)^T$ the weight vector, the output of a single neuron z.

$$Z = g(w^T X - b) = g(\sum_{i=1}^{d} w_i X_i - b) \quad (16)$$

where$g()$ is namely an activation function to decide whether the perceptron should fire or not. The sigmoid function $Sig(x) = (1 + ex)\,1$ is the most popular used activation function, others include $tanh$ and step functions, etc. Using the same process as to determine the output of a single neuron, the output of the whole network can be also calculated in a topological manner. This means that for each neuron its inputs from other neurons need to be computed before determining its output. As seen, the weight vector and the bias associated to each connection and each node will influence the outputted results, and they can be determined in training or learning process as follows. First of all, the topology of the ANN needs to be specified, and feedforward ANN is adopted as it has been widely applied for the classification of MCCs. A feed-forward ANN is a multilayer perceptron (MLP) which contains three or more layers of neurons, i.e. one input layer, one output layer and at least one hidden layer. With a given training set, a specified activation function and a learning ratio c where $c\ 2\ (0, 1)$, the learning process for supervised training using the well-known back-propagation algorithm.

V. Result and Discussion

The proposed system is experimented using MATLAB (version 2018a) with 3.0 GHz Intel i5 processor with 1TB hard disc and 8 GB RAM.

A. Evaluation Metrics

The challenge evaluation metrics are used for evaluating the both segmentation and classification performance of our method. For the segmentation, the evaluation criteria include sensitivity (SE), specificity (SP), accuracy (AC), Recall (R) and Precision (P). The performance criteria are defined is as:

$$SE = \frac{tp}{tp + fn} \quad (17)$$

$$AC = \frac{tp + tn}{tp + fp + tn + fn} \quad (18)$$

$$SP = \frac{tn}{tn + fp} \quad (19)$$

Where tp, tn, fp and fn denote the number of a true positive, true negative, false positive and false negative. As for the classification, there are four evaluation criteria, including sensitivity (SE), specificity (SP) and accuracy (AC).

B. Performances analysis

The performance of the proposed system has validated in various ways such, which are discussed in the below section, where two datasets are divided into five and six subjects, which is given as follows: Dataset 1 (subjects such us, aa, al, av, aw, ay) and dataset 2 (subjects such us, a, b, c, d, e, f, g). Initially, table 1 describes two subjects of dataset 1.

TABLE I.
CLASSIFICATION PERFORMANCE FOR aa AND al.

	Dataset 1 Subject aa			Dataset 1 Subject al		
Method	**SE (%)**	**SP (%)**	**ACC (%)**	**SE (%)**	**SP (%)**	**ACC (%)**
Without Feature extraction ANN	60.33	81.33	60	58.44	79.67	57
With Feature extraction ANN	63.51	84.33	66.89	77.23	80.11	63.40
With CSA selection Proposed ANN	69.67	80.66	75.99	69.72	75.64	68.87
Without Feature extraction Features KNN	59.41	79.13	61.12	63.90	70.14	59.41
With Feature extraction KNN	62.60	76.46	67.90	69.62	84.33	64.19
With CSA selection KNN	65.58	77.76	76.31	71.25	75.17	70.21
Without Feature extraction Features SVM	67.26	78.04	63.09	59.13	58.15	60.45
With Feature extraction SVM	68.15	78.27	78.62	80.32	73.06	67.34
With CSA selection SVM	69.62	79.67	89.69	62.60	80.66	78.35

Here, ensemble classifiers such as ANN, KNN and SVM are tested with feature extraction and without feature extraction as well as for feature selection. The two subjects such as aa and al for dataset 1 provides better accuracy, while implementing with feature extraction as well as feature selection. For instance, KNN achieved only 61.12% without feature extraction, where the same technique achieved 76.31% of accuracy, when implementing with CSA selection algorithm. In addition, SVM achieved better accuracy than other two classifiers, for sample, SVM with feature extraction achieved 78.62% of accuracy, where ANN and KNN with feature extraction achieved nearly 66% to 67% of accuracy. Table 2 and 3 explains the proposed method's performance for remaining subjects of dataset 1. Figure 4 depicts the average classification accuracy for all subjects of dataset 1.

TABLE II.
CLASSIFICATION PERFORMANCE FOR av AND aw.

	Dataset 1 Subject av			Dataset 1 Subject aw		
Method	**SE (%)**	**SP (%)**	**ACC (%)**	**SE (%)**	**SP (%)**	**ACC (%)**
Without Feature extraction ANN	62.54	84.33	63	54.33	88.33	68
With Feature extraction ANN	72.19	70.23	66.34	69.43	70.51	70.94
With CSA selection Proposed ANN	62.60	79.67	79.86	63.51	79.67	73.67
Without Feature extraction Features KNN	63.24	80.19	69.26	69.58	71.25	70.61
With Feature extraction KNN	65.86	80.43	73.87	69.62	71.33	72.97
With CSA selection KNN	69.30	81.24	77.45	79.15	81.60	76.09
Without Feature extraction Features SVM	59.98	84.33	66.51	59.44	75.29	68.67
With Feature extraction SVM	69.62	79.67	75.66	76.35	72.18	74.01
With CSA selection SVM	70.26	76.53	86.46	81.27	80.75	83.12

TABLE III.
CLASSIFICATION PERFORMANCE FOR *ay*.

	Dataset 1 Subject ay		
Method	**SE (%)**	**SP (%)**	**ACC (%)**
Without Feature extraction ANN	50.33	90.33	65
With Feature extraction ANN	59.41	69.26	72.45
With CSA selection Proposed ANN	69.62	84.33	76.71
Without Feature extraction Features KNN	58.54	63.47	67.40
With Feature extraction KNN	68.25	70.45	71.78
With CSA selection KNN	63.51	79.67	74.89
Without Feature extraction Features SVM	61.27	67.34	70.51
With Feature extraction SVM	69.04	76.38	77.45
With CSA selection SVM	69.62	79.67	81.56

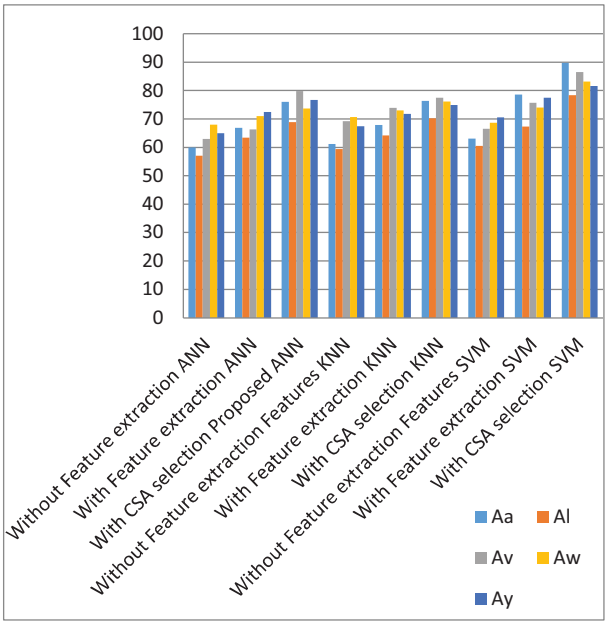

Figure 4. Average classification Accuracy for dataset-1.

While testing the ensemble classifiers, SVM with CSA selection algorithm achieved better accuracy for other three subjects. For instance, SVM with CSA achieved 86.46% of accuracy for av subjects, 83.12% of accuracy for aw subjects and 81.56% of accuracy for ay subjects. But, the KNN with CSA achieved 77.45% of accuracy for av subjects, 76.09% of accuracy for aw subjects and 74.89% of accuracy for ay subjects. The other set of experiments i.e. Table 4 shows the performances of the proposed methods for two subjects of dataset 2 are depicted as follows:

TABLE IV.
CLASSIFICATION PERFORMANCE FOR a AND b.

	Dataset 2 Subject a			Dataset 2 Subject b		
Method	**SE (%)**	**SP (%)**	**ACC (%)**	**SE (%)**	**SP (%)**	**ACC (%)**
Without Feature extraction ANN	51.33	57.33	60	43.68	77.39	59
With Feature extraction ANN	59.41	60.12	62.54	63.51	65.20	60.39
With CSA selection Proposed ANN	63.76	71.43	73.54	63.51	72.26	74.54
Without Feature extraction Features KNN	62.60	79.67	67.32	68.16	69.30	71.02
With Feature extraction KNN	62.60	84.33	70.51	62.60	72.70	76.32
With CSA selection KNN	78.24	77.45	81.05	63.51	67.69	77.45
Without Feature extraction Features SVM	63.51	79.67	75.08	68.01	68.34	70.25
With Feature extraction SVM	62.40	69.04	72.18	69.62	80.66	82.14
With CSA selection SVM	66.67	79.62	82.45	78.03	82.57	85.05

Various techniques are tested with ANN and results are tabulated, which shows that ANN with feature extraction achieved 60.12% of SP and 62.54% of ACC, where ANN without feature extraction achieved 57.33% of SP and 60% of ACC. But, while implementing with CSA selection technique, ANN achieved 71.43% of SP and 73.54% of ACC for a subjects. This proves that CSA provides better performance for ensemble classifiers. In addition, KNN with CSA achieved 81.05% of ACC for a subjects and 77.45% of ACC for b subject. However, SVM achieved better performance for two subjects than other ensemble classifiers. For sample, SVM with CSA achieved 82.45% of ACC for a subject and 85.05% of ACC for b subject. Table 5 provides the results for subject c and d in terms of ACC, SE and SP.

TABLE V.
CLASSIFICATION PERFORMANCE FOR c AND d.

	Dataset 2 Subject c			Dataset 2 Subject d		
Method	**SE (%)**	**SP (%)**	**ACC (%)**	**SE (%)**	**SP (%)**	**ACC (%)**
Without Feature extraction ANN	62.01	79.67	69.04	63.51	69.64	70.13
With Feature extraction ANN	69.33	86.33	80.3	72.25	83.24	81.00
With CSA selection Proposed ANN	62.60	70.24	77.45	69.62	74.85	81.58
Without Feature extraction Features KNN	63.98	64.33	78.05	70.14	75.47	77.59
With Feature extraction KNN	65.70	75.16	79.60	69.16	72.35	79.04
With CSA selection KNN	72.06	81.25	84.31	73.64	79.18	82.05
Without Feature extraction Features SVM	69.62	79.67	80.37	59.98	84.33	66.51
With Feature extraction SVM	68.10	75.25	80.86	69.62	79.67	75.66
With CSA selection SVM	70.62	79.36	82.56	71.03	75.24	83.46

KNN with feature extraction achieved 75.16% of SP and 79.60% of ACC, where KNN without feature extraction achieved 64.33% of SP and 78.05% of ACC. But, while implementing with CSA selection technique, KNN achieved 81.25% of SP and 84.31% of ACC for a subjects. This proves that CSA provides better performance for ensemble classifiers. In addition, ANN with CSA achieved 77.45% of ACC for a subject and 81.58% of ACC for b subject. However, SVM achieved better performance for two subjects than other ensemble classifiers. For sample, SVM with CSA achieved 82.56% of ACC for a subject and

CVR Journal of Science and Technology, Volume 21, December 2021
DOI:10.32377/cvrjst 2107

83.46% of ACC for b subject. Table 6 describes the classification performance of ensemble classifiers for remaining subjects of dataset 2, where Fig. 5 shows the average classification accuracy for all subjects of dataset 2.

TABLE VI.
CLASSIFICATION PERFORMANCE FOR *e* AND *f*.

	Dataset 2 Subject e			Dataset 2 Subject f		
Method	**SE (%)**	**SP (%)**	**ACC (%)**	**SE (%)**	**SP (%)**	**ACC (%)**
Without Feature extraction ANN	62.99	76.24	70.05	59.56	80.39	61
With Feature extraction ANN	63.04	78.15	72.45	63.51	72.85	76.32
With CSA selection Proposed ANN	65.38	80.25	76.32	62.99	79.67	80.16
Without Feature extraction KNN	79.67	84.33	76.66	65.28	68.10	72.38
With Feature extraction KNN	63.51	69.15	72.16	67.20	73.04	79.12
With CSA selection KNN	70.14	75.85	82.09	69.62	73.07	82.47
Without Feature extraction Features SVM	69.01	72.47	70.43	69.04	72.45	71.32
With Feature extraction SVM	65.34	74.08	73.14	69.95	84.33	77.45
With CSA selection SVM	69.62	79.67	85.45	72.01	78.04	84.32

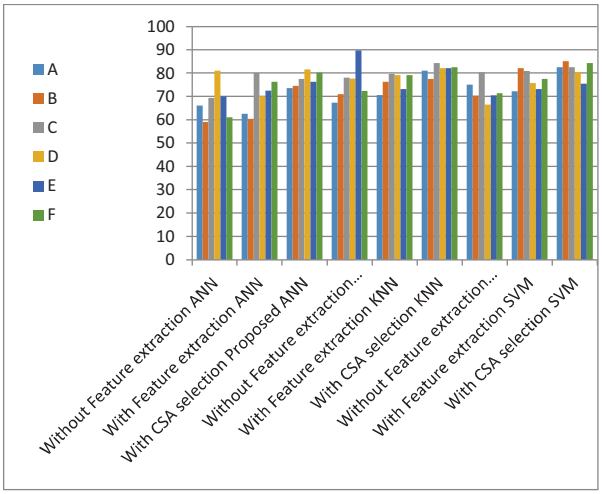

Figure 5. Average classification Accuracy for dataset-2.

Here, ensemble classifiers such as ANN, KNN and SVM are tested with feature extraction and without feature extraction as well as for feature selection. The two subjects such as e and f for dataset 2 provides better accuracy, while implementing with feature extraction as well as feature selection. For instance, KNN achieved only 76.66% of ACC without feature extraction, where the same technique achieved 82.09% of accuracy, while implementing with CSA selection algorithm for e subjects. In addition, SVM achieved better accuracy than other two classifiers, for example, SVM with feature extraction achieved 73.14% of accuracy, where ANN and KNN with feature extraction achieved nearly 72% of accuracy for e subjects. While testing the ensemble classifiers, SVM with CSA selection algorithm achieved better accuracy for other three subjects. For instance, SVM with CSA achieved 85.45% of accuracy for e subjects, 84.32% of accuracy for f subjects. But, the KNN with CSA achieved 82.09% of accuracy for e subjects and 82.47% of accuracy for f subjects.

VI. CONCLUSIONS

In summation, several interesting results regarding EEG motor imagery classification protocols is presented. Firstly, while the compared ANN, Bayesian classification, KNN classifiers networks may improve MI classification in some specific applications, the implementation of the classifier is still the most reliable of the three. Secondly, the efficacy of STFT and CMWT has been evaluated with the ensemble classifier model. Additionally, to improve the motor imagery Haralick features are extracted, and which are selected with the help of Crow search algorithm (CSA). Finally, the proposed method is validated based on the BCI competition dataset and laboratory measured data. The overall results shows feature selection algorithms CSA provides much better performance with EEG motor imagery classification. In future work could take a more in-depth look at the differences between networks of the same type but varying sizes, generalize this analysis to different datasets, or tackle the tuning of neural network hyper parameters by using other techniques, such as Bayesian optimization to guide the search in a more informed (and thus, perhaps more efficient) way.

REFERENCES

[1] Wolpaw JR, Birbaumer N, Heetderks WJ, McFarland DJ, Peckham PH, Schalk G, Donchin E, Quatrano LA, Robinson CJ, Vaughan TM (2000) Brain–computer interface technology: a review of the first international meeting. IEEE Trans Rehabilit Eng 8(2):164–173.

[2] Abdulkader, S. N., Atia, A., and Mostafa, M.-S. M. (2015). Brain computer interfacing: applications and challenges. Egypt. Inform. J. 16, 213–230.

[3] Friman, O., Volosyak, I., and Graser, A. (2007). Multiple channel detection of steady-state visual evoked potentials for brain-computer interfaces. IEEE Trans. Biomed. Eng. 54, 742–750.

[4] Ko, L.-W., Chikara, R. K., Lee, Y.-C., and Lin, W.-C. (2020). Exploration of user's mental state changes during performing brain-computer interface.

[5] Beuchat, N. J., Chavarriaga, R., Degallier, S., and Millán, J. D. R. (2013). "Offline decoding of upper limb muscle synergies from EEG slow cortical potentials," in 2013 35th Annual International Conference of the IEEE Engineering in Medicine and Biology Society (EMBC) (Lausanne: Swiss Federal Institute of Technology), 3594–3597.

[6] Yin, E., Zeyl, T., Saab, R., Hu, D., Zhou, Z., and Chau, T. (2016). An auditory-tactile visual saccade-independent p300 brain-computer interface. Int. J. Neural Syst. 26:1650001.

[7] Yu, Y., Zhou, Z., Liu, Y., Jiang, J., Yin, E., Zhang, N., et al. (2017). Self-paced operation of a wheelchair based on a hybrid brain-computer interface combining motor imagery and p300 potential. IEEE Trans. Neural Syst. Rehabil. Eng. 25, 2516–2526.

[8] Chikara, R. K., and Ko, L.-W. (2019). Neural activities classification of human inhibitory control using hierarchical model. Sensors 19:3791.

[9] Choi, K., and Cichocki, A. (2008). "Control of a wheelchair by motor imagery in real time," in International Conference on Intelligent Data Engineering and Automated Learning (Springer), 330–337.

[10] Belkacem, A. N., Nishio, S., Suzuki, T., Ishiguro, H., and Hirata, M. (2018). Neuromagnetic decoding of simultaneous bilateral hand movements for multidimensional brain-machine interfaces. IEEE Trans. Neural Syst. Rehabil. Eng. 26, 1301–1310.
[11] Chen, C., Zhang, J., Belkacem, A. N., Zhang, S., Xu, R., Hao, B., et al. (2019). G-causality brain connectivity differences of finger movements between motor execution and motor imagery. J. Healthcare Eng. 2019.
[12] Wang, K., Xu, M., Wang, Y., Zhang, S., Chen, L., and Ming, D. (2020). Enhance decoding of pre-movement eeg patterns for brain-computer interfaces. J. Neural Eng. 17:016033.
[13] Raudys SJ, Jain AK. Small sample size effects in statistical pattern recognition: Recommendations for practitioners. IEEE Trans Pattern Anal Mach Intell. 1991;13(3):252–264.
[14] Lotte F, Bougrain L, Cichocki A, Clerc M, Congedo M, Rakotomamonjy A, et al. A review of classification algorithms for EEG-based brain–computer interfaces: a 10 year update. J Neural Eng. 2018;15(3).
[15] Amaldi E, Kann V. On the approximability of minimizing nonzero variables or unsatisfied relations in linear systems. Theor Comput Sci. 1998;209(1-2):237–260.
[16] Guyon I, Elisseeff A. An introduction to variable and feature selection. J Mach Learn Res. 2003;3(Mar):1157–1182.
[17] Ortega J, Asensio-Cubero J, Gan JQ, Ortiz A. Classification of motor imagery tasks for BCI with multiresolution analysis and multiobjective feature selection. Biomed Eng Online. 2016;15(73). pmid:27454531.
[18] Corralejo R, Hornero R, Alvarez D. Feature selection using a genetic algorithm in a motor imagery-based Brain Computer Interface. In: International Conference of the IEEE Engineering in Medicine and Biology Society. IEEE; 2011. p. 7703–7706.
[19] Abootalebi V, Moradi MH, Khalilzadeh MA. A new approach for EEG feature extraction in P300-based lie detection. Comput Methods Programs Biomed. 2009;94(1):48–57.
[20] Kee CY, Ponnambalam SG, Loo CK. Multi-objective genetic algorithm as channel selection method for P300 and motor imagery data set. Neurocomputing. 2015;161:120–131.
[21] Lawhern VJ, Solon AJ, Waytowich NR, Gordon SM, Hung CP, Lance BJ. EEGNet: a compact convolutional neural network for EEG-based brain–computer interfaces. J Neural Eng. 2018;15(5).
[22] Acharya UR, Oh SL, Hagiwara Y, Tan JH, Adeli H. Deep convolutional neural network for the automated detection and diagnosis of seizure using EEG signals. Comput Biol Med. 2018;100:270–278.
[23] Davidson PR, Jones RD, Peiris MTR. EEG-based lapse detection with high temporal resolution. IEEE Trans Biomed Eng. 2007;54(5):832–839.
[24] Wang P, Jiang A, Liu X, Shang J, Zhang L. LSTM-based EEG classification in motor imagery tasks. IEEE Trans Neural Syst Rehabil Eng. 2018;26(11):2086–2095.
[25] Kumar S, Sharma A, Tsunoda T. An improved discriminative filter bank selection approach for motor imagery EEG signal classification using mutual information. BMC Bioinformatics. 2017;18.
[26] Kumar S, Sharma A, Tsunoda T. Brain wave classification using long short-term memory network based OPTICAL predictor. Sci Rep. 2019;9(1).
[27] Gaur P, Pachori RB, Wang H, Prasad G. A multi-class EEG-based BCI classification using multivariate empirical mode decomposition based filtering and Riemannian geometry. Expert Syst Appl. 2018; 95:201–211.
[28] Jiao Y, Zhang Y, Chen X, Yin E, Jin J, Wang X, et al. Sparse Group Representation Model for Motor Imagery EEG Classification. IEEE J Biomed Health Inform. 2019;23(2):631–641. pmid:29994055
[29] Saa, J. F. D., and Cetin, M. (2012). A latent discriminative model-based approach for classification of imaginary motor tasks from EEG data. J. Neural Eng. 9:026020.
[30] Suk HI, Lee SW. Subject and class specific frequency bands selection for multiclass motor imagery classification. Int J Imag Syst Tech 2011; 21:123–30.
[31] Wei, C., Chen, L., and Zhang, A. (2019). EEG emotion recognition based on integrated convolutional neural network. J. East China Uni. Sci. Technol. (Natural Science Edition) 45, 614–622.
[32] Liang NY, Huang GB, Saratchandran P, Sundarajan N. A fast and accurate online sequential learning algorithm for feed forward networks. Neural Networks IEEE Trans. 2006;7(6):1411–23.
[33] Zhang R, Lan Y, Huang GB, Soh YC. Extreme learning machine with adaptive growth of hidden nodes and incremental updating of output weights. Auto Intell Syst LNCS 2011; 6752:253–62. Jan.
[34] Padfield N, Zabalza J, Zhao H, Masero V, Ren J. EG-based brain-computer “Interfaces using motor-imagery: techniques and challenges," sensors (MDPI) in press 2019.
[35] Askarzadeh A (2016) A novel metaheuristic method for solving constrained engineering optimization problems: crow search algorithm. Comput Struct 169:1–12.
[36] Manogaran G, Varatharajan R, Lopez D, Priyan MK, Sundarasekar R, Thota C (2018) A new architecture of Internet of Things and big data ecosystem for secured smart healthcare monitoring and alerting system. Future Gener Comput Syst 82:375–387.
[37] Emery NJ, Clayton NS (2004) The mentality of crows: convergent evolution of intelligence in corvids and apes. Am Assoc Adv Sci 306(5703):1903–1907.
[38] Manogaran G, Vijayakumar V, Varatharajan R, Kumar PM, Sundarasekar R, Hsu CH (2018) Machine learning based big data processing framework for cancer diagnosis using hidden Markov model and GM clustering. Wirel Pers Commun 102(3):2099–2116.
[39] Zolghadr-Asli B, Bozorg-Haddad O, Chu X (2017) Crow search algorithm (CSA), advanced optimization by nature-inspired algorithms, 2017, pp 143–149.

E-ISSN 2581 – 7957
P-ISSN 2277 – 3916

CVR Journal of Science and Technology, Volume 21, December 2021
DOI: 10.32377/cvrjst2108

Comparative Studies on Different Radiation Hardened by Design (RHBD) Memory Cells

N. Surya Teja[1] and K. Lal Kishore[2]
[1]PG Scholar, CVR College of Engineering/ECE Department, Hyderabad, India
Email: suryateja12318@gmail.com
[2]Professor, CVR College of Engineering/ECE Department, Hyderabad, India
Email: lalkishorek@gmail.com

Abstract: **Electronic components and circuits, when they are working in radiation environment undergo radiation impact like Single Event Effects (SEE), Displacement Damage, Total Ionization Dose etc., These effects are mainly caused by deposition of Ionization energy in target material i.e., electronic components and circuits. These effects lead to wrong operation of circuit or may even lead to damage of the circuit. This paper mainly concentrates on Single Event Effects and in these effects, this paper focuses on Single Event Upset (SEU) and Multiple Bit Upset (MBU) phenomenon. Radiation Hardened by Design (RHBD) is a design technique used to design different RHBD memory cells to avoid SEU and MBU. RHBD is a design technique where the number of transistors of the design are increased and arranged in such a way that they avoid these effects by design itself. These different memory cells are designed and simulated using Cadence Virtuoso and Cadence Spectre in 45nm technology. The power, noise, delay analysis of different memory cells is done, and failure rate is calculated using Monte Carlo Simulation. The layouts of different memory cells are drawn using Microwind 3.5 tool. The results of different memory cells are compared.**

Index Terms: **Single Event Effects (SEE), Radiation Hardened by Design (RHBD), Single Event Upset (SEU), Multiple Bit Upset (MBU).**

I. Introduction

The presence of ionization radiation may affect the correct operation of electronic devices [1], both in the Terrestrial environment and Artificial man-made environment. Due to atmospheric neutrons and radioactive essentials inside the chip ingredients or in space, the surrounded particles, which have been released by the Sun and galactic cosmic rays in the terrestrial environment. In Artificial man-made environment, the radiation produced by biomedical devices, nuclear power plants and research on high energy physics, are the causes for radiation effect in electronic devices. The basic aim beyond radiation effect in electronic devices is to deposit energy in the target material. This may lead to different variety of effects like corruption of memory bits, glitches in analog and digital circuits etc., This may increase power and decrease in speed, and in some cases, the complete process of a device may change. The radiation effects mainly occur while scheming electronic systems that operate onboard satellites and spacecrafts. These also occur in high reliable schemes to be used in ground like bank servers, biomedical devices, and automotive machines. In Nuclear environments, like in areas around Nuclear Reactors and Nuclear projects, radiation effects are seen. There are three key classes of radiation effects:

1. Total Ionizing Dose,
2. Displacement Damage, and
3. Single Event Effects.

The first two effects in electronic device parameters are due to deficiency of semiconductor resources which are uninterruptedly hit by many ionizing elements. These mainly happen in space environments and artificial foundations of radiation. The Single event effects are mostly due to stochastic communication of a single ionized particle having high radiation with sensitive regions of the target electronic device. These events happen both in space and terrestrial environments.

There are different types of Single event effects, but this paper mainly focuses on the problem of Single Event Upset and Multiple Bit Upset.

Single Event Upset (SEU): This is corruption of a single bit, due to single ionizing particle in sensitive nodes of a memory cell. It is also known as soft error. The correct logic value can be usually reestablished by simply rewriting the bit.

Multiple Bit Upset (MBU): Corruption of two or more bits due to the passage of a single Ionizing particle. Here, 2 states will change due to radiation effects.

SRAMs carefully follow Moore's law and have developed the perfect standard to study the soft error sensitivity of a technology. In general, the charge formed by an ionizing particle is composed together at a sensitive region of a circuit to yield a trouble. Reverse biased p-n junctions are among the most effective areas in assembling charge. An ionizing component outbreaks one of the reverse biased drain junctions, like the drain of NMOSFET which is off, in the cross coupled inverter in the cell. Consequently, electron-hole pairs are shaped and composed by the depletion region of the drain junction. This causes a transient current, which follows through the junction that is hit while reestablishing transistor source current to the particle induced current. The reestablishing PMOS has a partial amount of current drive and a partial channel conductance, voltage drops at the hit node. If the voltage goes below the switching threshold and the drop lasts for a sufficient time, the response causes the cell to alter its initial logic state, creating a SEU. In the same way if it alters two or more bits due to ionizing particle, it causes MBU. Several features regulate the presence of SEU: radiation transfer through the bank end layers past the reverse biased junction, charge deposition and charge collection. In addition, the circuit response is also of importance.

Received on 02-07-2021, Revised on 01-10-2021, Accepted on 09-11-2021.

CVR Journal of Science and Technology, Volume 21, December 2021
DOI: 10.32377/cvrjst2108

II. Literature Review

I.-S. Jung, Y.-B. Kim, and F. Lombardi [2] have proposed two types of 10T SRAM cells that avoid soft errors by using Cadence Virtuoso 180nm technology. But it has high read Signal Noise Margin (SNM). This is the main problem with the design, and it needs two cells to avoid soft errors. S.M. Heinzman , D. J. Rennie, and M. Sachdev [3] projected a quad-node 10T soft error strong SRAM cell that offers differential read process for strong identifying. When associated to a basic 6T SRAM cell, the anticipated cell offers similar noise margin as the 6T cell at the half supply voltage, thus it is positively saving the leakage power. This cell is used as latch to design register files and flipflops. But it cannot avoid soft errors, while working in pure radiation environments. S. Lin, Y.B. Kim, and F. Lombardi [4] proposed a new hardening design of 11 transistor CMOS memory cell. By employing creative access and new mechanisms, the predicted toughened memory cell solves the issues that plagued the previous design. The data stored in the projected hardened memory cell does not change even when subjected to a transient pulse, according to the simulation of the anticipated cell. It costs more than twice as much of a basic memory cell. But this cell consumes high noise margin and speed is low. T. Calin, M. Nicolaids and R. Velazco [5] anticipated a new design strategy for storage which is immune to single event radiation disruptions. This approach is excellent for spreading high density ASICs and static RAMs, which uses submicron CMOS technology. The storage component uses 10 transistors for a simple latch arrangement and 12 transistors for a memory cell building. The problem with this design is, we need to design latch and a memory. S. Gupta, K. Gupta and N. Pandey anticipated the 7T cell with a noise margin free read process that as formerly been anticipated. The new mechanism also aids to decrease power alimentation by reaching a lower data holding voltage idea. A read aid has been anticipated to pointedly increase the act of the read process in subthreshold region. But the write operation capability is very low in it. CH Naga Raghuram, Bharat Gupta and Gaurav Kaushal [7] to reject the SEU and Sing le Event Double Node Upset, have projected a new Radiation Hardened by Design (RHBD) SRAM. The failure probability of SRAM cells is calculated using Monte Carlo Simulations. The predictable RHBD 15T SRAM achieved a zero percent failure chance for the specified charge source when attached to the newly labeled RHBD SRAM cells. The intended SRAM cell's read and write presentations are improved by using separate read and write circuitry at dissimilar nodes. The read, write, and power indulging delays are all reduced. However, they currently use separate circuitry for the read and write processes.

III. Design of Different SRAM Cells and SEU Recovery Analysis

A. Basic 6T SRAM Cell

The Basic 6T SRAM cell shown in figure 1, consists of 6 transistors. Out of these 6, 4 are NMOS and 2 are PMOS transistors [8]. The transistor N2, N4 are access transistors. For these two transistors gate is connected to WL which is high, then only read and write operation will occur. The bit lines BL that are connected to N2 and N4. The Q and Q| are output nodes. The read and write operation are same as 6T SRAM cell. When WL is low, it will be in hold operation and keeps its previous values. But problem with this cell is, it is easily affected by radiation and can change its operation or may be affected by SEU and MBU.

The cell can be easily affected by radiation when it is working in radiation environments and cause SEU and MBU. In order to avoid SEU and MBU, one needs to increase number of transistors or using a technique called RHBD. Using this technique different cells are designed. The figure 6 is the simulation of 6T cell and figure 12 is layout of 6T cell.

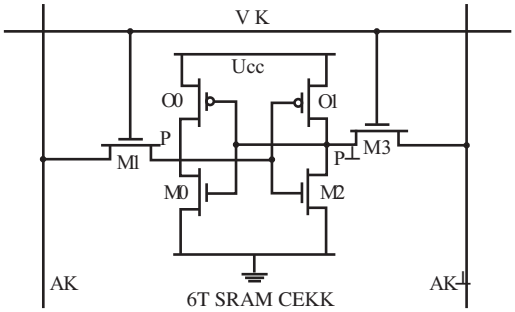

Figure 1. Basic 6T SRAM Cell

B. 10T SRAM CELL

The 10T SRAM cell shown in figure 2 is designed by using RHBD approach to keep away from radiation impacts like SEU and MBU [9]. This cell includes 10 transistors in which 6 are PMOS and 4 are NMOS transistors. The transistors N4 and N3 are access transistors and for these transistors, gate is hooked up to WL. When WL becomes high, both read and write operations will occur. The operation is same as the basic 6T SRAM cell, but it has additional two storage nodes Q, QN, S0, S1. The figure 7 is the simulation of 10T cell and figure 13 is the layout of 10T cell.

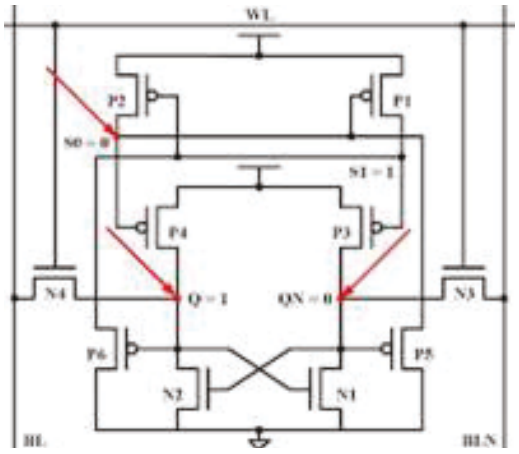

Figure 2. 10T SRAM Cell

The 10T SRAM cell shown in figure 2, is designed by using the RHBD approach to keep away from radiation impacts like SEU and MBU [9]. This cell includes 10 transistors in which 6 are PMOS and 4 are NMOS transistors. The transistors N4 and N3 are access transistors

CVR Journal of Science and Technology, Volume 21, December 2021
DOI: 10.32377/cvrjst2108

and for these transistors gate is hooked up to WL. When WL becomes high, both read and write operations will occur. The operation is same as the basic 6T SRAM cell, but it has additional two storage nodes Q, QN, S0, S1. The figure 7 is the simulation of 10T cell and figure 13 is the layout of 10T cell.

In the SEU recovery analysis of 10T cell, consider following scenario. Nodes Q, QN and S0 are three sensitive nodes in the 10T cell for the reserved value as 1, according to the SEU concept. If a charged element upturns the sensitive node Q to 0, transistor N1 will be tentatively OFF, and transistor P6 will be tentatively ON. However, the size of transistor P1 is 2 times that of P6, the voltage at node S1 will be in its exclusive state. Here to avoid the change of S1 state the transistor size P1 is made twice that of P6. The voltage of node S0 remains unaltered, which is significant. As a result, transistor P4 will turn on, in sequence. Finally, the voltage of the node Q will be compared to the early voltage. Both transistors P1 and P4 will be twisted OFF if the sensitive node S0 is concerned about a radiation element changing the original state. Due to capacitive effect, nodes Q, QN and S1 will be unaffected. As a result, transistor P5 will turn on in sequence, and the voltage at node S0 will be restored.

C. 12T SRAM Cell

The 12T SRAM cell shown in figure 3 is designed by using RHBD technique to avoid radiation affects like SEU and MBU. This cell consists of 12 transistors among which 8 are PMOS and 4 are NMOS. P5, P6 are access transistors and these transistors gate is connected to WL. When WL is low, read and write operations only will take place and the read and write operation is as that of basic 6T SRAM cell. When WL is high, the cell will be in hold operation and holds its previous values. It has four storage nodes Q, QN, S0, S1. Figure 8 shows the simulation of 12T cell and figure 14 shows layout of 12T cell.

In SEU recovery analysis, the drain region of the PMOS transistors P6 and P8, node Q is not a sensitive node and its holding value is 1. Q is a node that exclusively attracts positive pulses. In other words, the 1->1 pulse is utilized to extend Q node while maintaining its retained value. When the QN node is disrupted by the radiation component, the transistors P1 and P4 are turned off. The nodes Q and S1 then remain in a single logic state 1, with no voltage value at the end. As a result, N3 remains on. S0 is in the 0 state, transistors P7 and P2 are switched on, and QN returns to its original 0 state.

The voltage at nodes S0-QN or S1-QN can be restored due to the charge sharing effect. The dumping state of the 12T cell will change because, both P8 and N4 transistors will be replaced. As a result, the node Q will be stressed to state 0. This is like a write 0 process. When a radiation element damages node S0 or S1 or QN or node pair S0-S1 of the predicted 12T cell, damaged data can be amplified from the deposited data which cannot be improved when node pair S0-QN or S1-Qn is distressed. The capabilities of these multiple node upsets scenario can be condensed if the predetermination of the node QN and node pair S0-S1 is excessive enough.

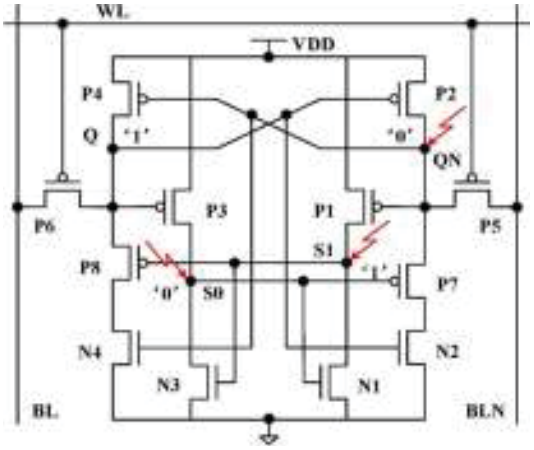

Figure 3. 12T SRAM Cell

D. 14T SRAM Cell

The 14T SRAM cell is shown in figure 4. It is designed by using RHBD technique to avoid radiation affects like SEU and MBU [11]. This cell consists of 14 transistors among which 8 are PMOS and 6 are NMOS. N4 and N5 are access transistors, and these transistor gates are connected to WL. When WL is high, both read and write operation will occur. When WL is low, the cell is in hold its operation and it holds its previous values. The 14T SRAM cell operation is as basic 6T SRAM cell operation. It has 4 storage nodes Q, QB, S0, S1. Figure 9 shows simulation of 14T cell and figure 15 shows layout of 14T cell.

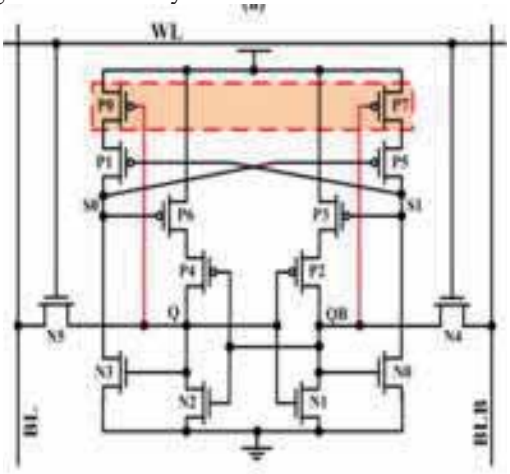

Figure 4. 14T SRAM Cell

Let the stored value be Q=1, QB=0, S1=1, S0=0 and the SEU recovery analysis for 14T cell is done for the same value. when an element hits the drain of P1, it accumulates a positive charge and raises the voltage of node S0, converting S0 from 0 to 1.P6 and P5 will be warped off because of this. However, impact of OFF/On states of extra auxiliary transistors nor it will affect the memory status of the Q and S1 nodes. As a result, the S0 switching pulse cannot be saturated within the cell. After the radiation effect the nodal logic level will be improved. When an element hits the drain of P2, it collects positive charge and raises the voltage at node QB, causing QB to change from 0 to 1. N2 and N0 will be turned on because of this, Q and S1 will be changed from 1 to 0. P0 and P1 will be warped on, and N3 will be OFF, before S0 is changed from 0 to 1. In the end, the storage

CVR Journal of Science and Technology, Volume 21, December 2021
DOI: 10.32377/cvrjst2108

state of the cell will be switched. The parasitic bipolar amplification result of P2 is calmed as the transistors are loaded and the topology is improved. As a result, the quantity of charge gathered by transistor P2 drain is condensed, increasing node QBs SEU tolerance.

E. 16T SRAM Cell

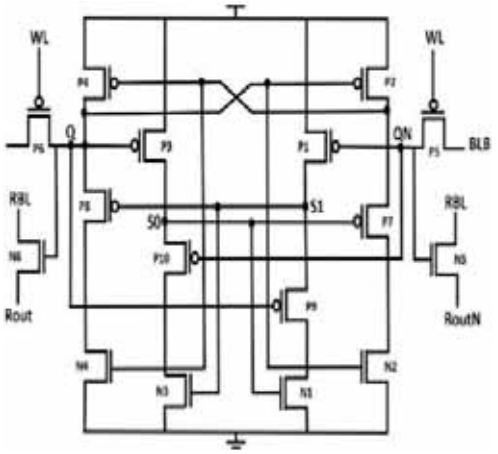

Figure 5. 16T SRAM Cell

The 16T SRAM cell is shown in figure 5 and designed by using RHBD technique to avoid radiation affects like SEU and MBU. This cell consists of 16 transistors among which 10 are PMOS and 6 are NMOS. Here in this P5, P6 are access transistors and the gates of these two transistors are connected to WL. When WL is low both read and write operation will occur. Here for write operation is as basic 6T SRAM cell but for read operation two transistors N5 and N6 are used and the gate of these two transistors is connected to storage nodes Q and QN. While read operation RBL is made high and through Rout and RoutN the value written in cell is read. When WL is high the cell is in hold operation and holds its previous values. Figure 10 and 11 shows the write and read simulation and figure 16 shows layout of 16T cell.

Single node and multi-node upset analysis of the projected RHBD 16T SRAM are reflected as explained below. Two primary and secondary networks are enclosed with PMOS devices. Consequently, only positive transient current has been shaped. So, 0 to 1 upset will happen, but not 1 to 0. Q is the primary linking where 1 is reserved and if component attack happens, only 1 to 1 upset will occur and RHBD 16T SRAM have four storage connections. Eight groups of multi-node upset are likely imaginable. When joining it QN is upset will alter into OFF state. But on the extra side, networks S1 and Q last the same, because P9 and P8 are swapped OFF. So, N3 will be in ON state. P7 and N2 are likewise On, at the same time. QN is pulled back to unique value 0. When connection S0 is inflated by a radiation attack, it will alter ON the device N1 and alter OFF the P7 transistor. But, P9 is swapped OFF, and the S1 value will not alter. P10 and N3 are swapped ON. So, S0 will pull back its original value of 0.

When networks QN and S1 are inflated by radiation elements i.e., 1 to 0 upset will not happen to junction S1. So, the model of the attack is done on P9 and N1 among P9 and N1. Since P9 is in OFF state, it will interrupt the S1 linking. And, as explained before, for QN single node upset, QN linking will drag back to the original value of 0. When S0 and S1 are inflated by element attack, S0 outbreaks will change ON N1 and change OFF P7 transistor. But Q and QN are in its original value P9 and P10 do not modify its state. Finally, also for the extreme group of multi-node upsets, RHBD 16T can advance the dropped data from the corrupted one. When joining pair QN-S0 is upset, the stored data can alter, because PMOS is used among all four inverters, and it takes gate inputs from the storage networks.

IV. Results and Discussion

A. Simulation results of different SRAM cells

The Simulation results of different cells are shown in figures 6,7,8,9,10 and 11.

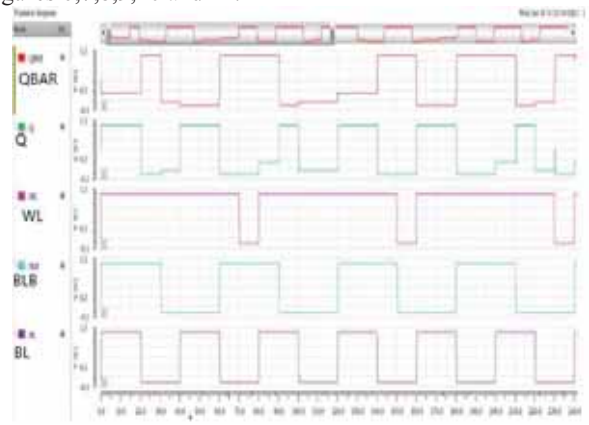

Figure 6. Simulation result of 6T SRAM Cell

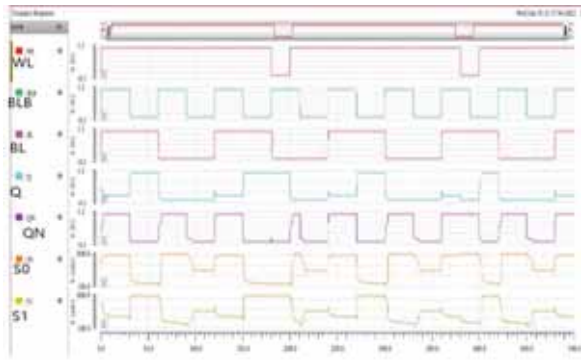

Figure 7. Simulation result of 10T SRAM cell

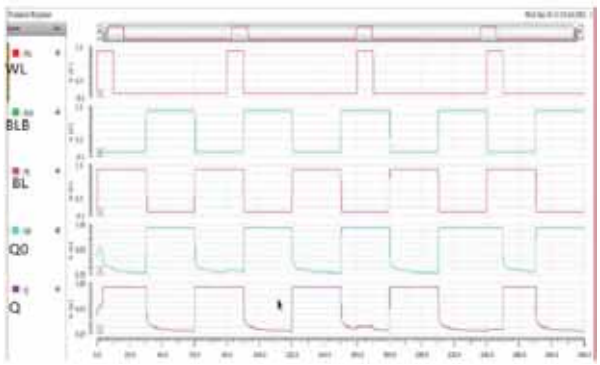

Figure 8. Simulation result of 12T SRAM cell

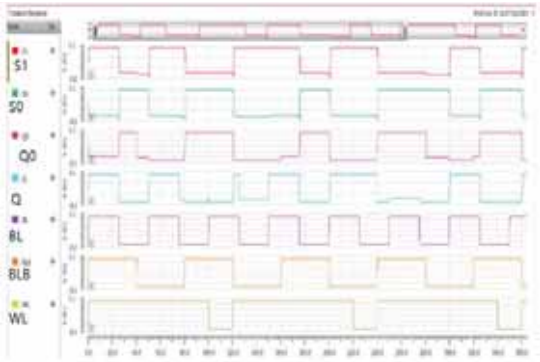

Figure 9. Simulation result of 14T SRAM cell

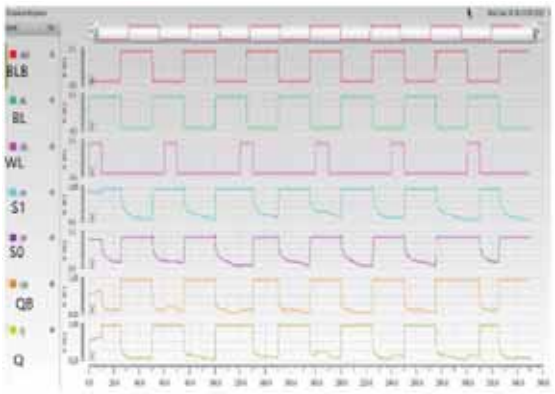

Figure 10. Simulation result of write operation of 16T SRAM cell

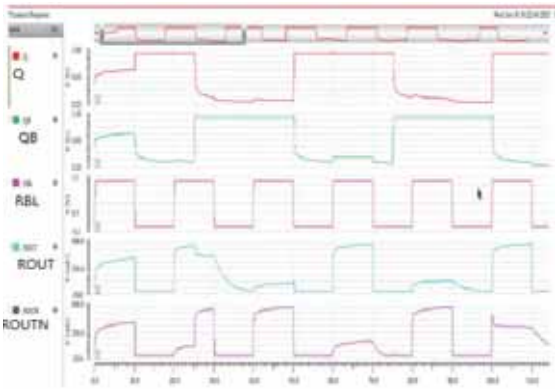

Figure 11. Simulation result of read operation of 16T SRAM cell

B. Noise Analysis

TABLE I.

Memory cell	Noise(mv)
6T	7.811399×10^{-2}
10T	1.813065×10^{-2}
12T	8.91399×10^{-2}
14T	4.26487×10^{-2}
16T	2.203408×10^{-2}

C. Power Analysis

TABLE II.

Memory Cell	Power(nw)
6T	17.47
10T	24.32
12T	33.42
14T	12.21
16T	14.13

D. Delay Analysis

TABLE III.

Memory Cell	Delay(ps)
6T	96.14
10T	30.71
12T	62.48
14T	20.3
16T	7.01

E. Monte Carlo Simulation

TABLE IV.

Memory Cell	Failure Rate
6T	92%
10T	71%
12T	88%
14T	72%
16T	11%

The monte carlo simulation is done to check whether the designed cells will sustain in radiation environment or not. Here 30fc charge is introduced in sensitive nodes of these cells using monte carlo simulation and failure rate is calculated.

The above tables are the results of different analysis like Noise, Power, Delay, and failure rate using Monte carlo Simulation of different SRAM Cells. From noise analysis both 10T and 16T have less noise. In power analysis 14T and 16T cells consumes less power. From delay analysis 16T cell has less delay and from monte carlo simulation 16T cell has less failure rate.

F. Layout Design of different cells

The layout of different memory cells is drawn using Microwind 3.5 Tool and shown in figures 12,13,14,15 and 16.

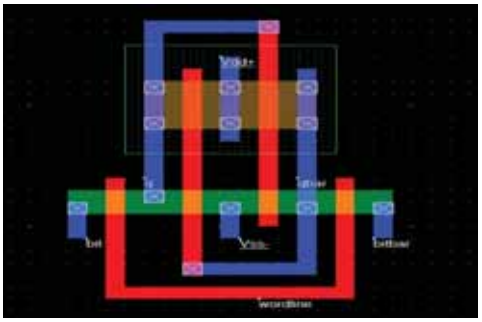

Figure 12. Layout Design of basic 6T cell

CVR Journal of Science and Technology, Volume 21, December 2021
DOI: 10.32377/cvrjst2108

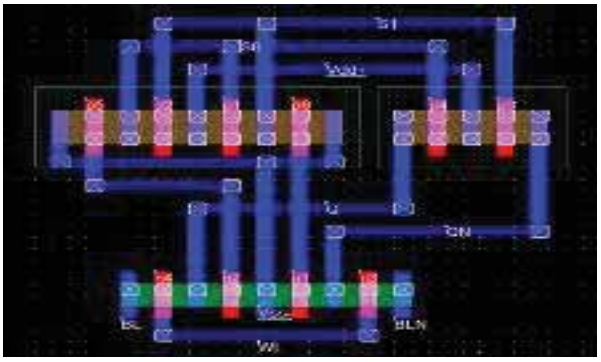

Figure 13. Layout Design od 10T cell

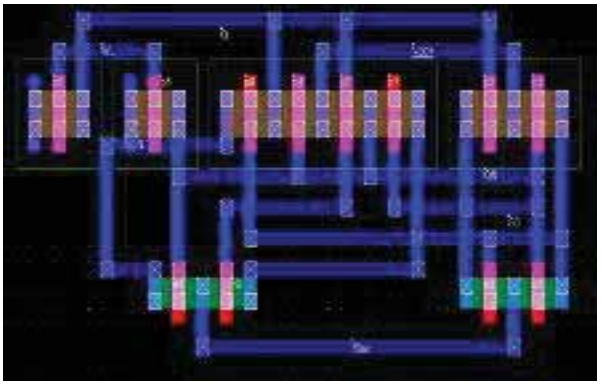

Figure 14. Layout Design of 12T cell

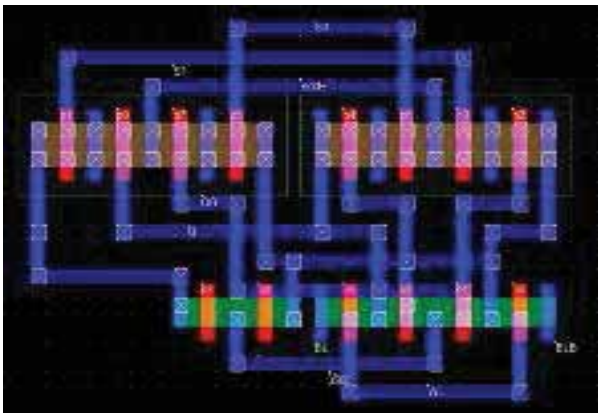

Figure 15. Layout Design of 14T cell

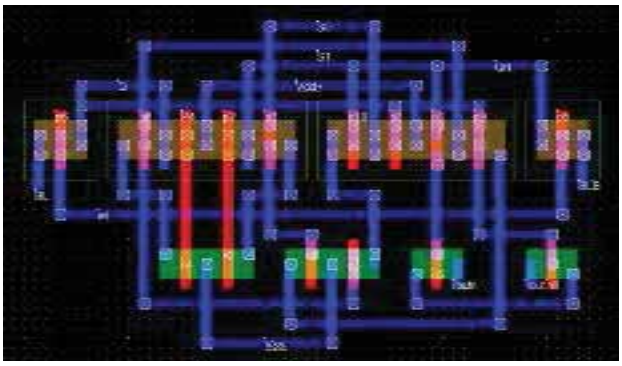

Figure 16. Layout Design of 16T cell

Here, the layout of different cells is drawn for reference to foresee any problems that arise during designing. Compared to all cells 16T memory cell can avoid both SEU and MBU. The 16T cell has less noise, power, delay and its failure rate is very less, when compared to the remaining cells. This cell consumes less power, because the storage junctions are separated by a PMOS device between the inverters. So, when working in radiation environments 16T cell is better compared to other cells.

V. Conclusions

In this work, different cells are designed using RHBD design technique to avoid SEU and MBU by design itself, using Cadence Virtuoso 45nm technology. Basic 6T SRAM cell is simple, but it cannot work properly in radiation environments. 10T cell is designed using RHBD technique. In this cell noise is less but it can avoid only SEU. 12T cell is also designed using RHBD technique. It can avoid both SEU and MBU, but its noise, power, delay, and failure rate are more. 14T cell is also designed using same RHBD technique where one can achieve less power and delay. But it cannot avoid MBU. Lastly, a 16T cell is designed using same RHBD technique. This can avoid both SEU and MBU and its power, noise, delay, and failure rate are very less compared to remaining cells. So, the 16T cell is better for use, when working in radiation environments.

References

[1] Marta Bagatin , Simone Gerardin, “ Ionization Radiation effects in Electronics”, by Taylor and Fancisgroup.
[2] I.-S. Jung, Y.-B. Kim, and F. Lombardi, “A novel sort error hardened 10T SRAM cells for low voltage operation,” in Proc. IEEE 55th Int. MWSCAS, Aug. 2012, pp.714–717.
[3] S. M. Jahinuzzaman, D. J. Rennie, and M. Sachdev, “A softerror tolerant 10T SRAM bit-cell with differential read capability,” IEEE Trans. Nucl. Sci., vol. 56, no. 6, pp. 3768–3773, Dec.2009.
[4] Sheng Lin, Yong-Bin Kim, and Fabrizio Lombardi “A 11-Transistor Nanoscale CMOS Memory Cell for Hardening to Soft Errors”,IEEE Transactions on Very Large Scale Integration (VLSI) Systems, Vol. 19, No. 5, May2011.
[5] T. Calinl, M. Nicolaidisl, R. Velazco, “Upset hardened memory design for submicron CMOS technology” IEEE Transactions on Nuclear Science, Vol 43, No6.
[6] S. Gupta, K. Gupta, and N. Pandey, “ A 32-nm subthreshold 7T SRAM bit cell with read assist” in IEEE Trans. Very Large Scale Integration. (VLSI) Syst., vol. 25, no. 12, pp. 3473–3483, Dec.2017.
[7] CH Naga Raghuram, Bharat Gupta, and Gaurav Kaushal, “Double Node Upset Tolerant RHBD 15T SRAM Cell Design for Space Applications” IEEE Transactions on Device and Materials Reliability, Vol. 20, No. 1, March2020.
[8] Manoj Padmanabha Murthy. T, Nithin. N, Pallavi. N, V. Rajashekar , “Performance Analysis of SRAM at Different Technologies using Cadence” IJESC2020.
[9] Jing Guo , Lei Zhu, Yu Sun, Huiliang Cao, Hai Huang, Tianqi Wang, Chunhua Qi , Rongsheng Zhang, Xuebing Cao, Liyi Xiao, and Zhigang Mao, “ Design of Area-Efficient and Highly Reliable RHBD 10T Memory Cell for Aerospace

Applications" IEEE Transactions On Very Large Scale Integration (VLSI) Systems ,2019.

[10] J.Guoetal.,"Novelradiation-hardened-by-design(RHBD)12T memory cell for aerospace applications in nanoscale CMOS technology," in IEEE Trans. Very Large Scale Integrated. (VLSI) Syst., vol. 25, no. 5,pp. 1593–1600, May2017.

[11] Chunyu Peng , Jiati Huang, Changyong Liu, Qiang Zhao, Songsong Xiao , Xiulong Wu, Zhiting Lin , Junning Chen, and Xuan Zeng , " Radiation-Hardened 14T SRAM Bitcell With Speed and Power Optimized for Space Application " in IEEE Transactions on Very Large Scale Integration (Vlsi) Systems, Vol. 27, No. 2, February2019.

E-ISSN 2581 –7957
P-ISSN 2277 – 3916

CVR Journal of Science and Technology, Volume 21, December 2021
DOI: 10.32377/cvrjst2109

Speculative Carry Addition Performance Improvement and Area Optimization using Modified Carry Generators

T. Subha Sri Lakshmi
[1]Asst. Professor, CVR College of Engineering/ECE Department, Hyderabad, India
Email: rupashubha@gmail.com

Abstract: **Carry Speculative Adder (CSPA) is a technique for reducing the critical path delay of an arithmetic circuit that is designed using the carry speculation technique, with an assumption that the carry-out bit generated at a given position of input bits is only a dependent on the previous 'x' bits but not the LSB bit. Carry predictor, internal carry generator, sum generator blocks, and multiplier blocks are used in this architecture. The n-bit CSPA is subdivided into smaller block adders, each of which runs in parallel. A carry predictor circuit serves as a selection line for the multiplexer, with its inputs coupled to the bit pattern generated by internal carry generators, one of which is connected to binary one (vdd) and the other to binary zero (gnd). Each block adder is y bits in size, and the CSPA has 'm' independent block adders and '(m-1)' carry predictor circuits, where p = (n/y). With Carry Speculative Addition, modified carry generators are employed to minimize critical path delays and the consequent need for area and power. Data latching circuits are adjusted to provide continuous data to the circuit. In order to obtain accurate results, the CSPA with Modified Carry Generators (CSPA-M) is built using error detection and error recovery circuitry (VLCSPA-M). The proposed Carry Speculative Addition with Modified Carry Generator architecture is developed using Verilog HDL in both FPGA and ASIC platforms, and the design is simulated using Xilinx ISE and Cadence 45 nm Technology libraries.**

Index Terms: **Carry Speculative Adder (CSPA), Modified Carry Generator (CSPA-M), Verilog - HDL, FPGA – Xilinx ISE, ASIC – Cadence.**

I. Introduction

An adder is a digital circuit that adds two numbers together. Adders are utilized in the Arithmetic Logic Units (ALU) of many computers and other types of processors. They are also used in other areas of the processor to calculate things like addresses, table indexes, increment and decrement operators, and other things like that. Although adders can be built for a variety of number representations, such as binary-coded decimal or excess-3, binary numbers are the most frequent, it is simple to convert an adder into an adder–subtract or in circumstances where two's complement or ones' complement are used to represent negative values. Other signed number representations necessitate additional reasoning in addition to the simple adder. Multiple bits can be supported by the adders. Half adder and Full adder are two fundamental adders that can add two or three bits. Ripple Carry Adder (RCA), Carry Look Ahead Adder (CLAA) [1], Carry Save Adder (CSAA), Carry Skip Adder (CSKA), Carry Increment Adder (CINA), Carry Select Adder (CSIA), and Carry Bypass Adder are the adders that handle multiple bits (CBYA).

The speculative methodology is an optimization methodology for improving the delay of arithmetic circuits based on a prediction mechanism. Speculative adders are based on the observation that in classic adders, the critical path is rarely activated [2]. Each output of a speculative adder is dependent only on the previous k bits, rather than all previous bits. A new function speculation methodology for designing variable latency adders with low area overhead and excellent performance is Static Window Addition (SWA). It is a series of consecutive bits that is referred to as a window. Putting input bits into blocks can approximate the carry chain length to a high degree of certainty. In spite of varying adder widths, Variable Latency addition utilizing SWA [3] based speculative adders can be 10 times faster than the quickest Design Ware adder. The Correlation Aware Speculative Addition (CASA) [4] is a lightweight improvement to traditional speculative adders that takes advantage of the correlation between the most significant bit in the input operand and the carry-in value in order to improve accuracy. It demonstrates that the CASA produces a large reduction in mistake rate with minimal timing and area overhead.

II. Carry Speculative Addition

A. Carry Speculative Adder

Speculative Carry Select Addition (SCSA) [5] is presented in [3] as an efficient method for building low error rate speculative adders while maintaining low area overhead, high performance, and reliability. Signals in a chain can be divided into equal blocks by dividing each block into equal spaces. Addends' input bits are divided into blocks, and the carry bits between blocks are deliberately truncated to zero. Theorizing all the outputs of the block together reduces the overhead problem due to the separation of the outputs. The SCSA-based technique reduces space requirements by 43% while improving performance by 10% [6]. Offers a carry speculative adder in which a standard full adder is split into two distinct carry generators and sum generators, each with one additional logic gate, increasing speed while lowering power consumption. Comparing the carry speculative adder to a carry selection adder, the carry speculative adder reduces simulation latency by 25.69 percent, area by 14.62 percent and power consumption by 18.03 percent. In order to reduce critical route delays, carry

Received on 24-06-2021, Revised on 03-07-2021, Accepted on 26-08-2021.

speculation is used in the Carry Speculative Adder (CSPA). Figure 1 shows the block diagram of the carry speculative adder (CSPA). It consists of three n-bit Carry Predictor Circuits that work independently, each with a tiny block adder. Each block adder with the exception of the leftmost one, has a size of y bits. In a CSPA, where p = (n/y), there are “p” independent block adders and “(p1)” carry predictor circuits.

This technique is based on predicting circuit delay in order to measure the effectiveness of the arithmetic circuits. According to speculative adders, a few critical paths are engaged in traditional adders.

Rather than including all previous bits in its outputs, a speculative adder only counts the last l bits as inputs. The Static Window Addition (SWA) method is proposed in [8] as an innovative function speculation technique for creating highly effective variable latency adders with minimal area overhead. Input bits contained within a window are arranged in a specific order. Putting input bits into blocks can approximate the carry chain length to a high degree of certainty. Using SWA-based speculative adders, Variable Latency addition employing adders ranging anywhere from 5 to 40% smaller is 10% faster than the quickest Design Ware addition. A correlation aware speculative addition [4] is made in [9], which intelligently uses the correlation between the significant bits of the input operands and the carry-in values to improve the accuracy of [9] speculative adders. Specifically, it shows that CSPA significantly reduces error rates and reduces overhead while reducing the time and area spent on errors.

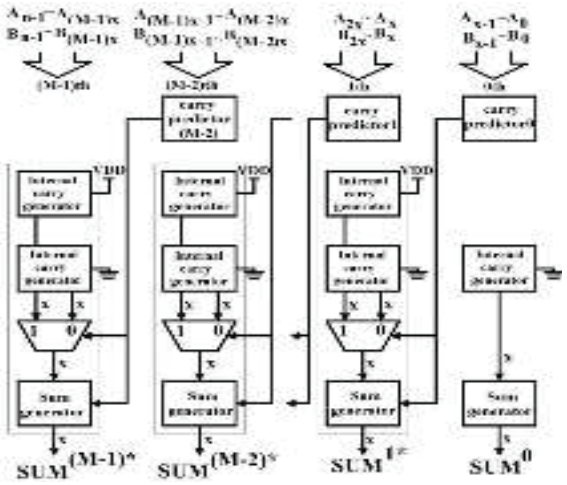

Figure 1. Block Diagram of Carry Speculative Adder

B. Carry Generator

As illustrated in Figure 2, the carry bit is created after three gate delays in a traditional full adder. Figure 2 illustrates how the carry and sum generators are separated in the CSPA's block adder, using a Modified Full Adder (MFA). A further logic gate is added to more efficient Transmission Full Adder (TFA), which produced an extra gate delay and increased power consumption. With two carry generators and a sum generator, CSPA [1] is implemented in block adders to save electricity.

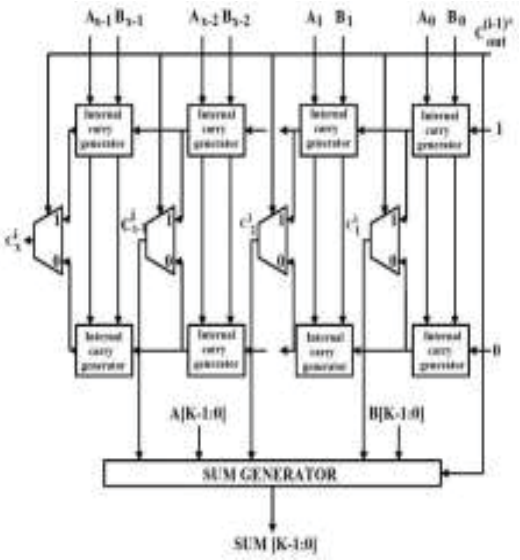

Figure 2. Structure of Block Adder

C. Modified Carry Generators

As for CSPA [6], it utilizes a modified full adder to split the Sum and Carry generators, which increases power consumption and area. To save space, the carry generator has been replaced with two distinct carry generators for Carryin=1 and Carryin=0, respectively. The structure of carry generator is shown in Figures 3(a) and 3(b). Ripple carry circuits have carry-outs of full adders that are as the incoming carry-in of the next most significant full adder. In spite of the fact that ripple carry occurs in each stage, it is called a ripple carry circuit. It is only during the subsequent carry-in of a ripple carry adder that bits for the sum and carry out of any half adder stage are valid. The logic circuitry should have propagated this delay through its logic circuits.

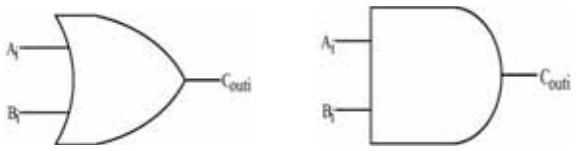

Figure 3(a) and 3(b). Structure of Modified carry Generator for Cin = 1 and 0.

Carryin = 0 and the logic gate AND is used as a replacement for the four-gated 1bit carry generator. A logic gate "OR" is used when Carryin is 1, as well as the four-gated 1-bit carry generator. There are two types of modified carry generators instead of two carry generators, so the block adders take up less space with one gate delay. To segregate the carry and sum generators in the CSPA's block adder, a Modified Full Adder (MFA) is used. Due to two gate delays and increased power consumption, MFA has an additional logic gate than TFA to lessen the carry bit delay. A CSPA chip consists of a multi-function adder with a sum generator and two carry generators to save power. As soon as an input pattern is received, the carry generators and carry estimator circuits are simultaneously active. Similarly, the

CVR Journal of Science and Technology, Volume 21, December 2021
DOI: 10.32377/cvrjst2109

internal carry generator generates equivalent internal carry signals when signals "1" and "0" are input. Carry predictors enable block adders to generate their expected carryout bits as shown in Figure 4.

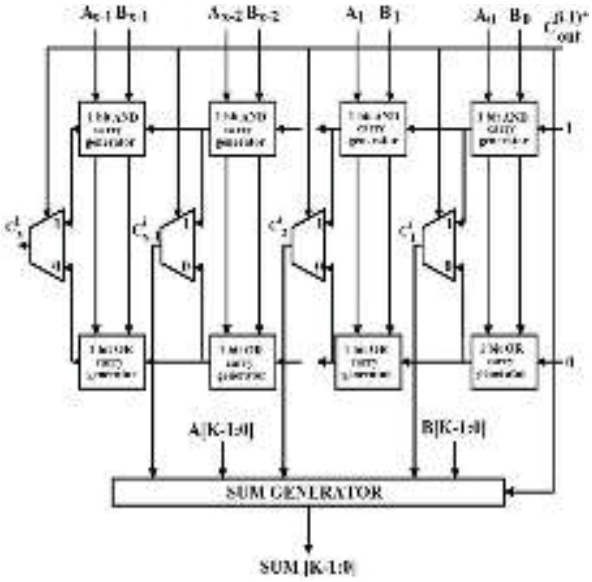

Figure 4. Block Diagram of Carry Speculative Adder

III. Variable Latency Circuit

A. Carry Speculative Adder

When the critical path delay is employed as the execution period, a variable latency design can reduce waste timing of the circuit. Two clock cycles are employed in variable latency design. The CSPA with error detection and recovery circuits is shown in Figure 5.

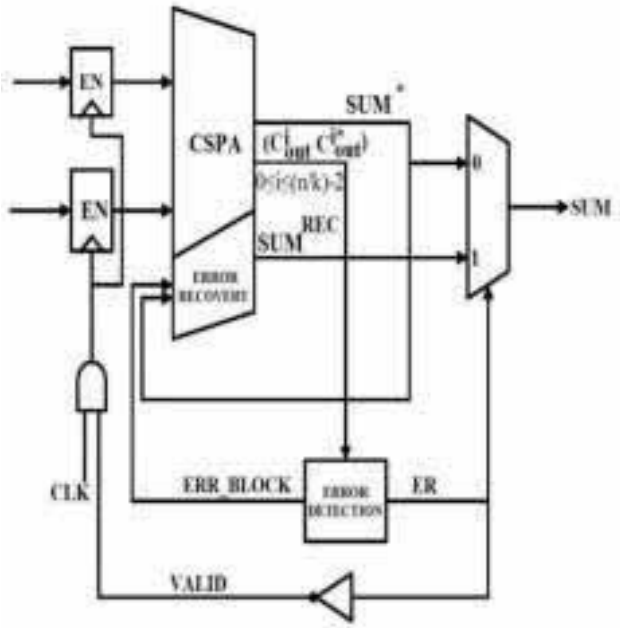

Figure 5. Variable Latency Carry Speculative Adder Circuit

The internal carry generators and carry estimator circuits function in parallel when an input pattern is received. With regards to carry in signals "1" and "0," the internal carry generator generates equivalent internal carry signals. The block adders expected carryout bits are generated by the carry predictor. Error_ block signals and error signals are generated by the error detection circuit. The error detection circuit generates Error block [4, 6] impulses, which specify which block circuit gave erroneous and precise measurements. The error signal indicates whether or not an error has occurred. When the error signal ER is set to "0" and the VALID signal is set to "1," the findings are correct. The results of the CSPAs are then verified as correct and used as the output. When the ER signal is "1" and the VALID signal is "0," the results computed by the CSPA are incorrect, and the correct results are recovered from the Error Recovery Circuit in the second cycle, and the result is presented as SUMREC (i.e. Recovered sum). The input registers are blocked if an error occurs, and no fresh input is stored into the device. Because the CSPA's error rate is low, the VLCSPA's average latency is more similar than that of the CSPA.

B. Carry Speculative Adder with Modified Carry Generator

Carry Speculative Adder, error - detecting circuit, error recovery circuit, and data latched circuit, and cascaded multiplexer is used in configurable latency carry speculative adder, as shown in Figure 6.

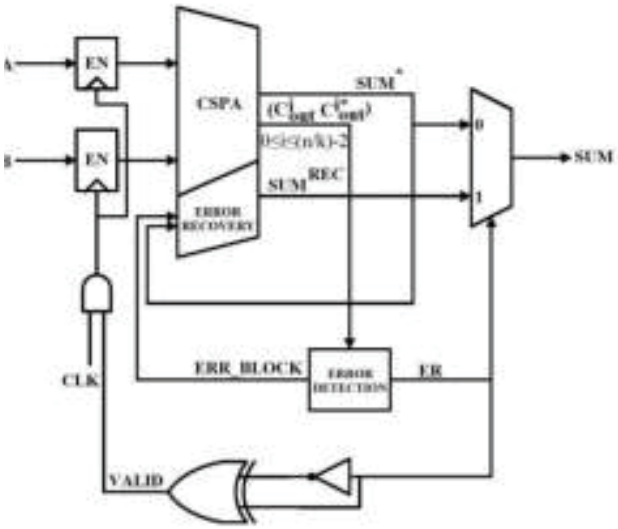

Figure 6. Variable Latency Modified Carry Speculative Adder Circuit

When an input pattern is received, VLCSPA returns the CSPA result in a cycle. Error_ block signals and error signals are generated by the error detection circuit. When an error appears, the error recovery circuit recovers the results based on the Error block. The results from the error detection circuit and CSPA are fed into a multi-bit multiplexer, and the error is utilized as the multiplexer choose signal. Whenever the ER signal is "1," the signal is recovered from the error recovery circuit. When the ER signal is "0," the CSPAM [5] (i.e. Carry Speculative Adder with Modified Carry Generators) results are selected. The input registers are deactivated when an error occurs, and no new input is latched in the circuit. The not gate in figure 6 is

CVR Journal of Science and Technology, Volume 21, December 2021
DOI: 10.32377/cvrjst2109

replaced by the XOR gate in this data latching. An exclusive or operation is conducted between the error signal and the counterpart of the error signal in the latching circuit. After the previous data has been recovered, the valid signal enables latching fresh data into input registers.

C. Error Detection Circuit

The addition operation in CSPA is based on guesswork, which might result in accurate or inaccurate results. An error detection circuit is used to determine if the output is accurate or not. The Block diagram of an error detection circuit is shown in Figure 7. The Error Detection Circuit also detects whether or not an error has occurred. The following is how error detection works. When the Ci out and Ci *out signals of each block adder are fed into the error detection circuit, it is checked to see if they are equivalent. This is accomplished by performing an exclusive or (XOR) operation on Ci out and Ci* out, where Ci out is the carryout bit of the ith block adder that is generated by the multiplexor and Ci *out is the projected carryout bit generated by the ith carry prediction circuit. If Ci out and Ci *out are the same, the carry out bit of the ith block adder is accurate. Otherwise, the Ci *out signal projected is not correct. The output of the OR operation on the XOR output of the gates yields the error signal. If the error detection circuit detects an Error, the error signal is "1," else it is "0" [6].

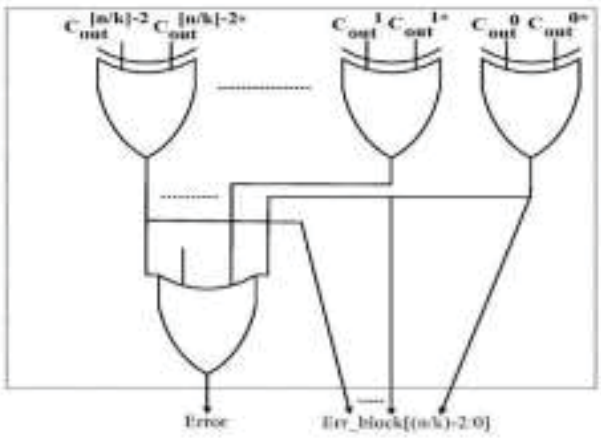

Figure 7. Schematic of Error Detection Circuit

D. Error Recovery Circuit

The Error Recovery Circuit corrects inaccurate partial sum bits [5] of the block adders based on the Error block signal. The Error Recovery Circuit block schematic is illustrated in Figure 8.

IV. Simulation Results

From conception to device programming with the Integrated Software Environment (ISE®) from Xilinx, you can approach your idea from conception to completion. The ISE Project Navigator supervises and processes your design as it proceeds through the ISE design cycle. The design entry phase of the IISEs is its first phase. You build your source files during design entry based on your design goals. Creating a top-level design file can be done using a schematic or a Hardware Description Language (HDL).

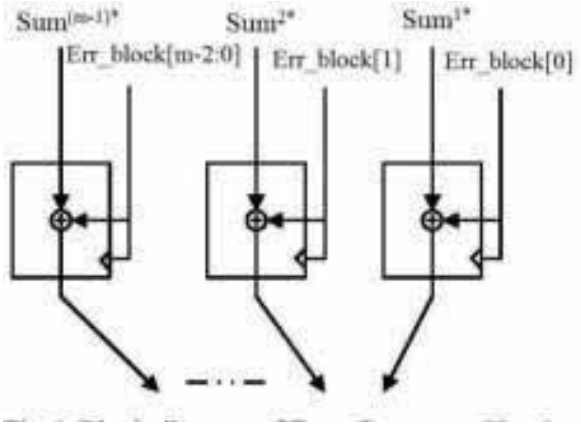

Figure 8. Structure of Error Recovery Circuit

There are a variety of file formats that are used to create the lower-level source files in your design. Design entry is followed by simulation, and then synthesis is conducted. The resulting netlist files are sent to be implemented, after which VHDL, Verilog, or mixed language designs are converted. The implementation of design is the process of converting the logical design into a physical format that a target device can use. In Design, each implementation procedure can be run independently or in one step. Implementing a Field Programmable Gate Array (FPGA) or Complex Programmable Logic Device (CPLD) has different results (FPGA). Throughout the process of designing, the functioning is continually tested. Simulator The software can be used to test the timeliness of your design and functionality. Simulators translate VHDL and Verilog codes to circuits and display logical results in the simulation to evaluate the function of the circuits. A programming file can be generated by Design and used to configure the device. Configuration of Xilinx devices involves downloads of programming files from a host computer and generation of configuration files from XST Synthesis.

The critical route delay of SCSA is 19 to 40% less than that of the Kogge-Stone adder for an error rate of 0.01 percent as shown in Table I and Table II. The critical route delay of SCSA is equivalent to that of speculative addition in VLSPA for an error rate of 0.01 percent. This suggests that SCSA has a lot of potential. The area of SCSA is 10 to 43 percent lower than Kogge-Stone adder at an error rate of 0.01 percent. The area requirement of the speculative adder in VLSPA is -20 to 8% for an error rate of 0.01 percent. For various bit widths, it can be seen that the area of SCSA is always smaller than that of VLSPA. This is due to the fact that SCSA speculates on the level of the window, whereas VLSPA speculates on the level of the individual bit position. In VLSPA, the critical path delay of a speculative adder is 12 to 27% less than that of a Kogge-Stone adder. However, the error detection block's critical path delay is 4 to 8% longer than the speculative adder's, negating the advantage of speculation. The error recovery block has a delay that is less than half that of the speculative addition and error detection blocks. VLCSPA, on the other hand, has nearly identical critical path delays for error detection and

CVR Journal of Science and Technology, Volume 21, December 2021
DOI: 10.32377/cvrjst2109

speculative addition, both of which are 14 to 36 percent faster than the Kogge-Stone adder. When speculation is true, the critical path latency of VLCSPA is 6 to 19 percent lower than that of VLSPA. The error recovery block's critical path delay is less than half that of speculative addition and error detection. VLSPA has a 14 to 32 percent bigger surface area than Kogge-Stone adder. This is related to the error detection and recovery blocks' area overhead. VLCSPA, on the other hand, has a -6 to 17% less area requirement than the Kogge Stone Adder. When the bit width is 512, the VLCSPA adder has a 6 percent smaller area than the Kogge-Stone adder. To put it another way, VLCSPA has the potential to be smaller and faster than the Kogge-Stone adder.

As a result of SCSA's lower critical path delays, errors of 0.010 percent and 0.250 percent result in ten percent less delays than those caused by Design Ware adders. SCSA, as width increases, has a 43.0 percent smaller area than Design Ware adder, with an error rate of 0.01 percent. The area of the SCSA is 21.0 to 56.0 percent smaller than the Design Ware adder for an error rate of 0.25 percent. SCSAs with a lower mistake rate have a larger surface area than those with higher error rates. The error rate and the type of error must be balanced as a result. Occasionally, the error rate can increase slightly when an application uses error-tolerant algorithms to minimize the failure area. A tradeoff is created between the error rate and the time needed for the task to be completed.

TABLE I.
COMPARISON OF VARIOUS ADDER WIDTHS W.R.T WINDOW SIZE

Adder Width	Window Size (P_{err} = 0.01%)	Window Size (P_{err} = 0.25%)
64	14	10
128	15	11
256	16	12
512	17	13

TABLE II.
COMPARISON OF VARIOUS ADDER INTERMS OF DELAY & POWER

Adder Type	Methodology	Delay	Time Complexity	Power
SCSA (16 bit)	Without Variable Latency Design	19. 279 ns	7.42sec	0.6 5 W
CSPA (16 bit)	With Variable Latency Design	16. 224 ns	6.52 sec	0.3 39 W
Modified CSPA (16 bit)	With Variable Latency Design	13. 08 ns	5.66 ns	0.1 14 W

Power consumption of carry speculative adder (CSPA) and modified carry speculative adder using carry generators (CSPAM) is shown in Figure 9 and 10 using Xilinx tool. The maximum combinational path delay of CSPA is 55.680 ns and for CSPAM are 11.367 ns

On-Chip	Power (W)	Used	Available	Utilization (%)
Logic	0.000	64	66560	0
Signals	0.000	129	—	—
IOs	0.000	98	784	13
Leakage	0.339			
Total	0.339			

Figure 9. Power Consumption of CSPA

On-Chip	Power (W)	Used	Available	Utilization (%)
Logic	0.000	64	33280	0
Signals	0.000	129	—	—
IOs	0.000	129	309	42
Leakage	0.114			
Total	0.114			

Figure 10. Power Consumption of CSPAM

In this paper both the designs i.e., CSPA and CSPAM are simulated and verified using both FPGA and ASC tools. Figure 9 and 10 results are given with the help of Xilinx x-Power Analyzer tool. By observing the power results the CSPAM has less power compared to CSPA due to modified carry generators used in it. Figure 11 shows the RTL schematic of CSPA which is generated with the help of Cadence RTL Compiler tool.

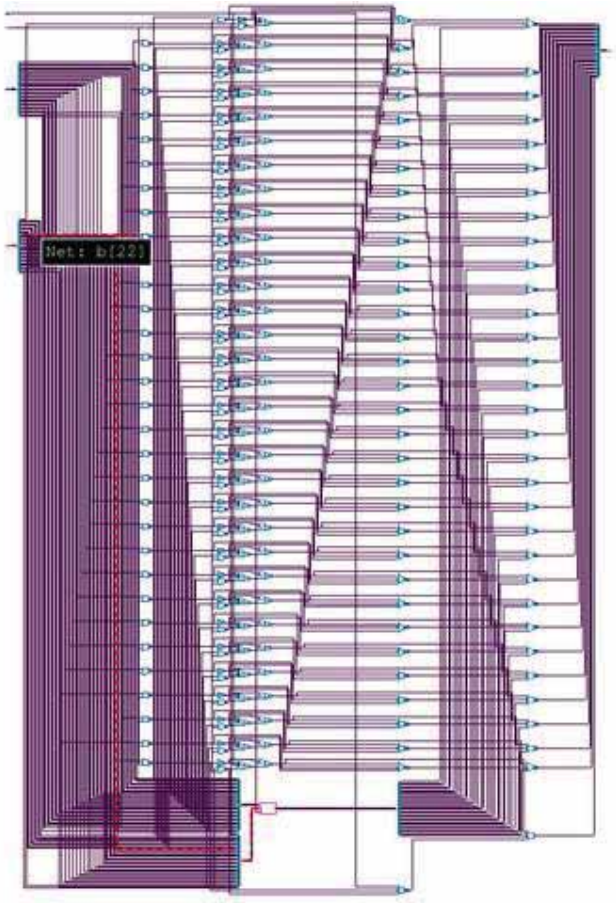

Figure 11. The RTL Schematic of CSPA

CVR Journal of Science and Technology, Volume 21, December 2021
DOI: 10.32377/cvrjst2109

Figure 12 give the Pre-synthesis timing report of CSPA in which it consists of 160 paths and the timing is 1.096 ns and there are no violating paths. Pre synthesis and Post Synthesis are performed with the help of Cadence SoC Encounter.

Setup mode	all	default
WNS (ns):	1.096	1.096
TNS (ns):	0.000	0.000
Violating Paths:	0	0
All Paths:	160	160

Figure 12. The Pre-Synthesis timing report of CSPA

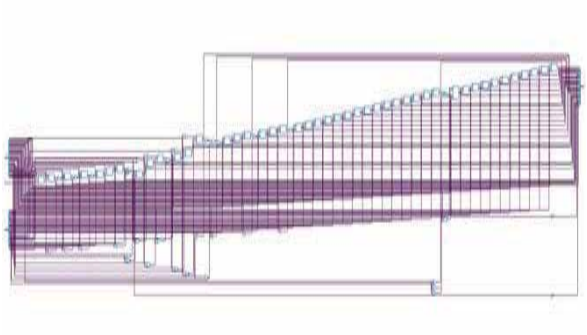

Figure 13. The RTL Schematic of Carry Predictor

Figure 13 shows the RTL schematic of carry predictor circuit which plays the major role in CSPA and CSPAM. Figure 14 shows the final chip layout structure of CSPAM.

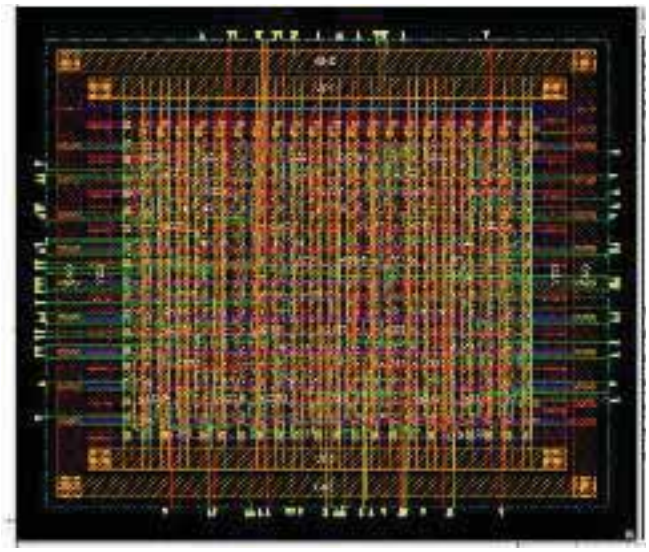

Figure 14. Chip Layout of CSPAM

V. Conclusions

First, the CSPA splits the carry and sum generators, allowing for faster calculation of the carry signal and partial sum bit. Secondly, the block adders suggested to carry predictor circuit only predicts the carryout bit using input bits near the MSB. The prediction circuit's hardware cost is lowered, while the CSPA's error rate increases just a little. Thirdly, an error model was presented to investigate the correlation between the quality of the block adder, the length of the carry predictor circuit, and the CSPA error rate. Fourthly, the EEDP model was presented to calculate the optimal block adder size for segmenting the "n" bit adder for balanced latency, power consumption, and error rate. Fifthly, when errors occur, the proposed error detection circuit identifies which block adder produced an inaccurate carry-out bit, and the error recovery circuit focuses solely on restoring block adders with incorrect partial sum bits. A variable latency adder that adds mistake detection and recovery to the speculative adder. The suggested variable latency adder outperforms the quickest Design Ware adder in both delay and area, according to simulation findings. To fully investigate the design space and its applications, such as non-uniform input distributions, non-uniform input arrival timing profiles, and other arithmetic operations like multiplication and multi-operand addition, more study is required. The ETA (Error Tolerant Adder) series of low-power, high-speed adders are more economical than traditional adders on the market, especially in low-accuracy applications. The possible uses of the ETA (Error Tolerant Adder) are mostly in sectors where accuracy is not a stringent necessity or where super low power consumption and high-speed performance are more important than accuracy. The DSP application for portable devices such as cell phones and laptops is an example of such applications. When compared to the trustworthy adder, the adder provided here is considerably faster. This approach is very beneficial in computationally intensive applications that are resistant to slight computation errors. A mechanism has also been provided for detecting and correcting mistakes. This produces a fast variable latency adder that is 1.5 times faster than a standard fast adder.

References

[1] V. Gupta, D. Mohapatra, S. P. Park, A. Raghunathan, and K. Roy, “IMPACT: IMPrecise adders for low-power approximate computing,” in Proc. Int. Symp, Low Power Electron. Design (ISLPED), Aug. 2011, pp. 409–414.

[2] N. Zhu, W. L. Goh, G. Wang, and K. S. Yeo, “Enhanced low-power high speed adder for error tolerant application,” in Proc. Int. SoC Design Conf. (ISOCC), 2010, pp. 323–327.

[3] K. Du, P. Varman, and K. Mohanram, “High performance reliable variable latency carry select addition,” in Proc. Design Autom. Test Eur. Conf. Exhibit. (DATE), Mar. 2012, pp. 1257–1262.

[4] Gai Liu, Ye Tao, Mingxing Tan, and Zhiru Zhang, Computer Systems Laboratory, Electrical and Computer Engineering, “CASA: Correlation-Aware Speculative Adders”, 2014.

[5] Junjun Hu and WeikangQian, Shanghai “A New Approximate Adder with Low Relative Error and Correct Sign Calculation”, 2014.

[6] Ing-Chao Lin, Senior Member, IEEE, Yi-Ming Yang, and Cheng-Chian Lin, “High-Performance Low-Power Carry Speculative Addition With Variable Latency”, IEEE transactions on very large scale integration (vlsi) systems, 2014.

[7] Du, P. Varman, and K. Mohanram, “Static window addition: A new paradigm for the design of variable latency adders,” in Proc. Int. Conf. Comput. Design (ICCD), Oct. 2011, pp. 455–456.

[8] N.V.Mujadiya, "Instruction scheduling on variable latency functional units of VLIW processors," in Proc. Int. Symp. Electron. Syst. Design (ISED), 2011, pp. 307–312.
[9] V. Gupta, D. Mohapatra, A. Raghunathan, and K. Roy, "Low-power digital signal processing using approximate adders," IEEE Trans. Computer.- Aided Design Integration. Circuits Syst., vol. 32, no. 1, pp. 124–137, Jan. 2013.
[10] Y. Chen et al., "Variable-latency adder (VL-adder) designs for low power and NBTI tolerance," IEEE Trans. Very Large Scale Integration. (VLSI) Syst., vol. 18, no. 11, pp. 1621–1624, Nov. 2010.
[11] Y. Liu, Y. Sun, Y. Zhu, and H. Yang, "Design methodology of variable latency adders with multistage function speculation," in Proc. 11th Int. Symposium. Qual. Electron. Design (ISQED), Mar. 2010, pp. 824–830.
[12] Zhu, W. L. Goh, K. S. Yeo, and Z. H. Kong, "Design of low-power high-speed truncation-error tolerant adder and its application in digital signal processing," IEEE Trans. Very Large Scale Integration. (VLSI) Syst., vol. 18, no. 8, pp. 1225–1229, Aug. 2010.

E-ISSN 2581 –7957
P-ISSN 2277 – 3916
CVR Journal of Science and Technology, Volume 21, December 2021
DOI: 10.32377/cvrjst2110

Touch-less Disinfecting Contraption using UV-C Light

Cholleti Mahathi[1] and Dhruva R Rinku[2]
[1]PG Scholar, CVR College of Engineering/ECE Department, Hyderabad, India
Email: mahathicholleti@gmail.com
[2]Assoc. Professor, CVR College of Engineering/ECE Department, Hyderabad, India
Email: dhruva.rinku@cvr.ac.in

Abstract: **An electro-mechanical disinfecting device is designed and implemented using UV-C (Ultraviolet-C Radiation light). This device is made completely touchless in an effort to avoid viruses from being contacted to the device. The outbreak of SARS-COV-2 has led to serious public health emergencies. The vital step for preventing the spread of coronavirus is sanitizing, disinfecting. Ultraviolet radiation as a disinfecting unit is preferable to chemical-based sanitation, with research studies proving its effectiveness in deactivating viruses when exposed to the radiation. The things to be disinfected are exposed to UV radiation in this closed chamber and the device is operated using sensors.**

The main objective is to design a cost-effective device that can be availed at any public place by anyone.

Index Terms: **SARS-COV-2, Covid 19, UV-C radiation, UVC lamp, Covid vaccine, Disinfecting, sanitizing.**

I. INTRODUCTION

The novel coronavirus has been a chaotic pandemic all over the world since Dec 2019. It left the world in a state of crisis in many areas, including the economy, health, education, and others. SARS-COV-2 (Severe Acute Respiratory Syndrome Coronavirus 2) is accountable for the emergence of COVID 19 (Coronavirus disease 2019). As a result, the world has been witnessing traumatic scenarios involving lakhs of deaths. Airborne, direct contact, indirect contact are the different transmission modes of coronavirus. Therefore, the most important thing people can do is to avoid transmission. People have been advised by the WHO (World Health Organization) to avoid the spreading of the coronavirus by wearing masks, regularly washing their hands, avoiding groups, sanitizing and disinfecting. There were no other precautions we could take. Although covid vaccination is on the rise, these precautions must be part of our daily activities without any negligence. During the early stage of the pandemic, the world was in dire straits that vaccines seemed to be out of the question. Developing a vaccine for the SARS-COV-2 was viewed as a challenge around the world. Scientists across the world collaborated to develop vaccines, treatments to save people and end this pandemic [6]. In order to develop a vaccine, five stages must be completed, involving numerous trials and time-consuming processes. After tremendous research, finally vaccines are available after almost one year since the outbreak of COVID-19. The majority of them are largely successful [6]. Initially, vaccine dosage was low as people were terrified by its side effects. However, these side effects are out of note compared to its nature of fighting against coronavirus. Ultimately, the WHO and the government are successful in bringing vaccines to the public's attention. Vaccines are to provide immunization against serious illness and death. Boosting the immune system by providing the highest level of immunity is what vaccines do. Getting vaccinated doesn't mean that people can cast away the precautions completely. Studies are being conducted to ascertain whether these vaccines can provide long-term protection [10]. Hence, the WHO guidelines should be followed on a regular basis.

Disinfecting and cleaning the often-used items are the requisite steps among the precautions conferred by WHO [1]. There are physical methods as well as chemical methods of disinfection. Physical methods include ultraviolet radiation, heat, sunlight exposure and chemical methods involve liquid sanitizers, bleaching and other chemical solutions. As chemical sanitizers leave residue behind, most of the materials can't resist them. Hence, physical disinfection methods are preferable to chemical-based methods. UV radiation is one of the physical disinfection methods and is considered to be the most effective. In the early 19th century, UV was first used for water treatment and sterilization. With the evolution of UV technology, Ultraviolet Germicidal Lamps (UVGI) are acknowledged as air and surface disinfectors. Moreover, it has been shown to kill 99.9% of viruses in studies. Mainly there are two drawbacks to using UV radiation,

- A significant health risk is posed by UV exposure such as skin cancer, skin burn. It not only effects the outer layer of the skin but also penetrates into deeper layers causing DNA damage.
- While using UV disinfectant, part of the item in the shadow region doesn't get disinfected, so this must be spotted.

Scientists have ascertained the effectiveness of UV radiation in deactivating corona virus and different designs of UV disinfection units are being implemented. Some are mobile units, some are open which condition the open rooms, some are closed chambers.

CVR College of Engineering
Received on 17-05-2021, Revised on 03-07-2021, Accepted on 19-08-2021.

E-ISSN 2581 –7957
P-ISSN 2277 – 3916

DOI: 10.32377/cvrjst2110

II. Related Work

A. UV Radiation

Ultraviolet radiation, an electromagnetic radiation form with the wavelength ranging from 10nm to 400 nm (corresponding frequency around 30PHz to 750THz) shorter than visible light and longer than X-rays [14]. UV is contained in sunlight and adds up to 10% of electromagnetic radiation from the sun. There are several sub-ranges in the range of the UV i.e., 10 nm to 400 nm, mainly UVA, UVB, UVC, N-UV, F-UV, H Lyman-α, E-UV, V-UV. UVA, UVB, UVC ranges are considered mostly [14].

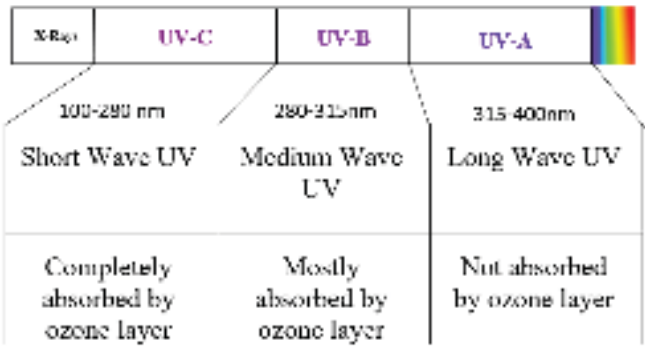

Figure 1. UV ranges in the electromagnetic spectrum

In the figure 1, the different types of UV radiation are grouped based on their wavelength range. In addition, their characteristics towards the ozone layer are described.

Thus, the majority of UV radiation reaching the surface of the earth is UV-A, with some UV-B showing up in portions [14]. Due to the ozone layer, UV-C light is not able to reach the Earth's surface and biological life on earth has not been exposed to this energy. But UV-C is more prominent as a disinfecting unit than others. Finally, researchers successfully invented lamps that can produce radiation in the range of UV-C. In the year 1901, the Germicidal lamp (Low-Pressure Mercury Lamp) that produces 254 nm wavelength radiation was invented. This is proven to deactivate bacteria, viruses and protozoa.

How does UV-C work? Despite being used for disinfection since the 19th century, the answer to this was recently found. UV-C deeply assimilates RNA and DNA heading to the structural havoc of the virus in a process called photodimerization [8]. DNA has nucleotides containing nitrogen base, deoxyribose sugar and phosphate group as elementary units. The nitrogen bases in DNA are Adenine(A), Thymine(T), Guanine(G) and Cytosine(C) whereas in RNA Uracil (U) is present instead of Thymine. A - T and G - C are the pairs that form DNA strands [2].

exposure to UV radiation DNA can be damaged in several ways. i) can break double-strand ii) can change the structure of the base, for example, G could look like A iii) can make either two T molecules or two C molecules to bond together [9]. DNA is thus disrupted in such a way that it becomes inactive to perform its cellular functions. While RNA makes up the Coronavirus, the effect is the same when exposed to UV radiation. UV radiation has a higher impact on C, T [2].

UV dose and UV intensity are commonly used terms to describe the amount of UV radiation penetrates. The former measures the amount of energy that penetrates through the surface multiplied by exposure time, while the latter measures the amount of UV energy penetration through the treated surface.

UV dose determines log reduction of pathogens.

- 1 log reduction = 90% reduction
- 2 log reduction = 99% reduction
- 3 log reduction = 99.9% reduction
- 4 log reduction = 99.99% reduction and so on.

The relation between percentage reduction and log reduction is given in [12] as

$$P = (1 - 10^{-L}) \times 100 \quad (1)$$

Where P is the Percentage in reduction and L is the log reduction.

According to [11] UV Dose is expressed in terms of UV irradiance and Time

$$UV_{dose}\left(\frac{J}{cm^2}\right) = UV_{irradiance}\left(\frac{W}{cm^2}\right) \times Time\ (s) \quad (2)$$

Where UV_{dose} is the radiation dose required in Joules per centimeter square, is the radiation emitted by th e source in Watts per centimeter square and is the time required to eliminate a virus in seconds.

UV LEDs have finally been found to kill 99.9% of the SARS-COV-2 virus in 30 seconds [3]. It is also demonstrated that UVC is more effective in inactivating SARS-COV-2 than UVA in [4]. SARS-COV-2 can be inactivated by UV-B, but it is less effective for other SARS viruses. Humans are more vulnerable to the harmful effects of UVB than UVC. It can penetrate through the skin and damage DNA. As such, it poses a risk [5]. It is widely recognized that UVC can disinfect the air, water, and surfaces and that it has been used for decades. Thus, it is called a germicidal lamp [5].

III. Proposed Model

The proposed system provides flexibility to the user to get their things physically sanitized. This system shows following new features from existing models,

- It is made touchless
- It has an interactive display
- It has adjustable disinfection timer features
- A curtain is fixed so that there is no chance for humans to get exposed to UV light.
- Items can be disinfected individually.
- This device can be availed at anywhere without any installation.
- It only needs a simple power source.

A. Design of the system.

This system includes both input and output devices. Input devices give input signals to Arduino boards and output devices take signals from Arduino boards. A motor driver, LCD display, buzzer, relay module, and ultrasonic sensor are the output components. An ultrasonic sensor, IR sensor modules and limit switches are the inputs. The input and output devices used to implement the device are:

CVR Journal of Science and Technology, Volume 21, December 2021
DOI: 10.32377/cvrjst2110

- Arduino Mega 2560
- LCD display
- DC motors
- IR sensor modules
- L298N motor driver
- UV lamp
- Ultrasonic sensor
- Limit Switches
- Buzzer
- Relay Module

B. Block Diagram of The Designed Model

As UVC is showing its efficacy in inactivating SARS-COV-2 different designs and technologies using UVC as disinfecting units are being implemented. Block diagram of design model is shown in Fig. 2. This model is an electromechanical device that can disinfect handheld items with a UV lamp as a disinfectant unit. A touch-free, closed chamber is designed to disinfect items within it. It is made touchless with the help of IR sensor modules. It has a user-interactive display (16x2 LCD display), ultrasonic sensor, relay module, UV lamp, two DC motors, limit switches and all components are controlled by Arduino mega 2560.

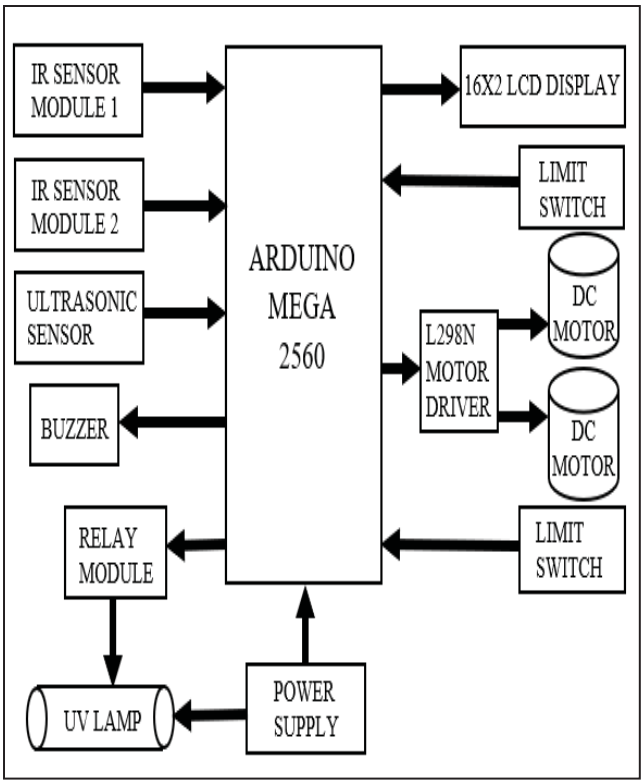

Figure 2. Block diagram of the designed model.

The closed chamber contains some mechanical parts like the main tray (which can be opened and closed by moving in and out of it), flipping tray (fixed on the main tray gets which can get flipped). Arduino is powered by 9 volts and UV lamp by 230 volts.

Arduino upon receiving signals from IR sensor modules triggers the events. Arduino sends signals to the L298N motor drive to drive DC motors when an opening or closing or flipping event is triggered. The movement of DC motors is stopped by limit switches where these limit switches send signals to Arduino when motors touch them.

IR sensor module is a sensor that detects the presence of an object in its proximity range. IR sensor modules are used in this design to operate the device. Two IR sensor modules are used IR1 and IR2. IR1 is for opening the tray and to set disinfecting time, IR2 is for closing the tray and for selecting different disinfecting times. The user interaction with the device is provided through a 16x2 LCD which has 2 lines each having the ability to print 16 characters. The default time for disinfection is 1 minute. It can be changed in accordance with the distance of the user's hand from the ultrasonic sensor. This device provides 4 different times for disinfection (1min, 3min, 5min, 6min) along with default time. For each time, the distance range is as follows

- 1cm < Distance < 5cm = 3 min
- 5cm < Distance < 10cm = 5 min
- 10cm < Distance < 15cm = 6 min

Ultrasonic sensor containing a transmitter and receiver measures the distance of the obstacle by transmitting ultrasonic waves and receiving the echo signals (reflected signals). It calculates the distance by measuring the time span between emitting the signal and receiving the echo signal. The formula that converts time-span to distance is

$$Distance\ (m) = \frac{Time\ span}{2 \times speed\ of\ the\ sound} \quad (3)$$

$$= \frac{Time\ span}{2 \times 29.1} \quad (4)$$

Two DC motors are used, one for opening and closing the main tray and the other to lift the mini tray. As DC motors require a large amount of current approximately 1A where Arduino can provide only 30-40 mA so a motor driver is required to drive the motors. One L298N motor driver can drive two DC motors at a time. An Arduino operates at 5V, far less than the 230V operating voltage of UV lamps, thus a relay module is used to handle that voltage. The Arduino turns on a relay that switches the UV lamp ON and OFF when an event occurs.

C. Circuit Diagram of the Proposed Model

The schematic layout of the implemented model is designed in Fritzing software and is presented below as a circuit diagram. Developers can use the Fritzing software to develop CAD software for the electronics industry. The Fig. 3 shows the circuit diagram for the model.

E-ISSN 2581 –7957
P-ISSN 2277 – 3916

DOI: 10.32377/cvrjst2110

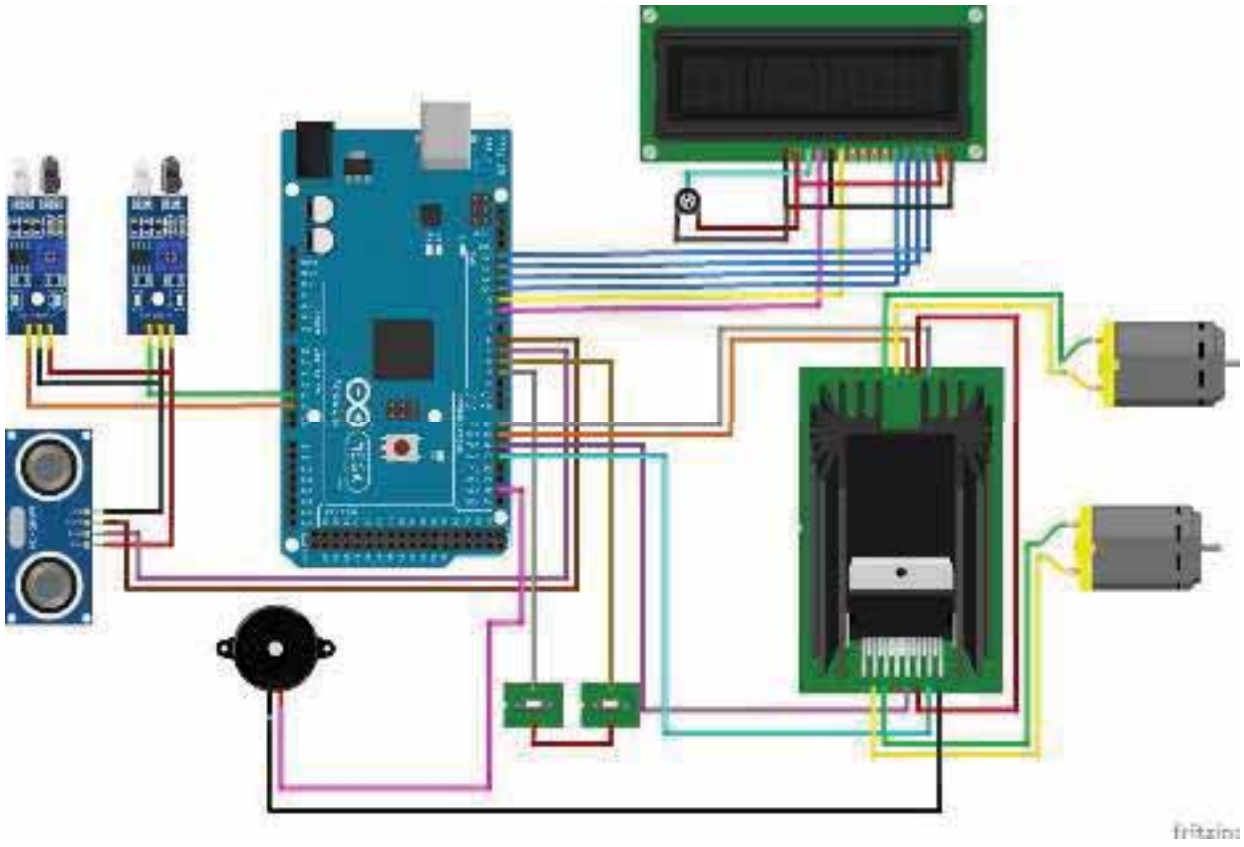

Figure 3. Circuit Diagram of the Touch-less disinfecting contraption implemented in Fritzing software.

D. Working of the Design

Upon turning ON the power supply, all the I/O devices will be initialized. The first message LCD displays is "UVC Based Disinfector" and "1 to open Tray". It's time for the user to trigger the event at IR1 by placing his/her hand in the proximity of IR sensor 1 then the tray gets opened. After the tray is opened, the item to be disinfected must be placed on the mini tray (flipping), which is mounted on the main tray (open/closed). "2 to close the tray" on the display indicates an event to close the tray to be triggered at IR2 by placing the hand in the proximity of IR sensor 2. The user now needs to select a disinfecting time. When the tray gets closed, the user has an option to select disinfection time. LCD displays "1 to Default time 2 to change time". Then IR1 to be triggered to select default time or IR2 to select different disinfection times. If IR2 is triggered, the user can select the given disinfection times by varying his hand from the ultrasonic sensor and the time in accordance to the distance range is displayed on LCD then the user can stop varying distance when desired time displays on LCD. Keeping the hand at that position, the user needs to trigger IR1 to select the time. Then the LCD displays the selected time, and the relay gets switched and the UV light is ON. The mini tray gets flipped after halftime has passed. Upon flipping the item falls on the main tray from the mini tray and disinfection continues. This helps the item to get exposed to the UV radiation on all sides. As soon as the disinfection gets completed the buzzer beeps and the UV lamp turns OFF simultaneously. Then the user can collect the item as per the instructions shown on the LCD display.

IV. RESULTS

In this section, the real-time images demonstrate the messages displayed on LCD while the device is in use. It also includes the appearance of the device. The following images were taken in one through of the disinfection process.

CVR Journal of Science and Technology, Volume 21, December 2021
DOI: 10.32377/cvrjst2110

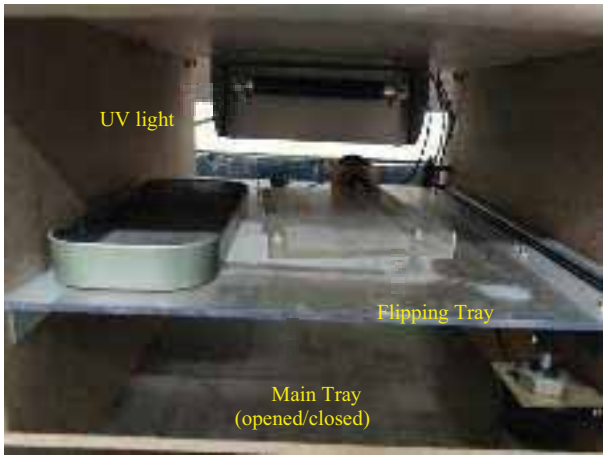

Figure 4. The interior mechanical parts of the implemented device

Figure 8. The front view of the implemented device

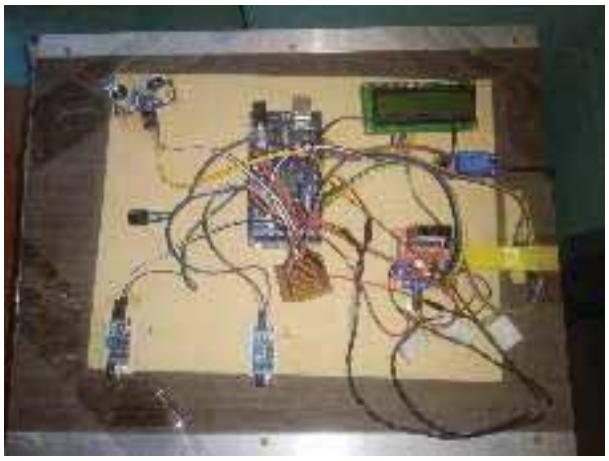

Figure 5. The top view of the device containing components.

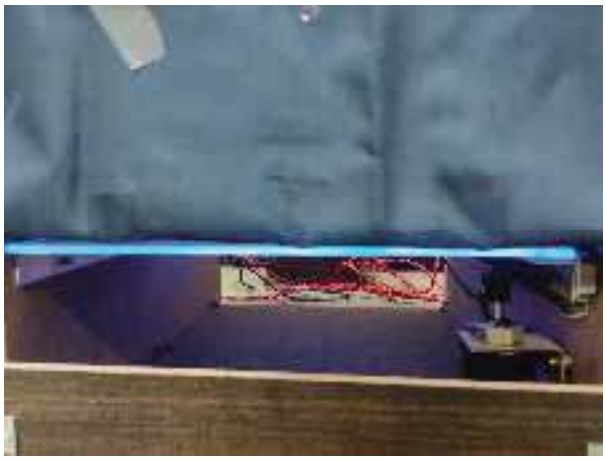

Figure 9. Blue light is observed when UV light is ON

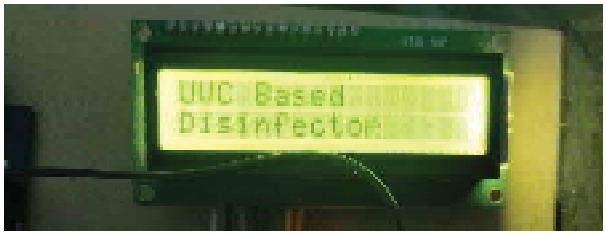

Figure 6. Display as soon as all devices initialize

Figure 10. Message on LCD during the opening of the tray

Figure 7. 1 in the display indicates IR1 to open the tray.

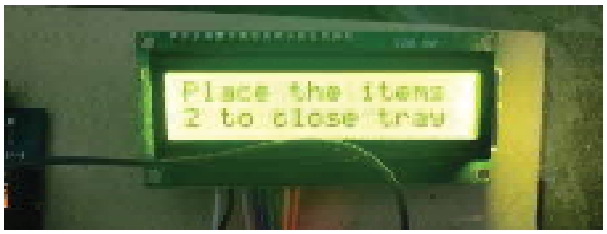

Figure 11. User need to place items on tray and 2 indicates IR 2

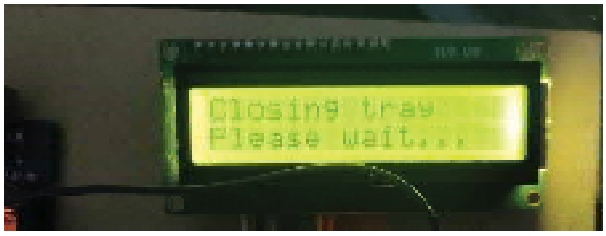

Figure 12. Instruction to user to wait during the closing of the tray

Figure 17. For first half of the time, time set is shown in milliseconds.

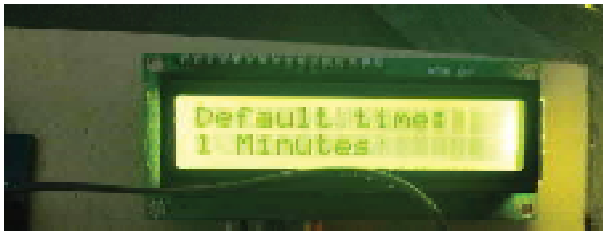

Figure 13. Displays the default time set as 1 minute.

Figure 18. After half time passed, flipping is done & it is displayed.

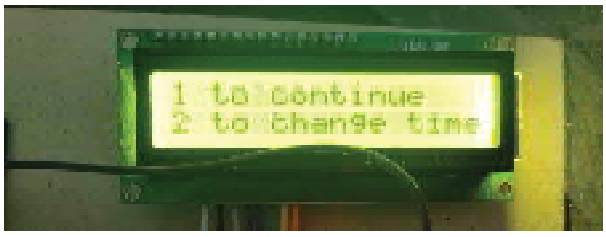

Figure 14. IR1 to continue with default time else IR2 to change time

Figure 19. Disinfecting is displayed during disinfection after flipping.

Figure 15. Displays time according to the varying distance from Ultrasonic sensor and desired time is chosen with IR1.

Figure 20. After disinfection time is passed, message as disinfection Completed is shown and Buzzer is ON and tray gets open.

Figure 16. After time is set, displays it on the LCD as timer set.

Figure 21. Last message shown after tray is closed by collecting the Disinfected items.

Figures 4 to 21 are the images that illustrate the general appearance of the device. The interior mechanical parts are shown in Fig. 4, top view of the device in Fig. 5, front view in Fig. 8 and observation of UV light during disinfection is shown in Fig. 9. Immediately after powering ON, users can see messages on Fig. 6 and Fig. 7. Figures from images labelled Fig. 10 to Fig. 21 show the messages displayed on LCD during the workflow of the device. Once the disinfection process has been completed, the buzzer blows, and the LCD displays "opening tray". When the tray is opened LCD displays "2 to close the tray" then the user has to collect the item and place his hand near IR 2 for the tray to close. When the tray is being closed, the LCD displays "closing tray, please wait". A final message "Thank you, CVR college" is displayed after one through of the disinfection process. To continue, the RESET button on the Arduino board is to be pressed.

V. Conclusions

In this paper, a physical disinfecting system is recommended to eradicate the spread of the devastating coronavirus from handheld devices. A completely touch-less contraption is designed successfully using economically available components. The Arduino mega 2560 is programmed using Arduino IDE software. Fortunately, it is working without any time lag. The LCD display provides comfortable interaction by displaying essential data without any uncertainties in time. As the device contains UV light which is extremely harmful to humans, the user must use the device with caution. The device is implemented with an idea to provide accessibility at any public place with an affordable cost of installation. It can be installed directly with a power supply and no peripheral devices are required. There is a large scope for the application of this device. The insistence on UV-C disinfecting gadgets has increased with the outbreak of coronavirus.

References

[1] WHO (WORLD HEALTH ORGANIZATION). (2020). Retrieved from COVID-19 transmission and protective measures

[2] ANDERSON, M. (2020). The ultraviolet offense: Germicidal UV lamps destroy vicious viruses. New tech might put them many more places without harming humans. IEEE Spectrum, 50-55.

[3] Berezow, A. (2020). COVID-19: UV LED Can Kill 99.9% Of Coronavirus In 30 Seconds. AMERICAN COUNCIL ON SCIENCE AND HEALTH.

[4] Christiane SilkeHeilingloh, Ulrich Wilhelm Aufderhorst, Leonie Schipper, Ulf Dittmer, Oliver Witzke, Dongliang Yang, Adalbert Krawczyk. (2020). Susceptibility of SARS-CoV-2 to UV irradiation. American Journal of Infection Control, 1273-1275

[5] UV Lights and Lamps: Ultraviolet-C Radiation, Disinfection, and Coronavirus. (2021, 01 02). Retrieved from U.S Food & Drug Administration: https://www.fda.gov/medical-devices/coronavirus-covid-19-and-medical-devices/uv-lights-and-lamps-ultraviolet-c-radiation-disinfection-and-coronavirus.

[6] COVID-19 Vaccines. (n.d.). Retrieved from WHO (WORLD HEALTH ORGANIZATION): https://www.who.int/emergencies/diseases/novel-coronavirus-2019/covid-19-vaccines.

[7] Derraik, J. &. (April, 2020). Rapid evidence summary on SARS-CoV-2 survivorship and disinfection, and a reusable PPE protocol using a double-hit process. ResearchGate.

[8] Understanding Genetics. (2011, March 30). Retrieved from The Tech Interactive: https://genetics.thetech.org/ask/ask402#:~:text=UV%20radiation%20in%20sunlight%20can.

[9] Coronavirus disease (COVID-19). (2020, OCT 12). Retrieved from WHO (WORLD HEALTH ORGANIZATION): https://www.who.int/news-room/q-a-detail/coronavirus-disease-covid-19.

[10] The History of Water Treatment. (n.d.). Retrieved from UV03 Ltd. The UV Disinfection Specialists: https://www.uvo3.co.uk/the-history-of-uv-disinfection-uvo3/#:~:text=The%20History%20of%20Water%20Treatment&text=UV%20light%20has%20long%20been,of%20water%20treatment%20and%20sterilisation.&text=The%20first%2C%20full%2Dscale%2C,disinfection%20was%20used%20.

[11] F. A. Juarez-Leon, A. G. Soriano-Sánchez, M. A. Rodríguez-Licea, & F. J. Perez-Pinal. (2020). Design and Implementation of a Germicidal UVC-LED Lamp, IEEE Access, 196951-196962.

[12] Log and Percent Reductions in Microbiology and Antimicrobial Testing. (n.d.). Retrieved from MICROCHEM Laboratory: https://microchemlab.com/information/log-and-percent-reductions-microbiology-and-antimicrobial-testing China, 2020, pp.1-4, doi: 10.1109/ICEPT50128.2020.9202924.

[13] Ultraviolet. (2021, May 5) In Wikipedia https://en.wikipedia.org/wiki/Ultraviolet.

[14] D.J. Weber, H. Kanamori, W.A. Rutala, 'No touch' technologies for environmental decontamination: focus on ultraviolet devices and hydrogen peroxide systems, Curr. Opin. Infect. Dis. 29 (4) (2016) 424–431.

[15] N. Mahida, N. Vaughan, T. Boswell, First UK evaluation of an automated ultraviolet-C room decontamination device (Tru-DTM), J. Hosp. Infect. 84 (4) (2013) 332–335.

[16] A. Beal, N. Mahida, K. Staniforth, N. Vaughan, M. Clarke, T. Boswell, First UK trial of Xenex PX-UV, an automated ultraviolet room decontamination device in a clinical haematology and bone marrow transplantation unit, J. Hospital Infect. 93 (2) (2016) 164–168.

[17] Y. Cao, W. Chen, M. Li, B. Xu, J. Fan and G. Zhang, "Simulation Based Design of Deep Ultraviolet LED Array Module Used in Virus Disinfection," 2020 21st International Conference on Electronic Packaging Technology (ICEPT).

[18] Reed N. G. (2010). The history of ultraviolet germicidal irradiation for air disinfection. Public health reports (Washington, D.C.: 1974), 125(1), 15–27. https://doi.org/10.1177/003335491012500105.

E-ISSN 2581 – 7957
P-ISSN 2277 – 3916

CVR Journal of Science and Technology, Volume 21, December 2021
DOI: 10.32377/cvrjst2111

Considerations to Achieving Pulsatility for Left Ventricular Assist Devices through BLDC Motor by using Closed Loop Control system with PID Controller

B. Ramesh [1], K. Shashidhar Reddy[2], Phani Kumar K.S.V[3] and Anil Kumar Puppala[4]
[1]PG Scholar, CVR College of Engineering/EEE Department, Hyderabad, India
Email: rameshbalagoni128@gmail.com
[2]Professor, CVR College of Engineering/EEE Department, Hyderabad, India.
Email: shashidhar.kotha5@gmail.com
[3]Asst. Professor, CVR College of Engineering/EEE Department, Hyderabad, India.
Email: phani5016@gmail.com
[4]Professor, Geethanjali College of Engineering and Technology/EEE Department, Hyderabad, India.
Email: apuppala@gmail.com

Abstract: **In the past few years, several people have been diagnosed with several heart failures. Implantation of the ventricular Assist life saving device, gives support for the heart to function normally. Mechanical circulatory support systems such as Ventricular Assist Devices (VADs) and Total Artificial Hearts (TAHs) are commonly used to replace a diseased heart and play an important role in saving people's lives. Mechanical circulatory devices known as left ventricular assist devices (LVADs), these devices are currently, the most commonly used to help patients with a variety of heart issues. In the beginning, pulsatile flow devices are used, and further advance switched to continuous-flow devices. Despite the fact that these devices have many benefits, they have reported several difficulties during work. Several trials were performed to prevent these problems. The aim of this study is to achieve pulsatility in Ventricular Assist Devices. This paper describes the design of a closed-loop control with a PID controller system that has been implemented to achieve pulsatile flow in a device by varying the speeds of the BLDC motor. Its performance is evaluated and should be compared with the standards.**

Index Terms: **Total Artificial Hearts,** ***Left Ventricular Assist Devices, Pulsatile flow, BLDC motor, PID controller***

I. Introduction

In the past few years, cardiac disease is the main cause of death for many people. Due to less availability of heart donors, many people who are having difficulty with heart disease are waiting for replacement of their hearts with normal hearts die. One of the best suitable solutions has come to this above problem; there is a need to develop a VAD device that will assist the circulatory system of the body [1]. This resulted in the development of Mechanical Circulatory Support Devices (MCSDs). The step towards the development of Mechanical Circulatory Support Devices (MCDs) [2] started in 1957 and the field of MCD was first introduced in 1964 [3-4]. Mechanical circulatory support devices are used to assist in pumping the blood circulation from the heart to other parts of the entire body in case of heart failure. In order to implant these devices in a patient's body, they have to undergo many clinical experiments, which involve various designs, an appropriate pump speed setting to achieve a desired blood flow rate based on the patient's body, detecting potential risk from inappropriate device operation, and different optimizations are required. In general, there are two types of devices. They are the Total Artificial Heart (TAH) and the Ventricular Assist Devices (VADs). The total artificial heart replaces the complete human heart and the ventricular assist devices assist the human heart in case of weakened heart or heart failure.

Since implantation of the initial ventricular assist devices, a constant development of the suitability of these devices has been made. The first-generation mechanical circulatory support devices were developed in 1964. They are very large-sized devices that are unreliable due to small fatigue cracks that require external power supply and control. Noise emission, infections of cannulas, and malfunctions induced by tears in the membrane or degradation of valves make everyday life difficult and sometimes cause fatal complications [5]. These mechanical circulatory pumps have a one- to two-year lifespan. The second-generation mechanical circulatory support devices were developed in the 1990's and improved patient outcomes by reducing size, susceptibility to infections, reducing noise, and providing continuous flow devices which are mechanically reliable and enhance the quality of life. The second generation of left ventricular assist devices is more frequently used. This paper presents various closed-loop control techniques to achieve pulsatile nature in continuous flow devices with the usage of Brush Less DC (BLDC) motor for both extracorporeal and implantable type TAHs & VADs. By regulating the speed of the motor & pump at the rate of required natural heartbeat pulsation flow is possible [6-7]. To get the required speed of the motor, we use different types of controllers. In this work, a closed-loop control system with a PID controller is used to control the speed of the BLDC motor to achieve the pulsatile flow of blood.

Received on 26-08-2021, Revised on 23-09-2021, Accepted on 13-11-2021.

CVR Journal of Science and Technology, Volume 21, December 2021
DOI: 10.32377/cvrjst2111

II. Literature Review

Praveen Kumar C et al., [1] explained the efficiency of the heart pump is very low (12-20%). Hence, in this paper variation of efficiency is discussed and they are considered the average value of efficiency as 15%. The developed device has three-phase twin axial flow BLDC motors that are inserted symmetrically for balancing the axial pull forces. In order to get a large volume in the pump chamber and lower speed, the pump impellers may be placed in this hole. The motor has a passive magnetic bearing that doesn't involve contact and friction, thus reducing blood damage.

Gregory K. MacLean et al., [2] explained, a comparison between Nickel and Cadmium (Ni/Cd) and lithium battery cells are taken and assembled into a multicell battery pack. In this, they used 2 different rectangular prismatic Ni/Cd cells and 5 different rechargeable lithium battery cells and determined the temperature at 37 °c by charge/discharge cycles.

P J Ayre et al., [3] conducted an experiment and investigated, to consider the effects of non-pulsatile and pulsatile flows utilizing in vitro mock loops, and acute (N=3) and chronic (N=6) ovine experiments. An average flow estimation algorithm was derived from the RMS pump impeller speed and RMS input power by utilising the non-pulsatile and pulsatile mock loops. Using this algorithm, we can estimate the flow effectively in a rotatory blood pump without implanting additional invasive sensors.

Allen Cheng et al., [4] discussed the comparison between the continuous-flow and pulsatile-flow left ventricular assist devices, and explained the disadvantages and advantages of various devices.

R. Basanth, Anil K. Puppala [5] discussed simulation models to achieve pulsatile flow of blood by using different controllers. A combination or hybrid model of PID and fuzzy logic controllers has given a good response with fewer ripples and a lower percentage of peak overshoot in the motor speed.

III. Design of Ventricular Assist Devices

Before knowing the workings of LVAD, the study has been done on the functioning of the heart. The human heart is one of the most important organs in the human body responsible for sustaining life. The human heart is divided into four chambers, namely two ventricles and two atria. The ventricles are the chambers that pump blood, and the atriums are the chambers that receive blood. The right atrium and ventricle make up the right portion of the heart, and the left atrium and ventricle make up the left portion of the heart. The right and the left regions of the heart are separated by a wall of muscle known as the septum. The chambers of the heart work together and relax to pump blood throughout the heart. The shown in figure 1 describes the structure and functioning of the human heart.

After studying the study on the functioning of the heart, the work of Ventricular Assist Devices, which are used to assist the pumping function of end-stage heart failure, is presented. These devices are implanted inside the body and are connected one end is attached to the apex of the left ventricle, this chamber is used to pumps blood out of the heart into the body and the other end is attached to the aorta which is connected as the main artery of the heart which is used to carry the oxygenated blood to the entire other organs body. The structure and functioning of the heart are shown in figure1.

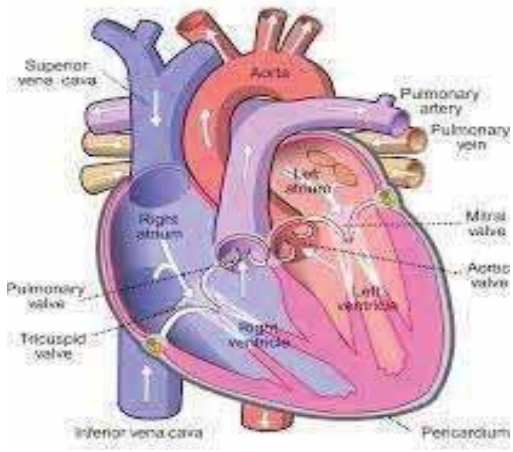

Figure 1. Structure and functioning of the heart.

Blood flows from the heart to the pump. It is continuously sent from the left Ventricle Assist chamber via the apical inflow canal and propelled through a pump housing where the magnetic field generated by a rotatory pump transfers blood through the outflow valve to the ascending aorta. A percutaneously tunnelled driveline connects the pump to the external system controller and power source. The figure shown in 2 shows how left Ventricular Assist Devices are implanted into the human body.

Figure 2. Left ventricular Assist Device connected to the heart with controller and battery assembly

The system's electronic controller is the main component that is placed outside the body. It has both manual and fixed settings that modulate pump speed, and provides signals and alarms that help to operate the system in case there is any malfunction in the device for future analysis. These Ventricular Assist Devices carry 4 to 10L per minute of blood at different speeds. VAD has a centrifugal, pulsatile flow, implantable rotatory pump presently in clinical

CVR Journal of Science and Technology, Volume 21, December 2021
DOI: 10.32377/cvrjst2111

practice. This Ventricular Assist Device operates via a hydro-magnetically levitated rotor without mechanical bearings and can deliver blood up to 4.5 to 5.5L/min through the heart. Firstly, by affording further decrease, this 140g pump can be implanted in the pericardial space, thus eliminating the need for the design of a pump pocket. This small pump size also makes the device more effective for minimally invasive implantation techniques. The absence of mechanical contact within the pump eliminates friction and heat generation which also improves device durability and reliability of the device. Generally, the pump is set at a speed in the range of 2400 to 3200 rpm to allow the blood to pass at a rate of between 3 and 8L/min. The battery packs which power the devices can deliver 4 to 6h of support when fully charged. This battery life span is 6 to 7 years. This cable connects the pump to the batteries through a small hole in the abdomen.

IV. Design of Left Ventricular Assist Devices

A. Internal Structure of LVAD

The structure of LVAD is shown in figure 3. The design of the LVAD must be done in such a way that it must be mini-sized and be able to fit inside the body. The design of LVAD requires different components.
They are;

- Motor
- Pump
- Rotor
- Inlet valves
- Outlet valves
- Impeller units.

The above all are assembling which is used as a covering for these parts of the pump. Before designing the LVAD there is a right to know about how the LVAD internal structure looks like.

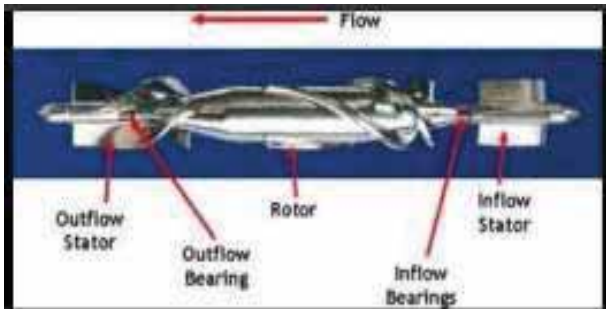

Figure 3. The internal structure of the LVAD pump

Figure 3 represents how the pump of the LVAD looks internally. It consists of an inflow stator from where the blood enters into the input to the pump from the inlet valve. It is attached to the one-end rotor of the motor with a shaft and bearings for smooth rotation of the inflow stator. This inflow stator will rotate when the rotor starts rotating and it is used to manage the flow of the blood inside the pump. After this inlet stator, there is a rotor that is a rotor known as the impeller part of the pump. This impeller unit consists of a blade around it. This impeller unit is used in this system because the impeller is a rotating part of the pump which is able to convert the mechanical energy given by the motor into pump output, which is fluid output by rotation. After the rotor, it consists an outflow stator which is also connected other end to the rotor with the help of outflow bearings. This will allow the blood to flow drive from the pump to the outlet valve.

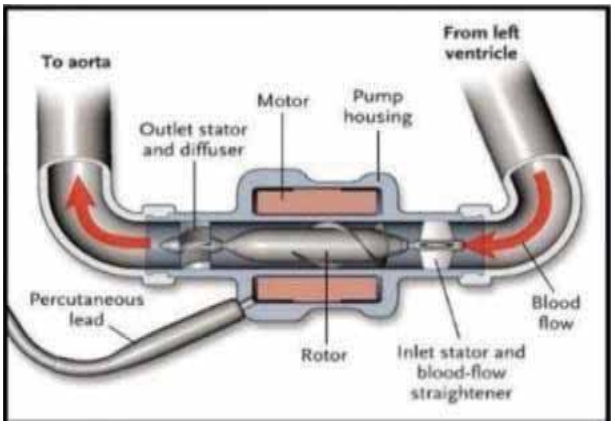

Figure 4. The internal structure of the LVAD with inlet and outlet valves

Figure 4 represents the entire internal structure of the LVAD which has an inlet and outlet stator valve. The inlet valve is connected at the left ventricle from where the rich blood will enter from the right ventricle. From this inlet valve, the blood pumps into the pump of the device. The outlet valve is connected to the Aorta, which is considered as the main artery of the heart, which will deliver rich blood to the entire body. From the output side of the pump, the blood will enter into the outlet stator valve and from there the blood will be pumped into the aorta. This outlet valve is attached to the pump with the help of strain relief. This strain relief is also known as bend relief, is required because it gives mechanical support to the valve when the load is applied to the valve.

B. The Brushless DC Motor

The internal structure of LVAD is discussed in above section A. From the above discussion, it is clear that the pump which is present in LVAD is the main key component in which the motor is present and due to which blood is allowed to flow from the LVAD to the entire body. The motor is an important part of the pump which should be very compact and can be fitted inside the pump. During this left ventricular assist device project, a Brush less DC (BLDC) motor was used. These Brushless DC motors are widely used nowadays in various applications, right from motor vehicles and industrial applications to aircraft for control applications. The main reasons for the increasing usage of brushless DC are less weight, miniature size to power ratio, better acceleration performance, less maintenance and electrical noise compared to a brushed DC motor.

A Brush less DC motor is a type of synchronous motor which is powered by direct current and provides the output in the form of alternating current by different switching signals. The construction of the Brushless DC motor is the same as the permanent magnet synchronous motor. There are many types of DC motors; however, two are common types of DC motors they are brushless DC motor and Brushed DC motor. The Brushed DC motor was invented in

CVR Journal of Science and Technology, Volume 21, December 2021
DOI: 10.32377/cvrjst2111

the 18th century. These DC motors consist of commutators and brushes assembly on the rotor. Due to these brushes, the rotor spin occurs, making contact with the stator, along with the rotating commutator segments, which ultimately causes power losses. They have a low-speed range due to limitations imposed by the brushes, and electromagnetic interference (EMI) generated by brush arcing, which can be significant in a low-power motor. Another disadvantage of a brushed DC motor is the resistance between the surface of the brush and the commutator of the sliding brush contact, which causes a voltage drop in the motor circuit, which is known as brush drop that consumes energy. So, considering the above disadvantages of the brushed DC motor, the common other type of motor is known as the Brushless DC motor (BLDC). These BLDC motors came into existence around the 1960's. The development of semiconductors in the solid-state electronics field allowed us to eliminate the commutator assembly in DC motors.

Figure 5. BLDC motor with Electronic Speed Controller

The figure 5 represents the BLDC motor which is being considered for testing purposes in this study. BLDC motors and synchronous motors are similar in construction and operation. They are powered by DC electricity with the help of an inverter circuit which produces AC electricity as an output which is used to drive each phase of the motor as a closed-loop controller. This controller will provide the current pulses to the motor windings, which will control the speed and torque of the motor. To rotate the BLDC motor, the stator windings must be energized in a sequence. The communication circuit the motor must know the position of the rotor in order to energize it following the correct winding. In order to this BLDC motor, have a hall effect sensor present inside the motor stator part during manufacturing. In a three-phase BLDC motor, typically there are three hall sensors mounted on the stator of the motor. Whenever the rotor magnetic pole moves near the hall sensor, it will produce a signal indicating the passage of a rotor pole near the sensor. Based on these switching of this three-hall effect sensor (from low to high or from high to low) combinations we can determine the position of the rotor information and according to the position, the stator windings are energized.

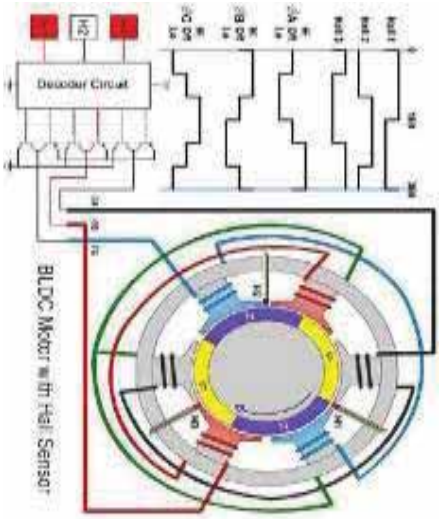

Figure 6. BLDC motor with hall sensors

The figure 6 represents the BLDC motor which is considered for testing purposes in this study. In VADs most commonly used motor is the Brush Less DC motor. This is because BLDC motor has many advantages over compared to other motors and the requirements for VAD's are meet by BLDC motor they are required speed and blood flow rate. This is because the BLDC motor has more advantages over many other motors and the requirements for VAD's are in the range of 15w to 20w. In this study, for testing of the motor, an A2212/1000kV BLDC Brush less DC motor was used, which has a 7V to 12V input voltage and 0.5A of no-load current. From the study of the functioning of the heart, it is clear that the heart must pump blood at 5 to 10liters per minute. The pulsatile flow of blood can be achieved by maintaining constant torque at variable speeds with a motor-pump-waterflow sensor set which is used in TAH and VADs. This is the reason for using BLDC motors in these VAD devices. The BLDC motor has many advantages, like high torque to weight ratio, less noise compared to a brushed DC motor, better acceleration performance, losses are less, increase in reliability, higher efficiency, and a longer lifetime. So, the BLDC motor is the perfect choice for TAHs and VADs.

C. Block Diagram of BLDC Motor with Other Devices

After studying the internal structure of the LVAD, it is clear that it uses the motor inside the pump which is used for the flow of blood through the left ventricle of the heart to the aorta in figure 7 .Before implanting the BLDC motor inside the pump to design the LVAD, the speed of the motor must be controlled by using a microcontroller and verified that when the power supply is given to the motor, it must rotate at the desired speed. This motor speed can be tested by using different components they are Arduino nano, BLDC motor, Potentiometer, Water flow sensor, Batteries, Pump.

E-ISSN 2581 – 7957
P-ISSN 2277 – 3916

DOI: 10.32377/cvrjst2111

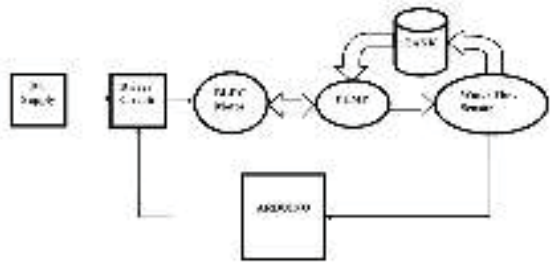

Figure 7. Block diagram of BLDC motor with water flow sensor

D. VAD prototype BLDC motor assembly of the centrifugal pump

In this, a self-designed proto type left ventricular assist device (LVAD) system was used as shown in figure 8. This system consists of a centrifugal blood pump, a BLDC motor, a control device, and a power supply system shown in the below figure.

Figure 9. VAD with centrifugal pump

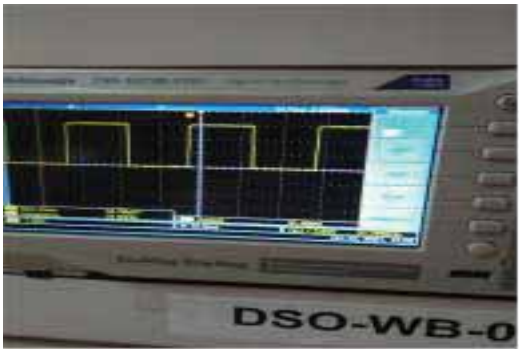

Figure 9. Output wave form view in CRO with pulse width modulation (Time period) of 31.4ms

TABLE I.
SPEED VARIATION WITH FREQUENCY FOR DIFFERENT PULSE WIDTH INPUT VALUES.

Speed (RPM)	Total Time (msec)	On-Time (msec)	Frequency (Hz)	Duty Cycle (t-ON/T)
1100	31.44	13	31.8	0.413
1200	32.76	17	30.5	0.518
1300	33.84	17	29.5	0.502
1400	34.4	17	29.1	0.494
1500	37.64	13	26.6	0.340
1900	49.76	25	20.1	0.502

Figure 9 represents the output wave form view in CRO with a pulse width (Time period) of 31.4ms and table 1 represents the speed variation with frequency for different pulse width input values.

E. Block Diagram of Closed-Loop Control System

From the figure shown below 10, it is seen that how the speed of the BLDC motor can be manually controlled by using a potentiometer and the speed of the motor can be determined by using the water flow sensor. In the below system, there is manual speed control of the motor is considered. But when the motor is used in the design of an LVAD, which is placed inside a person's chest, the speed of the motor must be automatically controlled by using a PID controller to achieve a pulsatile flow of blood.

So, this is the reason the closed-loop control system is considered in this study.

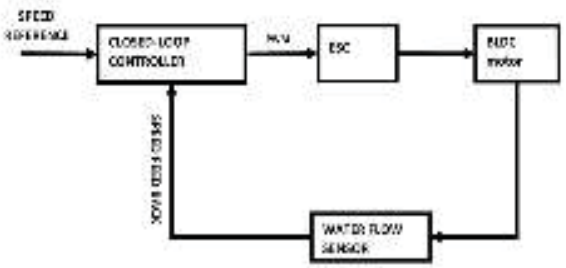

Figure 10. Block diagram for LVAD through BLDC Motor by using a closed-loop control system with a PID controller.

The above figure 10 represents the block diagram for the automatic speed control of the motor by using a closed-loop control system with PID controller. In this block diagram, the components used are the Arduino nano, BLDC motor, Controller (ESC), water flow sensor, and a battery that powers the BLDC motor.

F. Algorithm for Closed-Loop Control System

STEP 1: Set and initialize all the required variables, Input & Output, ARDUINO digital pins to use BLDC motor, Water flow sensor.

STEP 2: Integrate the BLDC motor, Water Flow sensor with ARDUINO and run the motor with initial speed.

STEP 3: Send the reference set speed values as input to the BLDC motor.

STEP 4: Calculate the error, change in error, e-speed previous, e-speed sum, using the flow rate obtained from the water flow sensor.

STEP 5: Pass the error and change error, e-speed previous, e-speed sum values as the inputs to the PID controller.

STEP 6: In PID controller parameters, proportional gain Kp, integral gain Ki, and derivative gain Kd affect the system's overall performance.

STEP 7: Repeat the steps from step three to STEP six until the error is zero or within the specified range.

CVR Journal of Science and Technology, Volume 21, December 2021
DOI: 10.32377/cvrjst2111

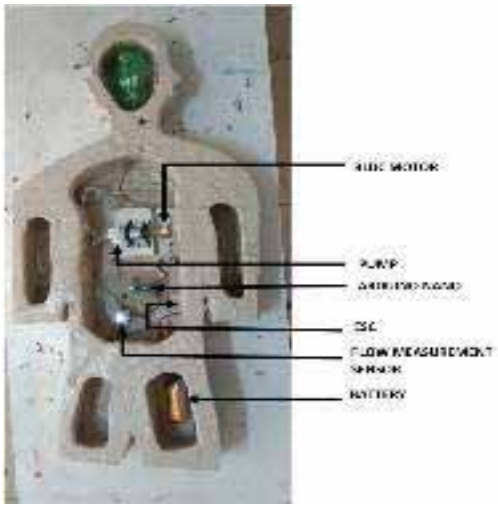

Figure 11. Experimental setup for closed-loop control system

Figure 11 represents the experimental setup of a closed-loop control system. By this setup, the code is written by using Arduino software and dumped in the Arduino nano board and the speed of the motor is varied at different speeds flow rate is recorded and are verified with the previous results.

V. Batteries Used And Energy Transfer In LVAD

The use of lithium-ion batteries has grown significantly in recent years. Lithium is the lightweight metal that has the greatest electrochemical potential and also has the high energy density per weight of all metals that are found in nature. Recently, in a wide range of applications, lithium-ion batteries have been used because their rate of self-discharge is much lower than half of the discharge rate of lead-acid batteries.

Despite the advantages of Lithium-ion, they have certain limitations. These lithium ions are brittle in nature. The batteries to maintain the safe operation, they require a protective device to build into individual battery pack. This protective device is also called a Battery Management System (BMS). This system limits the peak voltage of each cell during charging and prevents the cell voltage from dropping below a threshold during discharging. The BMS is a protective device which also overcharges and discharging currents, over voltage during charging, and monitors the cell temperature. The rechargeable battery pack used for Ventricular Assist Devices should be as small and light weight as possible for easy and effective operation. The use of rechargeable lithium cells in implantable medical devices may yield batteries that are smaller in size, lighter weight, provide more energy, require low maintenance and are environmentally safer than those of NiCad batteries. However, NiCad cells are less preferred than lithium batteries because of their high discharge cycle and longer life cycle. So, in recent studies for giving power supply to LVAD Lithium-ion batteries are more used. Two lithium-ion 14V battery packs were used to give power supply.

These battery packs are connected to the controller external to the body and the controller will supply the power to the motor which is implanted inside the body. In this study, we gave power supply to the motor by using a Lithium-polymer battery rated at 11.1V, 2200mAh, which is a very small size and weight. Various batteries were considered for supplying power to Ventricular assist Devices starting from Battery and external controller transfer energy via a percutaneous lead cable to an implanted VADs.

A. Percutaneous Cable Type Transmission

Percutaneous cables shown in figure 11 are used to transmit power from a source that is located external to the human body and control data between a controller and implantable pumps. These types of cables traverse through the patient's skin and supply power to the implanted motor. But these types of drive lines have many disadvantages, like they have a constant risk of bacterial colonization and infection. There is a high possibility that wired type transmission systems are easy to damage and high infection is the major cause.

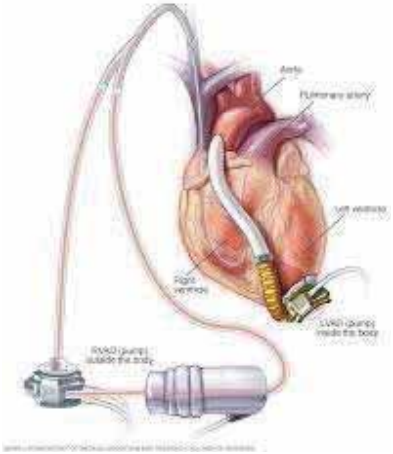

Figure 12. Percutaneous cable type transmission

VI. Experimental Results

This study implemented a closed-loop control system with a PID controller to achieve the pulsatile speed of the BLDC motor and the flow rate of the water flow sensor which is placed inside the pump which is used to design the LVAD.

A. Results obtained from serial monitor of a closed loop system with a PID controller

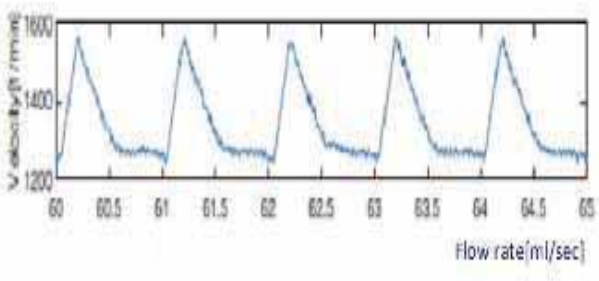

Figure 13. Expected Graph

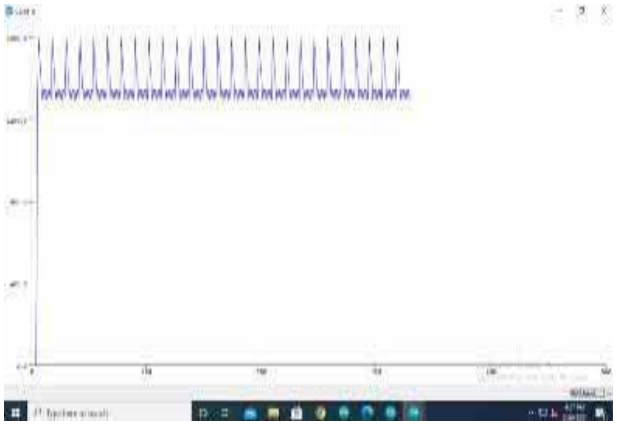

Figure 14. PID Controller Output graph (From Serial Monitor)

Figure 15. Flow rate output (From Serial Monitor)

From the above figures 13,14 and 15, it is observed in the serial monitor outputs that the motor speed and flow rate values vary at certain intervals of time.

So, this is how the speed of the motor can be varied and flow rate obtained by using PID controller from the water flow sensor which is used to design the Ventricular Assist Devices that are used to pump the blood in a pulsatile manner that is shown in figure 14 which represents the normal functioning of the heart. The speed of the motor is varied in a closed-loop control system with PID controller to achieve the blood flow in pulsatile nature. Due to these variations in the speed of the motor the blood which is pumped from the LVAD will resemble the normal heart pumping.

The experimental results for the closed-loop control system with PID controller are obtained for different speeds at different intervals and flow rates and are tabulated as below.

To get the pulsatile flow of blood, these are the speeds considered from the previous results and are used in this work. This work is done by using an Arduino nano through which the closed-loop control system with PID controller operation is done and made to rotate the motor at different required speeds and flow rates of the pump.

TABLE II.
DIFFERENT SPEEDS AT DIFFERENT INTERVALS OF TIME

S. No	Speed (rpm)	Time(sec)
1	1350	0+
2	1650	2
3	1600	4
4	1550	6
5	1500	8
6	1450	10
7	1400	12

TABLE III.
DIFFERENT SPEEDS AT DIFFERENT FLOW RATES

S. No	Speed (rpm)	Flow rate (ml/sec)
1	1350	0+
2	1650	373.33
3	1600	460
4	1550	457.78
5	1500	455.6
6	1450	420
7	1400	64.44

TABLE IV.
DIFFERENT SPEEDS AND FLOW RATES WITH ERRORS

S. No	Speed (rpm)	Flow rate (ml/sec) (S1)	Flow rate (ml/sec) (S1)	Error (S2-S1)
1	1350	0+	0	0
2	1650	373.33	368.02	-5.31
3	1600	460	461.3	1.3
4	1550	457.78	458.86	1.08
5	1500	455.6	456.2	0.6
6	1450	420	423	3
7	1400	64.44	67.06	2.62

These motor speeds, which are varied during specific intervals of time, are plotted in the graph and the graph shown below in figure 16 depicts the obtained output between speed and time.

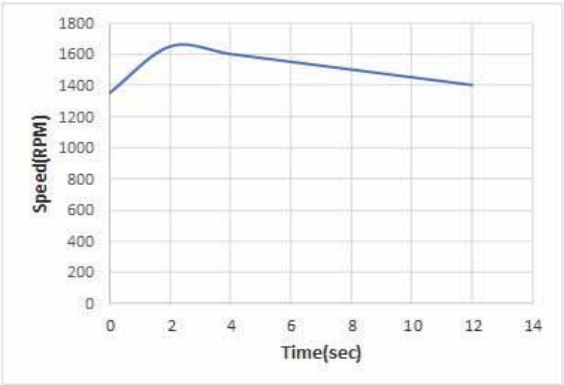

Figure 16. Pulsatile speed is obtained with the BLDC motor by using a closed-loop control system.

The little overshoot in the graph is observed, because initially, the heart is in a contraction state in which the blood is pumped with some pressure of the left ventricle to the aorta. Hence the closed-loop system is set up for starting speed to be high. After that, the heart will move into a relaxation state in which the heart is slowly relaxed. Due to this speed is gradually reduced and made constant.

VII. Conclusions

The pulsatile flow of blood in Ventricular Assist Devices can be achieved by varying the speeds of the motor. The BLDC motor offers a practical solution for VADs because of its weight, dimensions, and simplicity in control of the speed of the motor. Control of the BLDC motor speed can be achieved by using different methods. In this study, the design of a closed-loop control system with a PID controller was used to achieve the various speeds of the motor at different intervals of time. By using this closed-loop with PID controller system pulsatile flow of blood is obtained which resembles the normal functioning of the heart. Although this closed-loop system is easy to implement, it has some disadvantages. If there are no disturbances in the system, this closed-loop system works normally. But if there are any disturbances in the system like communication failure, it will affect the speed of the motor. Because of the disturbances present in the system ripples will form. These ripples may lead to instability flow of blood inside the body. To overcome this type of problem in this project, a PID control program was developed using error and change in error in flow rate to reduce the disturbance. With this control, the normal functioning of the heart is restored. In this way, the closed-loop with PID control system was developed. The closed-loop system with PID control reduces the ripples and smaller peak overshoots in motor speed compared to PI control. So, for the future, we can use a closed-loop control system with hybrid fuzzy with PI, PID control can also use to reduce smaller ripples furthermore effectively.

References

[1] Benedikt A. Pelletier, Yvonne M. Blaszczyk, Patrick Carstens, Gonzalo Alvarez, Felix Lamping, Marco Laumen, Thomas Finocchiaro, and Ulrich Steinseifer on “Novel Optical Position Sensing for Miniaturized Applications and Validation in a Total Artificial Heart” IEEE transaction on biomedical engineering, VOL. 63, NO. 3, MARCH 2016.

[2] James F. Antaki, Richard K. Wampler, Kormos. M. “Mechanical circulatory support. A companion to Heart disease”. Elsevier Saunders 1995.

[3] Leslie mertz on “From artificial kidneys to artificial heart and beyond”;14 IEEE PULSE MAY/JUNE 2012.

[4] SEAN PINNEY.P, on “Left Ventricular Assist Devices: The Adolescence of a Disruptive Technology” Journal of Cardiac Failure Vol. 21 No. 10 2015.

[5] T. Vakhtang, S. Phillips “Update in Artificial Heart Technology: Are We there yet?” Artificial Organs Vol 40., No.12,2016.

[6] Francis D. Pagani on “The quest towards the Holy Grail of mechanical circulatory support”; The Journal of Thoracic and Cardiovascular Surgery, September2015.

[7] R. Basanth, Anil K. Puppala “Considerations for Introducing Pulsatility in Continuous flow Ventricular Assist Devices by Modulation of Motor Speed,” IEEE International Conference on Innovative Technologies in Engineering 2018 (ICITE OU).

[8] Gregory K. MacLean, Peter A. Aiken, William A. Adams, Tofy Mussivand “Comparison of rechargeable lithium and nickel/cadmium battery cells for mechanical circulatory support devices”. ASAIO J 1994; 18:33–4.

[9] E Okamoto, K Tomoda, K Yamamoto, “Development of a compact, highly efficient totally implantable motor-driven assist pump system.” Artificial Organs 1994; 18(12):911–917.

[10] P J Ayre, N H Lovell, J C Woodard “Non-invasive flow estimation in an implantable rotary blood pump: A study considering non-pulsatile and pulsatile flows.” Physiol MEA 2003; 24:179–189.

[11] Allen Cheng, Christine A. Williamitis, and Mark S. Slaughter on “Comparison on continuous flow and pulsatile flow left ventricular assist devices: is there an advantage to pulsatility” Ann Cardiothorac Surg. 2014 Nov.

[12] Puppala A. K., Sonnati, V., & Gangapuram, S. (2020, March). “Additive Manufacturing for VADs and TAHs-a Review.” In Journal of Physics: Conference Series (Vol. 1495, No. 1, p. 12021). IOP Publishing.

[13] Praveen Kumar C, Neeth Antony A on “Designing and Modelling A Ventricular Assistive Device” IOSR Journal of Electrical and Electronics Engineering, Volume 11, April 2016.

[14] S. Takatani, Kazunobu Ouchi, M. Nakamura “Miniature, Totally implantable, permanent, Electromechanical pulsatile VAD system.” ASAIO J 2000 - Volume 46.

[15] William L. Holman, David C. Naftel, Chad E. Eckert, Robert L. Kormos, Daniel J. Goldstein, and James K. Kirklin, on “Durability of left ventricular assist devices: Interagency Registry for Mechanically Assisted Circulatory Support (INTERMACS)”; The Journal of Thoracic and Cardiovascular Surgery. August 2013.

[16] R. Basanth, Anil K. Puppala “Review of power delivery techniques and sources of power for VAD’s and TAH’s,” IEEE international Conference on innovative Technologies in Engineering 2018 (ICITE OU).

E-ISSN 2581 – 7957
P-ISSN 2277 – 3916
CVR Journal of Science and Technology, Volume 21, December 2021
DOI: 10.32377/cvrjst2112

Demand Response Unit Commitment using Modified Hybrid Method in Power System

K. Rajesh[1] and N. Visali[2]
[1]Research Scholar, JNTUA College of Engineering/EEE Department, Ananthapuramu, India
Email: 2016rajesh75@gmail.com
[2]Professor, JNTUA College of Engineering/EEE Department, Ananthapuramu, India
Email: nvisali@gmail.com

Abstract: **This paper presents a new modified hybrid method in predicting the optimal value of the demand response unit commitment optimization problem. Overloading the operation of generators during peak loads is cumbersome. Demand-side management is employed to smoothen the peak loads incorporated with unit commitment followed by dispatching of committed units for minimization of cost and emission. The modified hybrid method makes use of a modified non-dominant sorting genetic algorithm (MNSGA-II) and modified population variant differential evolution (MPVDE) techniques. In price-based demand response, customers are awarded incentives based on their contribution to the demand response program. The proposed modified hybrid method is effectively applied to two test systems.**

Index Terms: **Demand response, unit commitment, economic dispatch, incentives, and peak load.**

I. Introduction

In the present scenario, load demand varies continuously day-to-day and attains the different peak values. Due to variation in load demand, pertinent information is required for turning on/off the committed generating units. The course of action, planning, and selecting generating units over some time in equating load demand is termed unit commitment. Thermal units cannot be turned on/off instantly whenever it is essential to meet the load demand. In a power system, unit commitment is the problem of predicting the on/off states of the thermal units for the minimization of fuel cost value [1]. Unit commitment (UC) is the mixed integer programming, nonlinear and related to the combinatorial optimization problem which is tedious and complex in evaluating the optimal solution [2]. In the unit commitment optimization problem (UCOP) the total cost is the combination of running cost, startup cost, and shutdown cost.

Industrial power generation imposed a great challenge in the environmental regulation, due to pollution caused by the combustion of fossil fuel in thermal units during the power generation. The emission has become another important objective in power dispatch. Multi-Objective unit commitment (MOUC) is associated with two conflicting objectives as cost and emission are subjected to inequality and equality constraints [3]. Many techniques were proposed to achieve an optimal solution of a MOUC. Conventional methods require the exact mathematical modeling and chances of getting stuck in local optima rather than achieving global optimal value [4].

Some of the conventional methods are priority list method [5], branch and cut [6], Benders decomposition [7], Lagrangian relaxation [8], Quadratic programming, Linear Programming, Newton Rhapson implemented to solve economic dispatch (ED) with a piecewise linear cost function. Heuristic methods genetic algorithm [9], simulated annealing [11], particle swarm optimization [10] are used to predict optimal values in a feasible search space. To enhance performance and efficiency, a combination of methods is proposed. Some of the hybrid techniques are Lagrangian relaxation with Particle Swarm Optimization [12], Lagrangian relaxation with Genetic Algorithm [13], and Fuzzy Adaptive Particle Swarm Optimization [14].

Demand Response (DR) point-outs reshaping the demand curve by shifting load to off-peak periods or by reducing the load at peak periods [15]. Demand Response Programs (DRPs) offer customers to change their energy consumption in their demand response. Customers are encouraged by electricity pricing signals with associated network operators [16]. In general, DRPs are of two types, time-based rate programs, and incentive-based programs, these two categories are divided into further subgroups. In the incentive-based program (IBP), fascinated by the emergency demand response program (EDRP) in which incentives are offered to the customers by independent system operators (ISO) based on their contribution to DRPs. Voluntary customer participation is involved in DRPs and supported by ISO for enhancement of the participation of customers [17]. DRPs incorporated with UC are modeled to study environmental and economic dispatch [18] and include the cost of DR in total cost. Based on the robust optimization technique, day-ahead unit commitment with economic power dispatch is presented [19]. Implementation of demand response not only leads to diminishing loads in peak times but also reduces the need for new installation of generating units [27]. With the association of demand-side management in power systems, the effective utilization of energy takes place with efficient power system operation [26].

In this paper, Demand response is incorporated with unit commitment, with the percentage participation of customers in DRPs leads to a reduction in peak loads. Incentives are awarded to customers based on their participation followed by the unit commitment for dispatch of power over a period for the minimization of cost and emission. The modified hybrid method is applied for the optimization problem of DRUC in achieving the optimal value. The proposed method was applied on two test cases, IEEE 39 bus system with 10 generators and a 17 unit system. Section II discusses the problem formulation of MOUC and DR in section III, the methodology applied for solving the optimization problem is

Received on 10-05-2021, Revised on 03-07-2021, Accepted on 28-08-2021

CVR Journal of Science and Technology, Volume 21, December 2021
DOI: 10.32377/cvrjst2112

presented, and section IV presents the results and discussion applied on test systems.

II. Problem Formulation

A. Objective function

The two conflicting objectives, cost, and emission are considered and the corresponding objective function is represented. The total cost is the sum of running cost, startup cost, and repayment cost associated with customers implemented and its objective function is as follows

$$\min \sum_{x=1}^{M} \sum_{y=1}^{T} [F_x(P_{g_x}(y)) + SUC_x(1 - U_x(y-1))] U_x(y) + R_c(y) \quad (1)$$

where T equates to 24 hours' time period and M initiates to the number of generators and on/off status generating units is indicated as Ux. The quadratic form of the cost function is represented a

$$F_x(P_{g_x}(y)) = a_x + b_x P_{g_x}(y) + c_x P_{g_x}^2(y) \quad (2)$$

where $P_{g_x}(y)$is the real power generation of unit 'x' at time instant of 'y' and a_x, b_x, c_x indicates the cost coefficients. The start-up cost is expressed as

$$SUC(x) = \begin{cases} HC(x), & if\ MD(x,y) \le TC(x) \le MD_{yo} \\ CSC(x), & if\ TC(x) > MD_{yo} \end{cases} \quad (3)$$

where $MD_{yo} = MD(x,y) + CST(x)$

CSC and HC are the cold startup cost and hot startup of unit 'x', minimum downtime of unit 'x' is represented as MDx, off duration of unit 'x' is TC(x). Incentives awarded for customers in DRPs is expressed as

$$R_c(y) = \sum_{y=1}^{24} MI * \left(T_{c,y}^{in} - T_{cc,y}\right)^2 \quad (4)$$

Multilevel incentives awarded in cents/kw.min are indicated as MI. The repayment fee awarded to the customer 'c' at hour y is represented as $R_c(y)$. $T_{c,y}^{in}$ represents the indoor temperature of customer 'c' at hour y and $T_{cc,y}$ indicates a comfortable temperature of customer 'c' at hour y. The secondary objective function, emission can be expressed in terms of a quadratic form

$$E_x(P_{g_x}(y)) = d_x + e_x P_{g_x}(y) + f_x P_{g_x}^2(y) \quad (5)$$

emission coefficients of unit 'x' are represented as d_x, e_x, f_x and the corresponding constraints of unit commitment are

1. Power balance constraint

Real power generation from the thermal plants has to meet the demand which equals the power balance constraint.

$$\sum_{x=1}^{M} P_{g_x}(y).U_x(y) = d_o(y) \quad (6)$$

2. Generation Range

The real power generated from thermal units has to be maintained within limits of maximum and minimum generation.

$$P_{g_{x,min}} \le P_{g_x} \le P_{g_{x,max}} \quad (7)$$

where $P_{g_{x,min}} P_{g_{x,max}}$ are the minimum and maximum power generation limits of thermal units.

3. Spinning reserve

Maintaining the spinning reserve capacity of a system can be expressed as

$$\sum_{x=1}^{M} P_{g_x}(y).U_x(y) \ge d_o(y) + SR(y) \quad (8)$$

Spinning reserve at y hour is indicated as $SR(y)$

4. Minimum up and downtime

ON/OFF time of each thermal unit can be expressed as

$$X_{x,on} \ge MUT_x \quad (9)$$
$$X_{x,off} \ge MDT_x \quad (10)$$

where $X_{x,off}$ and $X_{x,on}$ is the off/on duration of unit 'x' and MDT_x and MUT_x are the minimum downtime and uptime of unit 'x'.

B. Economic Demand Model

The price elasticity model can be expressed

$$E = \frac{\partial d}{\partial \rho} = \frac{\rho_o}{d_o} \cdot \frac{dd}{d\rho} \quad (11)$$

where ρ_o is the electricity price ($) initially, d_o is the initial demand (MW)

1. Modelling of Multi period

Cross elasticity among y^{th} and j^{th} hour

$$E(y,j) \le 0\ if\ y = j$$
$$E(y,j) \ge 0\ if\ y \ne j$$

The function of linearity that indicates demand variation to price variation as

$$d(y) = d_o(y) + \sum_{y=1}^{24} E(y,j) \frac{d_o(y)}{\rho_o(y)} [\rho(y) - \rho_o(y)] \quad (12)$$

At hour y the demand function with incentives are expressed as

$$d(y) = d_o(y) + \sum_{y=1}^{24} E(y,j) \frac{d_o(y)}{\rho_o(y)} [\rho(y) - \rho_o(y) + I(y)] \quad (13)$$

2. HVAC appliance modeling

Load aggregators are crucial in making end-users participate in DRPs with their HVAC appliances. Based on

CVR Journal of Science and Technology, Volume 21, December 2021
DOI: 10.32377/cvrjst2112

the measure of comfort, the end user's HVAC is controlled. A close relationship between temperature and time of an HVAC unit is expressed as

$$T_{in}^{y+1} = T_{out}^{y+1} - (T_{out}^{y+1} - T_{in}^{y})\varepsilon; \quad s = 1 \tag{14}$$

$$T_{in}^{y+1} = T_{out}^{y+1} - \eta P_y / A - (T_{out}^{y+1} - \eta P_y / A - T_{in}^{y})\varepsilon : s = 0 \tag{15}$$

where T_{in}^{y+1} T_{in}^{y} are the room temperatures at y+1 and y hours, T_{out}^{y+1} , T_{out}^{y} are the ambient temperatures at y+1, y hours. 's' indicates the on/off status of the HVAC unit which is a controllable variable. 'ε' is the coefficient of heat dissipation and 'A' is the thermal conductivity coefficient. 'η' is the HVAC efficiency ratio and P_y rated real power at hour 'y'. The range of temperature over which the customers have to maintain their indoor temperature within the maximum and minimum temperature is indicated as T_{max} and T_{min}. Based on the supporting participation of customers in DRPs the incentives are awarded to the end-users. Over the range of temperature, the contribution of customers are awarded multilevel incentives and load balancing services are incorporated with baseline

$$M = \begin{cases} I_1 & if\ T_{min} \le T_{in} \le T_{max} \\ I_2\ if\ T_{in} \ge T_{max}\ and\ T_{in} \le T_{min} : Com = 1 \\ I_3\ if\ T_{in} \ge T_{max}\ and\ T_{in} \le T_{min} : Com = 0 \end{cases} \tag{16}$$

Based on the requirement of load reduction at peak periods utilities enforces the load aggregators to allow the customers to participate in DRPs with HVAC appliances. Load aggregators collect the customer's participation, in blocking off their HVAC unit or not based on their consolation. End-users maintaining the indoor temperature within the range of set point will be awarded I_1 and I_2 awarded for the customers who are violating the range of set point and compromise in blocking off their HVAC unit. Only under emergencies, I_3 will be awarded to the customers who don't compromise to turn off their HVAC unit, so to participate in DRPs this is a very rare case. Customers awarded with I_3 have to give up the opportunities of I_2 and I_1 in any situation. Customers violating the agreement and unfair for the participation of customers will not be penalized or punishable.

III. METHODOLOGY

A. Modified hybrid method

In this Modified hybrid method (MHM), both NSGA-II and PVDE are modified to achieve a better optimal solution than compared with a hybrid method (HM). MHM is employed for DRUC optimization problem to achieve optimal value with better diversity and the procedure is as follows

a) Initial parameters: population size, number of objectives, number of iterations, emission and cost coefficients, and decision variables are initialized.

b) Random generation of the parent population is generated which has maintained both equality and inequality constraints represented in equation (6) and (7).

c) Evaluate the cost and emission function values which indicate strength using equation (2) and (5)

d) With the application of MNSGA-II for fifty percent of the parent population, the non-dominant sorting, crowding distance, and ranking-based techniques are applied.

e) Binary crossover, and polynomial mutation takes place for the production of half the child population with the bisection of the parent population.

f) Remaining fifty percent of parent population is applied with MPVDE, in which interquartile [20] is replaced with a coefficient of quartile deviation associated with semi quartile range and mid quartile range for the refreshment of the population at the initial stage.

$$\text{Var} = \frac{P_1 - P_2}{P_1 + P_2} \tag{17}$$

Where P_1 and P_2 are the semi interquartile range and mid quartile range

P_1 = (high quartile - low quartile)/2;

P_2 = (high quartile + low quartile)/2;

g) The same sequence is applied in MPVDE as that of MNSGA-II in the initial stage followed by genetic operations for the production of the other fifty percent child population.

h) The two-child populations are combined to form a child population of original population size and combined with parent population of original population size.

i) From the twice original population best population of original size is selected based on Euclidean distance

$$D_{a,b}^{i} = (\sqrt{\sum_{m=1}^{n}(d_m^a - d_m^b)^2})/(n-1) \quad ; \text{i=1, 2, 3....} \tag{18}$$

If Ni > N then the best fitness population members are selected. If Ni < N then a new random population is generated which should lie in the range of Euclidean distance. Where N is the original size of the population, Ni is the total number of population combinations of parent and child population.

j) The process repeats until the maximum iteration is reached.

k) The best optimal value is selected based on the concept of fuzzy set theory.

IV. RESULS AND DISCUSSION

The MHM is applied to two test cases. Case 1 is applied to IEEE 39 bus with 10 generating units and case 2 is related to the 17 units system. In these test cases, the DRUC optimization problem is implemented for achieving an optimal value with inequality and equality constraints. A MATLAB program was developed using the operating system Windows 10.

Case1: In this case study, the DRUC problem was solved using a modified hybrid method which is the combination of MNSGA-II and MPVDE. The cost and emission coefficients, maximum and minimum generation limits [21], demand and price values [22] are considered. Participation of percentage customer compromise is considered in DRPs

i.e. 50, 80, and 100 percent is implemented in DRUC. Percentage of customer compromise represents maintaining room temperature within the prescribed limits of T_{max} and T_{min}. Without DRPs the scheduling of thermal units over 24 hours with a time horizon of one hour is shown in table 1.

The associated total cost and emission values are 565347.8 ($) and 44370.28(lb). Over the peak load, all the units are committed to power dispatch of load demand. The total cost and emission values are high in comparison with other load hours. The demand curve is shown in figure 1. With the incorporation of 50 percent customer compromise in DRPs, the total cost at peak load was diminished from 33950.162($) to 33902.89($) with miniature variation in emission values which can be observed in table 2. With the incorporation of DR with UC, change in load demand, cost, and emission values are encountered. The reduction in demand over the peak loads with the participation of customers in DRPs with fifty percent compromise is shown in figure 2.

Enhancement percentage of customer compromise in DRPs leads to an increase in the reduction of demand. The corresponding values of 50 percent customer compromise running cost, startup cost, repayment, total cost, and emission values are shown in table 2. The reduction in total cost and emission is 0.0087, 0.028 percent in comparison without DRPs. Figure 3 shows incentives awarded to the customers over the peak hours. Multilevel incentives are awarded to the end-users based on their contribution to DRPs. Incentives I_1, I_2, and I_3 are awarded a based range of room temperature.

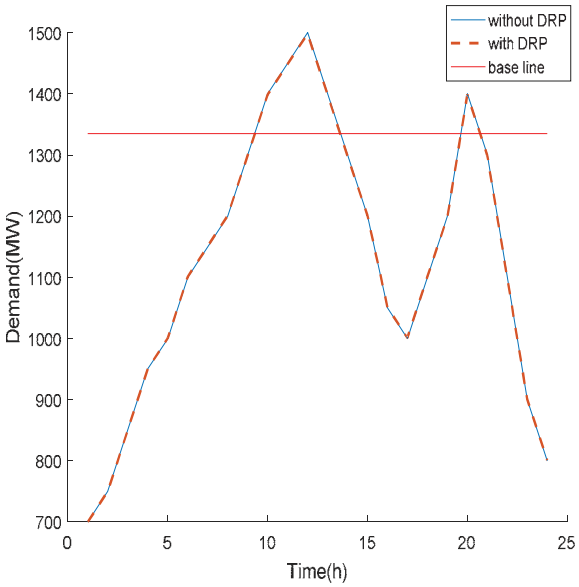

Figure 1. Load curve of IEEE 39 bus system

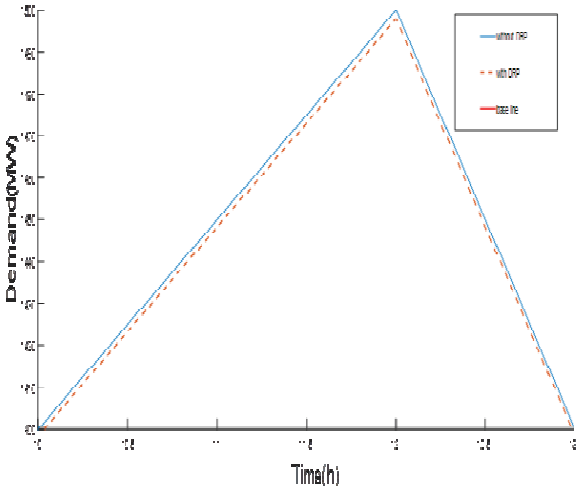

Figure 2. Peak load curve with and without DRPs

Case 2: In this case study of 17 unit system, the emission values are considered based on the strategy followed in [23], and the corresponding fuel cost coefficients and startup cost values are considered [24]. Parameters are initialized initially, population size 80, a maximum number of iteration was 100, and crossover and mutation values are 0.90 and 0.01. The load curve is shown in figure 4 with two peak load values. Figure 5 illustrates the repayment award for the end-users for the 100 percent customer's compromise participation in DRPs. The respective running cost, startup cost, repayments, emission, the total cost of the 17 unit system with 100 percent customer compromise is shown in table 3.

Comparison of 50 percent, 80 percent, and 100 percent end-user compromise of IEEE 39 bus system with 10 units using a hybrid method and modified hybrid method is shown in table 4. With the modification in NSGA-II and PVDE as a consequence, there is a reduction in emission followed by enhancement in percentage compromise reduction in running cost and total cost and fixed startup cost. The reduction in emission value with the modified hybrid method is 0.363 percent in comparison with the hybrid method. The running fuel cost and emission values are reduced in comparison with the hybrid method shown in table 5. Over 50, 80, and 100 percent compromise of end-users there is a corresponding reduction in all the parameters except startup cost illustrated in table 5. The startup cost is low in a hybrid method in comparison with a modified hybrid method.

V. CONCLUSIONS

The modifications in both NSGA-II and PVDE applied on IEEE 39 bus system and 17 unit system emphasize a reduction in emission value. The reduction in running cost, total cost, and emission is the enhancement percentage of customer participation in DRPs. The associated startup cost value is lower in a hybrid method in comparison with the proposed one. Participation of end-users in DRPs is beneficial to customers with the repayment,

CVR Journal of Science and Technology, Volume 21, December 2021
DOI: 10.32377/cvrjst2112

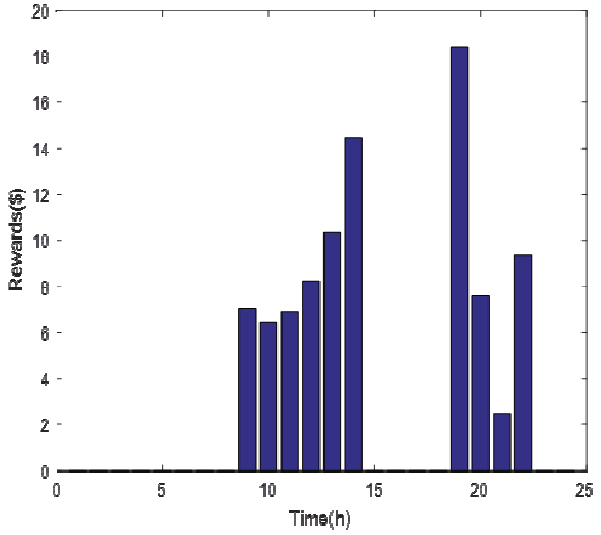

Figure 3. Reward Vs time for 50 percent customer compromise

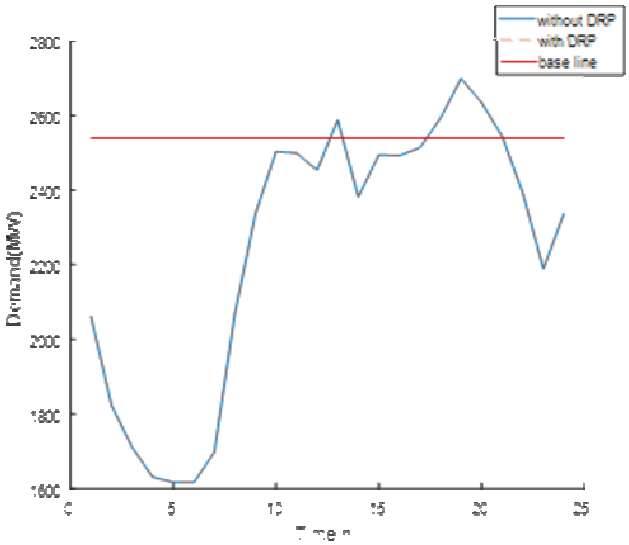

Figure 4. Load curve of the 17 unit system

as well as utilities for the demand reduction, total cost, and emission. With incorporation of DRPs with UC additional establishment of new generating unit is not required.

An ample of opportunities are available for the participation of customers DRPs in various categories. The proposed method has inferred that variation in NSGA-II and PVDE leads better optimal value compared with a hybrid method

TABLE I.
SCHEDULING OF COMMITTED THERMAL UNITS FOR 24 HOURS

S.No	PG1 (MW)	PG2 (MW)	PG3 (MW)	PG4 (MW)	PG5 (MW)	PG6(MW)	PG7 (MW)	PG8 (MW)	PG9 (MW)	PG10 (MW)	Total cost ($)	Emission (lb)
1	455	245	0	0	0	0	0	0	0	0	13683.129	956.39
2	455	295	0	0	0	0	0	0	0	0	14554.499	1055.03
3	455	370	0	0	25	0	0	0	0	0	17709.448	1270.793
4	455	455	0	0	40	0	0	0	0	0	18597.667	1558.926
5	455	390	130	0	25	0	0	0	0	0	20601.160	1556.594
6	455	360	130	130	25	0	0	0	0	0	23507.044	1552.705
7	455	410	130	130	25	0	0	0	0	0	23261.979	1704.245
8	455	455	130	130	30	0	0	0	0	0	24150.340	1863.089
9	455	455	130	130	85	20	25	0	0	0	28111.056	2191.277
10	455	455	130	130	162	33	25	0	10	0	30135.859	2618.669
11	455	455	130	130	162	73	25	10	10	0	31976.061	2945.212
12	455	455	130	130	162	80	25	43	10	10	33950.162	3229.393
13	455	455	130	130	162	33	25	10	0	0	30057.550	2599.17
14	455	455	130	130	85	20	25	0	0	0	27251.056	2191.277
15	455	455	130	130	30	0	0	0	0	0	24150.340	1863.089
16	455	310	130	130	25	0	0	0	0	0	21513.659	1424.165
17	455	260	130	130	25	0	0	0	0	0	20641.824	1318.625
18	455	340	130	130	25	20	0	0	0	0	23025.552	1520.623
19	455	415	130	130	25	20	25	0	0	0	25601.600	2004.263
20	455	455	130	130	162	33	25	10	0	0	30117.550	2599.17
21	455	455	130	130	85	20	25	0	0	0	27251.056	2191.277
22	455	360	130	130	25	0	0	0	0	0	22387.044	1552.705
23	455	420	0	0	25	0	0	0	0	0	17684.693	1426.932
24	455	345	0	0	0	0	0	0	0	0	15427.419	1176.67
											565347.8	44370.28

CVR Journal of Science and Technology, Volume 21, December 2021
DOI: 10.32377/cvrjst2112

TABLE II.
50 PERCENT CUSTOMER COMPROMISE OF IEEE 39 BUS WITH 10 UNITS

Fuel cost	SUC	Reward ($)	Total cost ($)	Emission (lb)
13690.73	0	0	13690.73	957.1515
14562.79	0	0	14562.79	1056.078
16817.78	900	0	17717.78	1272.171
18608.89	0	0	18608.89	1559.299
20060.79	550	0	20610.79	1558.288
22398.01	1120	0	23518.01	1554.463
23274.07	0	0	23274.07	1706.497
24165.26	0	0	24165.26	1863.525
27231.5	860	7.006	28098.51	2190.281
30021.34	60	6.468	30087.81	2598.217
31874.84	60	6.906	31941.74	2943.56
33834.67	60	8.226	33902.89	3229.396
30023.19	0	10.345	30033.53	2598.265
27215.41	0	14.436	27229.85	2189.467
24173.76	0	0	24173.76	1863.775
21531.83	0	0	21531.83	1426.607
20659.16	0	0	20659.16	1320.501
22874.93	170	0	23044.93	1523.531
25307.52	260	18.392	25585.92	1997.847
30027.86	60	7.611	30095.47	2598.387
27234.59	0	2.477	27237.07	2190.437
22366.47	0	9.357	22375.83	1549.416
17705.62	0	0	17705.62	1430.944
15446.16	0	0	15446.16	1179.531
561107.176	4100	91.228	565298.40	44357.632

TABLE III.
100 PERCENT CUSTOMER COMPROMISE OF 17 UNIT SYSTEM

Fuel cost	SUC	Reward ($)	Total cost ($)	Emission (lb)
37036.25	0	0	37036.25	37036.25
30736.1	0	0	30736.1	30736.1
28587	0	0	28587	28587
26741.44	0	0	26741.44	26741.44
26422.78	0	0	26422.78	26422.78
26401.13	0	0	26401.13	26401.13
28954.44	2650	0	31604.44	28954.44
36890.48	1489	0	38379.48	36890.48
43569.26	1201	0	44770.26	43569.26
48147.86	6659	0	54806.86	48147.86
48043.52	0	0	48043.52	48043.52
46827.4	0	7.006	46834.4	46827.4
50058.65	3334	4.088	53396.73	50058.65
44451.23	0	2.245	44453.47	44451.23
47646.03	2870	1.519	50517.55	47646.03
47594.13	0	1.950	47596.08	47594.13
48074.97	0	18.392	48093.36	48074.97
50158.08	3789	11.824	53958.9	50158.08
53035.07	632	6.233	53673.31	53035.07
51339.68	0	2.637	51342.32	51339.68
49224.4	0	3.652	49228.05	49224.4
45268.44	0	0	45268.44	45268.44
40219.68	0	0	40219.68	40219.68
43565.66	500	0	44065.66	43565.66
998993.67	23124	59.549	1022177.22	998993.67

TABLE IV.
COMPARISON OF COST AND EMISSION VALUES OF IEEE39 BUS SYSTEM WITH 10 THERMAL UNITS

customer	Modified hybrid method				Hybrid method [25]			
	Running cost	SUC	Total cost	Emission	Running cost	SUC	Total cost	Emission
50%	561107.1765	4100	565298.4052	44357.63262	559756.100	4090	563937.329	44519.50893
80%	561105.818	4100	565283.366	44354.99385	559755.6	4090	563923.1	44516.37
100%	561103.1788	4100	565263.8923	44352.2432	559754.624	4090	563905.338	44512.810

TABLE V.
COMPARISON OF COST AND EMISSION VALUES OF 17 UNIT SYSTEM

customer	Modified hybrid method				Hybrid method [25]			
	Running cost	SUC	Total cost	Emission	Running cost	SUC	Total cost	Emission
50%	999015.555	23124	1022256.853	999015.555	999996.792	17798	1017912.09	999996.792
80%	999005.389	23124	1022220.823	999005.389	999986.080	17798	1017875.514	999986.080
100%	998993.679	23124	1022177.229	998993.6798	999955.194	17798	1017796.472	999955.194

REFERENCES

[1] Bhardwaj, NS. ung, Shukla VK and Kamboj VK "The important impacts of unit commitment constraints in power system planning". Int J Emerg Trends Eng Dev 5(2):301–306, 2001.

[2] CAA Rajan, MR Mohan and K Manivannan, "Neural-based tabu search method for solving unit commitment problem". In: Proceedings of an international conference on power system management and control (conference on publication no. 488), London, pp 180–185, 2002.

[3] K. Chandrasekaran and S.P. Simon, "Multi-objective unit commitment problem with reliability function using fuzzified binary real coded artificial bee colony algorithm," in IET Generation, Transmission & Distribution, pp: 1060-1073, 2011.

[4] V. Kumar and SK Bath, "Single area unit commitment problem by modern soft computing techniques". Int J Enhanc Res Sci Technol Eng 2(3). ISSN: 2319-7463, 2013.

[5] G. Osórioa, J. Lujano-Rojasa, J. Matiasa and J. Catalão, "A new scenario generation-based method to solve the unit commitment problem with high penetration of renewable energies". International Journal of Electrical Power & Energy Systems, 64: 1063-1072, 2015.

[6] J. Alemany, F. Magnago, D. Moitre and H. Pinto, "Symmetry issues in mixed-integer programming based Unit Commitment". International Journal of Electrical Power & Energy Systems, 54: 86-90, 2014

[7] R. Jiang, J. Wang and Y. Guan, "Robust unit commitment with wind power and pumped storage hydro," IEEE Transactions on Power Systems, 27(2): 800-810, 2012.

[8] Q. Jiang, B. Zhou and M. Zhang, "Parallel augment Lagrangian Relaxation method for transient stability constrained unit commitment," IEEE Transactions on Power Systems, 28 (2): 1140–1148, 2013.

[9] A. G. Bakirtzis and V. Petridis, "A genetic algorithm solution to the unit commitment problem," IEEE Trans. Power Syst., vol. 11, no. 1,pp. 83– 92,Feb. 1996.

[10] Boniface O. Anyaka, J. Felix Manirakiza, Kenneth C. Chike Prince and A. Okoro, " Optimal unit commitment of a power plant using particle swarm optimization approach" Int J Elec & Comp Eng, Vol. 10, No. 2, April 2020 : 1135-1141.

[11] K.P. Wong and C.C. Fung, "Simulated Annealing based Economic Dispatch Algorithm," Proc. Inst. Elect. Eng., Gen., Transm. And Distrib., vol. 140, no. 6, pp. 509-515, Nov. 1993

[12] X. Yu, and X. Zhang, "Unit commitment using Lagrangian relaxation and particle swarm optimization," Int. J. Elect. Power Energy Syst., vol. 61, pp. 510-522, Oct. 2014.

[13] C. P. Cheng, C. W. Liu and G. C. Liu, "Unit commitment by Lagrangian relaxation and genetic algorithm", IEEE Trans. Power App. Syst., vol.15 no. 2, pp. 707–714, May 2000.

[14] A.Y. Saber, T. Senjyu, A. Yona and T. Funabashi, "Unit commitment computation by fuzzy adaptive particle swarm optimization", IET, Gener. Transm. Distrib. vol. 1, no. 3, pp. 456-465, May 2007

[15] T. Broeer, "Analysis of Smart Grid and Demand Response Technologies for Renewable Energy Integration: Operational and Environmental Challenges". Ph.D. Thesis, University of Victoria, Victoria, BC, Canada, 2015.

[16] V.S. Tabar, M.A. Jirdehi, and R. Hemmati, "Energy management in microgrid based on the multi-objective stochastic programming incorporating portable renewable energy resource as a demand response option". Energy, 118, 827–839, 2017.

[17] H. Aalami, G. R. Yousefi, and M. Parsa Moghadam, "Demand Response Model Considering EDRP and TOU Programs", accepted for presentation in IEEE/PES Transmission and Distribution Conference & Exhibition, 2008, Chicago, USA.

[18] A. Abdollahi, M. Moghaddam, M. Rashidinejad, and M.K. Sheikh-El- Eslami, "Investigation of economic and environmental –driven demand response measures incorporating UC," IEEE Trans Smart Grid, vol. 3, pp. 12-25, March 2012.

[19] A. Street, F. Oliveira, and J.M Arroyo, "Contingency-constrained unit commitment with N-K security criterion: a robust optimization approach", IEEE Trans. Power Syst., 2011, 26, (3), pp. 1581–1590.

[20] R. Swain, P. Sarkar, K.C. Meher, and CK. Chanda., "Population variant differential evolution based multiobjective economic emission load dispatch," Int Trans Electr Energ Syst., vol. 27, no. 10, pp. 1-25, Apr. 2017.

[21] Li Y, Pedroni and N, Zio E "A memetic evolutionary multi-objective optimization method for environmental power unit commitment". IEEE Trans Power Syst 28(3):2660–2669, 2013.

[22] K. Selva, K. Vijaya kumar and CS. Boopathi "Demand response unit commitment problem solution for maximizing generating companies profit", Energies 10:1465, 2017.

[23] Aghaei J, Alizadeh M "Critical peak pricing with load control demand response program in the unit commitment problem". IET Gener Trans Distrib 7(7):681–690, 2013.

[24] Dillon D, Walsh MP, Malley MJ "Initialisation of the augmented Hopfield network for improved generator scheduling". IEE Proc Gener Trans Distrib 149(5):539–599, 2002.

[25] Rajesh K, Visali N. "Aggregation of Unit Commitment with Demand Side Management". J. Electr. Eng. Technol. 16, 783–796, 2021.

[26] Deepika. B, Dr R. Vijay. "Energy management of stand-alone hybrid generation system", Vol 19 No 1 (2020): CVR Journal of Science and Technology.

[27] R Vijay, "Optimal allocation of electric power distributed generation on distributed network using elephant herding optimization technique", Vol 15 (2018): CVR journal of science and technology.

E-ISSN 2581 – 7957
P-ISSN 2277 – 3916

CVR Journal of Science and Technology, Volume 21, December 2021
DOI: 10.32377/cvrjst2113

A Novel Approach to Vocalize the Hand Gesture Movement for Speech Disabled

S. Harivardhagini
Professor, CVR College of Engineering / EIE Department, Hyderabad, India
Email: harivardhagini@cvr.ac.in

Abstract: **Mute People use sign language to communicate with each other. They face a problem to communicate with people who can hear and talk. Gesture Vocalizer is a device which reduces the barrier of communication between the mute community and the people not familiar with the concept of sign language, so that the messages that a mute person is trying to relay is understandable to a person with no knowledge of sign language. The aim of this paper is to show how a hand gesture vocalizer can be implemented using Proteus Software. This is a boon to people who suffer from MUTISM. Gesture vocalizer is a prototype made for a social purpose. We know that it is very difficult for deaf people to communicate with normal people. Deaf people communicate with hand gestures, and it is difficult for other people to understand their sign language. Gesture vocalizer is a device which detects the gestures of a deaf and mute person and displays the corresponding output on the virtual terminal. The main objective of this paper is to reduce the communication gap between communicative people and the mute community. It helps the mute community to be independent. A prototype is developed, and simulation is carried out using Flex sensors, an accelerometer, dynamic time warping, an Arduino Uno board, and an output device. The input to be converted is initiated through the Flex. This is given as input to Arduino. Using Dynamic Time Warping technique, a corresponding analog signal is generated and measured. This mapping is done using distance matrix. Later, optimal analog signal is converted into the digital signal. The Arduino module displays on android screen the digital equivalent of the flex and the gesture name associated with the digital value. The Bluetooth module on Arduino board gets connected to the android based mobile phone and converts the text into speech.**

Index Terms: **MUTISM, Gesture Vocalizer, Flex sensors, Dynamic Time Warping, Hand gesture vocalizer**

I. INTRODUCTION

Communication is the most basic and important form of interaction with anyone. Thus, for interfacing with deaf and dumb people, sign language or gestures are used. The mute people use their standard sign language which is not easily comprehensible by communicative people. Also, there is no standardized sign language defined across the world. The people who are having hearing and speaking inabilities are not able to work effectively with other people. Vocalizers convert the sign language into voice which is easily understandable by blind [9] and abled people. Gesture vocalizer is a device which is being designed to enable the communication around the dumb, deaf, and blind societies and their communication with abled people. The gesture Vocalizer project uses Flex sensors, Accelerometer, Arduino, and Bluetooth module to realize hand gestures [8],[10] and convert them to speech. The mute community use Sign Language for communication. A communication Gap exists between Communicative Person and them. Gesture vocalizer tries to reduce communication gap [11] between deaf people and hearing people. Deaf people make use of sign language or gestures to make understand what he/she is trying to say but it is impossible to understand by hearing people. Pablo Bonet paper [13] is considered the first modern treatise on phonetics and speech therapy, setting out a method of oral education for deaf children by means of the use of manual signs, in the form of a manual alphabet to improve communication with the deaf. It is suggested that Pedro Ponce de León developed the first manual alphabet from which Juan Pablo Bonet based his writings. This paper systematically reviews various efforts made in the Gesture Vocalization Design to strengthen its efficacy and exploitability. The review is made on nearly 30 research articles published in the leading journals of technology in the last 15 years. It also puts forth the architectural details of Gesture Vocalizer derived from literature. The articles are accessed by searching for articles with the keywords "Gesture Vocalizer", “American Sign Language”, “Flex Sensor” and “Accelerometer. According to the World Health Organization (WHO), 466 million people across the world have hearing loss (over 5% of the world’s population), of whom 34 million are children [12]. Statistics released by the United Nations also indicate that, in Egypt alone, 7.5 million people suffer from deafness or hearing impairment. Studies expect these numbers to rise to 900 million by 2050. There are about 137 sign languages [14]. American Sign Language (ASL) is a natural language that serves as the predominant sign language of Deaf communities [15] in the United States and most of Anglophone Canada.

II. LITREATURE SURVEY

P.Vijaylakshmi, M Aarthi [1] proposed “Sign language to speech conversion”. Flex sensor-based gesture recognition module is developed to recognize English alphabets and few words, and a Text-to Speech synthesizer based on HMM is built to convert the corresponding text. The number of gestures that can be converted to speech here is limited. Amiya Kumar Tripathy, Dipti Jadhav, S. A. Barreto, Daphne Rasquinha, Sonia S. Mathew [2] proposed "Voice for the Mute (VOM)" aims to develop a system that will take real time images and convert them to speech with text as an intermediate taking into considerations all the limitations observed by a 2D system. This paper considers only fingering spelling in our system i.e. Take input in the form of finger spelling of alphabetic signs and providing the resultant voice output. The system will be using a webcam for the input and processing of the signs will be done using Microsoft Visual Studio as an IDE and OpenCv modules. With this proposed system they aim to help the speech

Received on 01-10-2021, Revised on 15-10-2021, Accepted on 26-11-2021.

CVR Journal of Science and Technology, Volume 21, December 2021
DOI: 10.32377/cvrjst2113

impaired community. V.Padmanabhan, M.Sornalatha [3] proposed ”Hand gesture recognition and voice conversion system for dumb people”. In this system, all templates are kept in database. For every action the motion sensors get accelerated and give the signal to the microcontroller. The microcontroller matches the motion with the database and produces the speech signal. The output of the system is using the speaker. Lam T Phil, Hung D. Nguyen2, T.T. Quyen Suil, Thang T. Vul [4] proposed:” A development of a glove-based gesture recognition system for Vietnamese sign language has been addressed and illustrated in this paper. Flex sensors and accelerometer have been used to sense curvature of the fingers and detect motion of the hand respectively. For American Sign Language in addition to flex and accelerometer, contact sensors have been used to detect any contact between two fingers.” Ashish Sethi Hemanth S, Kuldeep Kumar, Bhaskara Rao N, Krishnan R [5] proposed” SignPro- An Application Suite for Deaf and Dumb”. They have come up four different approaches based on the methods used for gesture extraction and matching. A Comparative study of these approaches is also carried out to rank them based on time efficiency and accuracy. Other features in the application include the voicing out of text and text to gesture conversion. In [6] Anagha J. Jadhav, Mandar P. Joshi proposed an embedded system module which consists of wearable sensing gloves along with flex sensors which are used to sense the motion of the fingers. The Indian sign language is used for determining the words. Flex sensors and accelerometer are used as sensor, these sensors are mounted on the gloves, the movement include the angle tilt, rotation and direction changes, these signals are processed by the microcontroller and playback voice is generated indicating signs through speaker. Jong-Sung Kim, Won Jang, Zeungnam Bien [7] present a system which recognizes the Korean sign language (KSL) and translates into a normal Korean text. A pair of data-gloves are used as the sensing device for detecting motions of hands and fingers. For efficient recognition of gestures and postures, a technique of efficient classification of motions is proposed and a fuzzy min-max neural network is adopted for on-line pattern recognition.

III. Block Diagram

Figure 1 shows the block diagram of the system. The block diagram consists of 3 layers: Data Access Layer, Business Logic Layer, User Interface Layer

A. The Data Access Layer

It consists of Flex sensors and accelerometers. The gesture is made by the user is sensed by the flex sensors and it is used to measure the amount of deflection. The accelerometer is used to measure acceleration in one to three linear axes (x, y, z).

B. The Business Logic Layer

It comprises of an Arduino. This is connected to the flex sensor and accelerometer which converts the movement based analog signals into digital signals.

C. The User Interface Layer

It consists of a Bluetooth module and an android device. The Bluetooth module is wireless, and it is used to exchange data between microcontroller (Arduino) and Mobile. The Android device is used which is connected via the bluetooth module to the arduino which generates the output in textual and audio format.

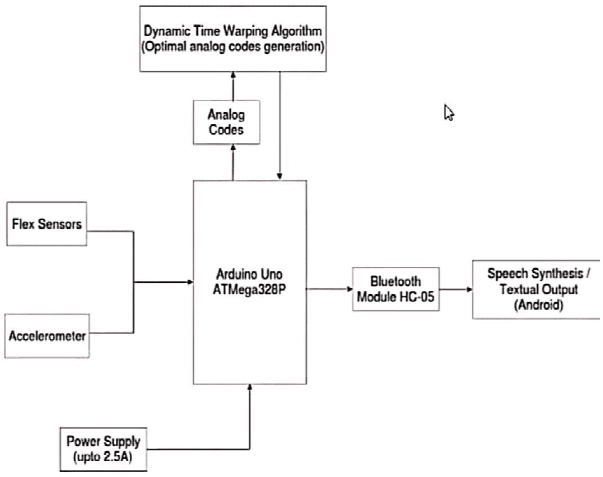

Figure 1. shows the block diagram of the system

III. The Description of System

The whole system is targeted to identify the movement indicated by the person to communicate. Hence, once the flex movement is observed, it is given as input to Arduino. Using Dynamic Time Warping, optimal analog signal is measured for mapping the gesture correctly using distance matrix. Optimal analog signal is converted into the digital signal. The Arduino module displays on android screen the digital equivalent of the flex and the gesture name associated with the digital value. The Bluetooth module on Arduino board gets connected to the android based mobile phone and converts the text into speech. Figure 2 shows the schematic diagram of the system. it consists of five logic toggles, five flex sensors, 1 Arduino UNO, 1 HC-05 Bluetooth module and Virtual terminal. The logic toggle is used to give the input to flex sensors depending on the bending in the fingers. If there is a bend in the finger, then the value of the logic toggle is ONE else ZERO. The flex sensor has 3 terminals (GND, VCC AND OUT) which are connected as shown. The organization of the flex sensors are as follows. The right most flex sensor represents the thumb finger, next flex sensor represents the fore finger, the third flex sensor represents the middle finger, the fourth represents the ring finger and the last flex sensor represents the little finger. The connections are made in the Proteus software based on the schematic diagram. The code is written in the Arduino IDE software and dumped into the Arduino UNO after verification and compilation. Now the simulation is run in the Proteus software and the output is checked on the virtual terminal. Figure 3 shows the flowchart of the system.

CVR Journal of Science and Technology, Volume 21, December 2021
DOI: 10.32377/cvrjst2113

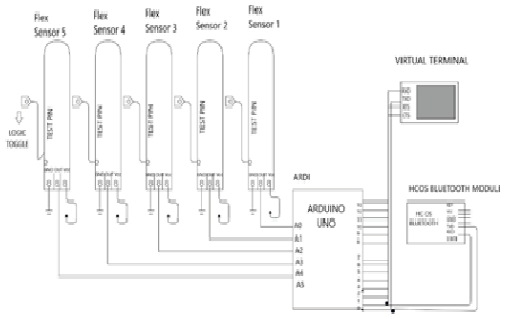

Figure 2. Schematic diagram of the system

The algorithm details are as follows:

1. Start
2. Set the baud rate
3. Input: For a gesture, sensor data inputs (5 flex sensors data and 3 axis accelerometer data) Flex Movement is observed, value=analogRead(flexPin);
4. Add delay of 10 milliseconds
5. Convert raw sensor data to meaningful data Using Dynamic Time warping, averaging value is calculated for mapping the gesture correctly.
6. The android app configured displays the digital equivalent of the flex.
7. The Bluetooth module on Arduino board gets connected to the android based mobile phone and converts the text into speech.
8. Go to step 3.

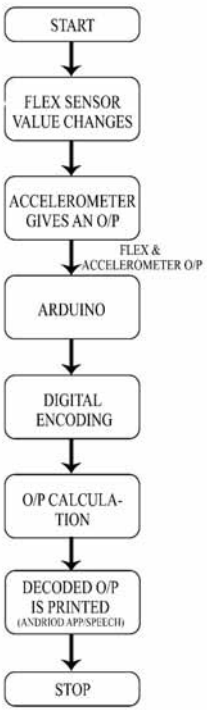

Figure 3. Flow chart of the system

IV. Results

To represent letter 'A' we need to bend all the fingers except the thumb finger. So, all inputs to the flex sensors as logic 1 except the right most flex sensor which represents the thumb finger. Now the output is visible on the virtual terminal as 'A'. Similarly, the outputs for other alphabets are obtained. Table 1 shown below depicts the mapping of respective inputs and the outputs obtained. Figure 4 and 5 show the results of simulations of letters S and C respectively. Figure 6. shows the complete simulation of the whole system.

TABLE I.
Outputs for Respective Inputs

FLEX SENSOR 5 *(Little finger)*	FLEX SENSOR 4 *(Ring finger)*	FLEX SENSOR 3 *(Middle finger)*	FLEX SENSOR 2 *(Fore finger)*	FLEX SENSOR 1 *(Thumb finger)*	OUTPUT ON VIRTUAL TERMINAL
1	1	1	1	0	a
0	0	0	0	1	b
1	1	1	1	0	c
1	1	1	0	1	d
0	0	0	1	1	f
1	1	1	0	1	g
0	1	1	1	1	i
1	1	1	0	0	l
1	0	0	0	1	u

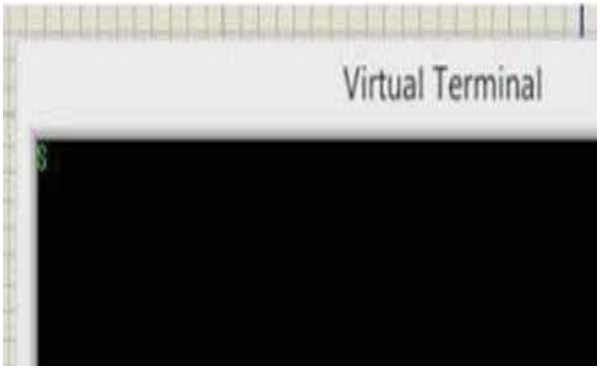

Figure 4. Letter 'S' at Simulation Virtual Terminal

CVR Journal of Science and Technology, Volume 21, December 2021
DOI: 10.32377/cvrjst2113

Figure 5. Letter 'C' at Simulation Virtual Terminal

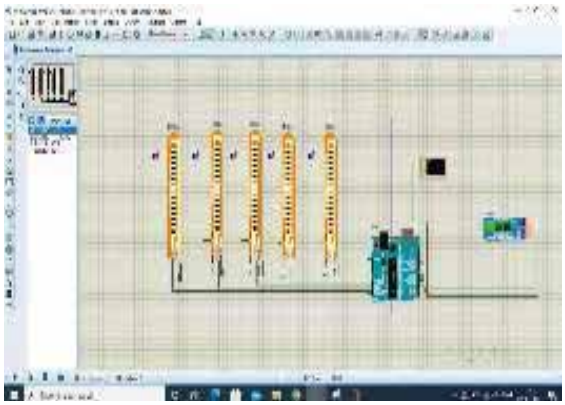

Figure 6. The simulation diagram of the whole system

Sign language is a useful way to ease communication between the deaf-mute community and abled people. However, there is a barrier between these communities with ordinary people where they must rely on human translators. In this paper, this technique is used to ease communication between deaf and dumb people. So, it is concluded that flex sensor based gesture recognition module is developed to recognize the English alphabets. Therefore, this system accurately converts the gestures to speech. The communication between mute people and other abled persons who are unfamiliar with the concept of sign language is possible only using gesture vocalizer device. Gesture vocalizer is a hand gesture based interface for facilitating communication among normal people and people with speech and hearing disabilities. The Gesture Vocalizer is a social initiative paper that helps bridge the communication gap between normal people and disabled people. The system can be easily implemented. The compact, portable design is its main advantage. It eliminates the need for having interpreter. Thus, this paper contributes to the upliftment of the deaf community and ensures that they also lead a life that is no different from the rest, thus breaking down the social stigmas which prevail in our society.

V. Conclusions

By introducing different languages, the flexibility is increased. Total 5 flex sensors are used so it increases the precision of the system. Upon addition of an accelerometer in collaboration with the flex sensors the wrist movement can be measured as well. Also, the system can be updated for sensing both hand gestures as well. This would help us increase the number of gestures by incorporating the wrist and finger movements of two hands thereby increasing the number of outputs. By interfacing with voice assistants like Siri or Alexa voice outputs can be generated rather than the vocalizer module. This would make the system more compact and be used on various platforms like mobile phones that would make it portable. Use hand gestures to control vehicles. This would be particularly useful for wheelchair bound people who find it difficult to manoeuvre it and require assistance of someone. Developing a custom vocalizer module that can provide more number of voice outputs than the standard one available in the market while at the same time reduce the cost if considered for mass production. Generate gestures for as many words as possible and develop a machine learning system that can interpret the various words generated and develop a sentence on its own. This would reduce the load on the system due to storage of large sentences and make the system more robust and adaptive.

References

[1] P. Vijayalakshmi and M. Aarthi, "Sign language to speech conversion," 2016 International Conference on Recent Trends in Information Technology (ICRTIT), Chennai,2016,pp.1-6.doi: 0.1109/ICRTIT.2016.7569545

[2] A. K. Tripathy, D. Jadhav, S. A. Barreto, D. Rasquinha and S. S. Mathew, "Voice for the mute," 2015 International Conference on Technologies for Sustainable Development (ICTSD), Mumbai, 2015, pp. 1-6.doi: 10.1109/ICTSD.2015.7095846

[3] Padmanabhan, M.Sornalatha."Hand gesture recognition and voice conversion system for dumb people", International Journal of Scientific & Engineering Research, Volume 5, Issue 5, May-2014

[4] Lam T. Phil, Hung D. Nguyen2, T.T. Quyen Suil, Thang T. Vul. "A Glove-Based Gesture Recognition System for Vietnamese Sign Language", 2015 15th International Conference on Control, Automation and Systems (ICCAS), Busan, South Korea,2015

[5] Ashish Sethi, Hemanth S, Kuldeep Kumar, Bhaskara Rao N, Krishnan R IJCSET "SignPro-An Application Suite for Deaf and Dumb" , May 2012 Vol 2, Issue 5,1203-1206

[6] Anagha J. Jadhav, Mandar P. Joshi "AVR based embedded system for speech impaired people" , 2016 International Conference on Automatic Control and Dynamic Optimization Techniques (ICACDOT), Pune, India ,2017

[7] Jong-Sung Kim, Won Jang and Zeungnam Bien, "A dynamic gesture recognition system for the Korean sign language (KSL)," in IEEE Transactions on Systems, Man, and Cybernetics, Part B (Cybernetics),vol. 26, no. 2, pp. 354-359, April 1996.doi: 10.1109/3477.485888

[8] Abhinandan Das, Lavish Yadav, Mayank Singhal, Raman Sachan, Hemang Goyal, Keshav Taparia, Raghav Gulati, Ankit Singh, Gaurav Trivedi, "Smart glove for Sign Language communications", Accessibility to Digital World (ICADW) 2016 International Conference on, pp. 27-31, 2016.

[9] A. Cazan, R. Varbanescu, D. Popescu, "Algorithms and Techniques for Image to Sound Conversion for Helping the Visually Impaired People - Application Proposal", Systems Signals and Image Processing 2007 and 6th EURASIP Conference focused on Speech and Image Processing 14th International Workshop on Multimedia Communications and Services., pp. 471-474, 27–30 June 2007.

[10] S. Ahmed, "MAGIC GLOVES (Hand Gesture Recognition and Voice Conversion System for Differentially Able Dumb People)", Tech ExpoThe Global Summit. London, 2012.

[11] Paris, Damara Goff and Katrina R. Miller. "Wearables and People with Disabilities: Socio-Cultural and Vocational Implications." In Wearable Technology and Mobile Innovations for Next-Generation Education, ed. Janet Holland, 167-183 (2016) doi:10.4018/978-1-5225-0069-8.ch009.

[12] https://www.almentor.net/en/course/Raising_A_Competent_Deaf_Mute_Child1

[13] Pablo Bonet, J. de , "Reduction de las letras y Arte para enseñar á ablar los Mudos." Ed. Abarca de Angulo, Madrid, ejemplar facsímil accesible en la [1], online (Spanish) scan of book, held at University of Sevilla, Spain, (1620).

[14] Lewis, M. Paul; Simons, Gary F.; Fennig, Charles D., eds. (2013), "Deaf sign language", Ethnologue: Languages of the World (17th ed.), SIL International, archived from the original on 2013-11-26, retrieved 2013- 12-03

[15] Karen Nakamura, "About American Sign Language", Deaf Research Library, accesses since 1995, http://www.deaflibrary.org/asl.html

E-ISSN 2581 – 7957
P-ISSN 2277 – 3916

CVR Journal of Science and Technology, Volume 21, December 2021
DOI: 10.32377/cvrjst2114

Speech Enabled Smart Home Automation

Santosh Kumar Sahoo
[1]Assoc. Professor, CVR College of Engineering/EIE Department, Hyderabad, India
Email: santosh.kr.sahoo@cvr.ac.in

Abstract: **Smart Home Automation is the major need nowadays and is gaining popularity because of the development of compact and smart as well as intelligent devices. In this proposed approach, a new scheme is introduced to operate the devices in home via a more intelligent manner with the help of smart technologies like speech enabled integrated Internet of Things (IoT), which uses the internet as a medium to establish a bridge between local device and the remote server. The main objective of this paper is to implement a new system which can support voice assisted home automation with extreme security and range-free localization principles. The idea of the proposed paper is integrating the power of IoT with Classical Home Automation as well as deviating from the regular home automation schemes. The proposed system is named as "Speech Technology enabled Smart Home (STeSH)", which gathers the voice from the respective user and checks whether the user is a registered person to the particular device to operate or not. If the user is an authorized person, the device will be operating accordingly based on the voice commands raised by the user.**

Index Terms: **Speech Technology, IoT, Home Automation, STeSH, Voice Processing, Speech Recognition.**

I. Introduction

Now-a-days smart devices and technologies rule the world with their powerful approaches and provide many intelligent services to people to operate their needs by using such devices. In parallel, the communication medium is another growing entity, which supports this gadget to work in an intelligent manner to provide ultimate support to people to meet their global communication needs. Specialists do connect computerized gadgets with scientific and authoritative devices to make complex frameworks for quickly extending attributes of uses and physical pursuit. For the advancement of intelligent urban areas, there is a need to switch to systematic mode for everything, so the idea of smart home automation framework is a thought, which is utilized to make the city shrewd. A Smart Home is one that gives solace, security and gives the comfort feel to individuals. Intelligent homes additionally receive some advantages such as less-current consumption and consistency in availability, for each person at home. Smart Home Automation implies the observing and control of family unit questions wisely for viable utilization. The family unit items ought to be shrewdly interconnected just as give data to better activities. SmartHome Automation expanded with the Internet of Things (IoT) gives better adaptability in overseeing and controlling family questions in a more extensive angle. This will bolster the interconnectivity of countless SmartHome for better asset use in more extensive territory. In this paper, we planned to integrate the latest technologies along with intelligent communication methods to automate the people's regular usable devices such as electronic gadgets, charging devices, A.C., Television and many more household devices. In this concert, we need to elaborate the two technologies further to clear, the first one (Figure-1) voice enabled services for operating the household devices with speech technology enabled services.

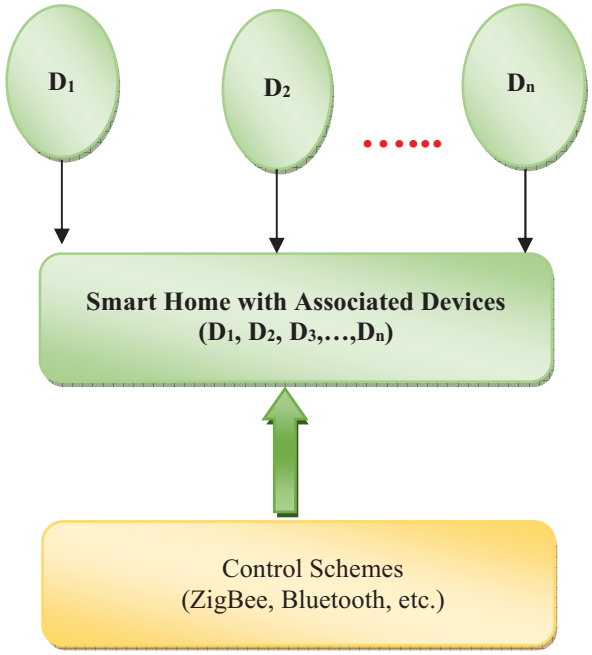

Figure 1. Classical Smart Home Automation System Working Model

These Speech Enabled Services are applied to our smart home automation services by means of triggering the devices using customer voice. In this position all of us have a question like, if any other person or third-person or other intruders operate the device by using their voice means, so here is a question mark for the device to manage this situation. And the second query is if we applied a classical communication scheme such as Bluetooth and ZigBee, the range of communication is within a few feet only, then management of the communication limits properly is also another task. So, the mentioned two queries are the major concern to deal with every smart home automation service. Those queries are rectified by using our proposed approach called Speech technology enabled Smart Home (STeSH), which collects the user voice and registers it for their own home usages at one time and provides the separate authorization and authentication norms for further operations or controlling of devices. And the second concern called communication range limitation deals with proposed powerful technology called Internet enable service IoT. The following section clearly illustrates the difference between

Received on 08-09-2021, Revised on 02-10-2021, Accepted on 18-11-2021.

CVR Journal of Science and Technology, Volume 21, December 2021
DOI: 10.32377/cvrjst2114

existing and proposed systems as well as the result and discussion area clearly illustrate the outcome proof with a proper prototypical model.

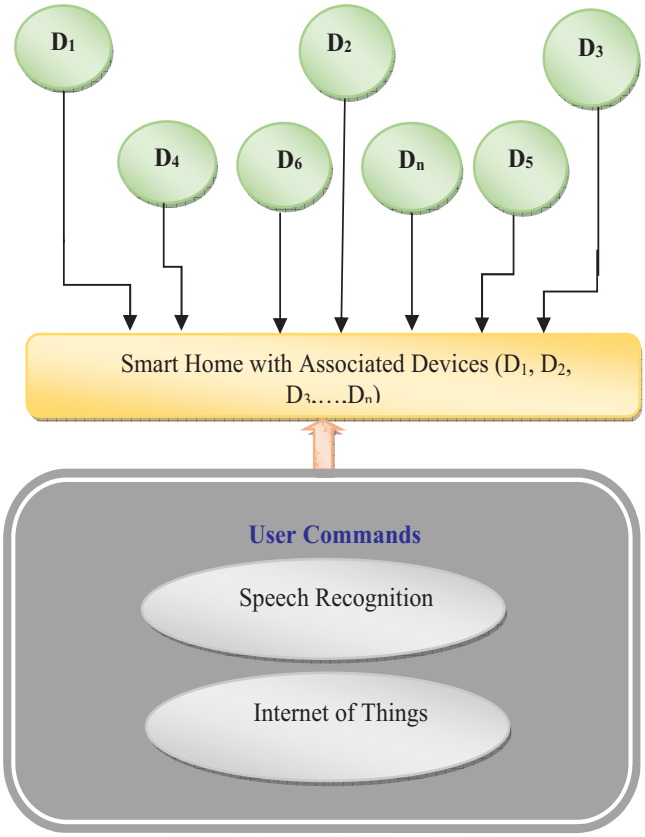

Figure 2. Proposed System Flow Diagram

Marie.A, Benedict.I et. al. proposed a SmartHome Automation Framework, which is based on Siri_Enabled application [1]. The main drawback of this application is as follows, which can be installed only in iOS_Apple devices. So, only the apple-mobile users only used this application, and they can only control the household devices by using this system. The implemented Siri_Enabled_Apple mobile application supports voice translation as well, so that the users feel free regarding languages and operate the application in fault free manner, but the major drawback of this platform supportivity and dependability makes this system poor and the budget of apple devices are usually highly compared to normal devices. So this Marie.A, Benedict.I et. al. (2015) implemented application fell into several flaws such as: (i) cost expensiveness, (ii) poor connectivity problems and (iii) platform dependability.

Piyare. R et. al [2] proposed the SmartHome Automation framework by using classical communication technology called Bluetooth, which can be able to connect up to 10 feet range and the connectivity problem of Bluetooth is really high compared to other connection enabled devices. In this system they applied Bluetooth services with an arduino_board base, which acts as a heart of the application to connect the system with Bluetooth and establish the communication interface properly to collect triggers and operate devices accordingly. But the main drawback of the implemented application is the short-range coverage area and the cost wise expense problems create the circuit more critical and make it not suitable for exact real-time applications.

Alshueili.H, Gupta.G et. al. [3] implemented a new approach in SmartHome application, which enabled household devices by means of human voices. This system collects the human voice and passes that signal as a trigger to the respective household device via communication interfacing and operates the device according to the respective voice trigger. The communication medium used in this paper (Marie.A, Benedict.I et. al. 2015) is called ZigBee, which can convert the human voice into a triggering signal and pass that to the controller for controlling the respective device. The major drawbacks identified in this paper are as follows: (i) Communication mode should be static, (ii) pulse based signaling is used in this approach, (iii) ZigBee can communicate up to the range of 20 feet and (iv) cost wise is expensive in practical scenarios.

Hidayat.S and Firmanda.S [4] implemented a new work, which can support a lot of SmartHome Automation framework. This approach integrates RaspberryPI as a main controller/CPU to the automation system, which collects the voice command from the users and converts the collected commands as a digital signal. The converted signals are passed as a command to the household devices and allow the device to operate accordingly based on the given trigger from the controller [5]. The main drawback found over this approach is that it uses RaspberryPI as a controller, for enabling internet connectivity. RaspberryPI is not the only solution to deal with. Instead of using RaspberryPI, if we use other Wi-Fi enabled devices it is cheap and powerful, because RaspberryPI is not meant for enabling internet support, it is like a minicomputer. The major drawbacks found over the paper (Hidayat.S and Firmanda.S, 2015) is as follows: (i) Cost expensive, because RaspberryPI is costly compared to other controllers available into the market, (ii) Circuit Complexity is really high if you go with standalone purpose of RaspberryPI and (iii) practical application possibilities to real-world situations are really high.

K. Pradeep Mohan Kumar, M. Saravanan, M. Thenmozhi and K. Vijayakumar (2019) proposed a concept and illustrated a logic for identifying the intruders by using classification logic [11]. The proposed system of STeSH applies the logic for identifying the intruders to unwantedly operate the home devices without user permission (K. Vijayakumar et. al. 2019). By applying the logic of the Genetic Algorithm classifier, the authors proved the identification mechanism so clear. So, our proposed logic is improvised by means of applying such techniques to prevent our system from attackers further.

M. Nithya and K. Vijayakumar (2020) proposed a paper for dataset segmentation by using ICD dataset collection [12]. In our proposed logic of STeSh it is planned to apply the dataset nature for identifying the face logics of the user and watch the robustness by using CCTV camera's along with speech verification in future. So, the proposed system is so robust and powerful in the future.

M. Anathi and K. Vijayakumar (2020), proposed a paper for identifying the dynamic network traffic restriction

methodology by using MAC address verification strategy [13]. In our proposed system of STeSH, we include the nature of MAC address verification to eliminate the time consumption process over triggering of loads in parallel as well as which leads the system more fast and robust compared to all other existing schemes.

II. METHODOLOGY

The proposed system (figure-2) implements a new approach to solve all the issues found over existing SmartHome Control application, which is termed as "Speech technology enabled Smart Home (STeSH)". This proposed STeSH enables the invention of many intelligent things integrated together. The integration of multiple unique and best things leads to robust and secured mechanisms over the operation of voice enabled SmartHome controlling. The integrated intelligent features are as follows: (A) Speech Recognition, (B) Internet of Things (IoT) and (iii) SmartHome Automation.

A. Speech Recognition

The Speech Recognition methodology collects the user speech and processes the speech into many norms with voice-based feature extraction strategy [6]. In this method each and every voice pulses are segregated and compare those pulses with the authorized user voice. If the user input voice signal is matched with the registered/authorized user voice, then the voice recognition mechanism recognizes the voice and gives the positive trigger to the controller to operate the respective household device [7]. The following algorithm illustrates the logic of the Speech Recognition algorithm step by step in detail.

ALGORITHM: SPEECH RECOGNITION

Input: Analog Human Voice
Output: Digital Conversion and Recognized Boolean Result
Step-1: Importing the respective Speech Recognition library.
Step-2: Create a class and object to assign the imported speech variables from library.
Step-3: Creating a class and object for audio recognition and it will recognize the audio is extracted from human voice or else any recorded medium (Ex. Class Audio_Recognizer(Audio_Source)).
Step-4: Assign the recognized voice into a variable (Ex. Aud = Audio_Recognizer([input];).
Step-5: Creating a loop for reading a voice from first to last.
Step-6: With Aud.Read() as Input, this statement will start the loop.
Step-7: Raise the printing statement to be intimate to the user to give a respective input voice to the system.
Step-8: System automatically changes the mode from query the user to listen to the voice.
Step-9: Aud = Audio_Source.Listen(Input).
Step-10: Add the exception statements to monitor the steps from 1 to 9 for managing the system robustness and fault tolerance from unpredictable exceptions.
Step-11: Extracting Proper Audio from input and change the modulation from input audio collected from the user.
Step-12: Analyze the audio input and store the result into a defined boolean variable (Ex. Boolean R).
Step-13: R = Resultant_Voice(Input).
Step-14: Return R.

The following Pseudocode illustrates the algorithm logic of Speech Recognition and describes the flow implementation step by step in detail.

PSEUDOCODE: SPEECH RECOGNITION

```
Import Speech-Recognition
define Speech-Recognition as SR_1;
define Audio-Identifier as Aud;

SR_1 = Audio_Recognizer (Audio_Source);
With SR_1.MicrophoneObject() as Input:
        PrintStmt("Input Voice Fully from start to End");
        Aud = Audio_Source.Listen(Input);
Try
        PrintStmt("System think you said improper word: "
        + Audio_Source.Listen(Input));
Exception SR_1.UnknownValueError
    PrintStmt("Could not understanding the audio input: "
    + Audio_Source.Listen(Input));
Exception SR_1.RequestSystemError as expc:
        PrintStmt("System Error{0}: " + expc);
End Try
```

The following figure-3 explains the input and out mechanism of voice signals and the processing like when it is encoded and decoded under certain circumstances.

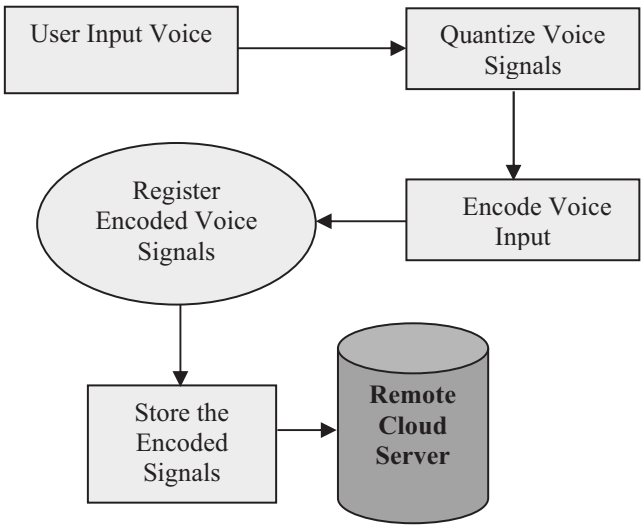

Figure 3. Voice Authorization Process Architecture

For this Speech recognition methodology, we use Google based Voice Assistance, which collects the user voice and matches that with existing authorized voice signals and

CVR Journal of Science and Technology, Volume 21, December 2021
DOI: 10.32377/cvrjst2114

provides the access permission to operate the corresponding devices. The entire process of speech recognition takes a few seconds and processes all these things based on input voice signals [8]. If the given/collected voice signals are not matched with the authorized voice signals, then the system informs the collected signal is based on an unauthorized person, please authenticate properly. So, that this system is proper for manipulating the user voices and provide good support to customers to operate the devices according to their convenience. The following figure-4 illustrates the overall workflow model including voice recognition and access control norms over the proposed system approach.

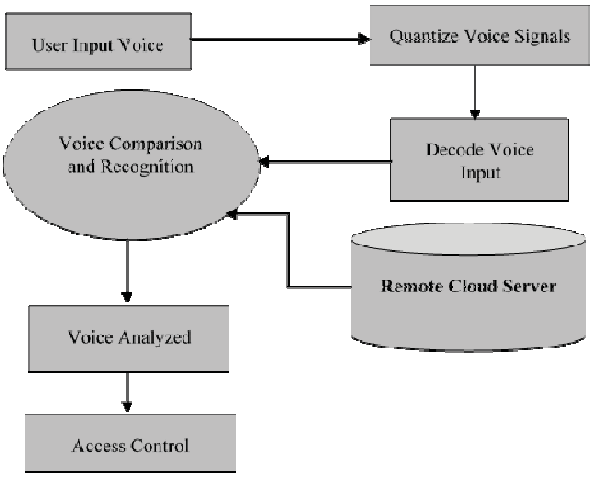

Figure 4. Voice Authentication Process Architecture

B. Internet of Things (IoT)

The term Internet of Things ruling a world with its power and connectivity, this is nothing but a refined form of network. IoT interconnect the remote cloud server with local devices, so that the user can communicate from anywhere at any time without any restrictions [9]. By using this internet enabled service user can speak and operate the device from anywhere in the globe without any range restrictions. So, that, the appliance of Internet of Things enables the system so secure and robust in many forms. The concept of IoT is illustrated in the proposed approach with the help of below defined equation, Eqn-1.

$$\text{IntEnable} \rightarrow \text{BCS} + \text{SxSy} + \text{Px} \rightarrow \text{T2R} \quad (1)$$

Where IntEnable is an object to indicate Internet Enable State, BCS indicates the basestation strength during internet establishment, SxSy indicates the total signal strength for the respective range coverage which belongs to X and Y surroundings, Px indicates the port number association with the defined connection and T2R indicates the total traffic ratio over establishing the internet connection.

C. Smart Home Enabling Model

The SmartHome Services are the major need now-a-days, which allows user to operate the household devices from anywhere in the world at any time, without any range restrictions.

This process happens only if the devices are properly bound over the communication medium, that support is launched by means of Internet enabled services over the proposed work model along with speech recognition procedures [10].

Figure 5. Internet of Things Service Model

The speech recognition system receives voice from the user and process the input according to speech verification norms and identify the authorized user is trying to operate the device or some others. If the authorized user is trying to authenticate the device means it permits the flow, but if an unauthorized user trying to login into the system, it cannot permit the user to flow further. The proposed framework is more secure and robust compared to the classical working model and it is more convenient to work with the proposed model because of its unlimited range support and easiness. For all the proposed system provides efficient and intelligent working model in results, which will be illustrated clearly in results further. The following algorithm illustrates the logic of SmartHome Enabling Model STeSH algorithm step by step in detail.

ALGORITHM: SMARTHOME ENABLING MODEL

Input: Human Voice or Recorded Speech input
Output: Convert Audio Transcriptions to Text and Triggered the Respective Load

Step-1: Importing the respective Speech Recognition library.
Step-2: Create an object to assign the imported speech variables from the library.
Step-3: Declare a voice_recognizing class to clearly recognize the speech from the user side. We are using google_speech recognition library over here.
Step-4: Speech file supported by speech_recognition in the format of "WAV/MP4".

CVR Journal of Science and Technology, Volume 21, December 2021
DOI: 10.32377/cvrjst2114

Step-5: Google recognizer reads English usually but need to add some language libraries for multilanguage supportivity.

Step-6: Match the input voice from the user voice repository.

Step-7: Identify the voice robustness and authenticity.

Step-8: Trigger the Respective Load according to the corresponding input.

Step-9: Return Triggered Load Details to User reflection area.

Step-10: Stop gathering Voice and go to Step-3.

This above-mentioned algorithm is technically derived by using the following equations. The following equations, Eqn-2 and Eqn-3 illustrate the nature of collecting human voice and maintaining it into the repository.

$$UV_x \rightarrow VX_i{:}1 \text{ to } n\ \Omega \quad \sum_{x=0}^{n} -1 \binom{n}{x}^{x} i_{v_{xi}} \qquad (2)$$

Where UV_x illustrate the storage of user voice input and x indicate the upper limit variations, VXi:1 to n illustrate the collected input voice range signals which is starting from 1 and ending in 'n'.

$$VR_X = 1 + \frac{Uv_x}{1!} + \frac{Uv_x^2}{2!} + \cdots, Uv_{xn} < N \qquad (3)$$

Where VR_X illustrate the storage of user voice storage repository and x indicates the upper range of the repository, Uv_{xn} illustrates the collected input voice range signals which are starting from 1 and ending in 'n'. All these voices are stored in order to the repository for managing the secured voice-based recognition to operate the smart home without any security issues.

III. Results And Discussions

In this summary, the result of proposed approach STeSH is explained clearly with output proofs, and it assures the proposed system robustness, classic method improvements, size compatibility and energy efficiency improvement scenario with graphical proof. The table-1 demonstrates the Comparison illustration of the Existing and Proposed system voice accuracy capturing and performance ratio, with respect to the comparison of checking the details with 50 different persons on different age groups between 10 and 60.

Figure-6 illustrates the Graphical Comparison View of the Existing and Proposed system voice accuracy capturing and performance ratio, with respect to the comparison of checking the details with 50 different persons on different age groups between 10 and 60.

Figure-7 exemplifies the Graphical Comparison View of the Existing Home Automation Technique and the Proposed Voice Based Home Automation Technique Time Consumption to trigger the Loads according to user control.

Similarly the figure-8 explains the Graphical Comparison View of the Existing Home Automation Technique and the Proposed Voice Based Home Automation Technique Energy Consumption ratio.

TABLE I.
Voice Capturing Accuracy Levels

Age Group	Existing Voice Capturing Accuracy	STeSH Voice Capturing Accuracy
10 to 15	80%	85%
16 to 20	79%	92%
21 to 25	78%	94%
26 to 30	82%	95%
31 to 35	84%	95%
36 to 40	85%	96%
41 to 45	80%	93%
46 to 50	85%	90%

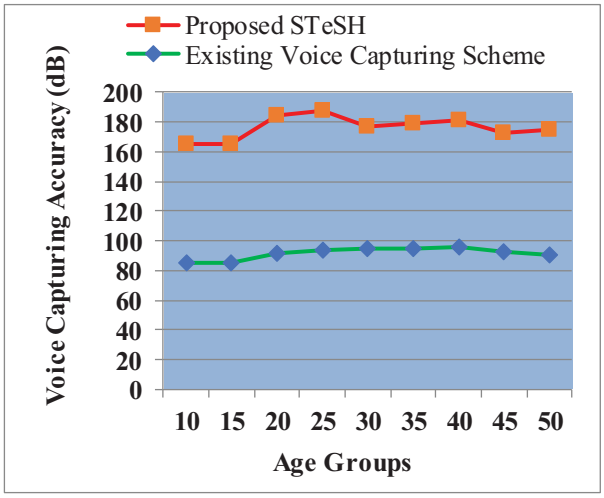

Figure 6. Graphical Comparison View of Existing and Proposed Accuracy Levels

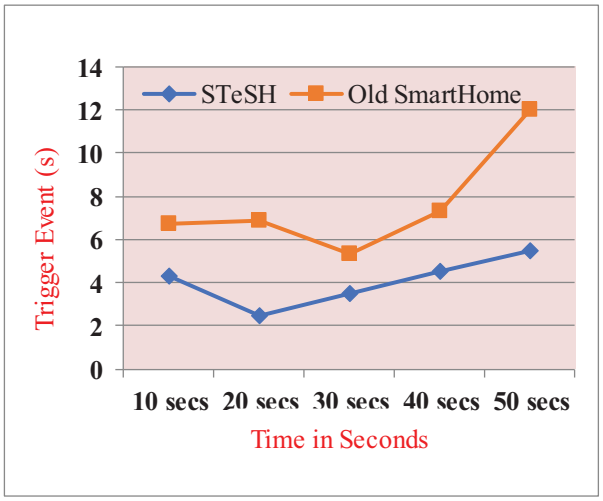

Figure 7. Graphical Comparison View of Existing and Proposed Time Consumption

CVR Journal of Science and Technology, Volume 21, December 2021
DOI: 10.32377/cvrjst2114

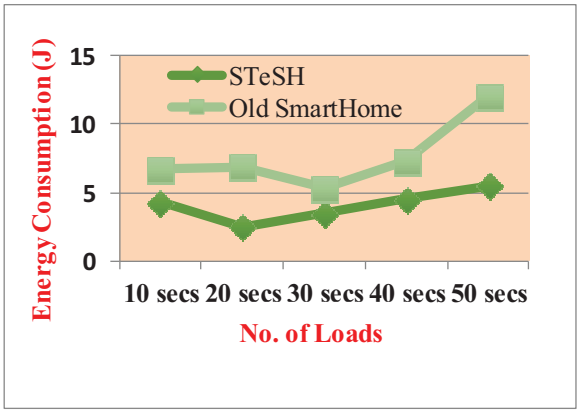

Figure 8. Graphical Comparison View of Existing and Proposed Energy Consumption

IV. Conclusions

The proposed SmartHome Application system is completed properly with advanced speech technology-oriented processing and intelligent operational features such as Voice/Speech Recognition strategy and Internet of Things. The Google based Speech collection system is used to collect the user voice and send that to the remote server for processing. The server-side system converts the entire speech signals into encoded raw commands and stored it into the remote cloud server with proper access right specifications. Once the user authenticates into the system, automatically it crosschecks the voice input with the processed voice input over the server. If it matches, the respective user is allowed to operate the home devices without any interruptions otherwise the system blocks the user to proceed further. For all the entire system guarantees that this SmartHome Application System ensures a secure and robust way to automate the home in an easy and scalable way.

References

[1]. Marie, A., Benedict, I., Zandrae, A., Neil, A., Gustilo, R. 2015 Home Automation Using Raspberry Pi through Siri Enabled Mobile Devices.

[2]. Piyare.R., and Tazil, M. 2011 Bluetooth based Home Automation System using Cell Phone.

[3]. Alshueili.H, H., Gupta, G., Mukhopadhyay's. 2011 Voice Recognition Based Wireless Home Automation System.

[4]. Hidayat, S., Firmanda, S. 2015 Scheduler and Voice Recognition on Home Automation Control System.

[5]. Jain, S., Vaibhav, A., Goyal, L. 2014 Raspberry Pi based Interactive Home Automation System through E-mail.

[6]. M. Narender, M. Vijaylakshmi, "Raspberry Pi based Advanced Scheduled Home Automation System through E-mail", IEEE International Conference on Computational Intelligence and Computing Research, pp: 1-4, 2014.

[7]. D. Pavithra, R. Balakrishnan, "IoT based Monitoring and Control System for Home Automation", Global Conference on Communication Technologies (GCCT), pp: 169-173, 2015.

[8]. B. Pandya, M. Mehta, N. Jain, "Android Based Home Automation System Using Bluetooth & Voice Command", International Research Journal of Engineering and Technology (IRJET), pp: 609-611, Volume: 03 Issue: 03, 2016.

[9]. A. Ramya, T. Srihari, "Raspberry Pi (Model B) Based Interactive Home Automation System", International Journal of Trend in Research and Development, Volume 3(1), pp: 1-4, 2016.

[10]. P. Hazari, A. Andurkar, "System for Voice and Facial Recognition using Raspberry Pi", International Journal of Advanced Research in Computer and Communication Engineering Vol. 4, Issue 4, pp: 438-440, April 2015.

[11]. K. Pradeep Mohan Kumar, M. Saravanan, M. Thenmozhi and K. Vijayakumar, "Intrusion detection system based on GA-fuzzy classifier for detecting malicious attacks", https://onlinelibrary.wiley.com/doi/epdf/10.1002/cpe.5242, 2019.

[12]. M. Nithya and K. Vijayakumar, "Secured segmentation for ICD datasets", Journal of Ambient Intelligence and Humanized Computing, 2020.

[13]. M. Anathi and K. Vijayakumar, "An Intelligent Approach for Dynamic Network Traffic Restriction using MAC Address Verification", Computer Communications, 2020.

E-ISSN 2581 – 7957
P-ISSN 2277 – 3916

CVR Journal of Science and Technology, Volume 21, December 2021
DOI: 10.32377/cvrjst2115

A High-Performance FIR Filter Architecture using Symmetry and Distributed Arithmetic Logic

Venkata Krishna Odugu[1], Janardhana Rao Bitra[2] , and Satish Bojjawar[3]
[1]Assoc. Professor, CVR College of Engineering/ECE Department, Hyderabad, India
Email: venkatakrishna.odugu@gmail.com
[2]Assoc. Professor, CVR College of Engineering/ECE Department, Hyderabad, India
Email: janardhan.bitra@gmail.com
[3]Assoc. Professor, CVR College of Engineering/EIE Department, Hyderabad, India
Email: satishbojjawar@gmail.com

Abstract: **In this paper, the symmetry type Finite Impulse Response (FIR) filters are described using distributed arithmetic (DA) logic. The direct-form type filter architecture is considered for the implementation. Direct-form is requires a fewer number of registers than transposed form architecture. The symmetry in the filter coefficients decreases the number of multipliers. Due to the reduction of multipliers, the area and power parameters are reduced by 50%, because multipliers complex block in terms of area and power. Further, the multipliers are completely replaced with shift and add operations to reduce the complexity using DA. In this work, the higher-order filters are decomposed into smaller filter blocks to reduce the Look-up-table (LUT) complexity. The proposed DA-based symmetry FIR filter is validated using FPGA and synthesized using Genus tools from Cadence in 90nm CMOS technology. The physical design is done using Innovus tools from Cadence and the layout of the proposed architecture is generated. The utilization of hardware blocks, delay, area, and power consumption parameters are compared with existing FIR filter architectures.**

Index Terms: **FIR filter, Distributed Arithmetic, symmetry filters, FPGA, and LUT.**

I. Introduction

Digital filters are two types as Finite Impulse Response (FIR) and Infinite Impulse Response (IIR) filters. The FIR filter is mostly used in many signal processing applications due to the stability, ease of design. The FIR filters can be implemented in direct type or transposed type architectures. Any filter architecture consists of delay elements, adders, and multipliers. From these blocks, the multiplier is a more power-consuming block and complex block. Hence, multiplier blocks are replaced with adders and shifters using Distributed Arithmetic (DA) logic. The DA logic-based multiplication process in the filter decreases the area, power, and delay.

In the work [1], a memoryless DA-based FIR filter is proposed for hearing aid applications using compressor circuits. An approximate 4:2 compressor is incorporated in the filter and mux-based logic is used to reduce the memory, area, and power consumption. In [2], Application Specific Integrated Circuit (ASIC) implementation of FIR filters is described using shared Look-Up Table (LUT) based DA logic to improve the VLSI performance metrics. The shared LUT concept reduces the hardware complexity and memory.

Park et al. [3] suggested Field Programmable Gate Array (FPGA) and ASIC-based architectures for reconfigurable FIR filters using DA logic. In this work, the throughput is improved using block processing and power consumption is reduced by the DA concept. The parallel DA-based low power The FIR filter architecture is proposed by Khan et al. in [4]. The bit-level parallel processing is used in DA-based filters to improve the speed, and the proposed filter architecture is compared with existing (Multiply and Accumulate) MAC-based filter architectures.

In the research paper [5], a novel DA-based FIR filter for efficient decision feedback equalizer is proposed. In this work, an approximate compressor is used to reduce the area and mux-based logic is considered in the filter to improve the speed. In the paper [6], two DA-based adaptive FIR filters are explained using smart modified LUTs to store the filter coefficients to improve the area, delay, and power parameter

A transposed type FIR filter is demonstrated in [7]. In this work, the conventional LUT is split into several ROM-LUTs to provide parallelism in the DA-based filter. Prakash et al. [8] proposed an efficient least mean square adaptive filter using the DA technique. In this paper, the coefficient storage unit is updated using offset binary coding (OBC) to improve the speed and throughput. In [9], a block-based FIR filter using DA logic is described for software-defined radio applications. The throughput and VLSI design metrics are improved by this proposed method. Park et al. [10] proposed a reconfigurable FIR filter based on the DA method. A shared LUT and distributed RAM-based techniques are incorporated in the proposed filter to improve the performance metrics.

The symmetry-based implementation of the FIR filter using DA techniques is proposed in this paper. The higher-order filter implementation using DA increases the complexity of the LUT. To overcome this, the filter is divided into filter blocks of L, and DA is applied to each filter block and the individual outputs are determined in parallel and the final output is computed by adding all filter blocks outputs using an adder tree along with appropriate shifters.

The rest of the paper is organized as follows: Section 2 describes the concept of DA logic and corresponding equations. The proposed architecture implementation is demonstrated in section 3. Section 4 explains the analysis of results. The paper is concluded in section 5.

Received on 28-03-2021, Revised on 04-05-2021, Accepted on 17-06-2021.

CVR Journal of Science and Technology, Volume 21, December 2021
DOI: 10.32377/cvrjst2115

A. Background work

The algebraic sum of convoluted impulse response coefficients and input samples is FIR filter output. The basic FIR filter output is expressed by (1).

$$y = \sum_{i=0}^{N-1} C_i X_i \tag{1}$$

Here, C_i is filter known coefficients and X_i is the input sample of the filter. The above equation is represented in the block diagram and shown in Fig. 1. A linear phase FIR filter is symmetric about the center value. This symmetry in the FIR filter reduces the number of power hunger multipliers required for the realization of the filter architecture. The symmetry type 10-tap linear phase FIR filter architecture is shown in Fig. 2.

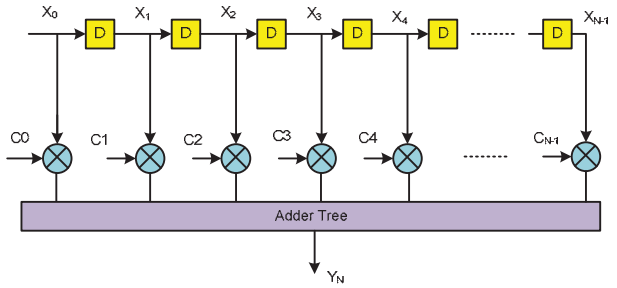

Figure 1. The general architecture of the N-tap FIR filter.

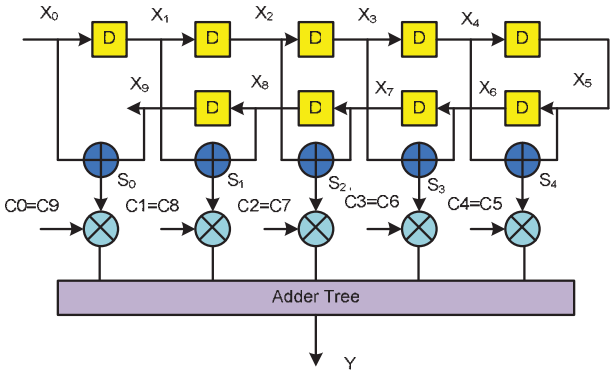

Figure 2. 10-tap symmetry type FIR filter

In the Symmetry filter, the input samples to be multiplied with the same coefficients are pre-summed before multiplication. Next, all the inner products are summed by the adder tree and produce the final filter output. The expanded filter output is represented in (2). In the architecture, the outputs of the adders are denoted by S_0, S_1, S_2, S_3, and S_4.

$$Y = C_0\,S_0 + C_1\,S_1 + C_2\,S_2 + C_3\,S_3 + C_4\,S_4 \tag{2}$$

II. Distributed Arithmetic Concept

The basic filter equation of the FIR filter is modified corresponding to the DA technique. From the input samples or coefficients, one of them is considered and modified into bits representation as shown in (3). The input sample is Xi is represented as,

$$Xi = \sum_{b=0}^{B-1} X_i\,[b] \times 2^b \tag{3}$$

Where $X_i\,[b] \in \{0,1\}$ and denotes the b[th] bit of input sample Xi. The input may consist of B-bits. Then the filter output expression (1) is modified as (4). The rearrangement is applied in (4) then the DA-based FIR filter output is shown in (5).

$$y = \sum_{i=0}^{N-1} C_i \times \sum_{b=0}^{B-1} X_i\,[b] \times 2^b \tag{4}$$

$$y = \sum_{b=0}^{B-1} 2^b \times \sum_{i=0}^{N-1} X_i\,[b] \times C_i \tag{5}$$

The simple DA-based FIR filter architecture corresponding to the above equation is represented in Fig. 3.

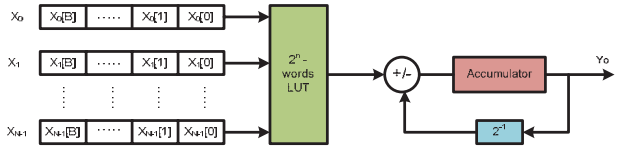

Figure 3. Basic DA based FIR filter

The DA-based filter architecture consists of shift registers, LUT, shifter, accumulator, and adder/subtractors. The parallel in serial out shift registers are required to feed the input sample bit-by-bit to the coefficient storage unit is LUT.

TABLE I.
PRECOMPUTED COEFFICIENTS STORED IN THE LUT FOR N = 4

S. No	Address Input bits	The stored value in LUT
1	0000	0
2	0001	C0
3	0010	C1
4	0011	C1+C0
5	0100	C2
6	0101	C2+C0
7	0110	C2+C1
8	0111	C2+C1+C0
9	1000	C3
10	1001	C3+C0
11	1010	C3+C1
12	1011	C3+C1+C0
13	1100	C3+C2
14	1101	C3+C2+C0
15	1110	C3+C2+C1
16	1111	C3+C2+C1+C0

CVR Journal of Science and Technology, Volume 21, December 2021
DOI: 10.32377/cvrjst2115

The LUT is a memory block, which is used to store the precomputed values of filter coefficients. The size of the LUT depends on the order of the filter N. The LUT storage elements for N = 4 are shown in Table I. The input bits from each sample are considered as the address of the LUT and the corresponding data stored in the LUT is fetched and given as the partial product. The partial product output is fed to the adder, which is added by the previous accumulated output. The previous output is generated by the shifter and is denoted by 2^{-1}.

III. Proposed FIR Filter Architecture using DA

In this section, the symmetry-based FIR filter architecture using the DA technique is described. If an order of the filter N is high, then the size of LUT becomes 2^N - words. For example, N =16, then 65536 words are required and it is very complex to implement the LUT. Hence, the N-th order filter is divided into L filter blocks. The individual filter blocks are transformed into DA form and filter block outputs are determined and the final output is computed by adding up all filter block outputs. The DA-based filter output equation is modified as (6).

$$y = \sum_{i=0}^{L-1} C_i X_i + \sum_{i=L}^{2L-1} C_i X_i + \sum_{i=2L}^{3L-1} C_i X_i + .. + \sum_{i=(\frac{N}{L}-1)}^{N-1} C_i X_i \quad (6)$$

The proposed symmetry FIR filter after decomposition into filter blocks is shown in Fig. 4. In the symmetry FIR filter after the addition of the same coefficients, the signals are denoted by $\{S_0, S_1, S_2, ... S_{N-1}\}$. For higher-order filters, these samples are decomposed into L blocks. The samples $\{S_0, S_1, \ldots S_L\}$ are fed to one LUT, which consists of 2^L words. Here the LUT size is reduced from 2^N to 2^L words. Table II compares the size of the filters with and without division of filter.

TABLE II.
. Comparison of LUT size for FIR filters

DA Filter	LUT size	Total Memory Space
Normal filter with no division	2^N words	2^N words
Filter with division into N/L blocks	2^L words	2^L x N/L words

The proposed FIR filter architecture consists of L number of filter blocks. Each decomposed filter block has an L number of inputs. The L number of input samples is given as inputs to the filter block. The internal structure of the filter block is shown in Fig. 5. The iteration process of DA filter logic in the filter block is represented in this figure. The L number of samples and each sample is represented by B bits. From L samples, bit-by-bit concatenated data is considered as the address and corresponding partial product stored in the LUT. The output of the LUT is shifted by the multiplication of 2^B, 2^{B-1}, and so on. Finally, all the individual outputs are accumulated and filter block output is computed. Similarly, all the individual filter blocks are generated and summated by the adder tree. If the order of the filter is large, then the complexity of the adder tree also increases.

In the adder tree, all the shifter's outputs need to be added. The shifted values in each level increase the number of bits in the outputs and the complexity of the adder tree is high and each summand requires large and different word lengths. To overcome this complexity, the shifters are embedded along with the adder tree levels. The shifters placing in each level of the adder tree are shown in Fig. 6.

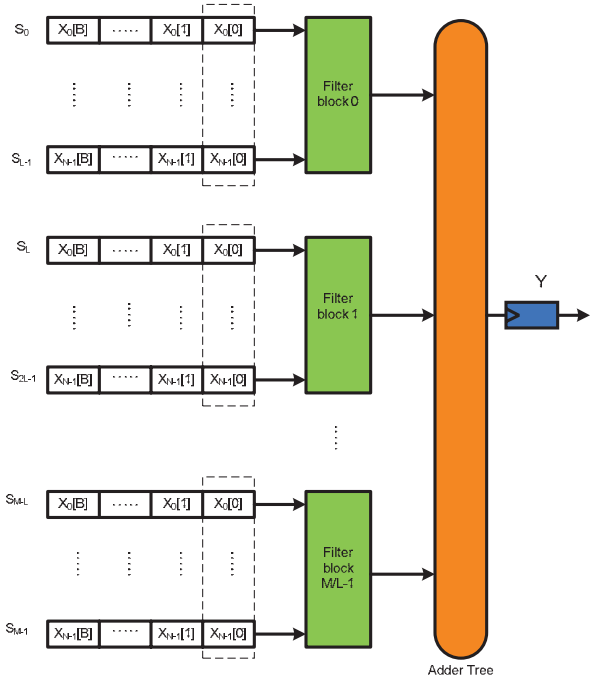

Figure 4. Higher-order Symmetry type FIR filter using DA

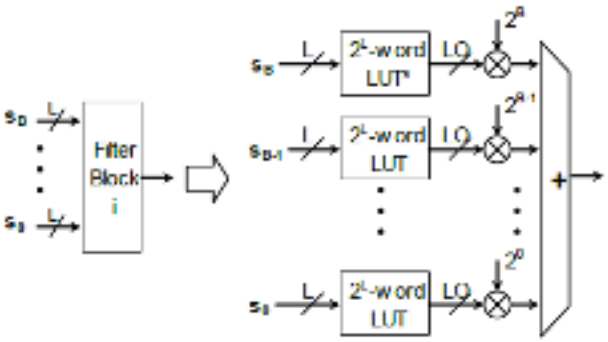

Figure 5. The internal structure of the filter block

IV. Results

The complexity of the filter architecture depends on the parameters of the filter, such as the number of taps, number of bits for filter coefficients, number of bits for input sample, and input size of LUT. In this work, FIR filter architectures are implemented using the proposed method for the order of N = 8, 16, and 32. The number of input samples and coefficients are denoted by 8-bits for all orders of the filters. These filters are decomposed with a factor or block size of L = 4, then the input size of the LUT is 4.

CVR Journal of Science and Technology, Volume 21, December 2021
DOI: 10.32377/cvrjst2115

The developed FIR filters are coded in Verilog HDL. The code is validated and synthesized employing FPGA as the target device in Xilinx tools. The utilization summary of all these filters is analyzed and compared in table III in terms of slice LUTs, slice registers, LUT-FF pairs, and adders. It can be noted that the filter architecture with symmetry required a fewer number of hardware blocks than filters without symmetry.

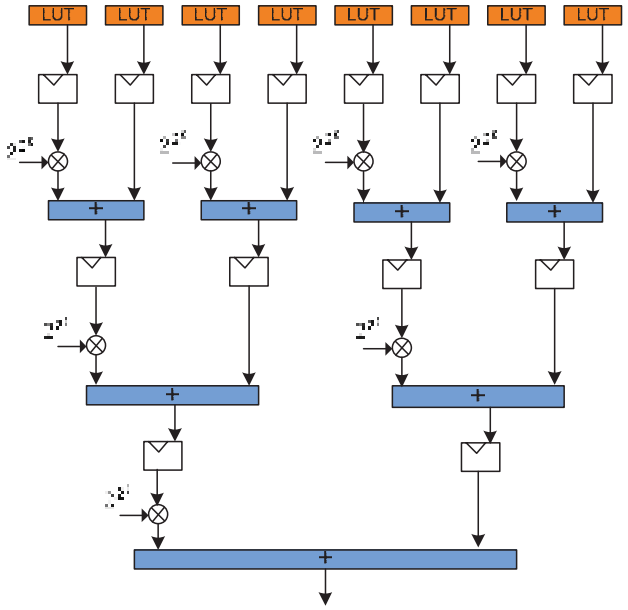

Figure 6. Adder tree and embed shifters in each level.

Next, the same Verilog codes are synthesized on the platform of ASIC design. The Genus tools are used to synthesize the design in CMOS 90nm library, and area, delay, and power reports are generated. The physical design is carried out by Innovus tools from Cadence. The final physical design layout of the chip is generated. The comparison of area, delay, and power values computed by synthesis tool for the proposed architecture with various order of the filters are presented in Table IV.

TABLE III.
FPGA UTILIZATION SUMMARY

Type of filter	Order	Slice Reg.	Slice LUT	No of LUT-FF pairs	Adder
Filter without symmetry	8	2582	98	34	67
	16	3562	146	58	132
	32	8759	193	62	215
Proposed filter with symmetry	8	2038	85	26	77
	16	3088	132	43	148
	32	7238	178	59	230

TABLE IV.
COMPARISON OF VLSI DESIGN METRICS

	order	Area (μm^2)	Delay (ns)	Power (mW)	ADP ($\mu m^2.\mu s$)
Proposed filter with symmetry	8	5965	8.256	1.956	11.66
	16	7986	8.986	2.489	19.87
	32	11255	9.012	3.089	34.76

The graphical analysis of delay and power consumption values of developed architecture with different values of N is shown in Fig. 7. The area comparison in the form of a bar chart of the proposed filter for N = 8, 16, and 32 is shown in Fig. 8.

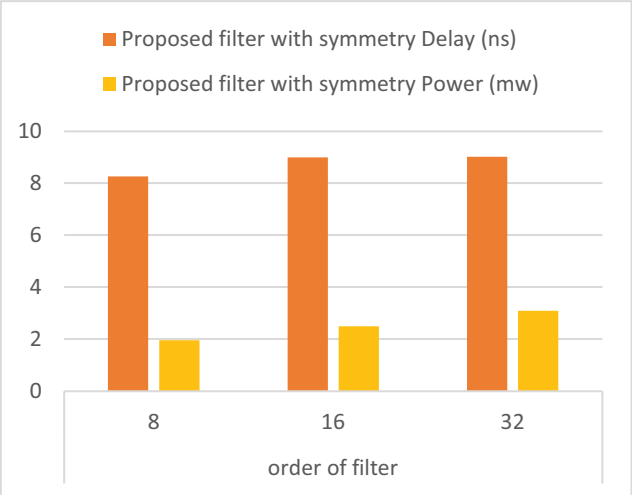

Figure 7. Delay and power values comparison with different order of the filter

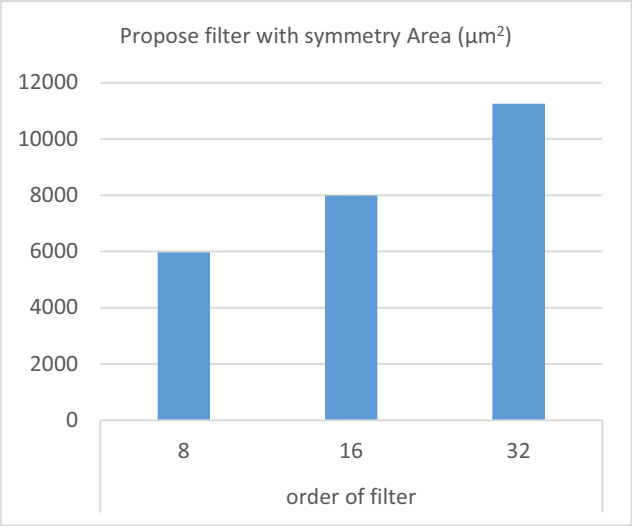

Figure 8. Area comparison with different order of the filter

CVR Journal of Science and Technology, Volume 21, December 2021
DOI: 10.32377/cvrjst2115

The VLSI design metrics of the proposed FIR filter architecture reported by ASIC design tools are compared with state-of-artworks in Table V. The graphical comparison analysis of delay-power, and area of proposed architecture with existing architectures are shown in Fig. 9 and Fig. 10 respectively. The final physical design layout is generated by Innovus tools presented in Fig.11.

TABLE V.
COMPARISON OF AREA, DELAY, AND POWER OF PROPOSED FILTER WITH STATE-OF-ARTWORKS.

Various works	order	Area (μm^2)	Delay (ns)	Power (mW)
Naga Jyothi et al. [9]	16	18956	7.45	16.1
Naga Jyothi et al. [10]	16	16688	1.38	9.42
Meher et al. [11]	8	14855	5.20	6.81
	16	29667	5.60	12.08
	32	59244	5.60	24.00
Proposed filter	8	9965	4.256	3.956
	16	12986	4.986	6.489
	32	17125	5.012	11.089

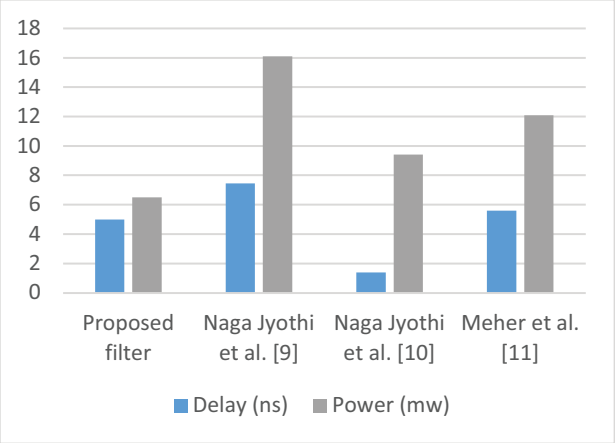

Figure 9. Delay and power comparison of the proposed filter with existing filters.

Figure 10. Area comparison with existing filter architectures

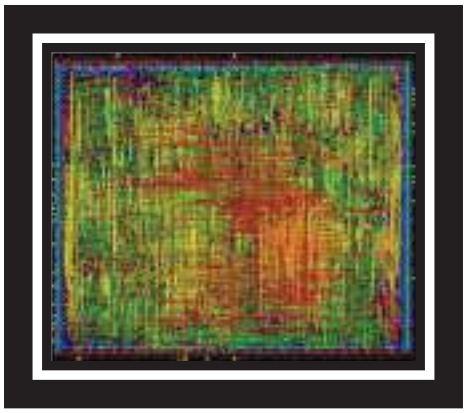

Figure 11. Physical design layout of proposed FIR filter architecture in 90 nm technology.

V. CONCLUSIONS

In this paper, an area, delay, and power-efficient DA-based FIR filters are implemented in the ASIC platform. The symmetry in the filter coefficients reduces the number of multipliers required for the filter architecture. Further, the multiplier complexity is decreased using the DA technique. In the DA-based filters, the multiplication is carried out by shift and add operations only using memory element LUT.

The Large size LUT is required for higher-order filters. This complexity of the LUT is overcome by the decomposition of the filter into an L number of filter blocks. In each filter block, DA formation is applied and the final output is generated using an optimized adder tree. The FIR filter architecture is implemented for N = 8, 16, and 32 using ASIC-based tools Genus and Innovus from Cadence. The area, delay, and power parameters of the proposed architecture are compared with state-of–artworks. The same design is validated and synthesized using Xilinx tools for the target device is FPGA. The utilization summary of HDL synthesis is also compared.

REFERENCES

[1] Rammohan, S. Radha, et al. "High-performance hardware design of compressor adder in DA based FIR filters for hearing aids." *International Journal of Speech Technology* 23.4, 807-814, 2020.

[2] Grande, N.J., Sridevi, S. Asic implementation of shared LUT based distributed arithmetic in fir filter. *In 2017 International Conference on Microelectronic Devices, Circuits and Systems* (ICMDCS), pp. 1–4. IEEE, 2017.

[3] Park, S. Y., & Meher, P. K. (2014). Efficient FPGA and ASIC realizations of a da-based reconfigurable fir digital filter. *IEEE Transactions on Circuits and Systems II*, *61*(7), 511–515.

[4] Khan, Shaheen, and Zainul Abdin Jaffery. "Low power FIR filter implementation on FPGA using parallel Distributed Arithmetic." *2015 Annual IEEE India Conference (INDICON)*. IEEE, 2015.

[5] Naga Jyothi, Grande, and Sriadibhatla Sridevi. "High speed and low area decision feed-back equalizer with novel memory less distributed arithmetic filter." *Multimedia Tools and Applications* 78.23 (2019): 32679-32693.

[6] Guo, Rui, and Linda S. DeBrunner. "Two high-performance adaptive filter implementation schemes using distributed

arithmetic." *IEEE Transactions on Circuits and Systems II: Express Briefs* 58.9 (2011): 600-604.

[7] Upadhyay, Ankit, and Uday Panwar. "High-Performance VLSI Architecture for Transpose Form FIR Filter using Integrated Module." *2018 International Conference on Computer Communication and Informatics (ICCCI)*. IEEE, 2018.

[8] Prakash, M. Surya, and Rafi Ahamed Shaik. "Low-area and high-throughput architecture for an adaptive filter using distributed arithmetic." *IEEE Transactions on Circuits and Systems II: Express Briefs* 60.11 (2013): 781-785.

[9] Jyothi, Grande Naga, Anusha Gorantla, and Thirumalesu Kudithi. "Asic implementation of linear equalizer using adaptive fir filter." *International Journal of e-Collaboration (IJeC)* 16.4 (2020): 59-71.

[10] Mohanty, Basant Kumar, et al. "A high-performance VLSI architecture for reconfigurable FIR using distributed arithmetic." *Integration* 54 (2016): 37-46.

[11] Park, Sang Yoon, and Pramod Kumar Meher. "Efficient FPGA and ASIC realizations of a DA-based reconfigurable FIR digital filter." IEEE Transactions on Circuits and Systems II: Express Briefs 61.7 (2014): 511-515.

[12] NagaJyothi, Grande, and Sriadibhatla Sridevi. "High speed low area OBC DA based decimation filter for hearing aids application." *International Journal of Speech Technology* 23.1 (2020): 111-121.

[13] Meher, P. K. (2006). Hardware-efficient systolization of DA-based calculation of finite digital convolution. *IEEE Transactions on Circuits and Systems II: Express Briefs*, *53*(8), 707–711.

[14] Meher, P. K., & Park, S. Y. (2011). High-throughput pipelined realization of adaptive FIR filter based on distributed arithmetic. *In VLSI and System-on-Chip (VLSI-SoC),* 2011 *IEEE/IFIP 19th International Conference on*, pp. 428–433. IEEE.

E-ISSN 2581 – 7957
P-ISSN 2277 – 3916

CVR Journal of Science and Technology, Volume 21, December 2021
DOI: 10.32377/cvrjst2116

A Survey on COVID-19 Future Forecasting using Machine Learning Models

Syed Asif Ali [1] and Bipin Bihari Jaya Singh [2]
[1] PG Scholar, CVR College of Engineering/ IT Department, Hyderabad, India
Email: syedasifali891@gmail.com
[2] Professor, CVR College of Engineering/ IT Department, Hyderabad, India
Email: bbjayasingh9@rediffmail.com

Abstract: **Predictive methods for Learning Machines (MLs) have proved their worth in expecting long-term performance results to improve decision-making over the course of future action. ML models have long been used in many application domains that need to be identified and prioritized against negative threats. Many prediction methods are widely used to manage prediction problems. This study demonstrates the ability of ML models to predict the future of affected patients by COVID-19 and they are currently considered to be a threat to humanity. Predictions are made by each Machine Learning model to determine the number of confirmed cases in upcoming days. In this paper, the review is undertaken for a few methodologies that are applied to the solution of COVID19 problem. The ML model architecture is proposed with a day wise and country wise analysis for confirmed cases of COVID19 problem.**

Index Terms: **COVID-19, Machine Learning methods, Time series methods future forecasting, adjusted R2 score, supervised machine learning**

I. Introduction

Over the past decade, machine learning (ML) has become an important element of research by solving very complex and sophisticated real-world problems. Applications include Healthcare, Autonomous Vehicles (AV), Business Applications, Natural Language Processing (NLP), Intelligent Robotics, Gaming, Climate Modeling, Voice and Image Processing. The goal of this research is to develop an early warning pattern for the spread of a new coronavirus, also known as SARS-CoV-2.

The World Health Organization (WHO) has designated COVID-19 as its official designation. COVID-19 is currently a major threat. Human life is under danger all across the planet. By the end of the year, the virus was first discovered in the Chinese city of Wuhan. When a huge number of people begin to experience symptoms such as Pneumonia It affects the human body in a variety of ways. severe acute respiratory syndrome with multi-organ failure that can result in mortality in a short period of time. Significant symptoms of COVID-19 flu include cough, shortness of breath and diarrhea in other patients. The biggest problem with the disease is that its symptoms usually appear after 14 days.

Estimates have been made for the number of new confirmed cases in the coming days. This work treats assessment as a regression problem; The research is therefore based on several state-of-the-art supervised machine learning regression models and time series models.

II. Literature Survey

E. Gambhir et al [1] This study attempts to give readers a better understanding of how a different Machine Learning model that is Support Vector Machine and Polynomial Regression Algorithm might be used in real-world scenarios. In SVM for classification or outlier detection, it creates a hyperplane or set of hyperplanes in an N-dimensional space. Linear Regression can be thought of as a specific case of Polynomial Regression. Linear regression works with continuous data that is known and two variables that are correlated (target variable and independent variable). What if we knew variables were associated but the connection did not appear to be linear? We could apply polynomial regression to fit a polynomial equation to our dataset.

In this study work, the current Covid-19 transmission trend in the world has been successfully studied. Estimating the prevalence of Covid-19, also known as the novel coronavirus, helps to implement appropriate control measures. In this article there is still a need for in-depth research of the viral outbreak scenario in India and further exploration for future improvements. Further research may include looking at datasets from India and estimating the number of cases in the future, as well as how the death rate will change as the number of cases increases.

Petropoulos F et al [2] The document details the timeframe of a live forecasting exercise with far-reaching ramifications for planning and decision-making, as well as objective projections for COVID-19 cases that have been confirmed. Simple time series forecasting algorithms are used to predict confirmed instances of COVID-19. The exponential smoothing family of models is used to provide forecasts. The exponential smoothing family has demonstrated strong forecast accuracy in several forecasting competitions, and it is particularly well suited to short series. Exponential smoothing methods can capture a wide range of seasonal and trend forecasting patterns.

The fact that the tendency slowed over this time indicated that COVID-19 would not cause major concerns, especially outside of Mainland China. That was not the case, unfortunately. The most recent predictions, covering the period 02/03/2020 to 21/03/2020, suggest a considerable increase in the global trend of cases, as well as a rise in the accompanying uncertainty. The study also featured a detailed analysis of the outbreak situation which must still be uncovered to make future improvements. We believe that our predictions will help governments and individuals make

Received on 30-09-2021, Revised on 03-11-2021, Accepted on 05-12-2021.

informed judgments and take the necessary steps to limit the virus's spread as much as possible.

Kim S et al [3] The document describes the slowdown in the spread of COVID-19 due to social isolation and behavioural adjustments in the Republic of Korea (ROK). In addition, if vaccines or antiviral drugs are not ready by the fall, the second wave of a pandemic is likely.

Furthermore, if no vaccine or antiviral medications are ready by the fall, a second wave of the epidemic is likely. The impact of non-pharmaceutical strategies on short- and long-term outbreak dynamics was studied in this study. A deterministic compartment model was used to create a dynamic model of COVID-19 transmission. Individuals were categorised into six categories: susceptible, behavior-changed susceptible, exposed, infected, isolated, and recovered. With the incubation of the virus, individuals in the susceptible group become infected and move to the exposed group. Individuals who have been exposed to the virus join the infectious group. As the number of confirmed and isolated cases grows, susceptible people change their behaviour and join the behavior-changed susceptible group, which has a decreased transmission rate.

When it comes to limiting the spread of new infectious diseases for which treatments are not available, social distance can be successful. It is important that the general public be actively involved and implement appropriate government policies. Susceptible individuals need to be aware of the risk of disease and follow proper preventive measures. On the other hand, it is not possible to remove COVID-19 by simply using non-pharmaceutical techniques. Long-term social isolation is linked to a substantial socioeconomic cost. The availability of vaccines and antiviral medications is critical to bringing the COVID-19 epidemic to an end. More research is needed to see how non-pharmaceutical and pharmacological therapies might be balanced.

O. Tutsoy et al [4] The Susceptible-Infected-Recovered (SIR) model, which is widely used to estimate COVID-19 mortality, is first reviewed, and analysed in this study. The paper next introduces the Suspicious-Infected-Death (SpID) model, which is a novel higher-order, multi-dimensional, tightly linked, and parametric model. The model's three compartments are represented by SIR. Susceptible persons are those who are at risk of becoming infected if they come into contact with infectious people. When the infection occurs, they might be patient. Infectious persons are represented by the infectious group. They can spread the disease to others who are susceptible, and they can recover in a set amount of time. The number of recovered pearson's R is not included in the SpID model as it is in the SIR model since the optimization algorithms primarily focus on minimization, such as the number of suspects, infected, and dead people, rather than maximising, such as the number of recovered people.

The results showed that the Susceptible-Infected-Recovered (SIR) model can accurately predict Turkey's casualties. Furthermore, the model forecasts that the number of infected and diseased people will be at their lowest in 300 days, while the number of suspicious casualties would be at its lowest in 1000 days. The suggested model considers suspicious, infectious, and death casualties, but excludes critical care and intubation, non-pharmacological policies, pharmaceutical policies, and unknown uncertainty. Due to this reason further research is required and needs improvement.

R. Kumari et al [5] The work examines recently established forecasting models in depth and anticipates the number of confirmed, recovered, and mortality cases caused by COVID-19 in India. For prediction, correlation coefficients and multiple linear regression were utilised, as well as autocorrelation and autoregressive to increase accuracy. The suggested model, the degree of variables in the dataset must be discovered and computed, and this information is useful in better preparing the dataset to fulfil the requirements of machine learning algorithms. Python software is used to do a recovery technique and a correlation analysis on data. It provides a statistical overview of confirmed, recovered, and death cases, as well as a high correlation between current data. With the use of confirmed and recovered cases, multiple regression analysis is utilised to forecast cases of death. More than one variable is used to predict the outcome in this regression procedure. When more than one independent variable is used to predict a target variable, it is useful. Multiple linear regression approaches are employed in predictive analysis to explain the link between two independent variables (confirmed and recovered cases) and one dependent variable (death cases).

The predicted and actual values are very close to each other. This prediction could be useful in resource management, such as health care, and prompt action could be performed with previous planning to decrease human life loss. The Multiple regression and Autoregressive model could be used to forecast when the epidemic would stop in a certain region. Further surveys are required to get exact results.

R. K. Singh et al [6] We show how a COVID-19 projection for India at various administrative levels may be produced using an easily transferable statistical model based on the standard Holt-Winters approach. We apply our statistical model to produce 48-day estimates of these values in India based on a daily time series of accumulated infections, active infections, and deaths, assuming little change in national coping strategies. Using these findings in conjunction with a supplemental SIR model, we predict that one-third of the Indian population could be infected with COVID-19 at some point, and that complete recovery from COVID-19 will take an estimated 450 days.

The Holt-Winters technique is a time series forecasting approach that can account for both trend and seasonality. The Holt-Winters approach is made up of three other, much simpler smoothing methods that are Simple Exponential smoothing (SES), Holt's Exponential Smoothing (HES) and Winters Exponential Smoothing (WES). In a closed community, a SIR model computes the theoretical number of people infected with an infectious illness over time. The name of this class of models comes from the fact that they use coupled equations to relate the number of vulnerable individuals, infected people, and recovered people.

CVR Journal of Science and Technology, Volume 21, December 2021
DOI: 10.32377/cvrjst2116

The results of short-term statistical forecasts using the Holt-Winters approach imply that this method could be suitable for producing operational COVID-19 forecasts in India at various administrative levels. In general, Holt-Winters models record the level and most recent trend of a time series and are thus inadequate for long-term projections in circumstances like this one where there is no seasonal signal. More advanced mathematical-epidemiological models are necessary for such forecasts, necessitating additional research.

V. K. Gupta et al [7] In this paper we are solely looking for COVID-19 cases in India, which includes confirmed, deceased, and cured cases. We are doing this study based on cases that happened in different parts of India at different times. We cleansed the data and selected features, then forecasted all classes using random forest, linear model, support vector machine, decision tree, and neural network, finding that the random forest model outperformed the others. As a result, the random forest is used to predict and analyse all the results. The K-fold cross-validation is used to assess the model's consistency. The random forest is a classification algorithm that uses numerous decision trees to classify data. When creating each individual tree, it employs bagging and feature randomization to generate an uncorrelated forest of trees whose committee prediction is more accurate than that of any one tree. Multinomial logistic regression is a classification technique that extends logistic regression to issues with more than two discrete outcomes. We are utilising feed-forward neural networks with a single hidden layer and maybe skip-layer connections in this example. SVM can be used to classify or predict data. The input features are represented as vectors that are projected onto a higher-dimensional space. After that, an ideal hyperplane is built to separate the different instances of confirmed, death, and cured cases.

Because Random Forest is an ensemble model that uses bagging for sampling, we were blown away by its performance when compared to other models. Because the research is restricted, more research is required.

III. METHODOLOGIES

Machine learning is a branch of computer science that allows computers to learn without explicit programming. Machine learning is one of the most interesting methods. As the name suggests, it provides the computer with the ability to learn, which makes it more human. Machine learning is in vogue right now, probably in far more places than expected. Humans can learn from their past experiences, but computers cannot. Machine learning is a branch of artificial intelligence that helps systems learn from their past experiences and improve them without the need for human intervention. In other words, machine learning is similar to gardening. Seeds algorithms, nutrient data, you gardeners, and plants programs. Its main purpose is to create computer programs. Machine learning is inextricably linked to data analysis and statistics since the effectiveness of a learning algorithm is determined on the data used. Learning techniques, in general, are data-driven methods that combine core computer science concepts with notions from statistics, probability, and optimization. Machine learning is used in a variety of industries, including pharmaceutical, military, marketing, and security. The system uses machine learning algorithms to analyze datasets, including daily actual past data, and make predictions for future days.

Neural networks currently occupy a very important place in machine learning. Using neural networks makes it possible to capture abstract features from original data and therefore fulfill our goal of assessing the epidemic situation in a novel manner. The simplest and most intuitive neural network is a fully connected neural network. The neuron is its most basic component. Neurons can extract input from previous neurons in the previous layer and use the activation function to perform nonlinear modifications. A sophisticated nonlinear task occurs when all neurons combine with the appropriate structure, weighting, and bias. A neural network can theoretically equip any complex task with infinite neurons, which allows it to perform any task. On the other hand, better performance and shorter calculation time are not favorable. It is important to design a network with a specific feature to balance performance and time consumption.

A. Linear Regression

Regression analysis is a statistical study of dependencies and the relationship between two or more independent variables. There are still many regression techniques, but linear regression is the most commonly used.

In regression analysis, linear models and linear regression are mostly used. In that sequence, linear regression was also used. Linear regression is based on variables that use a large number of independent variables. From day to day, the independent variables vary. The built-in linear model involves the relationship between the underlying parameters and the data points. To determine accuracy and prediction, the rail and test approach is used. The system can be trained and tested with autonomy before making estimates.

B. The KNN algorithm

The KNN algorithm (k-nearest neighbor) is also widely used. Both taxonomy and regression approaches can be used with KNN. In the field of regression analysis, the KNN regression model is widely used. As a result, the KNN model was implemented, and the method performed superbly. The result of KNN regression is an attempt to give prominence to the object. The average value is KNN. It sets the average numerical target of the algorithm. The distance function is the same in KNN regression and taxonomy. etal [14] KNN's next 90 days (k-nearest neighbor) forecast This is the KNN-based forecast result. Prediction Linear regression is similar to the prediction result. Trained data using train and test approach. The machine isolated all this information. It splits the train automatically and tests the data after learning the data. Dhaka City data were compiled differently, so linear regression and k-nearest neighbors gave the same result. Its accuracy is determined, which helps us to understand the operation of the whole model.

CVR Journal of Science and Technology, Volume 21, December 2021
DOI: 10.32377/cvrjst2116

C. Polynomial Regression

Linear regression can be considered as a specific context of polynomial regression. Linear regression works with both known continuous data and interrelated variables (target variable and independent variable). What if we know that the variables are connected, and the connection does not appear to be simple? We can apply polynomial regression to fit polynomial equations in our dataset. Polynomial Regression is a supervised Machine Learning Algorithm that is learned using previous data and then validated using another dataset.

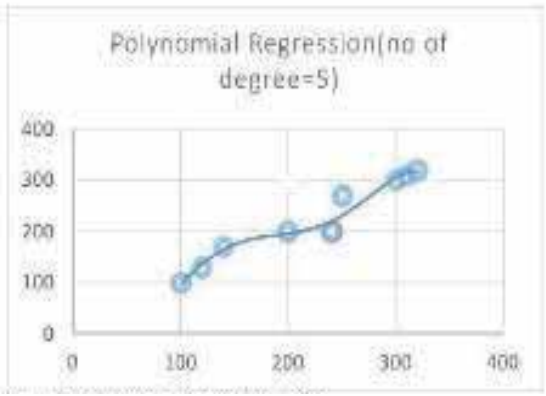

Figure 1. Polynomial Regression of degree 5

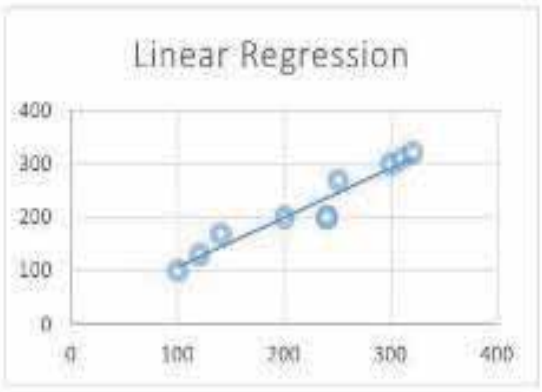

Figure 2. Linear Regression

M. Singh et al [13] Because the loss function and error rate in a simple linear model are high, the accuracy predicted by the simple linear model is lower than the accuracy predicted by the Polynomial model for non-linear data sets like those shown in Figures 1 and Figure 2. As a result, Polynomial Regression is a linear model with minor modifications that helps to improve accuracy for non-linear and complex datasets.

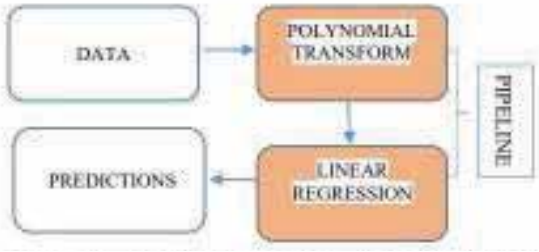

Figure 3. Pictorial representation of implementation of polynomial Regression

We utilize the Polynomial Features function to transform the data into a polynomial, and then use linear regression to fit the parameter in polynomial regression. The graphic illustration of this can be found in Figure 3. The polynomial characteristics convert the equation into an nth (degrees) equation. So, we must select it carefully because if the degree of polynomial is too low, the data will not fit, and if it is too high, the data will be overfit.

V. K. Gupta et al [7], The train and test data were converted for polynomial regression. the expected values from August 7, 2020, to August 28, 2020, as depicted visually. As a result, the polynomial Regression Algorithm has a 93 percent accuracy. Feature Selection To get the greatest results from our model, this stage involves feature extraction and selection. Having good and best features allows us to visualize the data's underlying structure. Feature Engineering has a substantial impact on the model's performance. It could entail separating or aggregating features to create new ones, or it could entail gathering data from external sources.

E. Gambhir et al [1], Dimensionality reduction makes it easier to evaluate and draw conclusions from a dataset. The dates were eliminated, and the useless parameters such as longitude and latitude were removed in order to draw better inferences from this dataset. Were transformed into a date-and-time object.

A. Bansal et al [10], Feature selection techniques are used in machine learning because they reduce training time, simplify the model so that users and researchers can understand it, reduce the dimensionality curse, and improve generalization. Another significant advantage of removing redundant or irrelevant features is that less redundant data translates to fewer decisions based on noise, resulting in less overfitting.

Information gain is used in mutual information feature selection to calculate the surprise or reduction in entropy caused by dataset transformation in some way. Typically, information gain is used by evaluating the information gain of each variable and then selecting the variable that minimizes entropy by maximizing information gain and splitting the dataset best into groups for effective classification. Each variable's gain in the context of the target variable is evaluated for the purpose of using information gain in feature selection. The calculation is reciprocal between the two randomly chosen variables.

CVR Journal of Science and Technology, Volume 21, December 2021
DOI: 10.32377/cvrjst2116

Recursive feature elimination removes recursive features and builds the model on the attributes that remain. The draper feature elimination technique is illustrated by recursive feature elimination. Model accuracy is used in this case to determine which attributes from the list of attributes would contribute the most to helping predict the target variable.

Correlation is defined as a measure of how two variables change in relation to one another in correlation feature selection. It is not uncommon for some features, despite being designed to measure different qualities, to be influenced by a common mechanism and to vary in tandem.

D. Fbprophet

Fbprophet An open-source algorithm developed by Facebook to estimate time-series data using an additive model to match non-linear trends with annual, monthly, and daily seasonal as well as holiday effects. It works best with time series with significant seasonal effects and multi-season historical data. The Prophet apologized for the missing data and trend shifts and it usually handles outliers well. We validate our data against the rolling mean, just like any other time series model.

There are three target classes in our dataset, each with many discrete instances. The following are the target classes:

(1) Confirmed cases: The number of instances that have been confirmed as of a specific date. It can be increased or decreased based on the following day, time, and location, which is only applicable to Indian states.

(2) Death cases: The total number of death cases at any given time. It can be increased or decreased based on the following day, time, and location, which is only applicable to Indian states.

(3) Cured cases: The total number of cured cases at any given time. It can be increased or decreased based on the following day, time, and location, which is only applicable to Indian states.

E. Performance Tuning

V. K. Gupta et al [7], The popular prediction models utilized in the investigation are listed in Figure 4, and the packages employed by these models are open-source libraries written in the R programming language and licensed under the GNU GPL. All of the packages are used here, each with its own way for model building. which are tuned for better results.

Model	Method	Required package	Tuning parameter
Random forest	randomForest	randomForest	mtry=2, ntree=500
SVM	svm	e1071	kernal=radial, degree=3
Decision tree	rpart	rpart	usesurrogate=0
Neural network	nnet	nnet	size=10
Multinomial logistic regression	multinome	nnet	maxit=1000

Figure 4. Machine learning models and their tuning parameters

IV. Study on Covid-19

Many researchers have participated in the study of the novel coronavirus after an outbreak in Wuhan, China in late December 2019 and developed a variety of models to predict its spread, transmission, and mortality. Some studies and research are related to drug development and a tool to diagnose the epidemic. Here are a few of the latest lessons discussed here.

Zhong et al. [15] developed a statistical model for forecasting timely coronavirus outbreaks in China. Hamzah et al. [16] developed an online platform for providing real-time information related to COVID-19 and statistical analysis of data. The Susceptible-Exposed-Infectious-Recovered (SEIR) prediction model has been used for daily forecasting. They have improved their small services to download data from different sources.

Morawska and Coo [17] discussed how COVID-19 spreads, especially in the air. Li et al. [18] investigated genetic mutations COVID-19 virus. This study has shown that the novel coronavirus has genetic similarities with the coronavirus found in rhinolophus sinicus, paradoxurus hermaphroditus, paguma larvata, aselliscus stoliczkanus, and civet, while homologous analysis shows that it is almost identical to the bat coronavirus.

Ma et al. [19] analyzed the effect of humidity and changes in the temperature of COVID-19 patients, but the study was limited to the city of Wuhan only. This study established a combination of temperature and humidity variations in daily deaths from the virus. Singh et al. [20] studied and compared SARS, MERS, and COVID-19 viruses based on transmission cycle, etiology, genetics, management, diagnosis, birth rates, laboratory diagnoses, clinical features, and radiation characteristics.

Pal et al. [21] showed the separation of ribonucleic acid bacterial group and origin of acute coronavirus respiratory and virion structure and genetic COVID-19 genes. Dutheil et al. [22] investigated the role of COVID-19 in reducing air pollution as many industries closed again and traffic is also very low.

Singh et al. [23] analyzed time series data and predicted the enrollment, death, and death rates for each reported case (death rate) based on COVID-19 global health data. This study concluded that the normal mortality of COVID-19 is positively correlated with the number of confirmed cases. It can also depend on the human diet process and the strength of the immune system. The study suggested that an emergency could arise prior to a proper injection. Other critical issues were assessed by several researchers, taking into account individual countries, provinces, and specific conclusions. Bhatnagar et al. [24] presented a detailed analysis of the COVID-19 epidemic with the help of boxplot and Q.

Ivanov et al. [25] analyzed and predicted the effects of the ongoing epidemic on land supply chains. They also performed a cost-based analysis of the condition of supply chains and the impact of COVID-19 on supply chains and associated risks. Hou et al. [26] conducted a SEIR model

CVR Journal of Science and Technology, Volume 21, December 2021
DOI: 10.32377/cvrjst2116

analysis to evaluate the functioning of the segregation of people especially the city of Wuhan and to develop new variations of the SEIR model. They conclude that isolation and separation are two powerful and unique tools to reduce the risk of infection. Roosa et al. [27] developed the COVID-19 predictive system in real time in China for some time. Tuli et al. [28] used the latest technology, such as machine learning and cloud computing, to predict the growth rate of the COVID-19 epidemic with the help of the Weibull model.

Xu et al. [29] described the pathogenesis of COVID-19 and compared it to SARS and MERS. These pathological features are very similar to SARS and MERS. The study provided some recommendations for doctors so that they could arrive on time, develop a patient treatment plan. Kucharski et al. [30] performed a mathematical model and analyzed four data sets. The study found that the transmission rate is between 1.6 to 2.6. Here they classify patients into four distinct categories: they can be infected, exposed (but not yet acquired), contagious, and removed (i.e., separated, recovered, or no longer infected). Yuvaraj et al. [31] A comprehensive neural network was used to analyze SARS-CoV-2 protein-ligand interactions against selected drugs. Other studies focused on the mental health of farmers involved in the poultry business [32].

Researchers are also working on experimental procedures and are trying to reduce the testing time. In this sequence, Assad et al [33] suggested that sample integration is the best way to do it, reducing the probationary period leading to a reduction in mortality but by a minimum of 10% positive cases. If the positive charges are very low, binary elimination algorithms are the best option.

V. Steps for ML Algorithms Implementation

Italy, USA, UK, and France are the two countries currently in Section 4 While India is in Section 3. This study attempts to establish a system for pre-distribution of the number of cases affected by COVID-19 using machine learning methods. The data used for the study include daily reports of cases of recent infections worldwide because of COVID-19. This is a shocking situation in the world as the number of confirmed cases is increasing day by day. The number of people affected by the Covid-19 pandemic in different parts of the world is not well known.

A. Data Preprocessing

The purpose of this step is to convert raw data into a form suitable for machine learning. Systematic and clean data allows the data scientist to obtain accurate results from the machine learning model used. This process includes data formatting, cleaning, and modeling. At the modelling stage, the data scientist trains many models to explain which one of them gives the most accurate predictions.

B. Model Training

The data scientists first collect the data and divide it into three subsets, he could proceed with model training. This process involves “feeding” the algorithm with training details. The algorithm will process the data and extract a model that is able to find the target value (attribute) in the new data - the answer you want to get by predicting analysis. The purpose of model training is to improve the model. Two styles of model training are very common - supervised and supervised learning. The choice of each style depends on whether you have to predict certain attributes or elements of group data in the same way.

Supervised Learning allows processing of data by targeted signals or labeled data. These qualities are mentioned in the historical data prior to training. With supervised learning, a data scientist can solve planning and deferred problems.

Unsupervised learning, with this training style, the algorithm analyzes unlabeled data. The purpose of model training is to find hidden connections between data objects and structural similarities or differences. Unsupervised learning aims to solve problems such as assembly, learning about the rules of assembly, and size reduction. For example, it can be used in data, furthering the phase to reduce the complexity of the data.

C. Model Testing

The purpose of this step is to develop a simpler model that is able to create a target value quickly and efficiently. A data scientist can achieve this goal by modifying the model. That is the use of model parameters to achieve the best performance of the algorithm One of the most effective methods of model testing and correction of the opposite

D. Cross Validation

Validation is very common and the planning method is used. Includes separate training database into ten equal parts (folders). The model provided is training only nine folders and then tested in the tenth (the one that had been left out). Training continues until the entire herd is set aside and used for testing. As a result of the model performance measurement, the specialist calculates the accumulated points for each set of parameters. A data scientist trains models with different sets of hyperparameters to define which model has the highest predictive accuracy. Guaranteed points fall on the performance of the middle model in ten catch folders. There the data scientist examines models with hyperparameter values that find the best guaranteed points. There are various error metrics for machine learning activities.

VI. Conclusions

Machine learning (ML) is the study of computer algorithms that improve themselves over time using data and experience. Artificial intelligence is considered a factor in this. Machine learning algorithms design a model based on sample data, referred to as "training data", without being specifically programmed to make predictions or decisions. Machine learning algorithms are used in a wide variety of applications, including medicine, email filtering, speech recognition and computer vision, where it is difficult or impossible to develop traditional algorithms to perform the required tasks. This paper highlights the recent research on Covid-19 Future forecasting using Machine Learning

Algorithms, focusing mainly on approaches based on number of newly infected cases, number of deaths and number of recovered. Different methods were compared in terms of processing time, complexity, discrimination, and rigidity. In terms of discrimination, complexity, and accuracy, we may conclude that Machine Learning approaches are the best option. By publishing this survey study, we hope that researchers in this field will be encouraged to pay more attention and collaborate on the use of localized approaches in machine learning systems.

REFERENCES

[1] E. Gambhir, R. Jain, A. Gupta and U. Tomer, "Regression Analysis of COVID-19 using Machine Learning Algorithms," *2020 International Conference on Smart Electronics and Communication (ICOSEC)*, 2020, pp. 65-71, doi: 10.1109/ICOSEC49089.2020.9215356.

[2] Petropoulos F, Makridakis S. Forecasting the novel coronavirus COVID-19. PLoS One. 2020 Mar 31;15(3):e0231236. doi: 10.1371/journal.pone.0231236. PMID: 32231392; PMCID: PMC7108716.

[3] Kim S, Ko Y, Kim YJ, Jung E. The impact of social distancing and public behavior changes on COVID-19 transmission dynamics in the Republic of Korea. PLoS One. 2020 Sep 24;15(9):e0238684. doi: 10.1371/journal.pone.0238684. PMID: 32970716; PMCID: PMC7514094.

[4] O. Tutsoy, Ş. Çolak, A. Polat and K. Balikci, "A Novel Parametric Model for the Prediction and Analysis of the COVID-19 Casualties," in IEEE Access, vol. 8, pp. 193898-193906, 2020, doi: 10.1109/ACCESS.2020.3033146.

[5] R. Kumari et al., "Analysis and predictions of spread, recovery, and death caused by COVID-19 in India," in Big Data Mining and Analytics, vol. 4, no. 2, pp. 65-75, June 2021, doi: 10.26599/BDMA.2020.9020013.

[6] R. K. Singh et al., "Short-Term Statistical Forecasts of COVID-19 Infections in India," in IEEE Access, vol. 8, pp. 186932-186938, 2020, doi: 10.1109/ACCESS.2020.3029614.

[7] V. K. Gupta, A. Gupta, D. Kumar and A. Sardana, "Prediction of COVID-19 confirmed, death, and cured cases in India using random forest model," in Big Data Mining and Analytics, vol. 4, no. 2, pp. 116-123, June 2021, doi: 10.26599/BDMA.2020.9020016.

[8] Y. Liu and Y. Xiao, "Analysis and Prediction of COVID-19 in Xinjiang Based on Machine Learning," 2020 5th International Conference on Information Science, Computer Technology and Transportation (ISCTT), 2020, pp. 382-385, doi: 10.1109/ISCTT51595.2020.00072.

[9] A. U. Mandayam, R. A.C, S. Siddesha and S. K. Niranjan, "Prediction of Covid-19 pandemic based on Regression," 2020 Fifth International Conference on Research in Computational Intelligence and Communication Networks (ICRCICN), 2020, pp. 1-5, doi: 10.1109/ICRCICN50933.2020.9296175.

[10] A. Bansal and U. Jayant, "Covid-19 Outbreak Modelling Using Regression Techniques," 2021 International Conference on Innovative Practices in Technology and Management (ICIPTM), 2021, pp. 113-118, doi: 10.1109/ICIPTM52218.2021.9388347.

[11] Z. Yang and K. Chen, "Machine Learning Methods on COVID-19 Situation Prediction," 2020 International Conference on Artificial Intelligence and Computer Engineering (ICAICE), 2020, pp. 78-83, doi: 10.1109/ICAICE51518.2020.00021.

[12] C. V. S. S. Nikil, H. Dalmia and G. J. R. Pavan Kumar, "Covid-19 Outbreak Analysis," 2020 International Conference on Smart Technologies in Computing, Electrical and Electronics (ICSTCEE), 2020, pp. 347-350, doi: 10.1109/ICSTCEE49637.2020.9276790.

[13] M. Singh and S. Dalmia, "Prediction of number of fatalities due to Covid-19 using Machine Learning," 2020 IEEE 17th India Council International Conference (INDICON), 2020, pp. 1-6, doi: 10.1109/INDICON49873.2020.9342390.

[14] A. Abdullha and S. Abujar, "COVID-19: Data Analysis and the situation Prediction Using Machine Learning Based on Bangladesh perspective," 2020 15th International Joint Symposium on Artificial Intelligence and Natural Language Processing (iSAI-NLP), 2020, pp. 1-8, doi: 10.1109/iSAI-NLP51646.2020.9376812.

[15] L. Zhong, L. Mu, 1. Li, 1. Wang, Z. Yin, and D. Liu, Early prediction of the 2019 novel coronavirus outbreak in the mainland China based on simple mathematical model, IEEE Access, vol. 8, pp. 51 761-51 769,2020.

[16] F. A. B. Harnzah, C. H. Lau, H. Nazri, D. V. Ligot, G. Lee, C. L. Tan, M. K. B. M. Shaib, U. H. B. Zaidon, A. B. Abdullah, M. H. Chung, et aI., Coronatracker: Worldwide COYID-19 outbreak data analysis and prediction, Bull World Health Organ, http://dx.doi.org/1O.2471IBLT.20.255695.

[17] L. Morawska and J. Cao, Airborne transmission of SARS CoY-2: The world should face the reality, Environment International, vol. 139, p. 105730, 2020.

[18] C. Li, Y. Yang, and L. Ren, Genetic evolution analysis of 2019 novel coronavirus and coronavirus from other species, Infection, Genetics and Evolution, vol. 82, p. 104285, 2020.

[19] Y. Ma, Y. Zhao, 1. Liu, X. He, B. Wang, S. Fu, J. Yan, J. Niu, 1. Zhou, and B. Luo, Effects of temperature variation and humidity on the death of COYID-19 in Wuhan, China, Science of the Total Environment, vol. 724, p. 138226,2020.

[20] A. Singh, A. Shaikh, R. Singh, and A. K. Singh, COYID-19: From bench to bed side, Diabetes & Metabolic Syndrome: Clinical Research & Reviews, vol. 14, no. 4, pp. 277-281, 2020.

[21] M. Pal, G. Berhanu, C. Desalegn, and V. Kandi, Severe acute respiratory syndrome coronavirus-2 (SARS-CoY-2): An update, Cureus, vol. 12, no. 3, pp. 1-13,2020.

[22] F. Dutheil, J. S. Baker, and V. Navel, COYID-19 as a factor influencing air pollution? Environmental Pollution, vol. 263,p.114466,2020.

[23] D. Singh, V. Kumar, V. Yadav, and M. Kaur, Deep convolutional neural networks-based classification model for COYID-19 infected patients using chest X-ray images, International Journal of Pattern Recognition and Artificial Intelligence, doi: 1O.1142/S0218001421510046.

[24] V. Bhatnagar, R. C. Poonia, P. Nagar, S. Kumar, V. Singh, L. Raja, and P. Dass, Descriptive analysis of COYID-19 patients in the context of India, Journal of Interdisciplinary Mathematics, doi: 10.1080/09720502.2020.1761635.

[25] D. Ivanov, Predicting the impacts of epidemic outbreaks on global supply chains: A simulation-based analysis on the coronavirus outbreak (COVID-19/SARS-CoY-2) case, Transportation Research Part E: Logistics and Transportation Review, vol. 136, p. 101922, 2020.

[26] C. Hou, J. Chen, Y. Zhou, L. Hua, J. Yuan, S. He, Y. Guo, S. Zhang, Q. Jia, C. Zhao, et aI., The effectiveness of quarantine of Wuhan city against the corona virus disease 2019 (COVID-19): A well-mixed SEIR model analysis, Journal of Medical Virology, vol. 92, pp. 841-848, 2020.

[27] K. Roosa, Y. Lee, R. Luo, A. Kirpich, R. Rothenberg, 1. Hyman, P. Yan, and G. Chowell, Real-time forecasts of the COYID-19 epidemic in China from February 5th to February 24th, 2020, Infectious Disease Modelling, doi: 10.1016/j.idm.2020.02.002.

[28] S. Tuli, S. Tuli, R. Tuli, and S. S. Gill, Predicting the growth and trend of COYID-19 pandemic using machine learning and cloud computing, Internet of Things, vol. 11, p. 100222, 2020.

[29] Z. Xu, L. Shi, Y. Wang, J. Zhang, L. Huang, C. Zhang, S. Liu, P. Zhao, H. Liu, L. Zhu, et aI., Pathological findings of COVID-19 associated with acute respiratory distress syndrome, The Lancet Respiratory Medicine, vol. 8, no. 4, pp.420-422,2020.

[30] A. J. Kucharski, T. W. Russell, C. Diamond, Y. Liu, J. Edmunds, S. Funk, R. M. Eggo, F. Sun, M. lit, J. D. Munday, et aI., Early dynamics of transmission and control of COYID-19: A mathematical modelling study, The Lancet Infectious Diseases, vol. 20, no. 5, pp. 553-558, 2020.

[31] N. Yuvaraj, K. Srihari, S. Chandragandhi, R. A. Raja, G. Dhiman, and A. Kaur, Analysis of protein-ligand interactions of SARS-CoY-2 against selective drug using deep neural networks, Big Data Mining and Analytics, doi: 10.26599/BDMA.2020.9020007.

[32] . Dhiman, The effects of coronavirus (COVID 19) on the psychological health of indian poultry farmers, Coronaviruses, doi: 10.2174/26667967019992 00617160755.

[33] A. Assad, M. A. Wani, and K. Deep, A comprehensive strategy to lower number of COYID-19 tests, SSRN Electronic Journal, doi: 1O.2139/ssrn.3578240

E-ISSN 2581 – 7957
P-ISSN 2277 – 3916

CVR Journal of Science and Technology, Volume 21, December 2021
DOI: 10.32377/cvrjst2117

Screening and Classification of Covid-19 from Lung Images using Deep Learning Models

Vijayagiri Ashritha[1] and B. Vikranth[2]
[1]PG Scholar, CVR college of Engineering/ IT Department (Data Science), Hyderabad, India
Email: vijayagiriashritha@gmail.com
[2]Professor, CVR college of Engineering/ IT Department, Hyderabad, India
Email: b.vikranth@gmail.com

Abstract: **The world is facing human mankind issues which made people quarantine. Real-Time Reverse Transcription Polymerase Chain Reaction (RT-PCR) detection of viral RNA from nasopharyngeal swab has a relatively low positive rate for the early-stage detection of COVID-19. The Computed Tomography is the first imaging technique that plays an important role in the early diagnosis of COVID-19 and their manifestations had their characteristics that are different from other non-COVID diseases like Influenza-A viral pneumonia. So this survey is trained to determine an early screening model to distinguish COVID-19 from healthy cases and Influenza-A viral pneumonia using 2D and 3D deep learning techniques algorithms like Inception-V3, Xception, ResNet, ResNeXt, etc., Further proceeding into the design, the candidate regions were first segmented using these deep learning models from the CT images by applying filter layers such as convolutional layer pooling layer other dense layers depending on the model selected and activation functions such as a sigmoid function or ReLU function and then these were categorized into COVID-19, influenza-A viral pneumonia and healthy groups with the best accuracy results and the promising screening.**

Index Terms: COVID-19, Deep Learning, CT images, Convolutional Neural Networks, Screening.

I. INTRODUCTION

At the end of the 2019, there was an outbreak of novel coronavirus disease 2019 pneumonia (COVID-19) [1] in Wuhan, Hubei Province, China. The health authorities did investigation inorder to characterize and control the disease and summarize the clinical characteristics indicating the common symptoms fever, cough, myalgia, fatigue etc., and some people ended up with lifetime diseases. Due to this some patients had pneumonia, the lung CT examination showed abnormalities and complications including acute respiratory distress syndrome, acute heart injury and secondary infections and observed the evidence of one person to another person transmission of COVID-19 through droplets or aerosols when an infected person coughs talks or sneezes. Now the covid-19 has reported different variants of it. It is spreading alot more than previous waves and is very dangerous as different mutations come together to form another mutant and the study tells the severity increases with the increase in the number of mutations.

As the situations are getting more worse day-by-day, the virus should be detected and diagnosed very early and accurately helps in controlling the spread of the disease .The manual method of detection of COVID-19 in human can be done using RT-PCR test i.e the detection of viral RNA from sputum or nasopharyngeal swab that resulted a low positive rate in the very early stage. However, the CT scan images were collected from the patients with the COVID-19 disease, who had their own characteristics different from other viral pneumonia diseases. So the RT-PCR testing has been replaced with the lung CT scan image detection as early diagnostic criteria for COVID-19.

There is rapid development in computer technology where digital image processing has been widely applied in the medical field including image segmentation, image enhancement for medical detection. Deep Learning technologies such as Convolutional Neural Network[2] have substantial applications in medical image processing.And deep learning models usage and applications have drastic impact on the efficiency of predicting , testing or classifying etc.

The objective of this study is finding the different models to early diagnose the disease from the CT lung images or the X-ray chest images and then classify the diagnosed images into different categories i.e either COVID-19 or healthy using binary classification and COVID-19 or Pneumonia or healthy using multiclass classification more accurately.

Generally, a deep learning model involves different workflow steps.

1. Collecting the data
2. Data preprocessing
3. Choose the model
4. Train the model
5. Evaluate the model.

As part of this study, the first step is to find the data related and to gather the data that is to be given as input to the network. And the data is preprocessed using different image processing techniques [3]. The preprocessing is a method to perform some operations on the low quality image to improve the quality of the image or extracting the useful information from the images and the feature extractions [4] are to be done. The next step is to select the deep learning model that works efficiently and gives the state-of-art results. Then training the model is the most important step in the process flow where complete evaluation is based on how the model is trained and the best model that is selected to train the data. The training model is a dataset that is used to train the model that takes the input data to correlate with the output data against the sample output which is used in modifying the model. This is known as the “Model fitting”. The final step involves the evaluation of the model that has been trained. The model will be tested in this step against the training and validation dataset with

Received on 24-07-2021, Revised on 21-08-2021, Accepted on 26-09-2021.

CVR Journal of Science and Technology, Volume 21, December 2021
DOI: 10.32377/cvrjst2117

the unused dataset. Some metrics are used to measure the performance of the model.

Fig. 1, is the generic process flowchart of our deep learning survey.

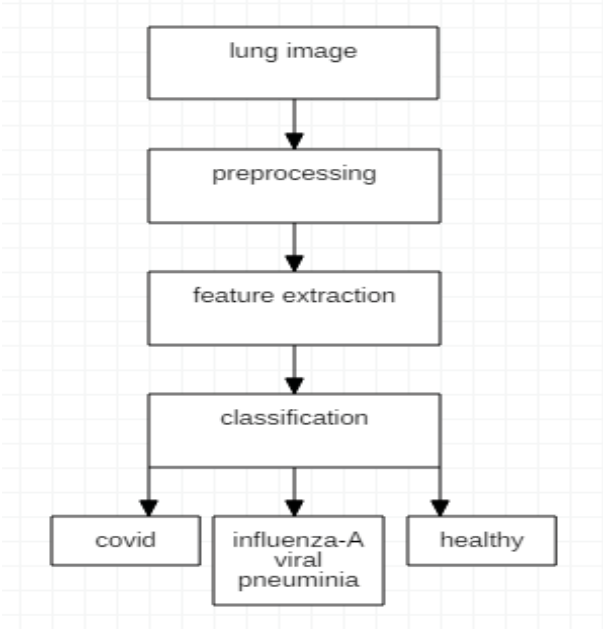

Figure 1. Generic process flowchart

The input we consider is either the lung CT scan image dataset or the chest X-ray image dataset from any open-source datasets. Further, the data is preprocessed to remove the noise from the data or to collect the important information from the images. The feature extraction is done to reduce the redundant or the unwanted features and extract the required characteristics which are most essential for classification. The final stage of the process is to classify the data using the selected deep learning models into binary classification (COVID-19 or healthy) or multiclass classification (COVID-19, pneumonia, healthy) with the best performance measures after training and model fitting the data.

Fig. 2, is the different types of CT lung images affected with COVID-19, Pneumonia and healthy.

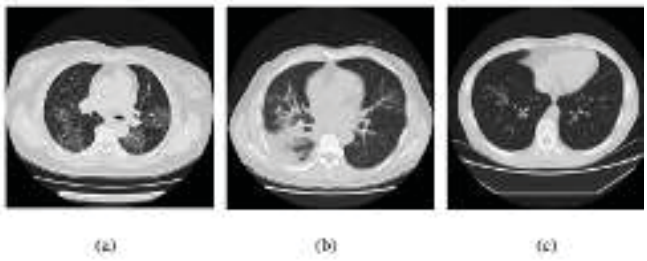

Figure 2. (a)CT lung image with COVID-19 (b) CT lung image with other pneumonia (c) healthy CT lung image

II. Related Literature

There were many models like Inception, ResNet, Transfer Learning, Deep Convolutional Neural Networks, Xception Networks, AlexNet etc., which are widely used in image classification, object recognition with best performances. In this section some of the existing techniques were explained.

A. Residual Network , Location Attention Mechanism:

(Xiaowei Xu, feb2020) aimed to develop an early screening model to detect and classify the COVID-19 from other pneumonia and healthy images in the early stage efficiently.

The data of total 618 Traverse Section CT samples from First Affiliated hospital of Zhejiang University were collected where 219 from 110 patients of COVID-19 , 224 from 224 patients with Pneumonia and 175 from healthy people. Of them 528 samples i.e 85.4% were used for training and remaining 189 samples i.e 14.6% were used for testing.

Fig. 3, is the process flow chart of this study where first the collected CT image dataset is used as input which were preprocessed to extract the pulmonary regions based on the HU values and is normalized to pixel value.

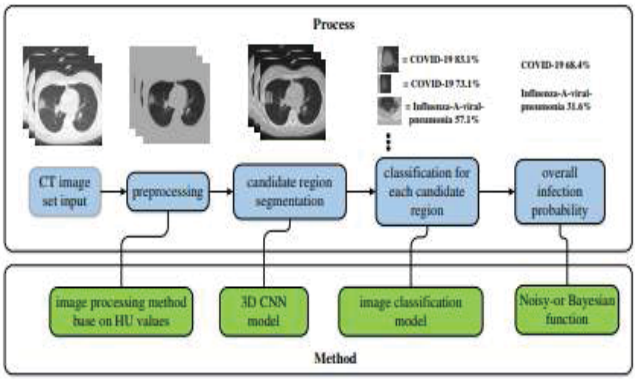

Figure 3. Process flowchart of model

The preprocessed images are then segmented using 3D CNN model i.e VNET based segmentation model called VNET-IR-RPN (VNET Inception ResNet Regional Proposal Network) [5] to separate the candidate regions ~ candidate patches from the images. Moreover, this is the model used for both segmentation and classification, but only segmented data were preserved.

Then the classification model was designed inorder to differentiate the infections by finding the relative-distance-from-edge that gives the location of the patches on the image. This is known as Location attention classification mechanism. First the minimum distance is measured from the mask to the center of the patch. Next, the diagonal of the minimum circumscribed rectangle of the image is obtained. Finally the relative distance from the edge is achieved by dividing steps 1 and 2.

The final step is finding the overall infection probability using the Noisy-or Bayesian function which classifies the image into one of the three categories considering the infection probability rate.

Fig. 4, is the Network Structure where two CNN classification models i.e ResNet based network and Location attention mechanism in fully connected layer were used by concatenating to improve the accuracy.

CVR Journal of Science and Technology, Volume 21, December 2021
DOI: 10.32377/cvrjst2117

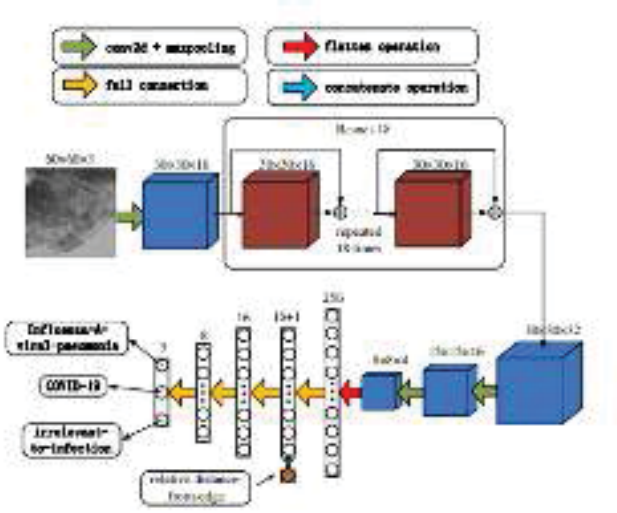

Figure 4. Network Structure

The ResNet model is used for feature extraction and pooling layers to prevent overfitting of the data by dimensionality reduction. Then the output is flattened to 256 dimension vector and then using Location attention mechanism it is again reduced to 16 dimension vector followed by three fully connected layers with the confidence scores are classified into any of the classes i.e COVID-19 or Pneumonia or healthy images with the overall accuracy rate of 86.7%.

The profit of using this model is, as the layers are increased using VNET-IR-RPN for segmentation and both ResNet and Location attention mechanism for classification leads to increase in accuracy and efficiency.

The major drawback in here is, it takes more time to train and evaluate the model as there were many layers for process.

B. Transfer Learning , Ensemble Classifier:

(M.Qjidaa, Y. Mechbal, A. Ben-fares jun 2020) aimed to develop an intelligent clinical decision support system to early diagnose COVID-19[6] from chest X-ray images easily accessible for the people in rural and remote areas.

The total of 566 X-ray images of COVID-19, pneumonia and healthy classes were collected from two open sources with public access. Of them 70% of the sample containing all the three classes were used for training and the remaining 30% of data was used for testing. As the data was collected was improper as it was collected from two different sources, it was subjected to preprocessing and augmentation.

I. **CNN and Transfer Learning:** The steps involved are first, several pre-trained neural networks where the classifier selects the network with the highest accuracy rate which transforms inputs into vectors. Then taking the advantage of these pre-trained models an ensemble model is built which outperforms all the remaining pre-trained models with the best performance.

II. **Pre-trained Neural Networks :** Using different pre-trained models –VGG16, VGG19, MobileNet, Inception V3, Xception, InceptionResNetV2, DenseNet121 as shown in Fig. 5, gives the output with the maximum prediction using Ensemble classification.

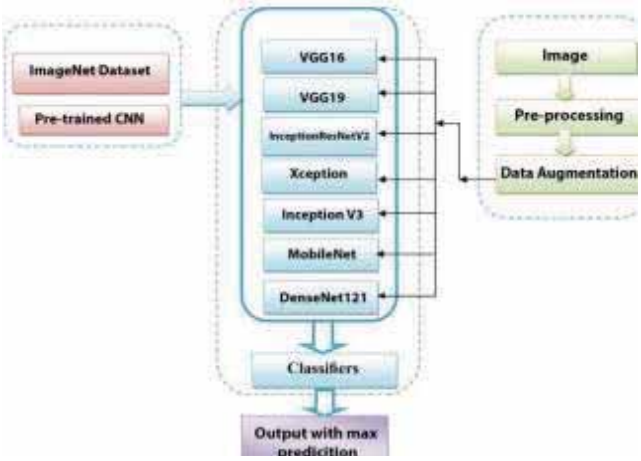

Figure 5. Model process

a) VGG16, VGG19: VGG network is a pre-trained image recognition model that has upto 19 layers where as VGG16 is one of the VGG network that has 16 layers and VGG19 has 19 layers deep. These are used as the pre-trained models in this survey.

b) MobileNet: It has depthwise separable convolutions to construct lightweight deep convolution neural network that is efficient for mobile applications. It is used as pre-trained model with trainable and non trainable layers in this survey.

c) InceptionV3, InceptionResNetV2: It is a Convolution Neural Network of the Inception family. This model InceptionV3 is developed of many improvements i.e label smoothing, batch normalization and widely used in image recognition and classification with depth of 48 layers and InceptionResNetV2 is the concatenation of both Inception and Residual network has residual connections helps in increasing accuracy. These are used as the pre-trained models with trainable and non-trainable layers.

d) Xception: It is an extreme version of Inception which was improvised in many aspects and is used as another pre-trained model.

e) DenseNet121: It is a Convolution Neural Network that connects to the layers that are deeper in the network i.e first layer is connected to 2^{nd} , 3^{rd} , 4^{th} layers and second layer is connected to 3^{rd} , 4^{th} , 5^{th} layers etc., so on and this is selected as the pre-trained model in this survey .

III. **Ensemble Classification:** It is the learning algorithm that constructs the classifier and then classifies the data using the maximum of the predictions. It is developed by combining several models that help in predicting with the highest of the pre-trained model's accuracy and efficiency. As shown in Fig. 6, in this study, the Ensemble

CVR Journal of Science and Technology, Volume 21, December 2021
DOI: 10.32377/cvrjst2117

classification is used to merge the prediction of all the seven pre-trained models with the prediction vectors as output and takes the majority voting as the final prediction class with the overall accuracy of 98% in this study.

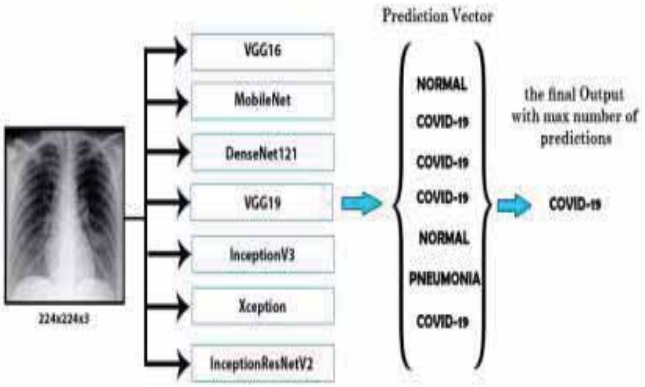

Figure 6. Ensemble Classification

The advantage of applying the Ensemble method on the different pre-trained models classifies with the best accuracy and efficiency.

The major drawback is although it improves the accuracy and efficiency, it costs more to create, train and deploy the model and sometimes new observations can confuse the model in classification.

C. Deep CNN using InceptionV3:

(Sohaib Asif, Yi Wenhui, Hou Jin sep2020) [7] aimed to detect the COVID-19 pneumonia patients automatically using X-ray images using Deep Convolutional Neural Network model by maximizing the accuracy and efficiency. This deep learning model was built so that it could extract the graphical features of COVID-19 that makes the work easier in classifying data into COVID-19, normal and pneumonia classes.

Total of 864 COVID-19, 1345 pneumonia and 1341 healthy X-ray images were collected. As the model selected works good for the large datasets, so the data was subjected to preprocessing and augmentation inorder to increase the dataset.

Transfer Learning: The transfer learning is used on smaller data set as this model is based on the concept of reusability i.e learns from the previous data. It is transfer learning best use. Whereas it does not work well with the large dataset as it is difficult for the experts to collect the data, label it which takes lots of time effort and cost.

InceptionV3: So InceptionV3 is used in this study as it works best on a large dataset. Fig. 7 is the InceptionV3 architecture that performs convolution, pooling, softmax and fully connected processes. It is a pre-trained Neural Network where one block can be used as the initial layer of the next block. It involves two steps where it uses the feature extraction of convolution neural network and the classification uses the softmax and fully connected layers.

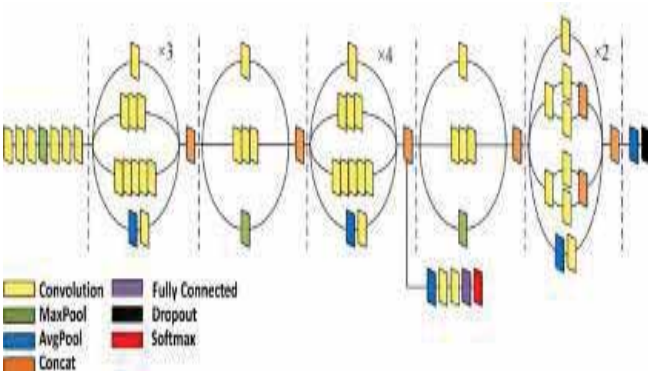

Figure 7. Inception Blocks

The step-by-step procedure of the classification of InceptionV3 model architecture is as shown in Fig. 8.

i. Recursively performs convolutions and pooling
ii. Then applies dropout and fully connections where the image is classified according to the training class labels.

Convolution is the process of extracting the features of the input image in which each pixel is responsible to produce the output. It is a feature extraction process.

Pooling layer is used to remove the noise from the obtained features. These are of two types: Average pooling and Max pooling.

The dropout is used inorder to avoid the over-fitting of data, Then the fully connected layer is applied to final classify the data.

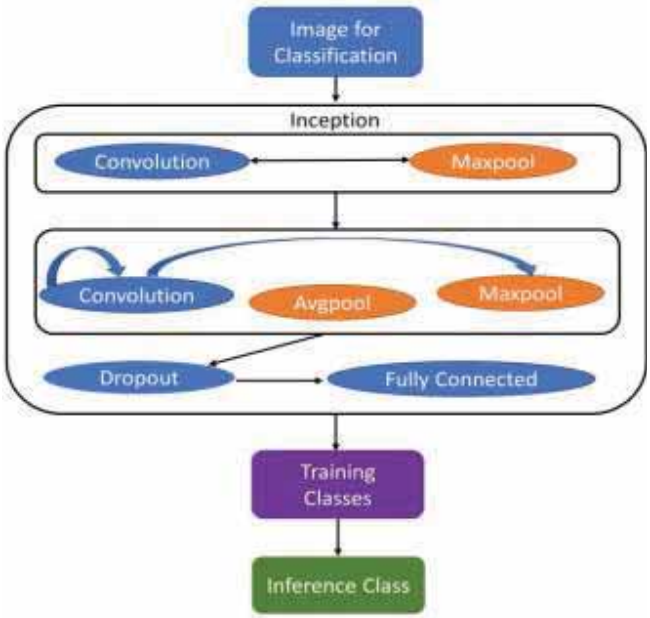

Figure 8. InceptionV3 model Architecture

The full schematic diagram of the model Deep CNN based InceptionV3 implied to classify the data into three classes i.e COVID-19, pneumonia and healthy as shown in the Fig. 9.

CVR Journal of Science and Technology, Volume 21, December 2021
DOI: 10.32377/cvrjst2117

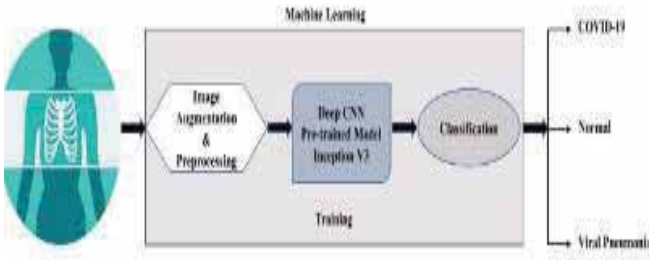

Figure 9. Schematic diagram of model

The X-ray images are used as the input images for the model. The images were augmented and preprocessed. The pre-trained model Deep Convolutional Neural Network based InceptionV3 is used for training the model having applied all the layers. After training the model, the data is classified according to the training models as COVID-19, pneumonia and healthy classes. This model then gives out the classified class that outperformed the existing models with the accuracy of more than 98%.
This is the algorithm for the model classification:

Step 1: Start
Step 2: Create list of images // Start training the model
Step 3: Provide a directory for storing the bottleneck value of each image
Step 4: Provide inference to the images // to create bottleneck values
Step 5: Create folder for all images of bottleneck values
Step 6: Generate bottleneck values for each individual image
Step7: Create new softmax layers and fully connected layers// end of training
Step 8: Test new image // input chest x-ray image to get the result
Step 9: Finish

Algorithm for classification

As the network used is deep Convolutional Neural Network where a model block is used iteratively with different layers embedded for feature extraction and denoising is the best advantage that helps in increasing the accuracy and the model outperformed than the other existing models.

But the drawback is that it uses a lot of parameters and takes a lot more memory to run the training model followed by testing.

D. Concatenation of Xception and ResNet50V2:

(Mohammad Rahimzadeh, Abolfazl Attar May2020) aimed to apply the deep learning methods to achieve best results in detection of COVID-19, healthy , pneumonia classes . The model is developed in such a way that it works better on unbalanced dataset also.

The dataset is collected from two open sources of chest X-ray images with 180 images from 118 COVID-19 cases, 42 from 25 pneumonia cases from the first source. And 6012 cases with pneumonia, 8851 normal cases from another source. All the data were combined into a single dataset. After that, the dataset is balanced to achieve good results for training and evaluation.

Networks: The Xception model is concatenated with the ResNet50V2 model in this study. Xception model is a pre-trained model which is the extreme version of the Inception model that has the depth-wise convolutional layers and point-wise convolutional layers. This model has given the best performance above all the networks that are existing using ImageNet dataset. ResNet50V2 is also a pre-trained network that consists of skip connections which tend to use the important layers and skips some of the layers that are not needed inorder to decrease the time of training and evaluation.

As shown in the Fig. 10, an architecture of concatenated models Xception and ResNet50V2 [8] , the dataset collected is used as the input for the concatenated model which is used parallely for deep feature extraction and these concatenated features are further connected to the convolutional layer with filters, using kernel and padding applied to it using no activation function helped in the extraction of valuable semantic features from the spatial points of all channels. Then the fully connected layer is added to flatten the channels, dropout layer is used to remove all the unwanted features followed by the classifier that classified the data into COVID-19, pneumonia or healthy classes with an outperformed accuracy rate of 99.50%.

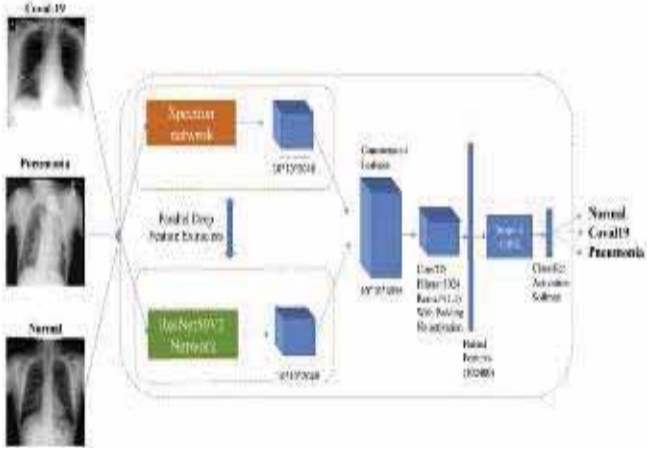

Figure 10. Architecture of model

As the Xception model has the depthwise convolutions and ResNet50V2 has skip connections, concatenating both have their unique features gives best results.

E. Deep CNN using DeTraC:

(Asmaa Abbas, Mohammed M. Abdelsamea sep2020) aimed to develop a deep convolutional neural Network called DeTraC to classify the COVID-19 chest X-ray images that has the speciality of removing the irregularities present in the data by exploring the class boundaries using decomposition mechanism.

The dataset is the package of 80 samples of healthy images, 105 samples of COVID-19 and 11 samples of pneumonia.

DeTraC: It is abbreviated as Decomposition Transfer Learning Composition [9] and there are steps involved in this model to classify the data into COVID-19 pneumonia or

CVR Journal of Science and Technology, Volume 21, December 2021
DOI: 10.32377/cvrjst2117

healthy classes. This model is used in order of decomposition followed by transfer learning and composition of the data.

The class decomposition is used in splitting up the data and takes the data that is required by considering the features taking the decision boundaries into consideration inorder to enhance the properties of the data and then the performance of the model.

The transfer learning is to transfer the insights gained from the previous model to the next model. This has three steps Shallow tuning, deep tuning, Fine tuning. Of them Shallow tuning takes only the last data parameters to merge with the new data whereas the deep tuning retains all the data parameters and Fine tuning trains more layers till the performance is achieved.

Composition is making up the data together that was decomposed inorder to increase the quality and improve the performance of the data.

The DeTraC architecture consists of three phases where in the first phase, the data is trained with the DeTraC model then the training is done using the Gradient Descent optimization. Finally, the class composition is applied to the data as shown in the Fig. 11.

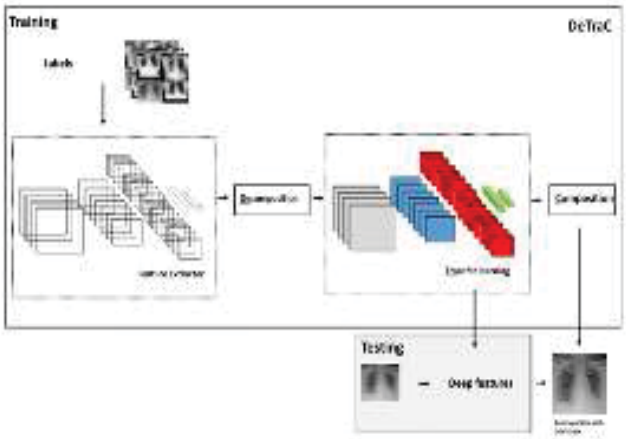

Figure 11. Architecture of DeTraC

In this class composition, a 2D feature space is considered from principal component analysis outputs consists of a number of classes where K-means clustering is further applied to divide each class into different subclasses where each class is associated with the centroid near to it based on Euclidean distance metrics. After the clustering is finished, each class is again divided into different subclasses as a new dataset. For the class decomposition AlexNet pre-trained model with shallow learning mode is used to extract the features of the classes.

In Transfer learning, the final classification layer from the class decomposition is considered and then the fine tuning is applied on the parameters adopted.

In the class composition, the subclasses that are segregated will be assembled back to actual classes as to produce the final prediction based on the actual classes with the accuracy rate of 97.35%. All the stages were explained in the algorithm as shown.

Algorithm: Procedural steps of DeTraC for COVID-19 detection.

1: Procedure

- Input:
  -CXR image set divided into training and testing sets.
  -Ground truth tables.
- Output:
  -Predicted labels.

Stage 1 Class Decomposition:

-Use an ImageNet pre-trained CNN model (e.g. AlexNet) as a feature extractor to construct a deep feature space from input CXR images.
-Apply PCA on the deep feature space for dimension reduction.
-Use reduced feature space of the input CXR images to decompose original classes into a number of decomposed classes.

Stage 2 Transfer Learning:

-Adapt the final classification layer of an ImageNet pre-trained CNN model to the decomposed classes.
-Fine-tune parameter of the adopted pre-trained CNN model.

Stage 3 Class Composition:

-Calculate the predicted labels associated to the decomposed classes.
-Refine the final classification using error-correction criteria.

Algorithm for DeTraC

This work deals with the most challenging problem i.e data irregularities and also fine-tuning is used in transfer learning helps in resulting the best output.

III. Results

This section describes the results of all the papers that have been included for the review. And the graphical representation and the tabular formats of the results for the respective models used.

Fig. 12 is the loss and accuracy curves for the two models belong to the first paper i.e Residual Network, Location attention mechanism. The graph is a comparison between the loss and accuracy ResNet+ Location-Attention and ResNet alone. The model with Location-Attention performed well with the accuracy better than the model without Location-Attention mechanism with the increase in the epochs. The loss values or the accuracy values did not increase or decrease suddenly. The models also converged without any over fitting.

The Precision, Recall and F1-score were also calculated for all the categories COVID-19, Pneumonia, and Healthy ct images which resulted in 90% recall , 93.1% precision, and 91.5% F1-score with the overall accuracy rate of 86.7%.

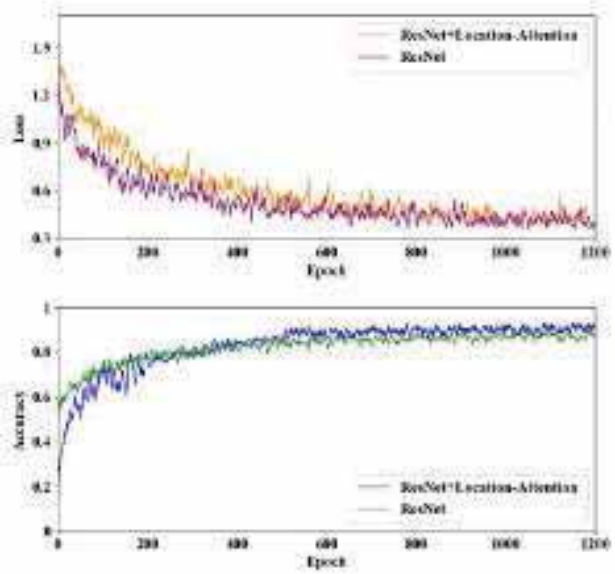

Figure 12. Graph of Loss and Accuracy between ResNet+ Location-Attention and ResNet

Table 1 is the results of all the models and the Ensemble methods for the model Transfer learning and Ensemble classifier. The test accuracy is calculated with the learning rate of 0.001 reduced for every 4 epochs, model configured for every 60 iterations. As shown, VGG-16 and VGG-19 accuracy is high 96.88 and 95.31. But after combining the entire models using the Ensemble classifier, the accuracy precision recall and F1-score increased as 98, 98.66, 98.33 and 98.30.

TABLE I.
RESULT TABLE FOR ALL THE MODELS AND ENSEMBLE CLASSIFIER

Model	Precision (%)	Recall (%)	F1-score (%)	Test Accuracy (%)
VGG-16	91.66	90	90	96.88
VGG-19	96.60	97	96	95.31
Inception ResNetV2	96	95.66	95.66	89.06
Xception	95.66	95	95.33	95.31
InceptionV3	92.33	93	92.66	92.66
MobileNet	92	89.66	90.33	89.06
DenseNet121	97	97.21	97.66	92
Ensemble Method	98.66	98.33	98.30	98

Fig. 13 is the training accuracy and cross entropy measured for the model Deep CNN using InceptionV3. The accuracy and Cross entropy are found for 4000 steps. Where the model has given the accuracy of 96% for 4000 steps for the training set and for the validation the model has given the accuracy of about 95.2%. Coming to cross entropy, the model has given the low cross entropy with the increase in the number of steps. The overall accuracy achieved with the DeepCNN using InceptionV3 model is 98%.

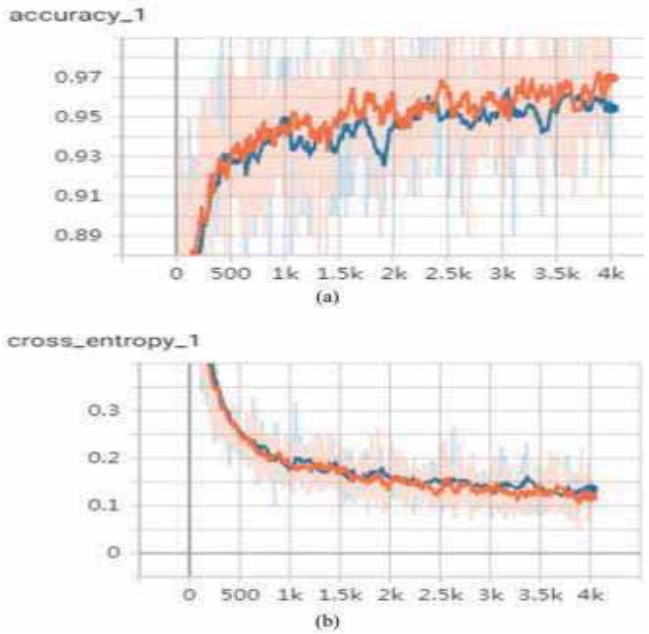

Figure 13. Visual of Accuracy and Cross Entropy.

There are some models that have an accuracy rate of 93.1% and 99.50%. But the difference is some of the models performed well for smaller data sets and some of the models performed well for larger data sets. Overall results were very accurate and efficient for all the models that were discussed in the paper.

IV. CONCLUSIONS

Among all the manual existing methods, Deep learning methods are very efficient in early detection and the classification of the COVID-19 from the Chest CT, X-ray images. This study is completely about the different deep learning techniques used with the different datasets collected from various open sources. The existing models have performed well with the data collected giving the best accuracy. And the advantages and the disadvantages were also explained after each model. With the processed datasets and the efficient models, the detection and classification would be more efficient.

REFERENCES

[1] B. Prabhu Christopher, S. Udhaya Kumar, D. Thirumal Kumar, "The rise and Impact of COVID-19 in India" 22 May, 2020, Frontier in Medicine.
[2] Vibhor Jain, Anju Mishra, Neha Sharma, "An Analysis of Convolutional Neural Networks for Image Classification" Volume 132, 2018, pages 377-384.
[3] Erdal Erdal, Ibrahim Masri, "Review Paper on Real Time Image Processing: Methods, Techniques, Applications" ResearchGate, June 2019.
[4] S. Suganya "Analysis of Feature Extraction of Optical Character detection in Image Processing Systems" Volume 3 – Issue 04, July 30, 2018.
[5] Xiaowei Xu, MD; Xiangao Jiang ,MD; Chunlian Ma ,MD ; Peng Du, MD; et al. "Deep Learning System to Screen Corona Virus Disease 2019 Pneumonia," arXiv, Engineering, Volume 6, Issue 10, October 2020, Pages 1122-1129.

[6] Y. Mechbal, A. Ben-fares, M. Qjidaa, et al. “Early detection of COVID19 by deep learning transfer model for populations in isolated rural areas” IEEE , 23 sep,2020.
[7] Si Jinhai, Sohaib Asif , Yi Wenhui , Hou Jin , , “Classification of COVID-19 from Chest X-ray images using Deep Convolutional Neural Networks” , IEEE , 12 feb, 2020.
[8] Mohammad Rahimzadeh, Abolfazl Attar, “A modified deep convolutional neural network for detecting COVID-19 and pneumonia from chest X-ray images based on the concatenation of Xception and ResNet50V2”. Elsevier Volume 19, 2020.
[9] Asmaa Abbas, Mohammed M. Abdelsamea, Mohammed Medhat Gaber, “Classification of COVID-19 in chest X-ray images using DeTraC deep convolutional neural network” Springer, sep2020.
[10] Dina M. Ibrahim, Nada M. Elshennawy, Amany M. Sarhan, “Deep-Chest: Multi-Classification deep learning model for diagnosing COVID-19, Pneumonia and lung cancer chest diseases” Volume132, May2021.
[11] Zhu N, Zhang D, Wang W, et al. “A Novel Coronavirus from patients with Pneumonia in china, 2019[J]. Jan 2020.
[12] Corman VM, Landt O, Kaiser M, et al. “Detection of 2019 novel coronavirus (2019-nCoV) by real-time RT-PCR” Jan 2020.
[13] Milletari F, Navab N, Ahmadi S A. “V-Net: Fully convolutional Neural Networks for volumetric Medical Image Segmentation” arXiv 2016.
[14] Lakhani P, Sundaram B. “Deep Learning at Chest Radiography: Automated Classification of, pulmonary Tuberculosis by Using Convolutional Neural Networks.”
[15] Wu W, Li X, Du P, et al. “A Deep Learning System That Generates Quantitative CT Reports for diagnosing pulmonary Tuberculosis” arXiv 2019.
[16] Zisserman, Andrew, Simonyan, Karen & Very Deep Convolutional Networks for Large-Scale Image Recognition. arXiv.
[17] Chollet F, “Xception: Deep Learning with depthwise separable Convolutions” IEEE CVPR, 2017.
[18] S. Loffe, C. Szegedy, V. Vanhoucke et al., “Inception-V4, Inception-ResNet and the Impact of Residual Connections on Learning” 2017.
[19] Muhammed Talo, Ulas Baran Baloglu, Ozal Yildrim, Tulin Ozturk, et al. “Automated detection of COVID-19 cases using deep neural networks with X-ray images” Elsevier, 2020.

E-ISSN 2581-7957
P-ISSN 2277-3916

CVR Journal of Science and Technology, Volume 21, December 2021
DOB: 10.32377/cvrjst2118

Attention-Based Multitask Model for Name Entity Recognition and Intent Analysis of Online Medical Questions

N. Yogitha[1] and R. Seetharamaiah[2]
[1]PG Scholar, CVR College of Engineering/ IT Department (Data Sciences), Hyderabad, India
Email: yogithanirmalkar123@gmail.com
[2]Professor, CVR College of Engineering/ IT Department, Hyderabad, India
Email: seethasyam03@gmail.com

Abstract: **In recent years, various methods of deep learning have been explored and are applied for solving Named Entity Recognition task which are considered as one of the prior task of Natural Language Processing.**

Named Entity Recognition has been recognized as a sub task of Information Extraction, where it recognizes and classifies proper noun into their given pre-defined categories like persons, location, organization, date and time etc. The survey mainly makes a focus on different methods of deep learning, which have been approached for NER task to work well along with relative multitask learning techniques to opt a novel model based on Neural Network architecture by performing sequence tagging and text classification for witnessing Named Entity Recognition task and Intent Analysis task for online medical questions.

Both the attention mechanism and multitask learning have been improved the performance of their respective tasks. This method has achieved superior performance in both Name Entity Recognition (NER) and Intent Analysis when compared with other methods. The present method is considered as light-weighted solution that can be suitable on every small server for its deployment. By making use of both the tasks a simple question-answering system has been developed.

Index Terms: **Name Entity Recognition, Intent Analysis, Attention mechanism, Multitask neural network, Sequence tagging, Text Classification.**

I. Introduction

Internet Technology has been developed rapidly with many medical related health-services from many Smartphone applications and online websites. This health related online website provides services to the people by sending a relative answer to their respective questions. There are several medical services which are helping people through online in obtaining some knowledge regarding the health issues and other relative aspects. These online medical service systems make use of medical expertise to build proper medical knowledge bases, thereafter, applying natural language understanding technologies to generate related answers to questions thereby obtaining the better quality of generated answers for the user's queries.

The two main tasks performed in the method are Name Entity Recognition (NER) [1] and text classification task conducted on Intent Analysis separately.

A. Name Entity Recognition (NER):

The Name Entity Recognition is considered as a form of Natural Language Processing where its main task is identifying and classifying entities. The NER is also referred as an entity extraction where it seeks to extract the named entities from a given unstructured text into some pre-defined categories like person's name, medical codes, locations, percentages, organizations, time expressions and many more. With the help of NER it is feasible to extract key information, to understand given text and further use it by collecting the important information thereafter storing it in a database. In the online medical question-answering services it helps the system to rightly provide the services to its users. For example, consider that a person asks a question like: "Can arrhythmia causes severe headache?". With the help of NER we can understand that the given question contains "arrhythmia" and "headache" as a disease name (or) disease word.

The working principle of NER model Fig. 1, is mainly carried out in two phases i.e. 1) Detecting the named entity from given text. 2) Categorizing the entities.

Figure 1. NER Pipeline

Here the first phase involves in detecting the string of words from the given corpus that form entities. During the first phase each word in the corpus is represented as token where the splitting of a sentence, phrase or paragraph has been processed into smaller units which helps in understanding the context and also helps to elucidate the meaning of the text in the corpus by analyzing the words given as sequence. This method is called Tokenization.

The second phase is Categorization phase where creation of entity classifying takes place.

However the problem with the working process of Natural Language Understanding is that, the algorithms of Machine Learning cannot work properly with any raw text. So to make this language processing work properly there is a need of some feature extraction methods that can convert the

Received on 24-07-2021, Revised on 21-08-2021, Accepted on 26-09-2021.

text into vectors. The resultant outcomes of these feature extractions are processed for data tagging, where the conversion of sentences to forms takes place where the forms consist of words and tuples. The list of elements for each tuple is in the form of (word, tags) where the tag is considered as POS tags which resolves ambiguities and classifies the given words based on their Parts-of-Speech types. Thereafter the named entities are created based on the text data, which classifies and recognize the words individually to perform good results on trained data for a given task of entity recognition.

B. Intent Analysis:

Intent Analysis [2] is also called as Intent Recognition, is a text classification technique which is a form of NLP. The task of intent classification is to understand the user's correct goal for which the system should leverage its intent detector to classify the user's statement into any one of the predefined classes which is known as intent.

This intent classification identifies the intentions behind any given statement, and displays it according to its predefined labels by classifying them as the intent of the given query for its easy understanding. For online Question&Answer medical services the intent classification helps the user's to correctly identify the intentions behind the medical query that has been asked. For example, if any query is given as "Can arrhythmia cause headache?" the intent classification for the asked array is given as "Syndrome". This will be helpful for the user to have an easy classification for a large form of text.

The working principal of Intent classification or Intent analysis Fig. 2 is carried out by providing the training data, where the training data is considered as a representative sample of raw text data which is labeled manually as user wants to design their respective model, to work automatically.

Once the labeling of data is done, the user can feed the data into the suitable Machine Learning (ML) model. Once the user is done with training the model the next process is Validation Process where another sample of raw data is used to validate the required model. This Validation Process is used to check whether the model performs well on the given type of data during its process of production. If the raw unlabeled data that is given to model perform well and obtain an accurate output, then it considers that the model is ready for production with good accuracy.

The method introduces a multi-task model [3] for sequence tagging and text classification where both intent analysis task and NER task can be trained. The model uses text data directly from online user questions that are considered as input and generate good results compared to other baseline methods.

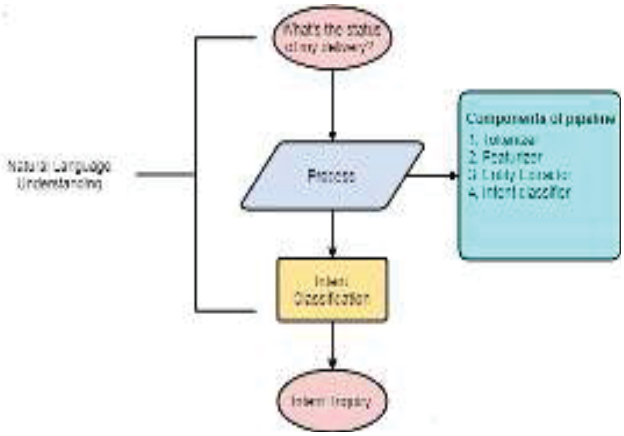

Figure 2. Intent Analysis

II. LITERATURE SURVEY

I . Attention based multi task model:

The attention based multi task model shares a word embedding layer and the Bi-LSTM layer to generate the NER tags and intent labels for given text. Word embedding [4] represents the words in an array in the form of continuous vectors. So, in the word embedding each token is transformed into a vector where we obtain some sequence of vectors that are considered as the inputs to the Bi-LSTM model. The type of word embeddings used here is word2vector representation to generate pre-trained word vectors. Here the corpus for word2vector pre-training model is collected from online health communities. Later the sequences of word vectors are sent as inputs to the Bi-LSTM layer.

The Bi-LSTM RNN architecture is a Deep Neural Network model Fig. 3, where it tends to learn bidirectional long term dependencies between the sequential data. It is considered as sequence parsing model where it consists of two LSTM's where one LSTM is input that is formed in forward direction and other in backward direction making use of Bi-LSTM models may effectively increase the amount of information available for a network. The usage of Bi-LSTM can be carried out in 2 ways for running the given input i.e. one from past to future and other from future to past. It stores the information for the future use and tries to predict the next words in the given sequential data.

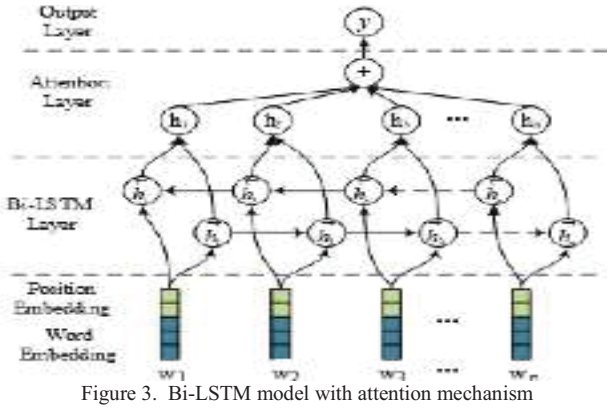

Figure 3. Bi-LSTM model with attention mechanism

Here when the word2vector output is given as input to the Bi-LSTM layer, its function is carried out in both forward and backward direction i.e. from past to future and future to past. The output of Bi-LSTM layer has some weights given using an attention mechanism, where the main function of attention mechanism [5] is to implement the action of selectively concentrating on most relevant information from the available corpus while ignoring the other.

The Bi-LSTM is used to generate a sequence of annotations i.e. h1, h2, h3 ...hnx for each given input sentence. The h1, h2 ...hnx are considered as vectors where it undergoes with some weights for given set of input annotations. Later on, the attention weights are being obtained to calculate with the Bi-LSTM output.

For NER model it contains attention layer for extracting several components of relevant information from a text sentence. Here the sequence of Bi-LSTM output is concatenated with attention layer and further it is given as input to the CRF layer for generating entity labels. For classification task also we make use of same attention layer as of for NER with some different annotations and annotation matrix is used for classifying different labels from the given corpus Fig. 4.

The model applied here is binary entropy as loss function and Adam optimizer. Both the tasks have their respective learning rates with better accuracies, differ from other baseline models.

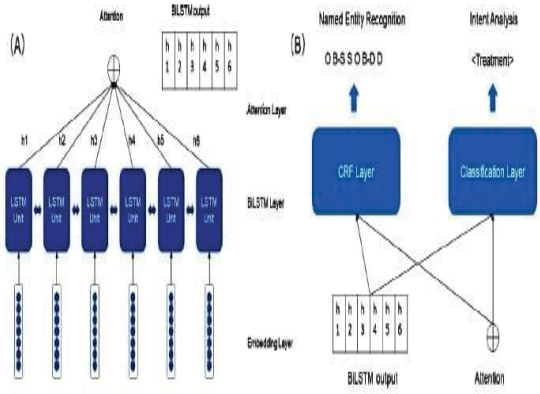

Figure 4. Bi-LSTM model with attention mechanism

The data that is made to use in the model is collected from health community website with around 60,000 user questions with their suitable answers and are stored in the MySQL database. For Intent Analysis the dataset contains 12,525 user questions with 7 types of intent labels for those questions. The intent labels are given as Diagnosis, Syndrome, Treatment, Reason, Concept, Complication and Prognosis. Thus, one user question may contain 0-7 different types of intent labels. For NER around 6,199 user questions were used with labels of 6 types of entities like Disease name, treatment, method, checkup body etc.

After training the datasets on both intent analysis and NER individually, the performance of both trained NER task and Intent Analysis task are calculated separately, and further compared with other models.

For NER task on test dataset the model used F1 score, precision and recall for evaluating the model's result and compared with SSVM, CRF, LSTM-CRF, LSTM-CRF-attention [6] BERT [7] and Multi-task attention models where the BERT model has higher F1 score of 0.8142 and recall of 0.8364 than others.

The second highest result was on model Multi-task attention with F1 score of 0.8135 and recall of 0.8168. The use of attention mechanism helps the model to focus on certain components of the sentences that components can be one or group of characters that are related to word representation, whereas for Intent analysis the model used accuracy, micro averaged F1 score and macro averaged F1 score for evaluation and is compared with CNN model [8], SVM model, Random Forest, BERT, Multi-task attention and other baseline models.

The results are given as; the present applied models obtained better score than CNN and SVM models with high performance of accuracy, Micro F1 score and Macro F1 score with 0.7588, 0.8652, and 0.6888 respectively.

The advantage of using attention mechanism with Bi-LSTM layer during training gave additional improvement for the model, to obtain good performance than other baseline methods and the overfitting of the model can be prevented by using multi-task learning model. The attention based multitask learning models have been generated by giving promising results for both the NER and Intent analysis tasks. It also states that the result suggests that both Attention mechanism and Multi-task learning can improve the Natural Language Understanding for given medical text by working together.

II . Multitask Bi-directional RNN model:

The authors Shanta Chowdhury, Xiangfang Li, Yi Guan and Xishuang Dong proposed a multitask bi-directional RNN model for extracting entity terms from Electronic Medical Records [9] on Chinese text. The model has been divided into two parts.

The first one is Shared layer and the other is Task specific layer. The shared layer is defined as a process of allowing a layer to link with other layers, so that the changes made in the original layer are produced on the shared layer. This sharing layer makes changes on multiple copies by applying changes on any of single linked layer. The task specific layer is defined as a process of performing multiple tasks that are given in a specific way by generalizing the domain specified information.

Many applications which use this task specific layer are given as Machine Learning, Natural Language Processing, Speech recognition, Computer vision.

Here for the proposed model the Fig. 5, gives the vector representation for each given word; the word is obtained as the concatenation of word embedding and character embedding. Later in Fig. 6, the bi-directional RNN [10] model is used in order to extract context information for any given sentence.

Later on, the given layers shared with two differently specified task layers i.e. NER task layer and other is POS tagging layer. Both the task layers are trained in an alternative manner where the knowledge learned from one task layer namely NER task has been enhanced by the knowledge gained from POS tagging task layer.

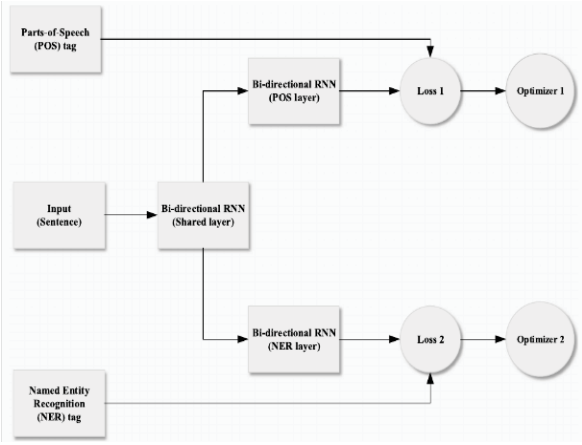

Figure 5. Framework of multitask bi-directional RNN model for NER

The framework proposed here is bi-directional RNN model that is used to exploit the past and the future context, since the RNN model is used to capture previous words and character information in a sequential manner and store in its memory for its further work as it has input layers, output layers, and hidden layers. So here in bi-directional RNN the forward hidden states compute with forward hidden sequence and the backward hidden states computes with backward hidden sequence.

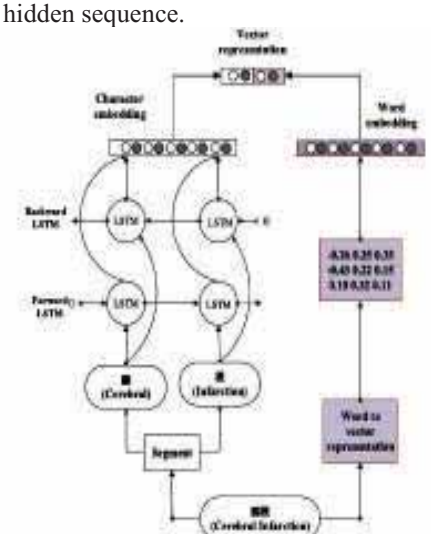

Figure 6. Vector representation as concatenation of word and character embedding.

Here the two bi-directional RNN models are used where one is used to extract features from word embedding by achieving word2vector representation and the other is character level feature extraction and represents it in character embedding. Later both the character embedding, and word embedding are concatenated to represent the words individually in a vector representation. Another bi-directional RNN is used for extracting context information from given text sentence.

Thereafter the outputs of words representation are shared by two different bi-directional RNN for both POS [11] and NER tasks separately. These two layers are trained alternatively, so that the performance of both tasks.

The model uses the EMR dataset which is collected from the department of second affiliated hospital available at Harbin Medical University by discarding the personal information of patients. The labeled corpus for the experiment consists of 500 discharge summaries and around 492 progress notes that were manually created. The data consists of 55,485 sentences that were written in Chinese language. The 5 types of entity labels are begin categorized as disease, treatment, test, symptom, disease group and for Part-of-Speech tagging the categorized entity types are labeled in BIO format where B stands for Beginning of the medical entity type, I stand for inside of the medical entity type and O is given as outstand of the entity type.

Thereafter the comparison results of accuracy on progress notes and discharge summaries are also improved from 5.66% to 9.41% points compared to CRF model and other baseline models for extracting features on NER task by introducing the prior-knowledge. Finally, it is observed that the best accuracy is given as 89.20% points in the test term and lowest performance is given as 36.00% points in recognizing disease terms on discharge summaries and similar results on progress notes.

The future enhancement for the given model can be designed by planning a joint loss function and joint optimizer that can reduce the training time and can later results in improving the performance accuracy on real datasets in better ways for its future research program.

III. Multiclass Classification Model using Deep Learning for NER:

Lijun Qian, Xishuang dong, Yi Guan, Jinfeng yang, Qiubin Yu and Lei Huang from computer science department, Prairie. View A&M university, Houston, USA proposed a model where a multiclass classification method which is based on Convolution Neural Network (CNN) of Deep Learning is used for NER by considering a constructed corpus of annotations which is obtained from Chinese EMR's where the corpus consists of 992 clinical notes in which it contain both Discharge summaries and Progress notes.

Later both the notes were tagged with certain entities and some baseline methods are also used to evaluate its performance. The method consists of two phases. The first phase is given as preprocessing and word embedding phase and the second phase is given as construction of multiclass classification based on CNN [12].

The proposed model constructs a CNN based multiclass classification method for extracting Named entities from the EMR's system Fig. 7. As mentioned earlier about two model's phases, it is given that in the first phase, the EMR's are gone through pre-processing for feature extraction, selection and representation for given words. Here the sentences are being extracted from EMR's with the text extractor tool where the same sentences from the text are been removed. This extractor extracts only the contents which are described by medical Natural Language from both Progress notes and Discharge summaries. These contents record the information which is important for the patients collected from its medical records like Treatment, Symptoms, and Tests etc.

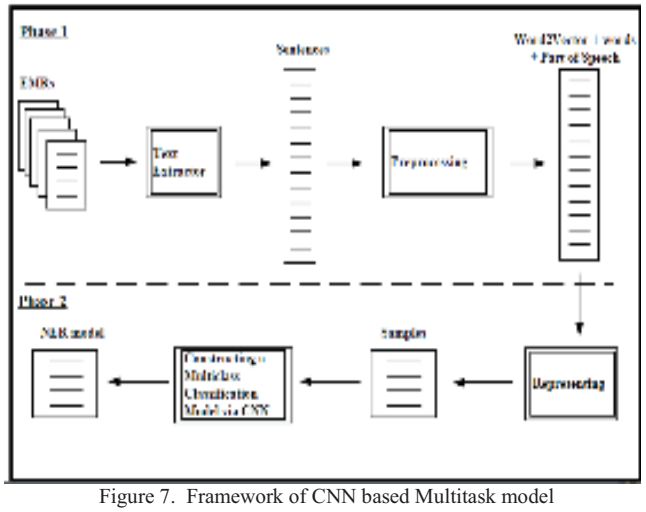

Figure 7. Framework of CNN based Multitask model

The second phase initially uses the word vectors to represent the samples, which are represented as pair of labels and group of word vectors Fig. 8. Then these samples are divided into some subsets with the one-vs-one strategy where the model to train on their subsets and are combined into a pair of labels. Then the CNN model is used to train the binary classifier [13] on each given subset to conduct multiclass classification model and for the prediction process the labels of test samples are generated in terms of voting to predict the results which are conducted by those classifiers.

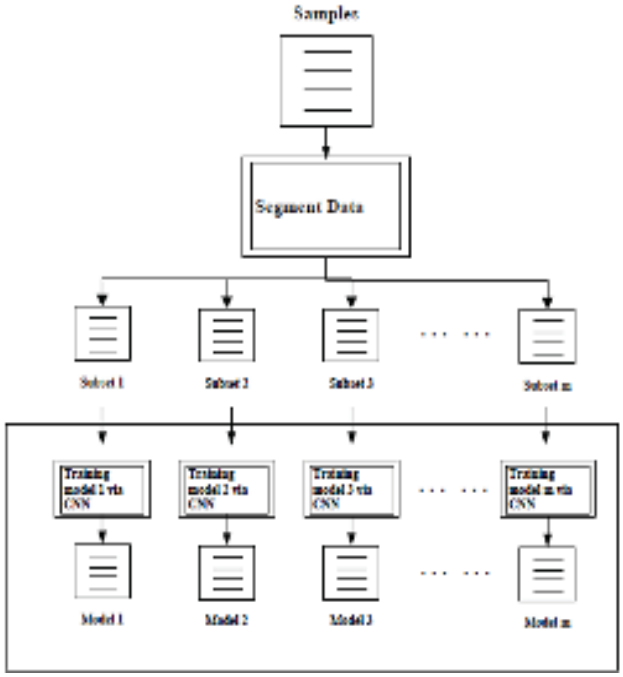

Figure 8. Framework of CNN model

The dataset collection consists of 992 EMR's taken from different departments from the second affiliated hospital, Harbin university of China, where the personal information of patients were removed from the EMR's. For the dataset collection two Chinese doctors were asked to label the records individually and then the results of labeling were merged only if both the doctors have same opinion, then the labels are been fixed otherwise some discussions were conducted till the agreement on the labels are reached by both the doctors.

To obtain more consistency on labeled corpus without any errors they are made to be corrected using some standard guidelines and later on a second round of labeling is been performed by considering two doctors to give a list of relative labels on given EMR dataset. Here if both of them have same opinions then those respective labels are considered as the final list of labels to annotate. There are 5 categories of Named entities that are annotated in the experiment and are given as Symptom, Test, Treatment, Disease name and Disease group.

It is given that the micro average F score of the CRF based method is considered as more than the SVM based method by 2.63% and also 1.87% for NER model based on discharge summaries and progress notes (Table1).

The micro F, micro P and micro R values are also evaluated on the models like Maximum Entropy, SVM and CRF on which the results shown that all the values are same since the testing samples of this model assigned with NER model on both discharge summaries and progress notes on proposed model are less than those of CRF by 1.51% and 3.80% respectively.

TABLE I.
RESULTS ON BASELINE METHODS

	Discharge Summary			Progress Note		
Algorithm	**Micro P**	**Micro R**	**Micro F**	**Micro P**	**Micro R**	**Micro F**
NB	78.07	77.91	77.99	79.42	79.37	79.40
ME	88.81	88.81	88.81	91.45	91.45	91.45
SVM	90.52	90.52	90.52	93.07	93.06	93.06
CRF	93.15	93.15	93.15	94.93	94.92	94.93
Our Model	**88.64**	**88.65**	**88.64**	**91.13**	**91.14**	**91.13**

Since the above results are not sufficient and do not show any effectiveness in the method, the accuracy of NER is investigated where the results of overall accuracies of NER using the proposed model shown lower results than CRF based method. It is given that if an entity which consists of one or more than one word, then the entity type for those words cannot simultaneously are made to be tested to their correct labels. The comparison results on recognition of different types of entities shown that the recognition accuracy on test entity type is considered as higher and the disease group entities as least. The performance results on NER model between CRF and proposed method are given as 3.77% on discharge summaries and 3.39% on progress notes (Table2).

TABLE II.
COMPARISON RESULTS WITH SAME FEATURES

	Discharge Summary			Progress Note		
Algorithm	**Micro P**	**Micro R**	**Micro F**	**Micro P**	**Micro R**	**Micro F**
CRF	92.41	92.41	92.41	94.52	94.53	94.52
Our Model	88.64	88.65	**88.64**	91.13	91.14	**91.13**

The method constructed on corpus of 992 Chinese EMR's with manually tagged entities of 5 categories. Then the performance evaluation is conducted on two methods for recognizing medical named entities from the corpus.

Later by obtaining the experimental results it is shown that the method achieved micro F score values of 88.64% and 91.13% on discharge summaries and progress notes respectively and for CRF method it is shown as 92.41% and 94.52% respectively on NER model.

These results have shown the effectiveness of proposed method for extracting named entities on Chinese EMR's. As future enhancement the method may build a dependency parser system for extracting the dependency syntactic relationship for improving NER performance on model and by integrating it with POS which can further improve its performance in its best ways.

IV. Named Entity Recognition based on Deep Learning Pretraining:

The Electronic Medical Records record different types of Symptoms, Disease lists and Test results that are taken by patients from their admission process to hospitalization, and based on their medical results proper disease diagnosis, other treatment methods are recommended by the medical professionals. But as this EMR's are not fully structured data. So, in order to convert the unstructured data into the structured form that can be used for Natural Language Processing technology for information extraction and text mining.

The basic task of Information Extraction [14] Text Mining [15] is, to recognizing the types of medical entities which include Disease, Tests, Symptoms and Operations etc based on patient's medical records. Though the method is used for recognizing the named entities on clinical EMR's it undergoes with some difficulties such as: 1. The clinical entities consist of large text data with various types with certain unregistered words such as unregistered drugs lists, disease group lists etc, which make it difficult to understand them and to construct a comprehensive dictionary on clinical text where it obtains different entity dictionaries. 2. These clinical entities are generally divided into complex and simple type of entities with some complex structures, with large no. of variables with lots of nesting, acronyms etc for clinical entities.

By considering the above problems and other deep learning method issues, the model proposed a method for understanding NER on Chinese EMR text based on pre-training, where it has word embedding pre-training model and other is fine-tuning of entity identification model which is pre-trained by having some relevant corpus. The method makes use of Transformers and Bi-LSTM models for feature extraction to recognizing the clinical named entities on Chinese EMR's.

The model makes use of two specific ways for implementing the pre-training mode of deep learning. In the first practice, the input has been initialized by the corpus of EMR's by embedding them and in the second, the entity recognition is pre-trained by the same field of corpus for fine-tuning.

The model performs a fine-tuning mode by pre-training the model and adding the functions of character embedding to Chinese EMR's. As the corpus of Chinese EMR is difficult to annotate based on their existing research method, the model is used to fine-tune the recognition task which is based on the model of clinical entity recognition by training a medical dataset Fig. 9.

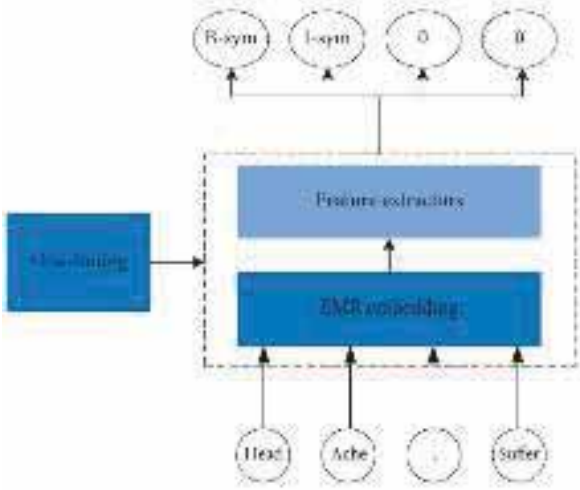

Figure 9. Pipeline model for Fine-tuning

Later the model uses Bi-LSTM model as a feature extractor with CRF for performing sequence annotation. This Bi-LSTM is used to convert the given input sequence through the embedding layer into the inputs formed by vector sequences with two LSTM networks, forming the forward and reverse with two hidden layers and the outputs formed are contacted with softmax layer for classification task. Since the LSTM model learns only the context relation of some features whereas not learning the context relation of tags, which may produce the outputs in wrong sequence tagging form. For this reason, the softmax layer is replaced with CRF layer where it works for sequence annotation and the Bi-LSTM works in producing automatic feature selection Fig. 10, which helps in improving the recognition performance on Chinese EMR's clinical named entity recognition model which is based on deep learning pre-training model.

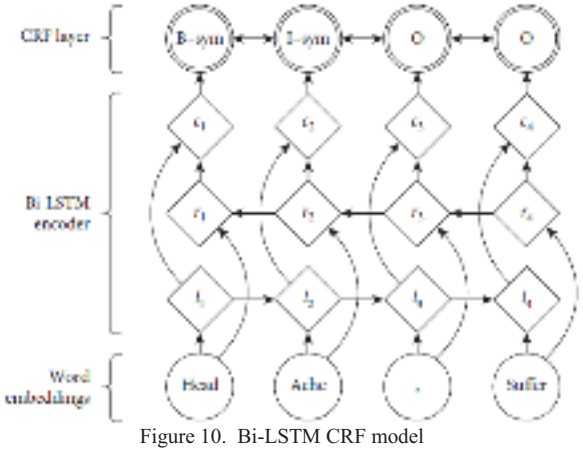

Figure 10. Bi-LSTM CRF model

The data consists of 1064 respiratory records and around 30,262 unrestricted records were collected from a website (https://www.iiyi.com). According to the annotation specification, 200 of 1064 respiratory department of EMR's manually created annotations with semantic types of English text indicating four categories of medical entities such as Disease, Drug, Operation and Symptoms.

The skip-gram model for word2vector used to adopt the word embedding for EMR's from 30,262 sets of EMR's which are considered as unmarked dataset and in addition to the first dataset the model used universal word embedding consisting of 268G of news corpus as second data. Later for the sequential annotation task for entity recognition, it is composed of two parts namely 1. The entity category tag and, 2. Location in the entity tag along with BIO representation which is used to represent the entity categories along with position of entity where BIO stands for B is beginning of entity, I is inside of entity and O is outside (not in) entity and the labeled corpus consists of 9 types of labels and 4 types of entities for its recognition in the given EMR's.

Here a pre-trained method is used on Chinese EMR's Name Entity Recognition model keeping in view of the Electronic Medical Records language features with many unclear entity boundaries, missing entities, annotation corpus difficulty etc. The pre-training method is classified into two steps 1. The first is to adopt the same set of corpus for pre-training word embedding along with Bi-LSTM and Transformer is used to identify Medical entities on Chinese EMR's, which acts as feature extractor and the second is fine-tuning the NER pre-training it with other relevant corpus having annotations for improving the effectiveness of recognition on Chinese medical entities, with results of Macro P having 75.06%, Macro R with 76.40% and Macro F with 75.72%. By considering the above performance results it can be concluded that the Chinese clinical named entity recognition model can improve its recognition performance effectively based on some deep learning pre-training methods.

V. Recognizing Named Entities by combining multi-task Bi-directional LSTM RNN with deep transfer learning:

Research Scholars' Shanta Chowdhury, Lijun Qian YiGuan, X. Dong, J. Yang and Q. Yu., from department of Electrical and Computer Engineering from praineview A&M University, Texas, United States of America, proposed a new model in order to overcome the liabilities i.e. combining the deep transfer Bi-directional RNN model with multitask Bi-directional RNN model [16] on Chinese EMR's in order to extract medical named entity terms, for both multitask deep learning and deep transfer learning which shows the potentials to strengthen Named Entity Recognition performance.

Here to build the proposed model, two steps were carried out i.e. In the first step, the model has obtained the general knowledge for Named Entity Recognition by considering some specific list of domains, by training Bi-directional RNN on Chinese corpus, and the second is to transfer the obtained general knowledge to construct multitask Bi-directional RNN model on Chinese EMR corpus. The proposed method applies a Bi-directional RNN model for extracting medical entity terms from EMR, where it is divided into two phases 1. Extracting domain knowledge phase 2. Multitask learning phase Fig. 11.

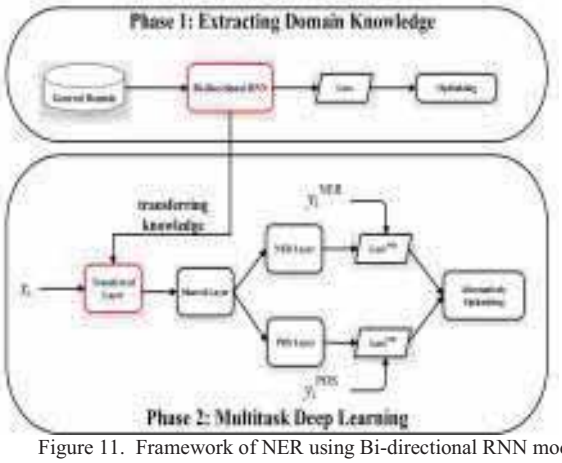

Figure 11. Framework of NER using Bi-directional RNN model

During the first phase, a Bi-directional LSTM RNN model is trained in a general domain, where it selects the optimal hyper-parameters like batch size, learning rate etc, which can obtain highest accuracy rate on extracting named entities from the specific domain. Later on by assuming that the obtained knowledge can uplift the performance of NER in a specific domain and then after transfer the knowledge for performing the complete extraction of NER on Chinese EMR. In the second phase, the knowledge has been transferred to the multitasking deep learning model by initializing the transferred layers as the suitable knowledge that could be activated for improving the accuracies of Named Entity Recognition on Chinese EMR's. In the next step the multitask Bi-directional LSTM RNN model is fine-tuned on transferred layer on the given Chinese corpus of EMR, and the output of this transferred layer is opted as input to the shared layer for extracting more accurate relationship between the words, later on these relations are shared with two different task layers which are given as Named Entity Recognition task layer and other is Parts-of - Speech tagging. Both the task layers are being trained alternatively in such a way that the knowledge which is learned from NER task layer can be upgraded by the knowledge obtained from Parts-of-Speech tagging.

In this model, the vector representations of each given word from both the phrases are concatenated by word embedding and the character embedding. Subsequently the shared layer undergoes two consecutive parts, during the first part, each of the given word is represented into a form of vector. This vector is built as a concatenation of both character embedding and word embedding. Here the word embedding is obtained by word to vector representation and the Bi-directional RNN with LSTM cell is used for extracting the features of characters and represent it as character embedding. Both the word and character are combined together to exhibit the vector representation for each word. This vector representation is then adapted as an input component for both transferred layer and shared layer.

Thereafter the output i.e. contextual word representation from both the layers are shared with two different Bi-

directional RNN with LSTM cell model for performing two different tasks such as Parts-of-Speech tagging and Named Entity Recognition. Both the tasks are trained alternatively in order to improve the performance of NER task Fig. 12.

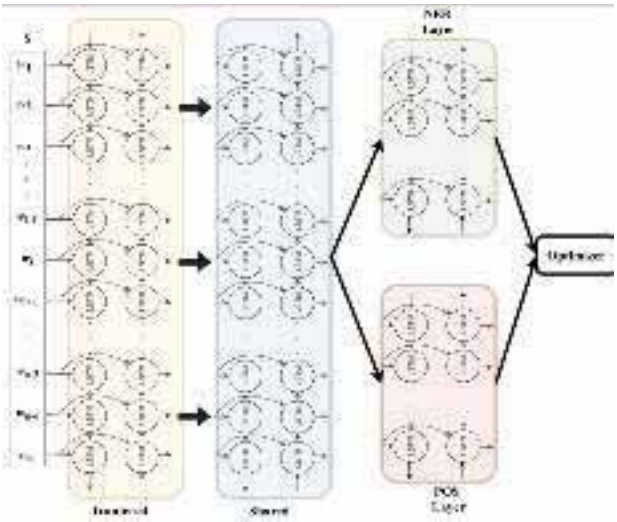

Figure 12. Architecture of transfer and shared layers for NER and POS

The datasets of EMR are collected from the department of Second Affiliated Hospital from the Harbin University, where the patient's personal information has been dispensed. Then the labeled corpus consists of 550 discharge summaries and the progress notes of 492 datasets which are manually created. There was total 55,485 sentences in EMR data written in Chinese language, and the labels were categorized into 5 entity types. The 5 types of entities are disease group, test, treatment, symptoms and disease.

For obtaining the results on the model, different metrics such as macro average F, micro average F score and accuracy have been used. The macro average is used to calculate precision, recall, and F-score on each class independently, whereas the micro average is used for aggregating all the classes for computing the average metrics. These three metrics are compared with classifiers such as Support Vector Machine (SVM), Naive Bayes (NB), Maximum Entropy (ME), Conditional Random Field, Multitask Bi-directional RNN, Transfer Bi-directional RNN [17] etc are used for resolving NER where Bi-directional RNN is considered as a baseline model and MBRNN is considered as state-of-art model where the micro F value of proposed model is improved with 2.55% points, from BRNN and CNN model it has improved its performance value to 4.85% points respectively on discharge summaries and, on progress notes the micro average F score value is been improved on proposed model by 2.23% points and 4.08% points when compare to other baseline models.

Later on the overall accuracy is also checked on both discharge summaries and progress notes where it is observed that the accuracy on discharge summaries is improved by 1.71% points but on progress notes it has decreased by 5.78% points compared to other state-of-art models and the best accuracy model is considered as 90.84% points on test term of named entity and lowest accuracy is recorded on disease group with 60.00% points on proposed model in case of discharge summaries.

III. Conclusions

By studying all the above models, the classification of Named Entities has been performed effectively on Chinese Electronic Medical Record (EMR's). Each of the models has their own deep learning techniques with some specific tasks which are meant to be carried out in such a way that the Named Entity Recognition tasks are correctly performed on the given words or sentences from its datasets. Many relative annotations/labels were created for NER task where the classification of words on given datasets works based on the listed entity types such as: Disease, Test, Treatment, Medication etc. For analyzing the performance rate and accuracy rate on each model different evaluation metrics such as macro average F score, micro average F score, precision & recall have been evaluated to retrieve the best performance results. Each of the individual models obtained best results based on their individual features on the given tasks. So, by considering all the above models it can be concluded that the Named Entity Recognition task on mentioned deep learning models opt the better results in terms of performance and accuracies on the clinical EMR datasets, but the best performance rate is obtained from TBRNN model for classifying the named entities on clinical corpus more effectively by creating the entity labels & by understanding the datasets which would help in improving its performance and accuracies results, and are used for its future enhancements.

References

[1] Aixin Sun, Jianglei Han, Chenliang li, Jing Li, et al., "A survey on deep learning for Named Entity Recognition, IEEE Transaction on Knowledge and Data Engineering, (2020).
[2] B Kasthuriarachchy, M Chetty, D Walls, G Karmakar, "Pre-trained language models with limited data for Intent Classification", IEEE International Joint Conference on Neural Networks (NN), (2020).
[3] Xishuang Dong, Lijun Qian, Jinfeng Yang, Lei Huang, Yi Guan, "A Multiclass Classification Method based on Deep Learning for NER in EMR", IEEE (2016).
[4] Habibi M, Weber L, Neves M, et al., "Deep learning with Word Embeddings to improve Biomedical NER, Bioinformatics, (2017).
[5] Zuko-hregoric A, Bachrach Y, Maksak B, et al., "Neural named entity recognition (NER) using self-attention mechanism", IEEE (2017).
[6] J Xie, C Luo, Y Jin, D Wu, W Guo, R Wang, "LSTM-CRF Neural Network with Gated Self-Attention for Chinese NER", IEEE Access (2019).
[7] Ming-Wei Chang, Kristina Toutanova, Keton Lee, Jacob Devlin, "BERT: Pre-training of deep Bidirectional-Transformers for language understanding", arXiv: 1810.04805v2 [cs.CL], 18 (Oct 2018).
[8] C Mao, L Yao, Y Luo, "Clinical text classification with rule-based features and knowledge-guided convolution neural networks", BMC Med. Information. Decision. Making, (2019).
[9] Licu, Shis, Hao Z, et al., "Improved deep belief network model & its application in Named Entity Recognition (NER) of Chinese electronic medical record (EMR's)", IEEE Big Data Analysis (2018).
[10] Qian Y, Zhao H, Wang P, et al., "A unified tagging solution: Bi-directional LSTM recurrent neural network with word embedding", arXiv: 1511.00215v1 [cs.CL], (Nov 2015).

[11] Xiaoling Cai, Shoubin Dong, Jinlong Hu, "A deep learning model incorporating Parts-of-Speech and self-matching attention for named entity recognition (NER) of Chinese electronic medical record (EMR's)", BMC medical informatics in (2019).
[12] S Reheman, A Farroq, M Awais, S Anwar, "A deep Convolution Neural Network based multi-class classification for Alzheimer's Disease using MRI", IEEE International Conference on Imaging System & Technique,(2017).
[13] S Abdhulla, A Alashoor, "An Artificial Neural Network for the Binary Classification of Network Traffic", International Journal of Advanced Computer Science and Applications, (2020)
[14] Rashmi Agarwal, Simran Kaur, "A Detailed Analysis of core NLP for Information Extraction", International Journal of Machine Learning & Network Collaborative Engineering, (2018).
[15] W Sun, Z Cui, Y Li, F Liu, et al., "Data Processing & Text Mining Technologies on electronic medical record (EMR's): A Review", Journal of Healthcare Engineering, (2018).
[16] S. Chowdhury, X. Dong, L. Qian, X. Li, J. Yang, Q. Yu, Y. Guan, "A multitask Bi-directional RNN model for NER on Chinese EMR's", BMC bioinformatics 19, (2018).
[17] J Yang, X Dong, S Chowdhury, L Qian, Q Yu, Y Guan, "Transfer bi-directional LSTM RNN for named entity recognition on Chinese Electronic Medical Records (EMR's)", IEEE 19th International Conference on e-Health Networking, Applications and Service in (2017).

E-ISSN 2581 – 7957
P-ISSN 2277 – 3916

CVR Journal of Science and Technology, Volume 21, December 2021
DOI: 10.32377/cvrjst2119

A Survey on Leaf Disease Detection Techniques

A.S Neelima[1] and CVS Satyamurty[2]
[1]PG Scholar, CVR College of Engineering/IT Department, Hyderabad, India
Email: alwalneelima@gmail.com
[2]Assoc. Professor, CVR College of Engineering/IT Department, Hyderabad, India
Email: satyamurtycvs@yahoo.co.in

Abstract: **Plants get affected by various diseases, different pathogens, fungus, bacteria, and viruses that affect the plants. Some affect leaves, stems, fruits, flowers, and other parts of the plant. Diseases in plants are one of their kinds in nature. There are a few diseases that can be fought by the plant immune system but there are a few diseases that need to be focused and a little care has to be taken to find the particular disease at an early stage and take an immediate measure. This helps the agriculturists to save time and increase productivity over a relative period of time. To encounter such types of problems automatically, computer science provides various technologies to detect diseases which include machine learning and deep learning algorithms which resolve the problem. The leaves are just as important as other parts of the plant. Mainly the leaf diseases are most common among many plants than the other diseases caused on different parts. Because in general, the leaf is the sensitive part of the plant, the changes in it which can be observed by the naked eye whenever there is a change in the weather, soil, fertilizer, etc. Plant diseases make farmers suffer, which may be any disease related to any part of the plant. Plant diseases are just abnormal effects that disturb the normal functioning of plant life. Thus plants are the most important factors to create ecological balance in the environment. This paper focuses on different diseases caused to leaves. This is a survey paper that represents the disease detection in various leaves, algorithms, and techniques used.**

Index Terms: **Leaf diseases, Deep Convolution Neural Network, GoogleNet, AlexNet, Image Subdivision.**

I. Introduction

Plants are organisms that have life. Similar to animals they also suffer from different diseases. All the plants including wild, cultivated and organic are prone to various kinds of diseases. Plants indicate their health condition by any of the following ways as shedding leaves, changing the color of leaves, white patch on leaves, and discoloration of the branch, thinning of a stem, bending of the shoot, premature fruits, and flowers drop off, the plant stops its growth. The plant diseases must be found at an early stage so that the plant can be saved. Diseases in plants affect agricultural productivity, huge losses to farmers, the GDP of the country coming from agriculture gets affected as more than 70% of the rural people do farming in India. Most of the diseases are caused on leaves where the pathogen first finds the source as a leaf to start its infection on a plant. There are many sources from which a disease can occur, some of them occur due to fungus, bacteria, virus, and other pathogens, worms, and insects. This survey paper describes the various diseases, techniques implemented on maize, cucumber, mango, and tomato leaves also factors influencing the techniques used. The common diseases caused in leaves are:

A. Southern leaf blight:

It is a fungal disease that is caused by Bipolaris maydis. They are particularly hosted by the maize plant. It forms diamond-shaped lesions with brown borders mostly form at the lower parts of the leaves and slowly move upwards towards the main plant.

B. Brown Spot:

It is caused by fungi known as physoderma maydis. Mostly affect in hot and humid conditions, they form tiny yellow spots which turn to brown later. Mainly develop on stealth, leaf blades. They form like stretched bands on the leaves. These fungi are hosted by the maize plant.

C. Curvularia Leaf spot:

It is caused by Curvularia lunata in the maize plant. It forms round brown border tan lesions with a yellow halo on leaves. They start with fewer lesions on leaves later spread throughout the leaf also these fungi travel through wind or water and affect the other plants.

D. Common Rust:

This is caused by a fungus named Puccinia sorghi. Initially, they form slightly tanned spots later they grow into powdery form and golden brown pustules scattered on both sides of leaves. Usually, the color of the spots changes into black as time progresses. Commonly hosted by maize, sorghum, millet plants.

E. Dwarf mosaic:

It is mainly caused by the maize Dwarf Mosaic Virus This virus has two strains A and B cause the yellowing of leaves followed by red patches along the margins of leaves. The effect of the virus depends on the growth of the plant. Mainly hosts Maize, Sorghum plants.

F. Grey leaf spot:

This is caused by Cercospora zeae-maydis. Initially, they form below the leaves as yellow halos further expand to the leaf veins , they are of many varieties as some of them appear black, yellowish, and brown spots. Sometimes they form silver coloured powdery form.

G. Anthracnose:

Anthracnose disease is a fungal disease that commonly occurs in almost all plants. It mainly affects the trees in general causing the leaves to have small irregular brown or yellow lesions later they develop largely and spread to other leaves as well. Anthracnose spreads fast during the rainy season.

H. Downy mildew:

It is caused by a fungus known as Pernosderospora. It is highly serious effects causing fungi to plants. The plants become brittle, do not develop properly, and thin. These are wind born and spread very quickly through the air and infect other plants.

Received on 16-04-2021, Revised on 04-05-2021, Accepted on 15-06-2021.

CVR Journal of Science and Technology, Volume 21, December 2021
DOI: 10.32377/cvrjst2119

I. Bacterial spot:

It is one of the most disturbing diseases caused in tomatoes and pepper. Mostly found in warm and humid places, once the disease is out of control it is not possible to reduce its effect. Plants show yellow lesions later develop into black which would be a serious issue causing, shedding of young leaves, and drying of premature fruits.

J. *Leaf mold:*

It is caused by a fungus known as Fulvia fulva. This stays alive feeding on the moisture present in plants especially on tomato plants making it dry, weak, and finally make the leaf dead one by one. This makes leaves develop purple color fuzzy texture under the leaves later the leaf starts to wither turning into yellow.

K. Spider mites:

Spider mites are small spiders that look like bugs. They can be noticed in different colors such as yellow, brown, red and green. These spider mites feed on plants mostly in the spring season. They lay hundreds of eggs on leaves which increases their population exponentially and damages the plant.

II. The Evolution of Various Convolution Neural Networks

The most predominant methodology used in detecting leaf disease is convolution neural networks (CNN or ConvNet). The convolution neural network has been used in various applications such as image recognition, image segmentation, object detection, etc. It consists of mainly the following layers: Convolution layer, Pooling layer, Fully connected layer, Dropout and activation functions.

A. The Convolution Layer:

This is the first layer in CNN architecture, it performs the convolution operations and extracts the features from the input image. The convolution is an operation that is performed by sliding an NxM filter on an input image to extract features.

B. Pooling Layer:

The pooling layer is followed by the convolution layer. The pooling layer is used to reduce the convoluted featured image which helps to reduce the computational cost. The pooling operations such as the max-pooling which calculates the maximum of the feature maps, the average pooling calculates the average of feature maps, the sum pooling calculates the total sum of the feature map elements.

C. Fully Connected Layer:

The fully connected layer is placed at last before the output layer. In the fully connected layer, all the neurons are interconnected with each of the other neurons. The flattened vector input is fed into this layer, later the classification process begins at this stage.

D. *Dropout:*

In the fully connected layer, all the features are very well Connected. This causes over fitting and creates a negative impact on the model performance. The dropout layer drops off few neurons at the time of training which reduces the size of the model enhancing the performance.

E. Activation Functions:

The activation function is the most important parameter in the CNN architecture. It is the main factor that decides which neuron needs to get fired and what neuron must act idle. The common activation functions used such as ReLU, SoftMax, Sigmoid, and Tanh functions.

There are many types of CNN's some of them are: LeNet was introduced by Yan LeCun et al 1998 it was used for the classification of numerics and was used at most of the banks to recognize the handwritten numbers on cheques, it had 7 convolutions layers with 60,000 parameters. AlexNet was introduced by Alex Krizhevsky, Geoffrey Hinton, Ilya Sutskever in 2012 which won the ImageNet challenge it is simple and consists of 60 million parameters. ZFNet was introduced by Matthew Zeiler, Rob Fergus in 2013 which is an improved version of AlexNet. Network in Network(NiN) uses multilayer perceptron convolution which adds to increase the depth of the network can be regularized by dropout, always used at the bottleneck of the CNN model. Also, the NiN uses GAP(GlobalAveragePooling) which reduces the number of parameters helps to generate low dimension feature vectors without reducing the dimensions of feature maps. VGG Net(Visual Geometry Group) was introduced by Simonyan Zisserman in 2014 this had a more simple architecture than the AlexNet and ZFNet with 138 million parameters. GoogleNet was introduced by Google in 2014 it consisted of inception modules which in turn has skip connections forming small modules and this forming of small modules are repeated in the whole network GoogleNet uses such nine inception modules and has about 4 million parameters with 22 layers and fewer parameters than VGG and AlexNet. The inception modules used in the GoogleNet architecture are just the 27 layers deep convolution layers. The inception module is the core concept of sparsely connected architecture, comes into the picture when the model is prone to overfitting, also when the number of parameters is more which increase the computational resources. The prerequisite for the inception layer is the Hebbian principle which says that "Neurons that fire together wire together", i.e. when building the subsequent layer one needs to focus on what has been learned in the previous layer. It works as an example, if the deep learning model has learned to identify the individual parts of a leaf it then the next layer must identify the overall complete leaf what kind of symptoms are there any dark spots, lesions or any other patterns are there on the leaf. To do all these the model must be aware of all kinds of appropriate filters which are available in Keras. ResNet(Residual Network)was introduced by Kaiming He in 2015 it consists of 158 layers for computation. FractalNet was introduced by Larsson et al which is based on the fractal design which is an advanced architecture of ResNet. This is based on the drop path which is a regularization approach to design large models. DenseNet was introduced by Gao Huang in 2017 consisting of densely connected CNN layers which are mostly used for feature reuse also by reducing the number of parameters.

Steps for leaf disease detection and classification:

1. Image acquisition
2. Image pre-processing
3. Image segmentation
4. Feature extraction
5. Detection of disease and classification

Image acquisition is the basic step in image processing. It is a process of acquiring an image by any source that may be hardware or software i.e. through the camera or from image dataset sites. These images collected have many disturbances and are unprocessed "Ref.[4]" Image processing is used to remove noise, contrast enhancement, image smoothing, image cropping, filters some of the filters such as average filter, maximum filter, Gaussian filter helps to get good insights for the model to perform well [4]. Image segmentation is mainly done to locate the regions which are more useful for the model than the other parts of the image. Usually, it creates pixel-wise masking to create a more meaningful image to analyse. Used to locate pixel boundaries or objects. Feature extraction plays an important role in image processing as the main features (color, texture, edges, shapes, etc.) of the image needs to be extracted by the model. "Ref. [4]" Color features are extracted by the color histogram, color moments, and color descriptor here refers to leaf color. Disease detection and classification is the last stage of the image processing where the images are classified according to their diseases and labelled accordingly after training and testing of the dataset by the classifiers. Classifiers such as SVM, CNN, ANN, KNN, etc. used for the classification and detection of diseases.

III. Literature Survey

Uday Pratap Singh et al. "Ref. [1]" has proposed a way that mainly focuses on developing a deep learning method which will classify the mango leaves infected by a fungal disease referred to as anthracnose disease. It mainly uses the multilayer convolution neural network for classification inspired by the AlexNet architecture. Two types of dataset repositories were used they are real-time mango leaf dataset and the other is PlantVillage repository. A total of 2200 images were used in the real-time captured are about 1070 images remaining 1130 images were taken from the plant village dataset. They were divided into 4 classes and labeled, given in table I.

The full dataset is divided into training and testing sets with 80%-20%, so for training 1760 images were used and for testing 440 images were used. The convolution neural network(CNN) is used here because it can handle complex pattern recognition and image classification process for large datasets which has been inspired by AlexNet architecture.

A. Methodology:

First, the dataset for both mango and other multiple leaves are collected from plantVillage and real-time mango leaf datasets for both disease and non-disease leaves. All the images are pre-processed by contrast enhancement and rescaling using 2methods such as:

1. Histogram equalization
2. Central square crop method

The histogram equalization is used for assigning uniform intensity values for each pixel, later the images are rescaled to128x128 using the central square crop method.

TABLE I.
Dataset Details

Type Of Image	Class_Label	No. Of Images
Mango Leafs Without Disease	C0	512
Mango Leafs With Disease	C1	558
Multiple Plant Leaf Without Disease	C2	520
Multiple Plant Leaf With Disease	C3	610

The task of the classifier is given in 3 steps they are:

STEP1: To find out whether the leaf is mango leaf or not

STEP2: Later to know if it is diseased or not

STEP3: Then classify is it as a diseased mango leaf or not

There are many different models of cnn they can be named as GoogleNet, AlexNet, ResNet, VGG many more. The convolutional neural network is a deep learning technique that has mainly the following layers to extract the information from the images sent from the input layer:

1. Convolution layer
2. Max pooling layer
3. Fully connected layer
4. Dropout layer
5. Activation functions

The convolution neural network model used in this paper given has:

1. The 1st 2nd layers are convolution layers of 128 filters with 3x3 size followed by Relu activation function after each of them. Next is the max-pooling layer with a size of 2x2 of the convoluted image.
2. The next 2 layers are convolution layers with 256 filters size of 3x3. Followed by a max-pooling layer with a convoluted image with the size of 2x2.
3. Again the next 2 layers are convolutional layers followed by a max-pooling layer with a convoluted image with a size of 2x2. Later followed by flattening layer with convert's images into 1d array.
4. The last two layers are fully connected layers where each neuron is connected with every other neuron.
5. There are about 512 neurons in the first fully connected and 3 output neurons in the last fully connected neuron it uses softmax function. Ultimately classify the image and produce the output class label.
6. There are dropout layers in between the network with the rate of 0.2-0.5.
7. The learning rate is given as 0.01.
8. The backpropagation algorithm or the stochastic gradient descendent is used here for training the network, refer figure 1.

CVR Journal of Science and Technology, Volume 21, December 2021
DOI: 10.32377/cvrjst2119

9. The accuracy achieved using multilayer convolution neural networks is 97.13%.

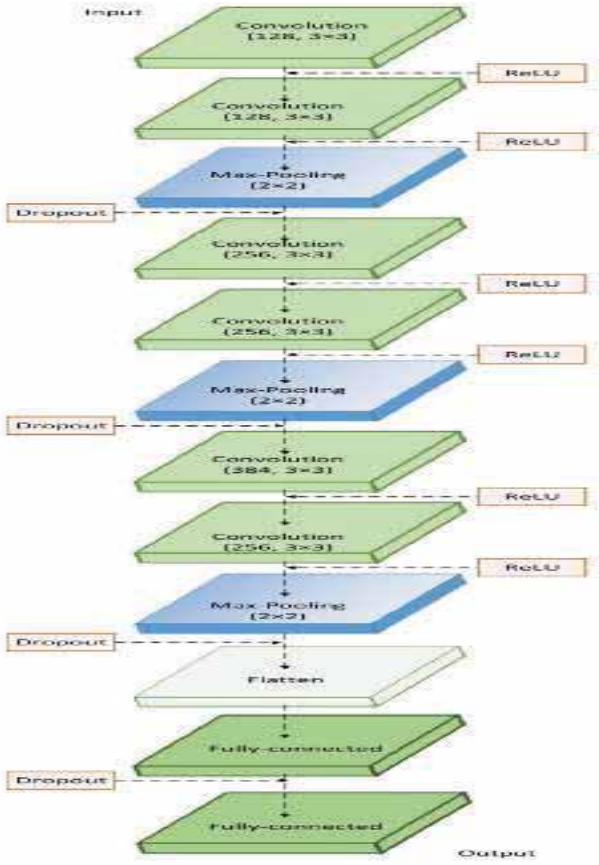

Figure 1. Convolution Neural Networks

Halil Durmuú et al. "Ref. [2]" describes the deep learning methods which have been implemented to recognize the diseases that occur in tomato plant leaves. The tomato Leaves were collected from the plant village dataset, a total of 10 classes of the different diseases was used along with healthy leaves. Only the tomato leaf images were considered which has 10 classes including the healthy leaves given has:

1. Bacterial spot
2. Early blight
3. Healthy leaf
4. Late blight
5. Leaf mold
6. Septoria leaf spot
7. Spider mites
8. Target spot
9. Mosaic virus
10. yellow leaf curl virus

B. Methodology:

Here in this paper 2 networks were used for disease detection AlexNet and Squeeze net. The AlexNet used here is from the Caffe library which is written in C++ language also has python binding which helps in easy implementation. SqueezeNet v1.1 was downloaded from GitHub. The training and testing were done on the NVidia Jetson Tx1. The training was done on GPU or GPU clusters which takes a long time and with a training batch of smaller size(20) which in turn reduced accuracy.

a. AlexNet Architecture :

It has the following layers: -

1. The input layer with image 227x227x3 resolution.
2. This network has 5 convolutional layers where each layer is preceded by the ReLu layer, preceded by the normalization layer, and pooling layer up to the conv2 layer.
3. A convolution layer (conv1) has 96 kernels with a 11x11x3 convoluted image.
4. Conv2 has 256 kernels with a 5x5x96 convoluted image
5. Conv3 has 384 kernels with 3x3x256 convoluted images preceded by Relu(relu3) function.
6. Conv4 has 384 kernels with 3x3x384 convoluted images preceded by Relu (relu4) layer.
7. Conv5 has 256 kernels with 3x3x384 convoluted images preceded by Relu (relu5) layer and the pooling layer (pool5).
8. The $6^{th,}$ 7^{th} layer is the fully connected layer with 4096 neurons preceded by the Relu (relu6, relu7) layer and dropout layer with the rate of 0.5.
9. The 8^{th} layer is the fully connected layer (FC8) helps to find the class probabilities preceded by the softmax function to find which class the image belongs to from the given 10 classes, refer figure 2(a).

b. SqueezeNet Architecture:

The Squeeze Net is introduced to increase the accuracy than the AlexNet which has been used earlier with 50 times fewer weights than AlexNet, also the SqueezeNet is lightweight architecture mainly built on 3 design strategy by reducing the filter size, input channel, and downsampling rate in the network. The input Layer with the RGB image with 227x227x3, refer figure 2(b).

c. Fire module:

The fire module has mainly 2 layers:

1. Squeeze Layer
2. Expansion Layer

d. Squeeze layer:

The squeeze layer has 1x1 size filters i.e. reducing the 3x3 filters used earlier in the input channel to reduce the parameters in the network.

e. Expansion layer:

The 1x1 convolutions are combined with the 3x3 convolutions. The 1x1 convolutions mix the earlier channels in various ways as they can't identify the spatial structures. The 3x3 convolutions can identify the structures in the image. By combining the 2 types of convolutions (1x1 and

CVR Journal of Science and Technology, Volume 21, December 2021
DOI: 10.32377/cvrjst2119

3x3) reduces the number of parameters and also makes the model expensive. These 2 layers (squeeze layer and expansion layer) are preceded by the ReLu layer.

In this paper, the Squeeze Net module uses 8 fire modules and one convolution layer as input and output layers along with a softmax classifier. The squeeze net uses the global

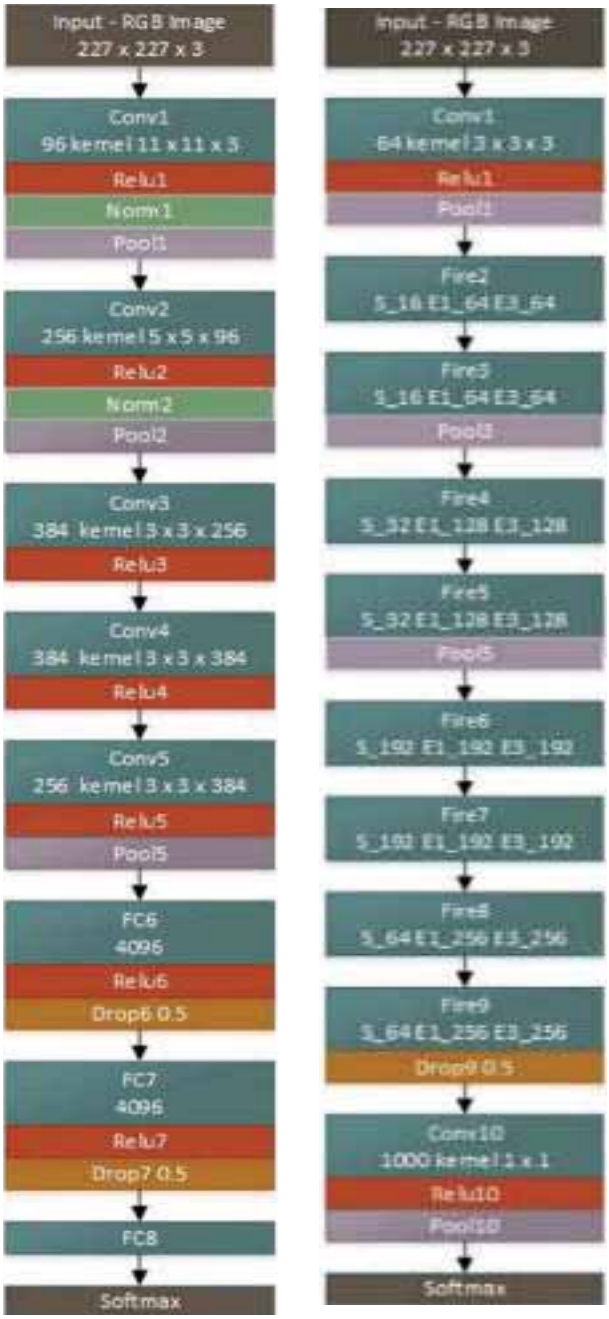

(a) (b)
Figure 2. (a) AlexNet (b) SqueezeNet

average pooling and the last convolution layer must have as many outputs to represent the output classes.“Ref. [3]” Both the AlexNet and Squeeze Net have their area of applications but Squeeze Net achieves the accuracy by 50x fewer parameters than of AlexNet, also benefits for model compression. The accuracy test onset of AlexNet and SqueezeNet is given as 0.9565 and 0.943~ 95.65% and 94.3%.

Juncheng Maa “Ref . [5]” has discussed a method used to recognize the cucumber diseases using DCNN by symptom-wise recognition, which would be useful without the effect of multiple diseases in a single leaf. This recognizes 4 symptom-based cucumber images refer to table II. The dataset was collected from the plantVillage and forestry sites symptom images such as:

1. Anthracnose obtained from the internet.
2. Downy mildew obtained from the internet.
3. Powdery mildew was obtained by using a digital camera.
4. Target leaf spots obtained from the internet.

The resolution of the images was 2592x 1944 pixels later resized to 800x600 pixels, for recognition the images were again resized to 20x20x3 as the symptom images were in little space. Segmentation was done using disease symptom segmentation along with comprehensive color features with region growing technique. The training was done by 80% and the validation by 20% rule. Feature extraction is performed, later segmentation is performed to extract the color and texture features to differentiate the diseases. The color features have mean and variance of the 9 channels from 3 color spaces including R,G,B(RGB space),H,S,V(HSV cpace) and L,a*,b* (CIEL*a*b*) refer figure 3.

The texture features were analysed using GreyLevel co-occurrence matrix for each channel which includes contrast, homogeneity, and correlation for the 9 channels. Confusion matrix prepared to check the performance of the classifier later the precision, sensitivity, f1score were also used to evaluate the performance.

TABLE II.
CUCUMBER LEAF DISEASE IMAGE DATASET

Name Of Disease	Number Of Symptom Images
Anthracnose	229
Downy mildew	415
Powdery mildew	332
Target leaf spots	208

The augmentation method used here doesn’t compress the size of the input image, a total of 12 sets of augmented images were produced. By rotating the images to 90,180,270 degrees, flipping horizontally and vertically. From the augmented training set 1600 symptom images were randomly selected from each class, also 400 images were selected from each class of the augmented test dataset. Where 5120 image were used for training, 128 images used for validation and 1600 images used for testing purpose

E-ISSN 2581 – 7957
P-ISSN 2277 – 3916

DOI: 10.32377/cvrjst2119

C. *Methodology:*

The architecture used here is analogous to Lenet5 which is robust, fast for the small image recognition task. The convolution neural networks were implemented in MATLAB.

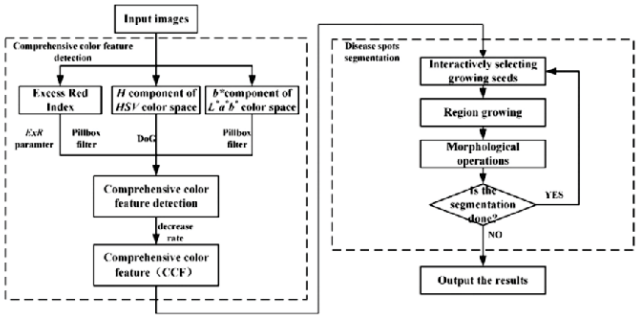

Figure 3. Image Color Feature Segmentation

The architecture is given as in figure 4. The input layer consists of the symptom images (RGB 20x20x3), the weights were optimized using stochastic gradient descendent (SGD) with a momentum of 0.9, and the maximum number of epochs used for training is 800.

The Learning rate was initialized for about 0.001 later reduced for about 20 epochs by a drop rate of 0.1 and the min batch of 128 was used. DCNN (Deep Convolution Neural Network) consists 4 modules such as:

The first module has *a* convolution layer with 20 filters with size 5x5. Max pooling layer with the filter size of 2x2 stride of 2(preferred down sampling). Module 2 consists of a convolution layer with 100 filters, size of 3x3. Max pooling layer with the filter size of 2x2 stride of 2. Module 3 has convolution layers with 1000 filters, size of 3x3. Module 4 has a fully connected layer with 1500 neurons. The output layer consists of the Softmax function has 4 neurons for each of the classified cucumber images. The accuracy of the confusion matrix given as 93.4%, the best performance was given by the downy mildew, also the AlexNet was used to evaluate the performance to compare with DCNN where the AlexNet outperformed the DCNN with the accuracy of 94.0%, 92.6%. The paper also describes various classifiers used in the field to detect the diseases and compare their performance with DCNN such as SVM was about 81.9 % accurate Random Forest was about 84.8 %. Mildew about 96.7%, powdery mildew as 98.2%, anthracnose 82.0%, and target leaf spots 91.8% using DCNN. The DCNN has given superior results for powdery mildew and downy mildew as there are larger than other classes.

Xihai Zhang et al. "Ref. [6]" has explained the automatic maize leaf disease detection using two improved models known as GoogleNet and Cifar10 models used to train and test the nine types of maize diseases, by regulating the parameters, modifying pooling combinations, appending dropout operation, using Relu function and decreasing the number of classifiers (achieving the accuracy of about 98.9% and 98.8 %). Around 500 images were collected from various online sources such as plantVillage dataset, and other image dataset websites. There are mainly 8 varieties of maize leaf diseases 1 variety of healthy leaves. The comparison procedure(cleaning) was applied to the images by using a python script which erased the redundancy of entities such as image name, size, date later the images were scrutinized by human experts. In the augmentation process the images are further required to expand to recognize the diseases properly by rotating them into 90°

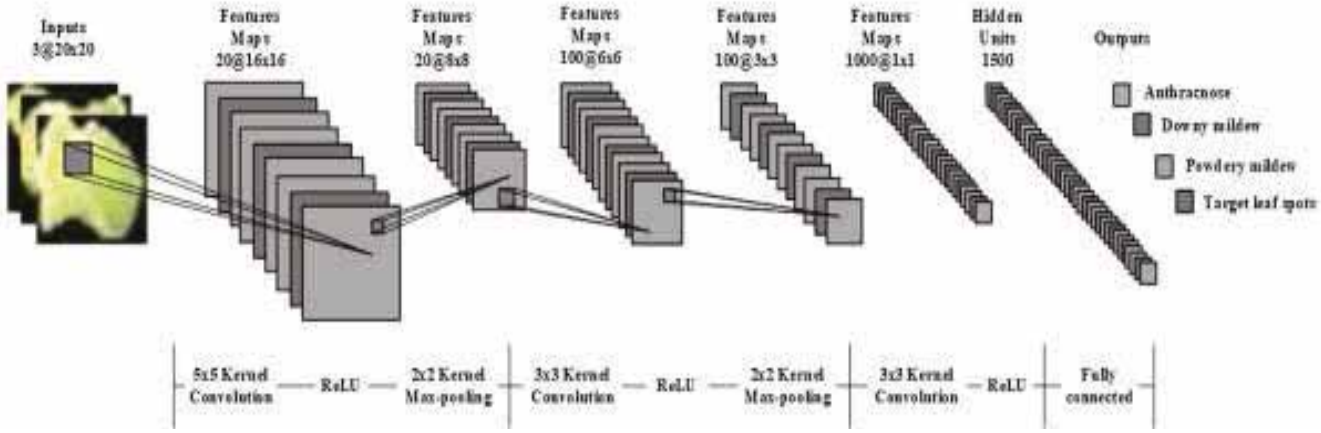

Figure 4. Architecture DCNN model for cucumber leaf disease detection

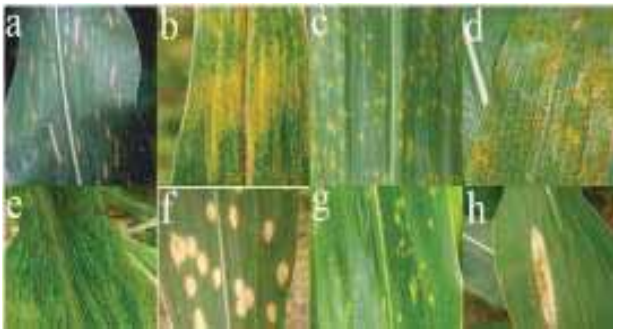

Figure 5.Various Leaf Diseases

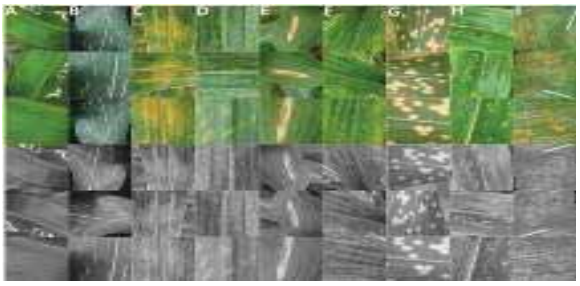

Figure 6. Augmented Leaf Images

a) Curvularia leaf spot
b) Rust
c) Dwarf mosaic
d) Grey leaf spot
e) Round spot
f) Northern leaf blight (refer to figure 5).

180°, 270° and mirroring each image also slitting the middle of the image later converting them into greyscale refer figure 6.A Shows the healthy leaf after rotating slitting and grey level conversion, from B shows the various infected maize leaves. They considered about 3060 images in total and 2248 images as the training set, 612 images as the testing set i.e. 80%(training) and 20% (testing). Images were normalized into 224x224 pixels and 32x32 dots per inch and pre-processed in python using OpenCV framework, for training all the images grouped and labelled by keyword search by agricultural experts which helps for better accuracy and validation also for better classification.

D. Methodology:

Caffe known as Convolutional Architecture for Fast Feature Embedding is a framework based on C++ language used for faster updating, flexibility expansibility in deep learning models such as CNN, RCNN, LSTM, and fully connected networks. GoogLeNet has provided a relatively less error rate by using fewer parameters than AlexNet and

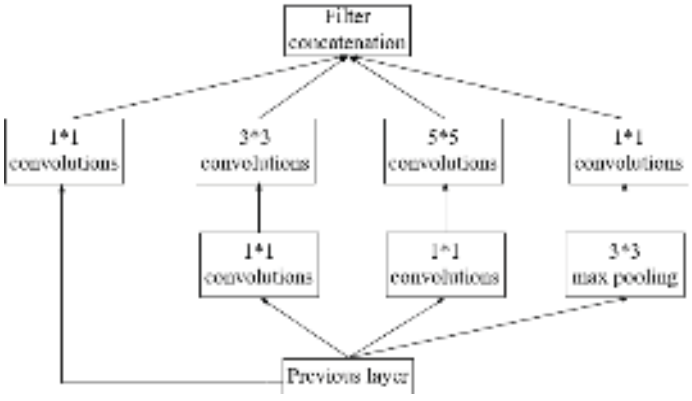

Figure 7. Inception Model

VGG which are mostly used in Network in Network concept applications. Here the GoogleNet uses a pyramid structure that enhances the capacity of width introduces the concept called the "inception model", refer figure 7. Inception model used to precisely optimize the local sparse structure, here 9 inception models used in GoogLeNet structure.

The 3 classifiers are used to compute top-1, top-5 accuracies, and system loss. In this paper only the first classifier is used for training and testing of all the 9 sample images, further decreasing the number of parameters not affecting the accuracy and the time needed for convergence. To obtain the increase in identification accuracy only the top-1 accuracy is measured in this paper. The Cifar10 model has 3 convolutional layers, 2 fully connected layers, and 1 loss layer, each convolutional layer is followed by a max-pooling layer and ReLu activation function. For training cifar10 modified model is used, Dropout (for reducing overfitting) and ReLu (to learn sparse features) used in between fully connected layers to enhance the recognition accuracy. The hyperparameters are the parameters that affect the performance of the model they include:

1. Solver type
2. Base learning rate
3. Momentum
4. Learning rate policy
5. Weight decay
6. Batch size

Here they discussed the original and modified models of both the GoogleNet and Cifar10 by changing the base learning rate of the Cifar10 model from 0.001 to 0.0002 and the GoogLeNet model from 0.01 to 0.001and batch size for ciafar10 from 100 to 10. Considering the remaining original parameter values same for both Cifar10 and GoogleNet models as Solver type SGD(Stochastic Gradient Descendent), momentum as 0.9, Learning Policy as fixed and step, Weight decay as 0.004, 0.0002 and Gamma as 0.96 for GoogleNet model.

In the original GoogleNet model after 10,0000 iterations the top-1 testing accuracy was given as 98.8%, 98.6%, and 98.2% given by the three classifiers. The top-5 accuracy is 99.6%, 99.6%, 99.6%. The experimental results of the original GoogleNet model are given in Figures 8 and 9

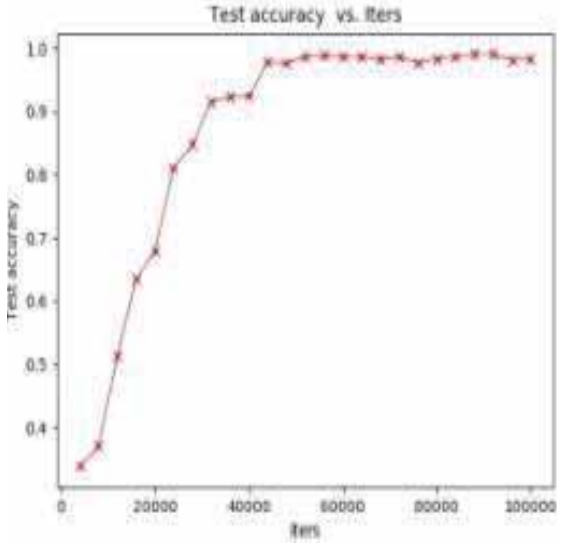

Figure 8. Top-1 Test Accuracy

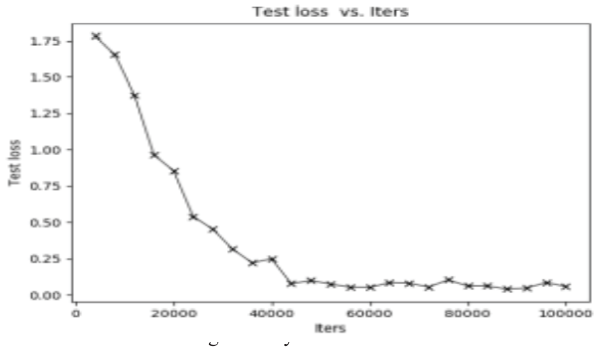

The original model has a large number of parameters where the recognition accuracy and the system loss converge after 40,000 iterations the training and convergence of the original model also consume a larger time. In the GoogleNet first classifier is used to perform the 50,000 iterations on the maize leaf dataset in this test. After every 100 iterations, the top-1 accuracy and the loss of the model are measured. Figure 10 and shows the modified GoogleNet model, after 10,000 iterations top-1 accuracy tends to 1 and the loss tends to 0, they explain that the average accuracy 98.9% and the loss is 1.6% for the modified GoogleNet model for both training and testing. All the classifications are done by the first classifier of the modified GoogleNet model. The top-1 recognition accuracy of the modified model is more than 0.4% compared to the original model. The system loss is about 14.2% lower than the original model.

In the modified model the after 10,000 iterations the top-1 testing accuracy approaches to 1 and the loss approaches to 0 both become stable but in the original model, they converge after 40000 iterations which take most of the time and computational resources. So there is an improvement in the modified model than the original model in terms of convergence which in turn enhances the recognition efficiency also.

In the Cifar10 model altering the Dropout operation, the recognition rate and testing accuracy is improved. The correlation between the dropout probability and the recognition rate is given as:

In common the dropout probability rate is taken as 0.5 later increased till 0.75, where the recognition accuracy increased with the increase of the dropout rate. It was found that when the dropout probability was 0.65 the recognition accuracy was about 97.8% this is about the original Cifar10

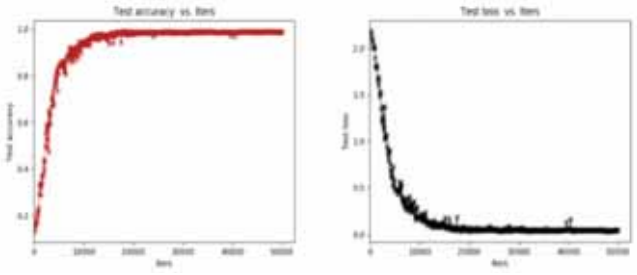

(a) Top -1 Test Accuracy (b) System Loss

Figure 10. Modified GoogleNet model

model. The Max-Max-Avg pooling combination is chosen on the remaining pooling combinations. In the original Cifar10 model the 4,000 iterations were considered for training the dataset, after 1,200 iterations the testing accuracy and the loss approach to a stable state the average testing accuracy is 97.1% the loss of the system be 17.8% refer to figure 11. When the pooling combination is Max-Max-Avg the training accuracy is 98.8% and the testing accuracy is 97.8% after 20,000 iterations they converge refer to figure 11. Using modified Cifar10 the testing accuracy enhanced by 0.7% and the loss reduced by 10.2%.

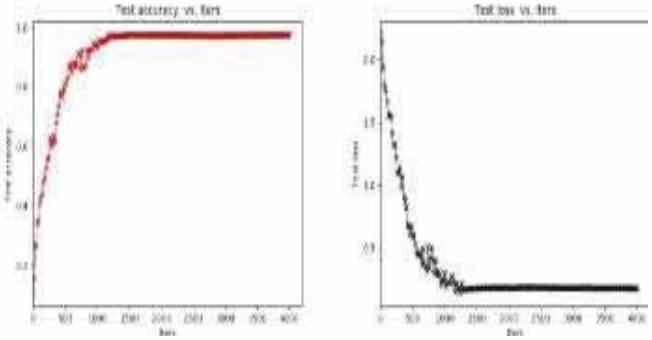

(a) Top -1 Test Accuracy (b) System Loss

Figure 11. Original Cifar10 Model

This paper showed the contrast between 2 networks i.e. GoogleNet and the Cifar10 model which have their own advantages and by changing the parameters acquiring the better version of both the individual models. The top-1 identification accuracy given by the GoogLeNet model is 98.5% and the Cifar10 model 97.1% using both original models. By using modified GoogleNet and Cifar10 models the high identification accuracy is given as 98.9% and 98.8%.

Jayme G.A. Barbedo , "Ref. [7]" has mentioned that deep learning has its significance in image classification and recognition. It solves complex problems like image recognition, text classification and also implemented in disease detection within the field of agriculture. This paper describes the parameters that affect the design effectiveness and factors that influence the deep neural networks. The image data were collected from the repository referred to as the digipathos repository which has about 50,000 images freely available. The corn leaf samples are considered during this paper for work. Totally 9 diseases of corn leaf were considered. Anthracnose, Tropical rust, Southern corn rust, Scab, Southern corn leaf light, Pheaosphaeria leaf spot, Diplodia leaf streak, Physoderma brown spot, Northern leaf blight.

E. Methodology:

In this paper, the GoogleNet was used using transfer learning implemented by neural network toolbox a library given by MatLab. The unprocessed images were first trained to three different CNN's where each CNN had its own operation on images. The 80% for training and therefore remaining 20% for validation were used. The training datasets were augmented. As a result, the training set size was increased 12 times and therefore overfitting was decreased. In Cnn1 worked by using actual unprocessed images, later in Cnn2 by using manually removed background in an image, in Cnn3 using subdivided images

i.e. the each of the images was subdivided into small images which contain individual symptoms of every disease of every image leaf following some rules for consistency within the subdivision. Finally in Cnn4 was implemented employing a reduced version of trained subdivided dataset images.

The parameters used for training are given as:-

1. Learning rate : 0.001
2. No. of epochs : 5
3. Momentum : 0.9
4. Min batch size : 06

The 10 fold cross-validation approach was used to get the final accuracy. The accuracy achieved in this work done by GoogleNet is given in table III as:

TABLE III.
CORN LEAVES IMAGES ACCURACY USING VARIOUS 3 CNN'S

Dataset	Training Images	Accuracy
Original	1584	76%
Background removed	1584	79%
Subdivided (completely)	100608	87%
Subdivided(reduced)	1584	81%

The accuracy for subdivision of image dataset completely gave more accuracy than all the techniques used in each of the cnn's. The accuracy was about 87% for 100608 images. The high accuracy is due to larger size of the dataset so the model learns a large set of features to detect accurately. The factors for the misclassification of images were identified, they were about 9 factors affecting the classification and overall performance of the CNN. There are extrinsic and intrinsic factors that affect the accuracy of the model for the classification of corn leaf diseases.

A. The Extrinsic Factors:

a. Annotated Datasets:

Annotating the datasets has many disadvantages. Continuous labeling of the images is an expensive, tedious, and a lot time-consuming tasks. If the labels have some uncertainty in them the training process wouldn't be enough which is a serious problem concerning some of the social networks. Mislabeling often occurs especially in labeling large datasets concerned with the plant disease databases with looks impractical.

b. Representation Of Symptoms:

Some datasets do not adequately represent the symptoms which are problematic for the model to classify the diseased class. Symptoms occur due to some of the external factors such as heat, cold, mechanical damage, toxicity, pests many more so that a good model needs to be available to handle the large classes. When the tools for disease recognition handle the real-world data, they have to find the correct class among all often leading to misclassification when they were trained on limited subset diseases. Very rare diseases more often tend to be misclassified.

c. Covariate Shifts:

Covariate shift is a phenomenon where the source domain distribution (training data) is completely different from the target domain distribution (testing data). This says that when a particular model is trained on some plantVillage dataset but when tested with some other trusted online data used i.e. collection site images immediately the accuracy fell to 50%. So, the detecting capability of the model affects it drastically.

d. Image Background:

Learning images with the heterogeneous background is a complex task. Deep neural networks also work in a busy background environment. The experiments conducted with different background produced an accuracy of 76% but for the images with background removed the accuracy was about 79%, this is because the model assumes the elements in the background as part of image symptoms, leaves and learns the background images as well which leads to error. So the leaf segmentation and background removal is a complex task. Selecting the region of interest by the user before the classification process in the touchscreen smartphone tool than placing the panel behind the image.

e. Image Capturing Conditions:

Capturing the images under controlled conditions and later using them is a type of process which includes dealing with images that were captured by various people, environment, intensities, and different angles. Many of them just ignore or treat superficially during analysing the results. Various experiments were carried out when the trained CNN's success rate decreased from99% to 68% when the training was done in field condition images but used the model with laboratory condition images. Some unrelated illumination effects also cause irreversible information loss. Peculiar reflection can be reduced by changing the image capturing angle or changing the position of the leaf.

B. The Intrinsic Factors:

a. Symptom Segmentation:

When the symptoms are localized, and the regions are isolated and segmented which contains the most relevant information. It would be more flexible for the system if the user selects the appropriate individual regions before classification which is more effective by touchscreen technology of smartphones. The model has to deal with multiple diseases with the same characteristics. It is a worth advantage in noticing the regions of interest by focusing on those particular symptoms.

b. Variations in Symptoms:

Each of the diseases have their own symptoms such as they differ in color, texture, shape, size. Variations in the

symptoms to the most create difficulty to the image-based diagnosis. If all the various stages of the symptoms (mild to severe) are given in the training the deep learning tool can handle the challenges held along with the diversity of symptom diseases. Practically it is very difficult to give all range of symptoms.

c. Simultaneous Disorders:

When the plant is infected with a particular disease its immune system is weekend which results in the attack of other diseases or pests or insects in turn increases the symptoms in plants or leaves, which is known as multiple simultaneous disorders. If removing or considering the region of interest by the user which is a very tedious task involves noticing every detail of the symptom and submit every one of them to the system. If this would have been done automatically would create many of the errors.

d. Disorders with the same Symptoms:

The occurrence of similar symptoms that can't be properly be identified by the plant pathologists also. although the image is captured with nearly perfect quality where the symptoms are so similar to diagnose. Human experts also consider other issues such as current data, historical data to analyse and draw accurate symptoms, which can be incorporated into systems to improve the classification. Some of the cases can only be solved through laboratory analysis. So, currently too unrealistic to have an automatic disease detection system to have perfect accuracy.

Other few of the factors such as over fitting, and systems that only rely on only one part of the plant, considering one dataset site or dataset downloading sites where all images are made freely available.

IV. Conclusions

"Ref. [1]" has used MCNN to detect the anthracnose disease in mango leaves the highest accuracy achieved by this model is 97.13%. The model used here can also be improved by involving IoT i.e. remote monitoring of the plants which is a good field where the MCNN can be implemented. Also, the use of some other activation functions that enhances the performance of the model can be used. Using other plant parts such as stem, fruits, flowers can also be used to detect the diseases. Also, by using various ensemble methods which can boost the performance along with the current deep learning models.

"Ref. [2]" has used the AlexNet and SqueezeNet on tomato leaves disease detection where the accuracy of the AlexNet was about 95.65% SqueezeNet accuracy was low as it is 80 times smaller than the AlexNet.The inference time of 150ms for AlexNet and 50ms for SqueezeNet. This model fits well on the field which can be deployed on to a robot that can detect the tomato leaf disease on the field itself.

"Ref. [5]" Among all the techniques which have been used this paper gives almost the best solution in this disease detection domain as it uses DCNN using symptomatic images are considered the accuracy of only 2 classes have large value because there were large image sets in those particular two classes (mildew and powdery mildew). This model can be enhanced by using other plant datasets with more in number to train the model well and achieve a good amount of performance on the remaining classes as well. The less accuracy is mainly due to low number of images used.

"Ref. [6]" This paper has used GoogleNet and Cifar10 models to detect the maize leaf diseases. Both models were trained by using original and improved models by changing the hyperparameters in them resulting from better results than the original models. This idea can be implemented in other domains and technologies to know and experiment on the techniques used which also enhances the scope of domain knowledge and gives the experimental results.

"Ref. [7]" has described the various factors affecting the design and performance of the DCNN models in plant pathology, these are the main factors that reduce the performance without the knowledge of the experimenter by displaying the drastic variation in results and accuracy of the models. These factors can be considered while developing a model, developing the image dataset required for that particular domain, the images also get effected which are also included in this paper they give goo insights on the images which are much important while maintaining a model and working on it. These factors can make or break a model's performance. Few other factors need to ignore while improving on other factors so has to balance the model to have good accuracy and performance with less amount of loss.

This survey paper has discussed various methods useful in detecting the diseases in various leaves which have their technique to implement. Each technique has its uniqueness also each of them have their advantages and disadvantages. This paper mainly focusses on the various convolutional neural network where various researchers have used the AlexNet, GoogleNet, SqueezeNet as their models which are good enough to detect the leaf disease but there is a need for improvement in each of the case like as mentioned as to increase the number of image dataset using ensemble methods along with the CNN's which can boost the performance of the model also by implementing various image processing techniques which give better results than current ones. This also includes best image processing supporting languages such as python, MatLab, Caffe, C++, C# gives better results when used where nowadays C++ is used as they are faster in processing. These Languages are mostly used in advanced computing in various AI, ML, and DL, NLP applications. There are various libraries given such

CVR Journal of Science and Technology, Volume 21, December 2021
DOI: 10.32377/cvrjst2119

as TensorFlow, OpenCV, Keras, IPSDK for smart segmentation smart classification mostly used in computer vision, and many more for analysing and improving the models performance. Thus for detecting the leaf diseases one can use suitable technique by enhancing the performance of the techniques previously used or develop a new enhanced model.

TABLE IV.
COMPARISION CHART FOR VARIOUS CONVOLUTIONAL NEURAL NETWORKS USED FOR IDENTIFICATION OF LEAF DISEASES

Sno.	Author Name	Type Of CNN Used	Name Of The Leaf	No. Of Leaf Diseases Used	Name Of The Leaf Diseases	Accuracy
1.	Uday Pratap Singh, Siddharth Singh Chouhan, Sukirty Jain, And Sanjeev Jain	Multilayer Convolution Neural Network	Mango	1	Anthracnose	97.13%
2.	Halil Durmuú, Ece Olcay Güneú, Mürvet KÕrcÕ	AlexNet and SqueezeNet	Tomato	10	1. Bacterial spot 2. Early blight 3. Healthy leaf 4. Late blight 5. Leaf mold 6. Septoria leaf spot 7. Spider mites 8. Target spot 9. Mosaic virus 10. Yellow leaf curl virus	AlexNet 95.65% SqueezeNet 94.3%
3.	Juncheng Maa, Keming Dua, Feixiang Zhenga, Lingxian Zhangb, Zhihong Gongc, Zhongfu Sun	DCNN	Cucumber	4	1. Anthracnose 2. Downy mildew 3. Powdery mildew 4. Target-Leaf Spots	Anthracnose (82.0%) Downy mildew (96.7%) Powdery mildew (98.2%) TargetLeaf Spots (91.8%)
4.	Xihai Zhang, Yue Qiao, Fanfeng Meng, Chengguo Fan, Mingming Zhang	DCNN	Maize	8	1. Southernleaf blight 2. Brown spot 3. Curvularia leaf spot 4. Rust 5. Dwarf mosaic 6. Greyleafspot 7. Round spot 8. Northern leaf blight	GoogleNet (98.9 %) Cifar10 (98.8 %)
5.	Jayme G.A. Barbedo	GoogleNet used for training Mainly used 3 types of Cnn's	Corn	9	1. Anthracnose 2. Tropicalrust 3. Southern corn rust 4. Scab 5. Southern corn leaf light 6. Pheaosphaeria leaf spot 7. Diplodia leaf streak 8. Physoderma brown spot 9. Northern leaf blight.	For completely subdivided Images accuracy was 87 %

CVR Journal of Science and Technology, Volume 21, December 2021
DOI: 10.32377/cvrjst2119

V. Abbreviations and Acronyms

AI	Artificial Intelligence
CAFFE	Convolutional Architecture for Fast Feature Embedding
CNN	Convolutional Neural Network
DL	Deep Learning
DCNN	Deep Convolutional Neural Network
GAP	Global Average Pooling
GDP	Gross Domestic Product
IoT	Internet of Things
IPSDK	Image Processing Software Development Kit(SDK)
ML	Machine Learning
NLP	Natural Language Processing
NIN	Network in Network
ResNet	Residual Network
VGG Net	Visual Geometry Group

References

[1] Uday Pratap Singh, Siddharth Singh Chouhan, Sukirty Jain, And Sanjeev Jain, “Multilayer convolutional neural network for the classification of mango leaves infected by the anthracnose disease”, in press.

[2] Halil Durmuú, Ece Olcay Güneú, Mürvet KÕrcÕ, “Disease detection on the leaves of the tomato plants by using deep learning”, in Proc. 6th Int. Conf. Agro-Geo-informatics, Fairfax, VA, USA, Aug. 2017, pp. 1–5, in press.

[3] Forrest N. Iandola, Song Han, Matthew W. Moskewicz, Khalid Ashraf, William J. Dally, KurtKeutzer, “Squeezenet: alexnet-level accuracy with 50x fewer parameters and < 0.5MB model size” review as a conference paper at ICLR 2017, in press.

[4] Arpita Patel, Mrs. Barkha Joshi, “A survey on the plant leaf disease detection techniques”, Vol. 6, Issue 1, January 2017, in press.

[5] Juncheng Maa, Keming Dua, Feixiang Zhenga, Lingxian Zhangb, Zhihong Gongc, Zhongfu Sun, “Recognition method for cucumber diseases using leaf symptom images based on deep convolution neural netwoks”, August 2018, in press

[6] Xihai Zhang, Yue Qiao, Fanfeng Meng, Chengguo Fan, Mingming Zhang, “Identification of maize leaf disease using improved deep convolutional neural networks”, unpublished.

[7] Jayme G.A. Barbedo, “Factors influencing the use of deep learning for plant disease recognition”, 2018, in press.

E-ISSN 2581 –7957
P-ISSN 2277 – 3916

CVR Journal of Science and Technology, Volume 21, December 2021
DOI: 10.32377/cvrjst2120

Mechanical Characterization of Kevlar Epoxy Composites derived from 3D Printing process

A. Suresh
Asst. Professor, CVR College of Engineering/Mechanical Engg. Department, Hyderabad, India.
Email: suri0341@gmail.com

Abstract: **Additively fabricated polymer based composites exhibit ascendancies over the conventional manufactured polymer products because of their tweaked delineation pliability, dwarf cadence fixture of model-to-fabrication process for shortening the waste of material and cost of investment. Emphasis on short fiber included thermo-plastic reinforced composites is increasing now-a-days and the investigation for analyzing the mechanical properties is enhancing day-to-day. On the other hand, derivation of thermo-plastic composites from 3D-printing process involves more porosity and less mechanical strength. To overcome the existing drawbacks in the present work the analysis of producing short Kevlar based reinforced epoxy composites using additive manufacturing is made. The fabrication is thus archived with the customized setup of direct-write additive manufacturing. The vibration integrated parameters involved in the fabrication process are analyzed meticulously. With this experimentation, high dense and high viscous Kevlar composite is made with a maximum of 6.1% Kevlar fibers. The produced Kevlar composite links are contrasted with the unreinforced Kevlar links with 3-point bending setup. The analysis carried out in static and dynamic aspects. At the end of the experimentation, it is observed that mechanical strength, strength to weight ratio and ductility are improved for the work pieces obtained from additive manufacturing. Hence, it is evident that the adoptability practices for the Kevlar composites using additive manufacturing are more beneficial with respect to aerospace structural applications.**

Index Terms: Kevlar composites, Additive manufacturing, 3-Point Bending.

I. Introduction

3 dimensional printing (3D) or additive manufacturing (AM) is a material deposition technique in a layer-by-layer method to produce more accurate and intricate parts. The deposition using AM of the material is a fine tuning of the expectations from the maker's point of view and strength considerations [1]. Using the 3D printing process produced outcomes are readily re-designable, easy to modify, low material waste without altering the objective function is archived. Because of the above mentioned advantages, AM is used for wide range of applications in the field of high strength wear resistant materials [2].

The chief advantage lies with AM of Kevlar composites is the weight that material has, most required property for polymers is their easy processing and specific reduction of weight. To replace the conventional materials in the field of aero space and novel structural applications additively made polymer composites are best choice [3]. The induced vibrations in the fabrication of composite material for the specific application depend on controlling the parameters. The controlling of the process parameters for obtaining the desired quality and quantity of the product is archived meticulously by the 3D printing process [4]. With respect to the mechanical performance aspects polymers of various reinforcements like carbon, glass and natural fiber are added to the composites. The choice of using the fibers depends on two options one is continuous fibers and the other is short fibers. Hence, the adoptability of fiber depends upon various factors like their elongation, shear strength and the application.

Yet, in the present work the usage of short fibers is made due to the advantage of ease in adding the fiber to the machine and also the flow-ability of the material for producing the intricate parts [5]. In addition to it, the length of the fibers to be used in AM id decided based on the previous experimentations. There is no direct verdict that length of the fiber alone can decide the strength of the material [6]. But, at the same time it is also important to use the appropriate length of the Kevlar fiber. Usually, the short fibers are made wither by milling of chopping them into smaller parts of required size [7].

The feed stocking of the Kevlar is archived by simple mixing of the Kevlar fibers with the matrix material such as thermo plastic composites. It will reduce the complexity of the fabrication to great extent and then it shows the versatile properties [8]. One more important advantage is that the thermal stability and strength most likely it happens that the usage of the Kevlar composite is made in novel structural applications and aero space applications [9]. In both the cases the material is subject to more fluid attack that leads to wear and cracks over the surface. The additively made Kevlar composite can make the components rigid and firm to face the forecasted challenges [10]. In this voyage, the credit must be given the additive manufacturing setup and also finely chopped Kevlar composite. The real time functioning and testing of the composites is made a 3-point bending experiment and also the results are compared and contrasted with the conventional outcomes [11].

II. Methodology

A. Concocting of short fibers of Kevlar using laser cutting process

The activity of generating uninterrupted, mono-directional fibers of Kevlar material with a size of about 7.5-micron radius is schlepped out by maneuvering the laser cutting process [12]. The separated fibers are then riddled to circumvent the integral segments of Kevlar folio and separate the undivided fiber fascicles.

After completion of laser cutting of fibers the investigation of the boundaries of cut fibers below a

Received on 08-08-2021, Revised on 03-10-2021, Accepted on 25-11-2021.

CVR Journal of Science and Technology, Volume 21, December 2021
DOI: 10.32377/cvrjst2120

microscope (optical) then investigated the laser cutting procedure [13]. During the investigation just about hundred microns cavernous blazed suburbs from fiber verge at every side. Hence, the chosen stretch of fibers, four crimps eight hundred microns that is greater than complete flicker span to prune the smoldering reverberation of laser next to incise suburbs.

After the cutting of the Kevlar fibers using laser cutting process, Scanning electron microscope (SEM) is employed to discern the arrangement of short Kevlar fibers [14]. To proceed with the SEM imaging for minimizing charging of Kevlar fiber a layer of about 1-1.5nm of thickness is used for coating on the surface. The fibers are maintained under the pressure of 50 milli-torr (vacuum) for about 28 seconds with super scribing coating instrument [15].

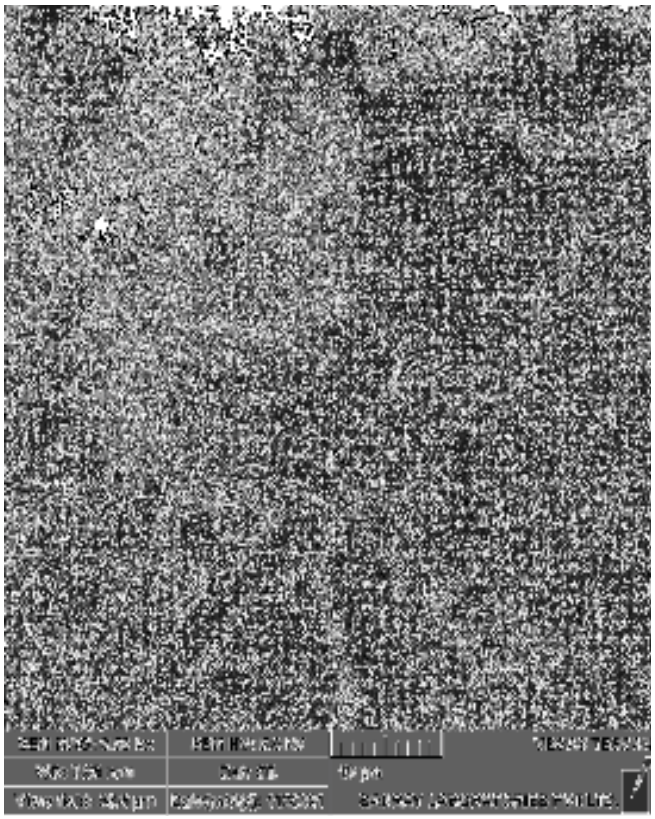

Figure 1. SEM image showing the single and bunch of fibers

In the above figure 1 of SEM analysis observation is made a magnification level of 3530x and the image showing the fibers are at a scale of 10 microns. In the figure it can be clearly seen that the single fibers and bunch of fibers are present.

Fibers are rationally separated to a required length maneuver the detailed technique as shown in Figure 1. In this figure, detached, unique fibers along with the bundles of fiber in this the fibers aren't fully detached are also descried.

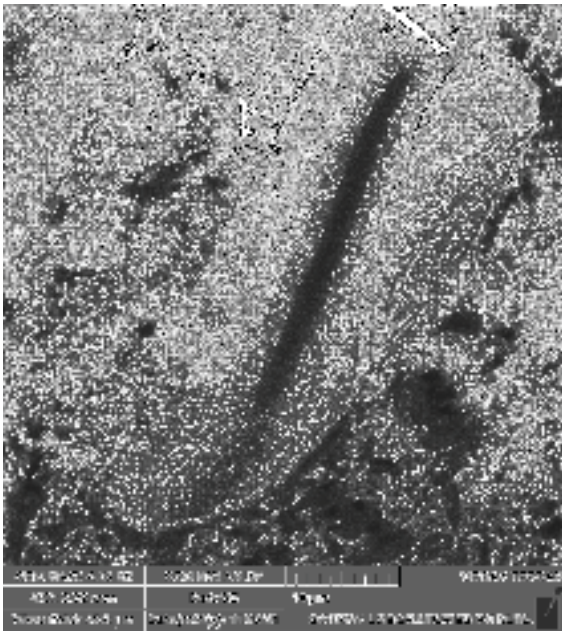

Figure 2. SEM image showing single fibers

In the above figure 2 of SEM analysis observation is made a magnification level of 4230x and the image showing the single fibers are at a scale of 10 microns.

B. Printing Ink concocting approach

Hexion an epoxy is chosen as thermo-set resin during the current work. The making of composite ink is initiated with addition of nano-clay material, a form of additive to make the epoxy resin by revamping the physiochemical combination of the ink [16].

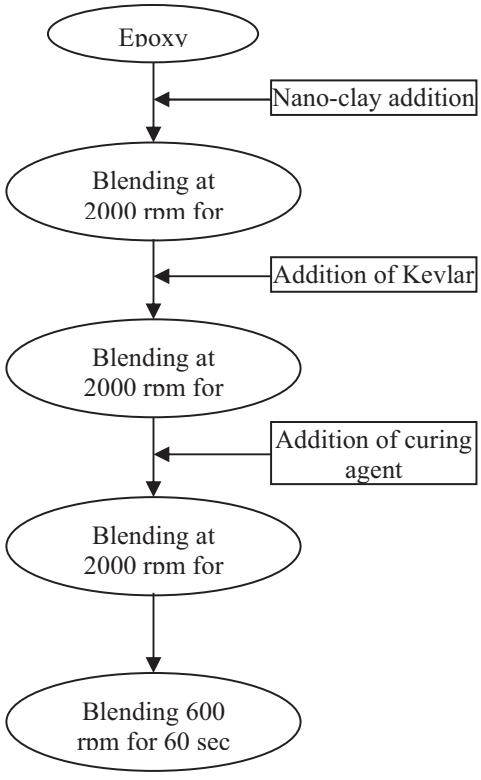

Figure 3. Preparation of ink for 3D printing

CVR Journal of Science and Technology, Volume 21, December 2021
DOI: 10.32377/cvrjst2120

In the next step, separated Kevlar fibers are pretended into a mixture made up of nanoclay-epoxy comprehensively prior to outstretch to a paramount quantity of Kevlar fibers. Its quality is improved in terms of nano-clay reduction and densification of ink mixture [17]. The mixture obtained has a viscosity that is proportional to the conventional paint or ink. To obtain the desired dense mixture of paint the quantification of nano-clay addition is achieved with trial and error method with the quantities of 0, 3.7 and 6.1%. The below figure 3 depicts the 3D printing procedure.

Fiber content in the fabricated ink was found out by making the calculation with densities of constituents and also the mass fractions. The density of the ink is calculated by taking the density of the epoxy as 1.15 $\frac{g}{cm^3}$, nano-clay as 1.97 $\frac{g}{cm^3}$, Kevlar as 1.45 $\frac{g}{cm^3}$ and curing agent as 1.05$\frac{g}{cm^3}$.

C. Flow characterization of ink

The flow characteristics of the prepared ink for all the specimens are pervaded maneuvering the using the Rheometer. Appraising topology is institute on a eight mm plumb plate accompanied by a cranny apogee of 500 mm. Preceding to everyone scrutiny, specimens are put through a 60 seconds constraining juncture at a unceasing rate of shear of about 0.1 sec^{-1} accompanied by a two minute repose stretch for reconversion of structure of structure kindred to erstwhile swatting [18]. Specimen's viscosity is sedated as concomitant of rate of shear with panoramic by way of superintended with rate of shear 0.004^{-19} s^{-1} and depositary & mislaying modulus of elasticity are determined as the concern of shear stress in a kindred vogue.

D. Additive manufacturing of Kevlar ink maneuvering direct write method

Figure 4 details the outline of direct write additive manufacturing approach required in present work for juxtaposition with prosaic fused filament manufacturing procedure. The defects in the fused filament manufacturing can be seen in the below figures as compared to direct write AM.

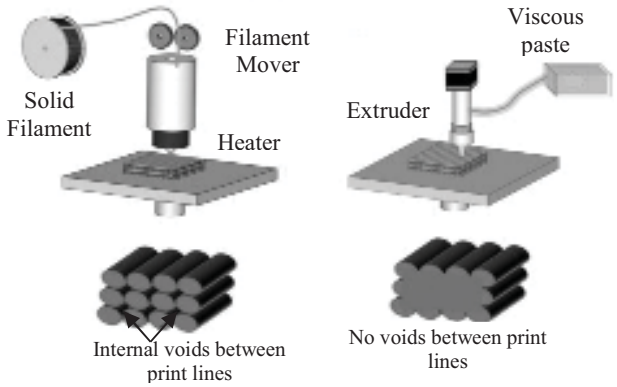

Figure 4 Difference between Fused filament manufacturing and Direct write additive manufacturing

In the above figure 4 the difference in between the two processes are shown in detail. There are some voids present in between the produced bars as seen in printed lines with the fused filament process whereas in the direct write AM the probability of getting the voids is less and hence in the present work it is considered.

The printing of the Kevlar composite is made at a temperature of 100°C for about 15 hours. The additively manufactured made Kevlar composite material specimens are made by extrusion process with a nozzle of 2mm diameter and the jet processes the printing with a velocity of 40mm/sec. During the process of direct injection, the vibration of the nozzle becomes a significant criterion. It happens due to the problem of solidification of the injecting fluid. Because of mismatch in temperature inside the nozzle and outside the solidification may take place. This problem is popularly known as nozzle clogging. During the experimentation, the nozzle clogging problem is taken into consideration. The issue of nozzle clogging happens mainly due the high loading of the fibers. The increase in loading of fibers inside the nozzle leads in "nozzle clogging". The problem of nozzle clogging is resolved by introducing the vibration motors along with the direct write AM [19]. The vibration motors make the injecting nozzle position in dynamic position that in turn makes the nozzle function without jam. The surface plate is coated with the Teflon to avoid the sticking of the Kevlar composite.

The following figure 5 shows the images of specimens before and after curing process of base ink. Figure 6 shows the images of specimens before and after curing process of Kevlar composites.

Figure 5. Additively manufactured specimen of base ink

Figure 6. Additively manufactured specimen of Kevlar composite

III. Results and Discussions

The testing of the Kevlar composite specimens is made using a three point bending experiment. In the three points bending experiment a total of 4 samples are tested. The major constituents of the Kevlar fiber are about 3.5% and 6.3% of Kevlar fiber and about 7% of the nano-clay. The

CVR Journal of Science and Technology, Volume 21, December 2021
DOI: 10.32377/cvrjst2120

experimentation is carried out in a static and cyclic loading condition.

The fatigue calculation is made by the repeated experimentation with the increment in loads. The loads increased are tested for about standard number of cycles in the present case it is considered as 2 million cycles. Soon after the initiation of the experimentation of the Kevlar composite the failure point is observed by taking the reading at the first crack generated in the specimen.

Right from the lower loads to the continuous incremental loads experiment is performed. From the experimentation it is found that the highly loaded Kevlar composite has shown high strength and yielded more modulus. And in the specimens that has less Kevlar composition the modulus is found as low. The highest strength against failure is found to be 300kPa and shear strength of 1000Pa observed for 6.3% of kevlar. In the case of Kevlar composite with 3.5% composition the values are found as 160 Pa and 630Pa.

The below figure 7 shows the comparison of the results for various Kevlar composite specimens.

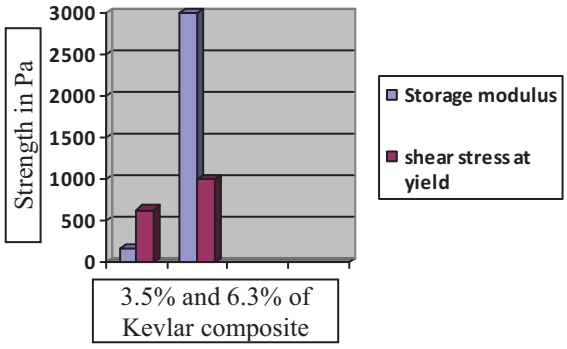

Figure 7. Comparison of Kevlar composites specimen 3.5% and 6.3%.

Similarly the flexural strength, flexural strain and flexural modulus of the Kevlar composites are compared after the experimentation. The comparison in between the base ink, Kevlar composite of 3.5% and Kevlar composite of 6.3% is made with the following graphs.

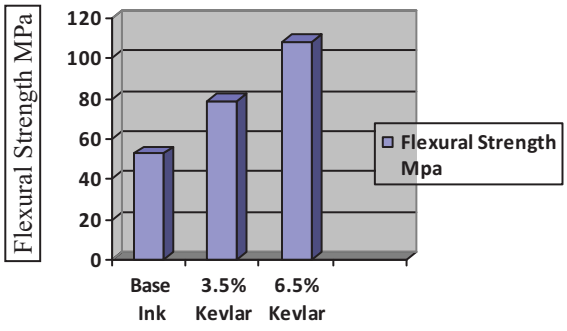

Figure 8. Comparison of Kevlar composites specimen 0%, 3.5% and 6.5% for Flexural Strength.

From the above figure 8 the flexural strength of the direct injected additively manufactured Kevlar composite specimens of 0%, 3.5% and 6.5% is compared. The specimen comprise 0% Kevlar that is base ink is having a flexural strength of 52.63 MPa. The specimen having 3.5% Kevlar has shown a flexural strength of 78.30 MPa. The specimen having 6.5% Kevlar has shown a flexural strength of 108 MPa.

From the below figure 9 the flexural modulus of the direct injected additively manufactured Kevlar composite specimens of 0%, 3.5% and 6.5% is compared. The specimen comprise 0% Kevlar that is base ink is having a flexural modulus of 3.24 GPa. The specimen having 3.5% Kevlar has shown a flexural modulus of 3.84 GPa. The specimen having 6.5% Kevlar has shown a flexural modulus of 4.23 GPa.

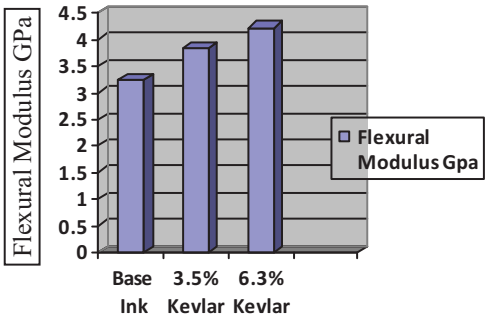

Figure 9. Comparison of Kevlar composites specimen 0%, 6.3% and 3.5%.for flexural strength

From the below figure 10 the flexural strain of the direct injected additively manufactured Kevlar composite specimens of 0%, 3.5% and 6.5% is compared. The specimen comprise 0% Kevlar that is base ink is having a flexural strain of 1.6%. The specimen having 3.5% Kevlar has shown a flexural strain of 2.2%. The specimen having 6.5% Kevlar has shown a flexural strain of 3.15%.

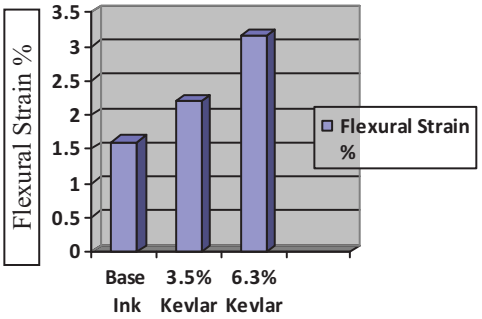

Figure 10. Comparison of Kevlar composites specimen 0%, 6.3% and 3.5%.for flexural strain.

From the below figure 11 the flexural fatigue strength of the direct injected additively manufactured Kevlar composite specimens of 0%, 3.5% and 6.5% is compared.

The specimen comprise 0% Kevlar that is base ink is having a flexural fatigue strength of 3.24 MPa. The specimen having 3.5% Kevlar has shown flexural fatigue strength of 3.84 MPa. The specimen having 6.5% Kevlar has shown flexural fatigue strength of 4.23 MPa.

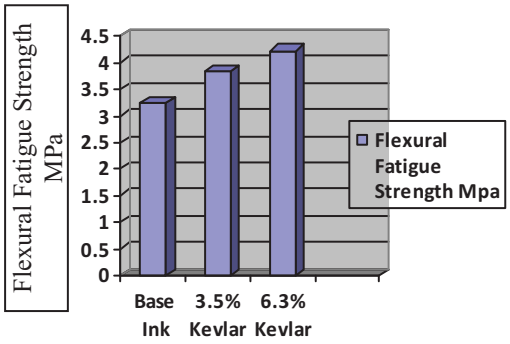

Figure 11. Comparison of Kevlar composites specimen 0%, 6.3% and 3.5%.for flexural fatigue strength

IV. Conclusions

In the present work, investigation and analysis of Kevlar composite material made from direct write additive manufacturing is made. The short Kevlar and nano-clay composite material static and flexural strengths are made and results are analyzed and the following conclusions are made.

- The void free Kevlar fiber composite is made by direct write additive manufacturing as compared to other manufacturing procedures.
- There is a significant improvement in the storage modulus and shear stress at yield with improvement of Kevlar composite from 3.5% to 6.5%.
- There is a significant improvement in the flexural strength with improvement of Kevlar composite from 3.5% to 6.5%. The flexural strength improved from 52.63 MPa to 78.30 MPa.
- There is a significant improvement in the flexural modulus with improvement of Kevlar composite from 3.5% to 6.5%. The flexural modulus improved from 3.84 GPa to 4.23 GPa.
- There is a significant improvement in the flexural strain with improvement of Kevlar composite from 3.5% to 6.5%. The flexural strain improved from 2.2% to 3.15%, for the base ink it is found to be 1.6%.
- There is a significant improvement in the flexural fatigue strength with improvement of Kevlar composite from 3.5% to 6.5%. The flexural fatigue strength improved from 3.84 MPa to 4.23 MPa, for the base ink it is found to be 3.24 MPa.

References

[1] G.D. Goh, H.K.J. Tan, Y.L. Yap, G.L. Goh, S.L. Sing, W.Y. Yeong, (2019), Process-structure–properties in polymer additive manufacturing via material extrusion: a review, Critical Review Solid State Mater. Sci., 1–21, doi: 10.1080/10408436. 2018.1549977.

[2] V. Shanmugam, O. Das, R.E. Neisiany, K. Babu, S. Singh, M.S. Hedenqvist, F. Berto, S. Ramakrishna, (2020), Polymer Recycling in Additive Manufacturing: an Opportunity for the Circular Economy, Mater. Circ. Econ, 2 (11), doi: 10.1007/s42824-020-00012-0.

[3] V. Shanmugam, O. Das, K. Babu, U. Marimuthu, A. Veerasimman, D. J. Johnson, R. E. Neisiany, M.S. Hedenqvist, S. Ramakrishna, F. Berto, (2021), Fatigue behaviour of FDM-3D printed polymers, polymeric composites and architected cellular materials, Int. J. Fatigue, 143,p. 106007,doi:10.1016/j.ijfatigue.2020. 106007.

[4] S.M.F. Kabir, K. Mathur, A.F.M. Seyam, (2020), A critical review on 3D printed continuous fibre-reinforced composites: history, mechanism, materials and properties, Compos. Struct., 232, p. 111476, doi: 10.1016/j.compstruct.2019. 111476.

[5] A. Nasirov, I. Fidan, (2020), Prediction of mechanical properties of fused filament fabricated structures via asymptotic homogenization, Mech. Mater., 145 (2020), doi: 10.1016/j.mechmat.2020.103372.

[6] P. V. Sai Swaroop, A. Suresh, (2021), Effects of Fiber Orientation on Mechanical Properties and Analysis of Failures for Kevlar Epoxy Reinforced Composites, CVR Journal of Science and Technology, 20(1), June, p 142-146, doi: 10.32377/cvrjst/2022

[7] S. Wickramasinghe, T. Do, P. Tran, (2020), FDM based 3D printing of polymer and associated composite: a review on mechanical properties, defects and treatments, Polymers, 12 (2020),p. 1529, doi: 10.3390/polym12071 529

[8] N. van de Werken, H. Tekinalp, P. Khanbolouki, S. Ozcan, A. Williams, M. Tehrani, (2020), Additively manufactured carbon fibre-reinforced composites: state of the art and perspective, Additive Manufac., 31, p. 100962, doi: 10.1016/j.addma.2019.100962

[9] H. Wu, W.P. Fahy, S. Kim, H. Kim, N. Zhao, L. Pilato, et al. (2020), Recent developments in polymers/polymer nanocomposites for additive manufacturing, Prog. Mater. Sci., 111, doi: 10.1016/j.pmatsci.2020.100638

[10] M. Mohammadizadeh, A. Imeri, I. Fidan, M. Elkelany, (2019), 3D printed fibre reinforced polymer composites - structural analysis, Compos. B Eng., 175, p. 107112, doi: 10.1016/j.compositesb.2019.107112

[11] E.A. Papon, A. Haque, (2019), Fracture toughness of additively manufactured carbon fibre reinforced composites, Additive Manufac., 26, pp. 41-52, doi: 10.1016/j.addma.2018.12.010

[12] A.D. Pertuz, S. Díaz-Cardona, O.A. González-Estrada, (2020), Static and fatigue behaviour of continuous fibre reinforced thermoplastic composites manufactured by fused deposition modelling technique, Int. J. Fatig., 130, p. 105275, doi: 10.1016/j.ijfatigue.2019.105275

[13] G. Sodeifian, S. Ghaseminejad, A.A. Yousefi, (2019), Preparation of polypropylene/short glass fibre composite as Fused Deposition Modeling (FDM) filament, Results Phys., 12, pp. 205-222, doi: 10.1016/j.rinp.2018.11.065

[14] Z. Liu, Q. Lei, S. Xing, (2019), Mechanical characteristics of wood, ceramic, metal and carbon fibre-based PLA composites fabricated by FDM, J. Mater. Res. Technol., 8, pp. 3743-3753, doi: 10.1016/j.jmrt.2019.06.034

[15] Ms. B. Reetha, Mr. B. Nikhil, Ms. P. Mamatha, Mr. A. Suresh, (2021), Evaluation of Mechanical Properties and Simulation of Kevlar Epoxy Reinforced Composite with Silicon Carbide Filler, International Journal of Advances in Engineering and Management, 3(5), PP 33-42, doi: 10.35629/5252-03053342

[16] M. Heidari-Rarani, M. Rafiee-Afarani, A.M. Zahedi, (2019), Mechanical characterization of FDM 3D printing of continuous carbon fibre reinforced PLA composites, Compos. B Eng., 175, p. 107147, doi: 10.1016/j. compositesb.2019.107147

[17] L. Sang, S. Han, Z. Li, X. Yang, W. Hou, (2019), Development of short basalt fibre reinforced poly lactide composites and their feasible evaluation for 3D printing applications, Compos. B Eng., 164, pp. 629-639, doi: 10.1016/j.compositesb.2019.01.085

[18] A. Suresh, P. Bhargavi, M. Kiran Kumar, (2021), Simulation and mechanical characterization on kevlar epoxy reinforced composite with silicon carbide filler, 38(5), p 2988-2995, https://doi.org/10.1016/j.matpr.2020 .09.321

[19] S. Garzon- Hernandez, D. Garcia- Gonzalez, A. Jérusalem, A. Arias, (2020), Design of FDM 3D printed polymers: an experimental-modelling methodology for the prediction of mechanical properties, Mater. Des., 188, doi: 10.1016/j.matdes. 2019.108414

E-ISSN 2581 –7957
P-ISSN 2277 – 3916

CVR Journal of Science and Technology, Volume 21, December 2021
DOI: 10.32377/cvrjst2121

Design and Fabrication of Seabin Project for Efficient Collection of Water Waste Using Solar Energy

Sarat Kumar Sahoo[1], Ahmed Nizami[2], Shaik Wahajuddin[3] and Gampa Smruthi[4]
[1]Asst. Professor, CVR College of Engineering/ Mechanical Engg. Department, Hyderabad, India
Email: saratkumar222@gmail.com
[2]UG Scholar, CVR College of Engineering/ Mechanical Engg. Department, Hyderabad, India
Email: taffazul47@gmail.com
[3]UG Scholar, CVR College of Engineering/ Mechanical Engg. Department, Hyderabad, India
Email: shaikwahajuddin417@gmail.com
[4]UG Scholar, CVR College of Engineering/ Mechanical Engg. Department, Hyderabad, India
Email: 16B81A03J2@cvr.ac.in

Abstract: **Water bodies across the world are facing existential crises. The human settlements are regularly dumping off the garbage and refuse to clean the water bodies. This is a major environmental hazard and causes a degradation of water bodies and affects the overall food chain. This work is emphasized on the design and fabrication of a floating debris interception device i.e. Seabin to curb this problem. The idea is simple if we can have garbage bins on land, why not have them in the ocean as well. The Seabin works in such a way that the water is pumped out of the catch bucket that is already submerged in the water. Through this suction, the water with all its floating litter collects in the bucket. The catch bag accumulates litter, separating it from the water. The water is again pumped out of the bucket. This whole process takes place simultaneously and fresh batches of litter settle down in the catch bag until the limits get exhausted.**

Index Terms: **Seabin, Environmental hazard, Plastic waste, Debris**

I. INTRODUCTION

Plastic products are commonly utilized by the maritime industry. For example, fishing nets and strapping bands used to secure cargo are typically composed of plastic. Plastic materials are also used to package food products and other items consumed by the crew members on commercial vessels. Disposal at sea has been the normal procedure that commercial vessels have followed to discard packaging materials and other waste products.

The discarding of waste products in sea is not new. What has changed in recent decades is that lot of products are now made of plastic. Another form of plastic litter is the raw material used by the plastic industry to manufacture their products. Raw plastic usually is fabricated into tiny pellets, or spherules, then shipped to factories where it is transformed into consumer products. Plastic pellets are also used for packing and insulating material for cargo transportation. In both instances, these pellets can enter rivers and seas by accidental or deliberate discharge.

Plastic materials threaten the marine environment for the same reasons they are a commercial success: durability and economic affordability. Because of its low cost, plastic is readily and ubiquitously utilized as a source of disposable material. It is the durable properties of plastic, however, that pose the greatest threat; plastic materials persist in the marine environment long after they have been thrown away.

Plastic pollution is the most widespread problem affecting the marine environment. It also threatens ocean health, food safety, and quality, human health, coastal tourism, and contributes to climate change.

The most visible and disturbing impacts of marine plastics are the ingestion, suffocation, and entanglement of hundreds of marine species. Marine wildlife such as seabirds, whales, fishes, and turtles, mistake plastic waste for prey, and most die of starvation as their stomachs are filled with plastic debris.

Wang et al. [1] presented the distribution of atmospheric microplastic (MP) abundance over the ocean based on a survey conducted in Pearl River, South China Sea and East Indian Ocean. They revealed that MP undergoes a long-range distance, more than thousand kms away, through the atmosphere becomes the main source of oceanic MP. Winton et al. [2] identified the prevalent MP items in freshwater of Europe, specifically plastic, that could be possibly reduced by creating awareness among the (actions of the) public, industry, and the government. Their investigation addressed the variation of reported MP in freshwater and oceanic atmospheres. Gallo et al. [3] studied the impending impacts of macro and MP waste on marine biodiversity and human life. They suggested analytical method on production and consumption of plastics and waste management and tough plan actions to control unnecessary plastic packet, ban on single-use plastic bags, intensification of the collection rate of plastic waste, deposit-refund arrangements for plastic beverage bottles that have a proven a high rate of victory in many countries. Krishnakumar et al. [4] found white irregular shaped polyethylene and polypropylene debris in their research in the Andaman and Nicobar Islands beach sediments in 2018. The main cause of plastic litter was due to tourists, shipment and improper handling of solid wastes disposed in the marine environment carried by tides, circulates around the island, and finally reaches the coastal areas and cause threat to the marine life.

CVR College of Engineering
Received on 14-04-2021, Revised on 24-04-2021, Accepted on 08-05-2021.

CVR Journal of Science and Technology, Volume 21, December 2021
DOI: 10.32377/cvrjst2121

Zhu et al. [5] investigated the presence of plastic debris on 1 seabird species and 2 shorebird species from Yongxing Island of South China Sea and found a 56 items of plastic debris in 4 of 9 birds, with size ranging from 0.67 to 8.64 mm. Maximum portion (92.9%) of the total items of MP found with size < 5 mm and predominated by polypropylene-polyethylene copolymer 83.9%. The main color of collected MP debris was blue 91.1% and shape was thread 89.2%, sheet 8.9%. This work concluded that marine birds could mistake plastic debris as food items. Sonam et al. [6] analyzed the impact of the marine pollution and utilized oceanographic model of coasting trash dispersal by rectifying for wind-driven vertical blending, gauged at least 5.25 trillion particles weighing 268,940 tons. They marked a huge loss of micro plastics from the ocean surface contrasted with anticipated paces of discontinuity, that recommends systems at play that expel <4.75 mm plastic particles from the sea surface. Xu et al. [7] developed a simple, fast and low-cost method to treat oily wastewater by synthesizing corn straw fiber via conventional impregnation. By using chemical coupling agent, they could increase absorption capacity and absorption efficiency, that has great potential for treatment of oily water.

Tan et al. [8] proposed a distinctive eco-friendly corn straw material with preferable super hydrophobicity and superoleophobicity for separating oil from liquid mixtures. The modified corn straw found to have preferable chemical durability and environmental continuance, allowing it to both selectively adsorb oils and completely repel water. The designed corn straw provides an eco-friendly alternative for the cleanup of oil spills, as well as a means to relieve the environmental problem of agricultural waste disposal. Jian Dai et al. [9] presented the various features in the progress of the floating modular photovoltaic system. They designed a system encompasses several standardized floating modules prepared by high density polyethylene that serve as either photovoltaic panel floaters or maintenance walkways. They also presented details of the launching of the proposed floating photovoltaic system at the testbed and assesses the power generation of the system.

II. Methodology

This project aims to create a debris collector (SEABIN) to collect floating debris or waste materials from water. The idea proposed here is very similar to the existing SEABIN PROJECT with a few changes in its performance parameters. We have studied keenly the different types of cleanup programs and have taken inspiration from all of them. Our version of Seabin is estimated to catch 1.5 Kg of floating debris per day (depending on weather and debris volumes) including microplastics up to 2 mm small. The project works in such a way that the water is pumped out of the catch bucket that is already submerged in the water. Through this suction, the water with all its floating litter collects in the bucket. The nylon catch bag accumulates litter, separating it from the water. The water is again pumped out of the bucket. This whole process takes place simultaneously and fresh batches of litter settle down in nylon catch bag until the limits get exhausted.

A design of the component has been prepared and shown in Figure 1.

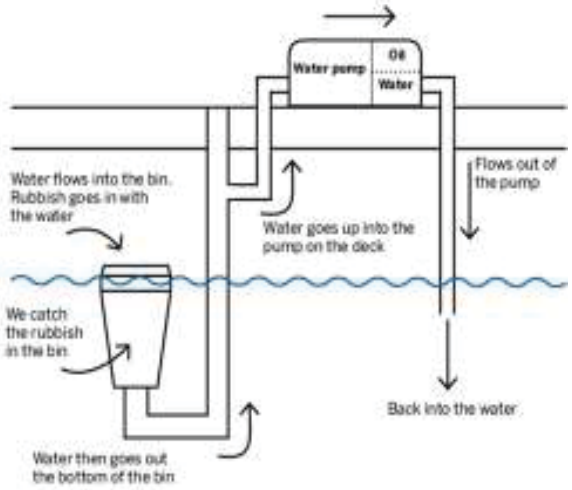

Figure 1. Design of the component

III. Experimentation

The following components have been used to prepare the designed seabin model.

A. L-shaped Aluminum Vertical Post

This component is the primary one as it forms the base of the project. This vertical post is hollow for weight reduction and is made of aluminum. Aluminum is a material having less density and is non-corrosive in nature. These properties of aluminum are ideally suitable for the component as it has to remain in contact with water most of the time. Figure 2 shows the dimensions of the vertical post

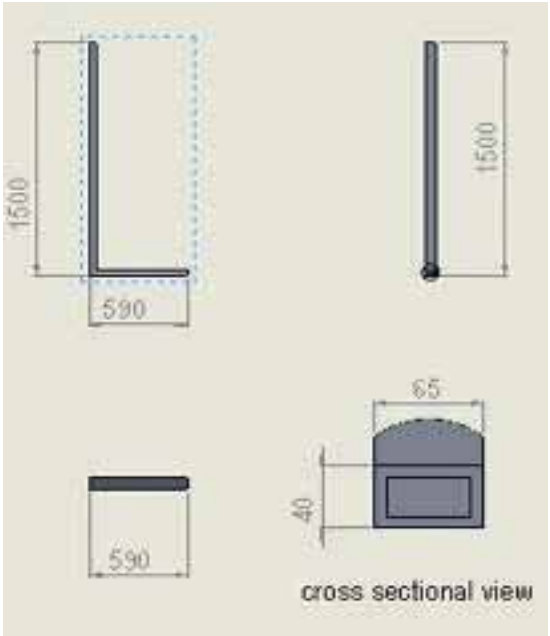

Figure 2. The dimensions of the vertical post

CVR Journal of Science and Technology, Volume 21, December 2021
DOI: 10.32377/cvrjst2121

B. Debris Collector

This component is a cylindrical collector with a varying cross-section holding the main filter that collects all the floating trash in it as the suction is created and acts as a basin interacting with the whole structure. Apart from this, because of the decreasing cross-section, a pressure difference in the pump is created that helps in the suction of water under unusual cases of water head. The capacity of this bucket is 5 liters and collects up to 2 Kg of trash when submerged in the water. Design of the debris collector has been given in Figure 3.

The catch bag we have used here is made up of nylon material added with corn straw fiber in powder form, which helps to separate oil from water as well. The metal sheet is sewed into a bag corresponding to the size and shape of the bucket.

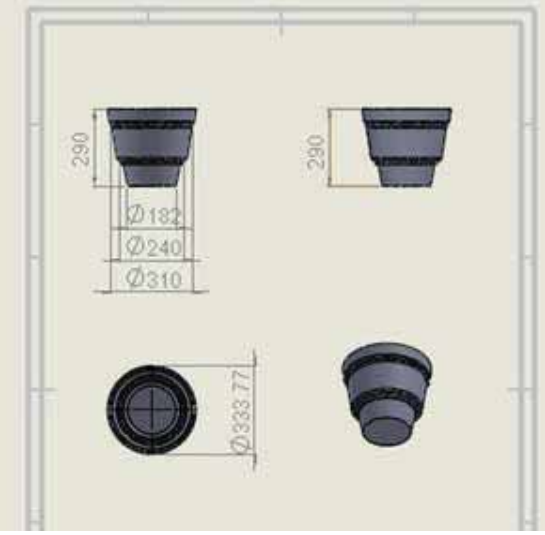

Figure 3. Design of the Debris Collector

C. Water Pump

The water pump used here is mainly for the suction force through which the water with the floating litter enters into the bucket. The trash gets trapped in the bucket while the water is pumped again into the tank.

Specifications:

1. Single-phase Water Pump
2. In-built Thermal Over Load Protector
3. Power Rating: 0.37 kW
4. Power Supply: 180 V - 240 V
5. Motor Power: 0.5 hp
6. Capacity: 6 lpm
7. Head: 6 - 26 m.

D. Solar Panels

The use of non-conventional energy sources is the major highlight of this project. This reduces the burden on conventional electrical sources and reduces largely the operational price of the setup, particularly in remote places.

We have incorporated the use of the installed solar panels in the present organisation for power generation that will be supplied to the pump for suction. We can store solar energy in a battery for constant use throughout the day. This makes the project run with 100% renewable energy.

E. Corn Straw Fiber

Unlike many other water cleaning projects, this project focuses on additional problems such as removing oil from the water. Oil spills and oil contamination also pose a similar threat to marine life. This gives rise to a necessity for the separation of oil from water. Therefore, this project incorporates the use of corn straw fiber (in powder form) as an oil absorbent. Figure 4 shows the corn straw fiber in powder form.

Figure 4. Corn Straw Fiber

F. Final assembly and Working

The final setup and testing have been performed on the water storage tank at the gate 2 of the present organization. The clamps used to hold the vertical post and bucket assembly in place for jerk free operation. We have attached 4 clamps in sets of 2 on a brick combination. Figure 5 shows the final assembly and working of the designed seabin model.

IV. Result and Discussion

This version of Seabin is estimated to catch 1.5 Kg of floating debris per day (depending on weather and debris volumes) including microplastics up to 2 mm small. This project works in such a way that the water is pumped out of the catch bucket that is already submerged in the water. Through this suction, the water with all its floating litter collects in the bucket. The nylon catch bag accumulates litter, separating it from the water. The water is again pumped out of the bucket. This whole process takes place simultaneously and fresh batches of litter settle down in nylon catch bag until the limits get exhausted.

V. Conclusions

- The cost of the model is estimated to be around Rs.3000/- which is quite cheap, to be used in general purpose.
- This work shows a very effective method to remove solid waste even if oil material from the water bodies.
- The materials used in this model are durable and environmentally acceptable.
- The installation of the model is an easy and feasible task with a touch of little technical knowledge.

- This model more efficient than a manual worker skimming the floating debris as it is semi-automatic.
- This model can operate on any type of weather and will be helpful in important cleaning programs taken up by the government of India.
- This model shows an efficient and cost-effective way to clean water bodies as well as environment.
- Presently working on energy from solar panels to make it pure renewable. Depending on the situation other from renewable energy like ocean energy, wind energy, etc. can also be used. The size of the project is enough to catch 2 to 3 kg of litter every day and can be increased depending upon the usage. Certain eco-friendly chemicals can be used to separate oil from water and kill bacteria. This type of project can be used country-wide to clean small water bodies, rivers, ponds, etc.,

Figure 5. Final assembly and working of seabin model

REFERENCES

[1] Xiaohui Wang, Changjun Li, Kai Liu, Lixin Zhu, Zhangyu Song and Daoji Li, "Atmospheric microplastic over the South China Sea and East Indian Ocean: abundance, distribution and source", Journal of Hazardous Materials, Elsevier, vol. 389, pp. 1–9, 2020.

[2] Debbie J. Winton, Lucy G. Anderson, Stephen Rocliffe and Steven Loiselle, "Macroplastic pollution in freshwater environments: Focusing public and policy action", Science of the Total Environment, Elsevier, vol. 704, pp. 1–9, 2020.

[3] Frederic Gallo, Cristina Fossi, Roland Weber, David Santillo, Joao Sousa, Imogen Ingram, Angel Nadal and Dolores Romano, "Marine litter plastics and microplastics and their toxic chemicals components: the need for urgent preventive measures", Environmental Sciences Europe, Springer, vol. 13, pp. 1–14, 2018.

[4] S. Krishnakumar, S. Anbalagan, K. Kasilingam, P. Smrithi, S. Anbazhag and S. Srinivasalu, "Assessment of plastic debris in remote islands of the Andaman and Nicobar Archipelago, India", Marine Pollution Bulletin, Elsevier, vol. 151, pp. 1–12, 2020.

[5] Chunyou Zhu, Daning Li, Yuxin Sun, Xiaobo Zheng, Xianzhi Peng, Ke Zheng, Beibei Hu, Xiaojun Luo and Bixian Mai, "Plastic debris in marine birds from an island located in the South China Sea", Marine Pollution Bulletin, Elsevier, vol. 149, pp. 1–4, 2019.

[6] Chaturvedi Sonam, Yadav Bikarama Prasad, Siddiqui Nihal Anwar and Chaturvedi Sudhir Kumar, "Mathematical modelling and analysis of plastic waste pollution and its impact on the ocean surface", Journal of Ocean Engineering and Science, Elsevier, vol. 5, pp. 136–163, 2020.

[7] Yang Xu, Haiyue Yang, Deli Zang, Yan Zhou, Feng Liu, Xiaochen Huang, JoShu Chang, Chengyu Wang and ShihHsin Ho, "Preparation of a new superhydrophobic/ superoleophilic corn straw fiber used as an oil absorbent for selective absorption of oil from water", Bioresources and Bioprocessing, Springer, vol. 5, pp. 1–11, 2018.

[8] Xuefei Tan, Hui Min David Wang, Deli Zang, Lijun Wu, Feng Liu, Guoliang Cao, Yongping Xu and Shih Hsin Ho, "Superhydrophobic/ superoleophilic corn straw as an eco friendly oil sorbent for the removal of spilled oil", Clean Technologies and Environmental Policy, Springer, vol. 23, pp. 145–152, 2020.

[9] Jian Dai, Chi Zhang, Han Vincent Lim, Kok Keng Ang, Xudong Qian, Johnny Liang Heng Wong, Sze Tiong Tan, Chien Looi Wang, "Design and construction of floating modular photovoltaic system for water reservoirs", Energy, Elsevier, vol. 191, pp. 1–53, 2020.

E-ISSN 2581 –7957
P-ISSN 2277 – 3916

CVR Journal of Science and Technology, Volume 21, December 2021
DOI: 10.32377/cvrjst2122

Optimizing the Process Parameters for controlling the Vibration in Turning of TWIP Steel Rod

B. Appala Naidu[1], K.T. Balaram Padal[2], A. Suresh[3]
[1]Assoc. Professor, CVR College of Engineering/Mechanical Engg Department, Hyderabad, India.
Email: bnaidua@gmail.com
[2]Professor, Andhra University/Mechanical Engg Department, Vishakapatnam, India.
Email: ktbpadaldme@gmail.com
[3]Asst. Professor, CVR College of Engineering/Mechanical Engg Department, Hyderabad, India.
Email: suri0341@gmail.com

Abstract: **Turning process embodies the separation of the metal atop exterior surface of a pirouette work piece in cylindrical shape. It is one among the most commonly used technique of cutting largely when finishing of the product. The pennant of turning variables for instance, speed of cutting, rate of feed and cut of depth, in the turning process need to be designated cautiously to ameliorate the turning potency by amplifying the productivity and minimizing the total cost of manufacturing for each integrant. A high vibration ushers to penurious surface finish and reduces the productivity followed by shortening of tool life, in order to avoid that the vibration of the cutting tool must be controlled. In this experimental work, an investigation is made to understand the reverberations of these turning parameters in the voyage of a work piece, made up of twinning induced plasticity (TWIP) steel, by using response surface methodology. Statistical tools are used for designing of the experiments. Then the process parameters were optimized by maneuver of analysis of variance, regression analysis and techniques of optimization to accomplish the context of minimum tool vibration and low chip frequency, consequently ameliorating the surface roughness in the wake of turning process.**

Index Terms: Optimizing, Process parameters, Vibration, Turning, TWIP steel.

I. INTRODUCTION

Machining operations, such as milling, turning, and drilling are paramount in production industries. Turning by definition is the process of removal of metal or material from a cylindrical surface of the work piece that leads to a reduction of the diameter to a specified dimension. Usually the reduction of the turning process is done with the rotating work piece and relatively stationary cutting tool. However feed is provided to the cutting tool to advance it for the removal of the metal from the work piece. The turning process usually requires a maximum surface finish with minimum amount of residual stresses. In the manufacturing cramming, to obtain a maximums surface finish with minimum residual stresses the cutting tool vibration must be maintained less. At the outset the vibration of the cutting is targeted to be less instead of zero because of the fact in turning vibration of the cutting tool is unavoidable. This unavoidable phenomenon which strive the quality of the work piece, accuracy of machining, cutting tool life and increase in the operation cost. The grail of manufacturing industry has always emphasized the low-cost manufacturing and products of high-quality in a dwarf time. Modern manufacturing industries endeavor to escalate these attributes. To attain the high cutting staging, manufacturing industry necessitates wielding of optimal turning variables [1]. Correspondingly, cutting variables such as speed of cutting, rate of feed and cut of depth in the course of the turning process are to be chosen agreeably to maximize the productivity, for reduction of total manufacturing cost of each work piece, or to accomplish a preconceived congruous criterion.

Since the cost of digitally controlled machine tools is high, as juxtaposed with the prosaic counterparts [2], their working desideratum to be energetically discharged to churn out the desired product [2]. During the turning process, vibrations arise due to the friction in between the tool and the work piece. Therefore, the staging of the machine hang on deliberately on vibration due to the turning subpoena, in this a vibration less schema sooner required. The rate of retrogression rate and inexactitude which increase with the utilization of the cutting tool that can be set on by monitoring of vibration [2]. Theories of vibration are theories of coupling situation that have embellished prominent [3]. The research has also super scribe the amalgamate sitch, emanate out of vibration apropos the position of the momentum [3], which engenders vibration in direction of cutting force and conversely, paramount to a multi-directional esplanade [4]. It also urges that escalate in the clearance of flank, rake angle is spurt the solidity of dynamic procedure of turning due to the dissimilitude effects. Furthermore, a mathematical model and a linear differential correspondence is opted for cutting speeds, high and low dynamic action of cutting also the tool rake is lodged. Furthermore, the process variables are influenced the vigor of initial friction.

The turning activity of TWIP steel rod explored in respect of work piece wear and the surface quality deportment of cutting tools. Investigation flaunted the inter-relationship in between the input &output variables such as tool insert nose radii, feed rate and the coating insert methods. The study has given little results towards the right selection of tools in turning of TWIP steel rods. In the investigation of the turning experiments are exhibited on 3 different composed TWIP steels rods at 3 different turning feeding rates, depths and non-coolant associated cutting speeds. In addition the investigation targeted mainly for reducing both ruggedness of the surface and also consumption of power by evaluating the optimized turning parameters. The repercussions of the

Received on 08-08-2021, Revised on 23-10-2021, Accepted on 15-11-2021.

CVR Journal of Science and Technology, Volume 21, December 2021
DOI: 10.32377/cvrjst2122

turning parameters and hardness of work piece over the surface roughness, power consumption and sound level and are assessed. The detection manifested that feed rate has the most significant impact in turning process, particularly over the power consumption and surface roughness. The cutting speed and depth of cut also have shown meticulous effects followed by feed rate.

This can be accessed from literature survey that some papers are delineated on optimization of parameters influencing the vibration attributes of the turning of TWIP steel rod by applying the response surface methodology in view of the mathematical & analytical study. Accordingly, this analysis is accorded to the inspection of ramification of the turning feed rate, turning speed and tool depth of cut over the frequency of chip and tool vibration concomitantly for the turning of TWIP steel work pieces with the response surface methodology, the experiment establish the optimized process parameters with the help of 2 heuristic algorithms [5].

II. Methodology

The methodology accustomed to explore the process parameter optimization of turning process of the TWIP steel rod with the RSM as shown in the figure 1. In addition, to it the sequence of operating procedure is elucidating as follows:

Step 1: Review of literature on turning process, machining vibration, RSM and the required terms. Step 2: scheming of experiment. During this step, design of RSM is made to estimate the repercussions of the process parameters over the surface roughness succeeding the process of turning. Step 3: Investigational procedure involve in designating the significant material, that is the TWIP steel rod and then performing the process of turning maneuver theCNC-M392 machine. Step 4: Analysis of the data with the RSM towards optimizing process variables of turning. In the next step the outcomes & colloquy are used for substantiating the enactment of the experiments.

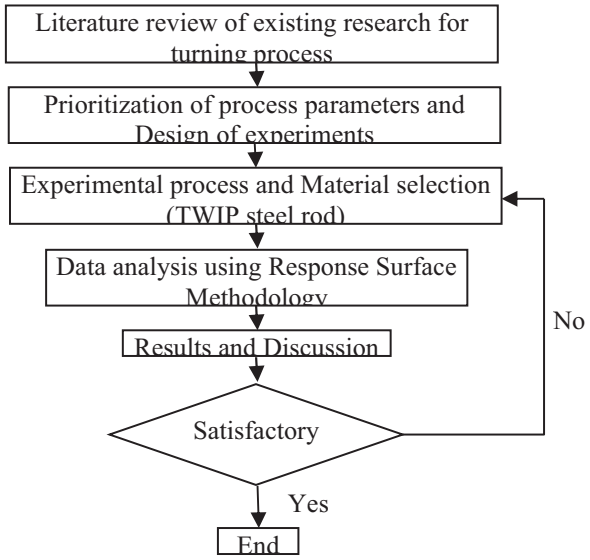

Figure 1. Flow chart showing the methodology of Turning

III. Experimental Work

Material used: In this experiment, twining induced plasticity steel rods are used.

Arrangement of TWIP steel rod in CNC Machine for turning. The implementation of the experiment is carried on a CNC lathe machine as given in the Figure 2 that has 5.8 kW power and also 2200 rpm of spindle speed (maximum). The work piece is a medium carbon TWIP steel, as detailed in the above literature. The diameter and length of work piece are100 and 500 mm. Work piece is mounted over the tailstock that requires good support. After finishing the establishment of CNC machine, the surface of work piece exhibited to remove the external surface layer of work piece that is robust, as given in the figure 3.

A. Cutting Tool Holder and the Insert

As shown in figure 2 the considered insert that is the TWIP steel turning grade. Titanium carbide and Tungsten carbide of insert the caper bound because of the cobalt (Co). The tool insert is prepared with the face centered cubic (fcc) structures to enable the precision and cutting speed of process, hence developing the smoothness to the TWIP steel rod work piece. By dint of the distinctive properties, such as high resistance and low friction against the crack, wear and diffusion and coated tools also be utilized at reducing the time, high cutting speeds and cost used for the turning processes. Then after tool insert can be fasten to tool holder, the tool clamp is further tightened with the help of clamp screw, as given in the figure 5. Two marshalling of the tool overhang (65 and 130 mm) are utilized. Then after, tool holder can be reinforced over the tool turret and cutting tool can be explicitly centered, in view of center of CNC tailstock tool.

B. Design of Experiments with Response Surface Methodology (RSM)

The RSM is utilized for evaluation of emphasis of appurtenances towards the turning process variables by complying roughness of rod surface. Feed rate, Speed &depth of cut are unfettered parameters that are selected for the analysis using RSM and in competence with previous literature study [6,7]. The Figure 3validates the subservience alliance among the dependent parameters and the independent variables (chip frequency and vibration variables) that are crucial to peruse the roughness of the surface.

The prowess of user can be divided as the slacken variable that has the strong unforeseen effect over the alliance of variables. By disparity, the fidelity can be utilized as the liaise vacillating that supremacy of the outcomes. In the present research, the central composite design (CCD) is the manner plump for design of experiment. The approach can be integrated with the RSM to set up a quadratic type model for a variable response [8]. CCD has the most prominent amid the categorization of the RSM depiction because of some the patronage reasons:

(i) CCD is cleaving into 2genusscrutinize that act for poles apart the effects that can be shrewdly performed. The former one resembles the impact of linear &the later one resembles the convexity ramification. In accordance, when speculative analysis has the informative points towards the

maiden subset for having non-significant type of curvature effect.

(ii) CCD is one of the effective technique in optimization, which facilitates the intelligence over the assessment variables such that the overall investigational error with the slightest indispensable reciprocity.

(iii) CCD is to be cast-off in the copious investigational areas. CCD accommodates a new fractional factorial or design factorial of central points, which are associated with the set of optimum points, empower a faultless guesstimate of curvature.

In CCD, 2set of hypothetical designs that can be plump for (small or full). For the following experiment, a small type of CCD is selected, as depicted in the Table 2.

C. Vibration cum Detector framework

The intuitive Dasy Lab software is used to quickly and easily scrutinize the vibration statistics by waged with unveils straight over the screen. In addition to it the accelerometer is accustomed to recognize and attain the vibration statistics.

An accelerometer can be laid down over the wedge to be examined [9]. Accelerometers can be established with the noteworthy wax as they are having a good ascend tool for the lightweight detector in ad interim investiture.

III. Results And Discussions

This fragment contributes the RSM outcomes deploy on the quantifications of chip frequency and vibration. Further, their associations with turning process parameters are computed with the interaction plots, main effect plots and surface plots. Furthermore, optimization and mathematical models are furnished. Table 2 bestows the disposition of experiments along with the chip frequency and vibration outcomes.

A. Development of the Vibration Model

Variance Analysis: Estimated coefficients of regression for the vibration that are shown in the Table 2show that the numerals are statistically different. Main effects are obtained from p - value, such that the value is lower than 0.05, then it could be made that the outcome is significant. Although the feed rate, cutting speed and depth of cut were remarkable to the model of response is at 0.05.

Residual Plots-Vibration: The below figure 8 depicts the plots of residual at odds with the proportion and the fitted values and frequency in dataset& the index of observation. These outcomes are disseminated desultory hinged over the contoured values and the index of observation.

Furthermore, the outcomes depict that p value of residuals (0.213), more than that of 0.05 towards the vibration. Then a linear relationship cans be discerned then the residuals were made in opposition with the percent of values [10]. The data depicts the proportions of each of the turning parameter also their amalgamation, which has been assessed from the equation no (1).

The amalgam of the depth of cut and cutting speed has the biggest endowment for the vibration, which is accompanied with the depth of cut, cutting speed and feed rate.

$$\text{Contribution} = \frac{\text{adjusted sum of squares for each other}}{\text{total adjusted sum of squares}}$$

B. Plot of Interaction for the Vibration

As the figure 4 depicts the ascendency of feed rate and depth of cut on the vibration. Accordingly, increase of the feed rate (C) & the depth of cut (B) bestows the escalate in vibration.

C. Plot of Contour for Interaction Factor

The figure 5 shows the contours of vibration at all of the different proportions of turning speed variables. Accordingly, the rise in the depth of cut promotes to the hike in the vibration rise.

The below Table 1 shows the experimental design-values of the process parameters.

TABLE I.
Experimental Design

Standard order	Order of Run	Cutting speed in mm/s	Depth of cut in mm	Feed rate in mm/s	Vibration Volt	Chip frequency Hz
1	1	50	1.9	0.21	0.092	2079.8
12	2	45	1.4	0.15	0.0701	1004.8
3	3	190	1.4	0.16	0.149	6789.5
8	4	120	1.5	0.9	0.10589	7199.4
6	5	122	0.78	0.15	0.1213	9101.8
11	6	125	2.22	0.16	0.10248	1135.87
13	7	125	1.4	0.16	0.10311	5459.2
7	8	124	1.6	0.15	0.10278	5134.8
10	9	126	1.5	0.16	0.10239	5432.8
15	10	125	1.5	0.15	0.1209	6215.9
14	11	201	1.0	1.1	0.1509	6188.2
4	12	200	2.1	1.9	0.1608	2124.9
5	13	49	1.2	1.1	0.05	2011.8
9	14	124	1.4	1.6	0.11577	1578.9
2	15	126	1.52	1.6	0.10340	4819.7

Figure 2. Experimental setup

TABLE II.
Variables of ANOVA

Source	DF	SS	Adj SS	F value	p value
Model	9	0.012541	0.001415	10671.88	≤0.0011
Linear	3	0.000210	0.000891	291.4	≤0.001
A: Cutting speed	1	0.000071	0.0009	619.8	≤0.001
B: Depth of Cut	1	0.00021	0.000125	128.7	≤0.001
C: Feed rate	1	0.00009	0.00021	35.11	0.0019

D. Surface Plot showing Vibration

The figure 5 shows the plots of surface for vibration lie upon the depth of cut and feed rate. The quarry vibration is then accomplished. Consequently, there is a less quantity of the depth of cut and more quantity of feed rate.

The vibration (V) set up procured from stratagem in the antecedent fragment act for the equation (2).

Vibration:

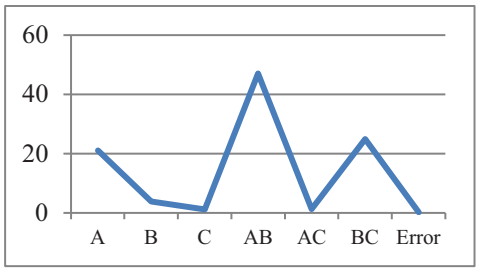

Figure 3. Percentage contribution of variables

$V = 0.08627 - 0.000497A - 0.02857B - 0.1079C + 0.0000021A^2 - 0.008091B^2 - 0.34638C^2 + 0.000271AB + 0.000418AC + 0.2698BC.$

Build out of the Chip Frequency Setup

Analysis of the Variance: The ANOVA given in the data details each of the terms of model (A, B, A B, A C, B C, A2 &C2) are needful for detailing frequency of the chip formation because of the less p value. Moreover, the outcomes of the setup show the more accurate as that of R-square value that is more (98.73%).

As the forecasted coefficients of regression analysis towards the frequency of chip are compared. The outcomes of coefficients are notably different. And the p values are less than 0.05 towards the linear term, which is the set of variables, can show the deportment of frequency of chip. Cutting speed & depth of cut were noteworthy to the model of response at p = 0.05.

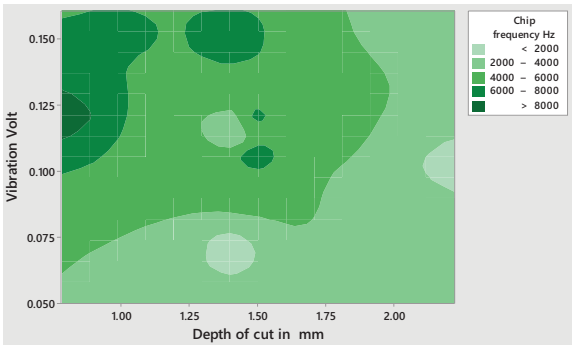

Figure 4. Graph showing depth of cut vs Vibration

Plots of Residual for the Frequency of Chip: The Figure 6showsplots of residual for the frequency of chip in opposition to the ration and the fitted values and frequency of numerals are in dataset along with the index of observation.

The outcomes are apportioned contingently established on the values of fitted hypothesis and index of observation. Hence, the outcomes depict that value of p of the residuals (0.078) is greater than 0.05 towards the frequency of the chip. A linear alliance is then perceived along with the plotted residuals against percentage values.

Figure 7shows the benefaction of everyone noteworthy variable and their amalgam. Cutting speed has giant benefaction for the frequency of the chip, accompanied with combination of process parameters.

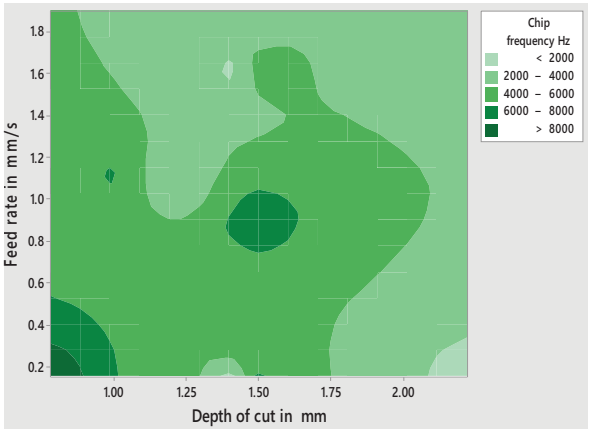

Figure 5. Depth of Cut vs Feed rate

E. Plot of Interaction for the Frequency of Chip

The below Figure 4 depicts supremacies the coalescence offered rate, cutting speed, depth of cut and chip frequency. The reciprocity plot proclaims that escalate in cutting speed marshal to lessen the chip frequency. By disparity, the frequency of chip escalated with depth of cut.

Plot of Contour for the Chip Frequency: The Figure 5unveil the frequency of chip silhouette each and every disparate the amalgamations of cutting parameters.

Accordingly, the increase in chip frequency with feed rate and dwindles with cutting speed. The Figure 5 reveals the frequency of chip silhouette each and every disparate amalgamation of turning process parameters.

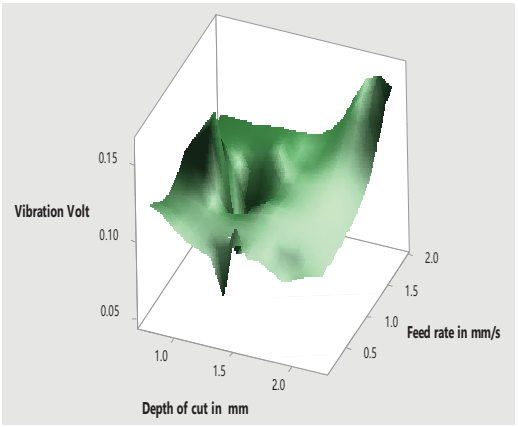

Figure 6. 3-D graph showing vibration, feed rate and depth of cut

F. Plot of Surface for the Chip Frequency

The Figure 6 excels the plots of surface for the frequency of chips. Deploy on the weave the feed rate, cutting speed & depth of cut accordingly.

Numerical Set up for the Frequency of Chip: Frequency of chip setup derived from stratagem in antecedent fragment speak for in patronage equation:

Chip frequency= $- 4287 + 371A + 4301B - 129561C - 0.3541A^2 - 1354B^2 + 93286C^2 - 123AB - 364.51AC + 58971BC.$

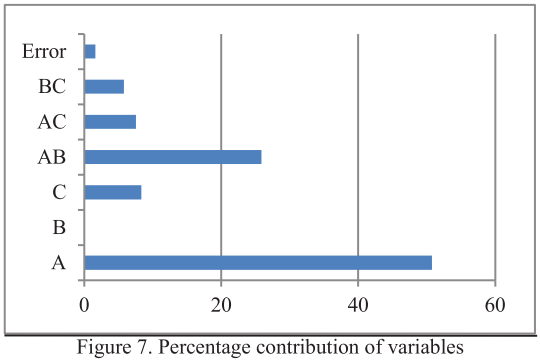

Figure 7. Percentage contribution of variables

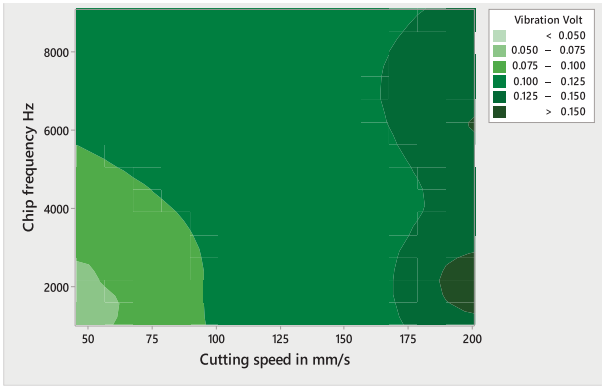

Figure 8. Chip frequency vs cutting speed

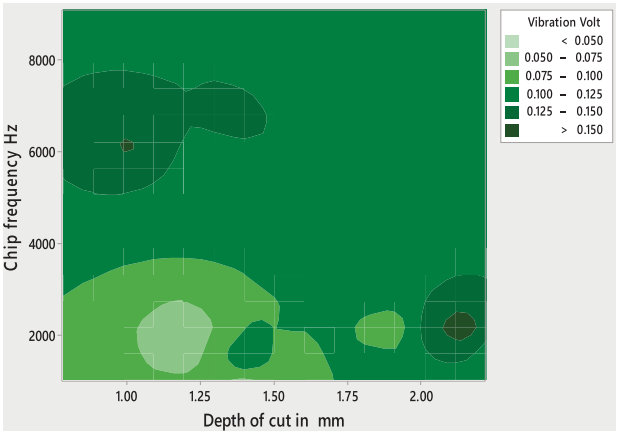

Figure 9. Chip frequency vs depth of cut

Figure 7,8, 9 and 10 shows the percentage of contribution of the variables and also the graphs in between the chip frequency vs cutting speed and depth of cut. The grail of optimization is for obtaining the nadirs the chip frequency and vibration along with abet of statistical optimization manner by altering the turning set up.

Consequently, this analysis will decipher the optimization stumbling back by coalescence the RSM chip frequency and vibration set up along with simulated annealing algorithms and tabu search have been vastly in favor of solution the problems of optimization.

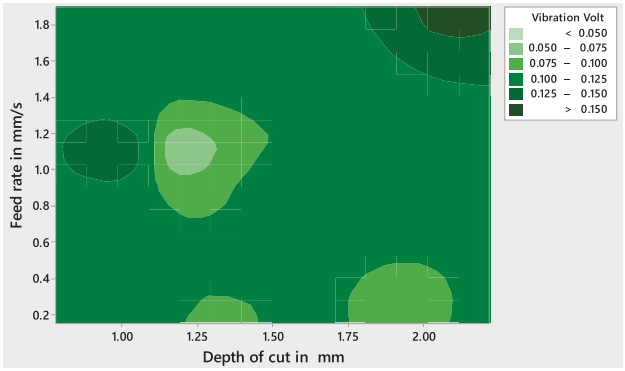

Figure 10. Contour plots Feed rate vs depth of cut

Figure 11 and figure 12 shows the contour plots in between the feed rate vs depth cut and feed rate vs cutting speed. The vibration is shown in the contour and legend against the feed rate, depth of cut and cutting speed.

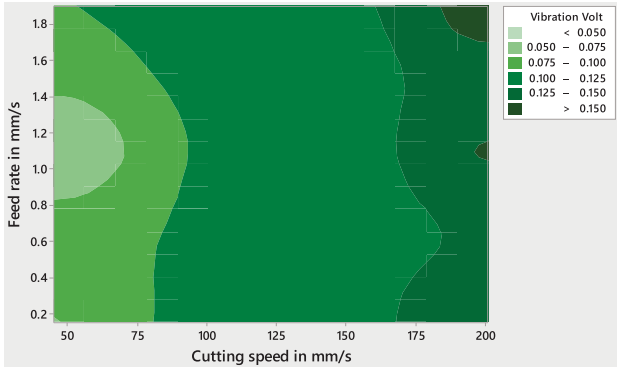

Figure 11. Contour plots Feed rate vs cutting speed

TS (tabu search) maneuver the memory for retrenchment search counsel this succor circumvents the precursory tincture that are visited. Tabu list is then rationalized at each of the iteration with the TS.

Owing to the curtailment over tabu list, the peril of the rejection of colloid that were not yet engendered may transpire. Figure 13 and Figure 14 shows the surface plots in between the chip frequency vs feed rate vs cutting speed and chip frequency vs feed rate vs depth of cut.

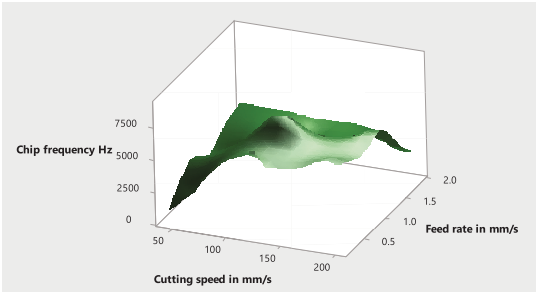

Figure12. 3D graph of Chip frequency vs feed rate vs cutting speed

Tabu tinctures are consequently scrutinized for unequivocal position, known for criteria of aspiration.

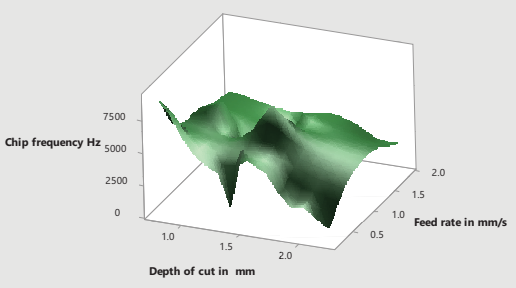

Figure13. 3D graph of Chip frequency vs feed rate vs depth of cut

If tabu outcomes are preferable than the supreme objective benefit obtained so far, tabu outcome can be obtained and then its step will gain eliminated from the tabu list [8]. In the case of a denigration problem, the prevailing TS algorithm could be dispensed as given in the Algorithm 1 [9]. The approach of simulated annealing is for solving the combinatorial type of optimization muddle. This greets point to a unswerving resemblance in this liquids preserve and materialize or those metals cools down and anneal. The simulated annealing (SA) methodology is established on the drudgery or deciphering the combinatorial type of optimization problems. Predominantly, the alter in the energy of system the nit unites to a anchored "frozen" plight by soliciting a chilling process towards system that is simulated by the Metropolis's algorithm [10]. SA reconnoiter the case of all the possible outcomes and minimizing plausibility of psyche cohesive for local optima with accepting the moves, which may aggravate the desirability of equitable function to clear out from local optima then travel apropos a new territory in the outcome space. The preferable budge is invariably accepted. Believing the minimization problem of S as solution space the objective function as f and also the neighborhood be as structure N, then the normal SA algorithm could be indicates as given in Algorithm 2 [10,11]. Optimization of the frequency of chip and vibration are contrived in the established formats.

Chip frequency:

(i) Find: A (cutting speed), B (depth of cut), C (feed rate)
(ii) Minimize CF (A, B, C)
(iii) Subject to
(iv) $A_{max} \geq A \geq A_{min}$
(v) $B_{max} \geq B \geq B_{min}$
(vi) $C_{max} \geq C \geq C_{min}$

Vibration

(i) Find: A (cutting speed), B (depth of cut), C (feed rate)
(ii) Minimize V (A, B, C)
(iii) Subject to
(iv) $A_{max} \geq A \geq A_{min}$
(v) $B_{max} \geq B \geq B_{min}$
(vi) $C_{max} \geq C \geq C_{min}$

Tendered algorithm (TS) is administered in MATLAB software (R2018a). The numerals of TS & SA algorithm variables ascend its staging. For aforementioned reason, test scamper are implemented for the heterogeneity of the TS & SA algorithm variable numerals and best feasible milieu is chosen and shown in the Figure 8,9.

By deciphering optimization problem, the Minitab optimizer TS&SA anticipated the optimum frequency of chip and vibration for the turning of the TWIP steel in a chosen turning context realm. Figure 10,11 conveys optimal conditions for the minimum chip frequency and vibration.

In this context, cutting speed is limited to 50 mm/s, depth of the cut is limited to 0.79 mm, and feed rate is limited to 0.80 mm/s. Optimum chip frequency and vibration are 0.067 Volt an 10187 Hz, sequentially. In reckoning, Figures 12& 13proclaim the culminating graph that shoes the results for variable convergence graphs in chip frequency and vibration optimization.

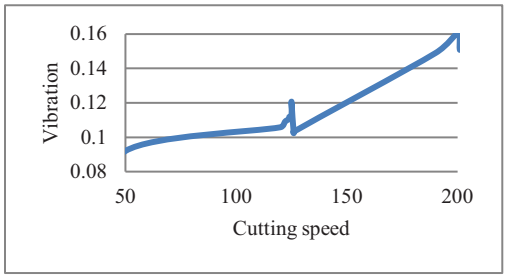

Figure 14. Graphs between vibration vs cutting speed

Figure 14 shows the interrelationship in between the cutting speed and vibration.

As the cutting speed is increased the vibration is increased and the maximum is found at 201 mm/s cutting speed for the vibration value of 0.16 volt.

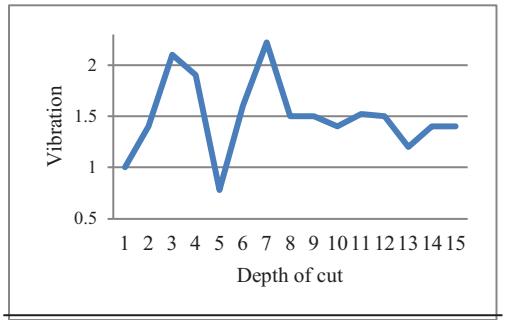

Figure 15. Graphs between vibration vs depth of cut

Figure 15 shows the interrelationship in between the depth of cut and vibration.

As the depth of cut is increased the vibration is changed in zig- zag manner and the maximum is found at 7.1 mm depth of cut for the vibration value of 2.3 volt.

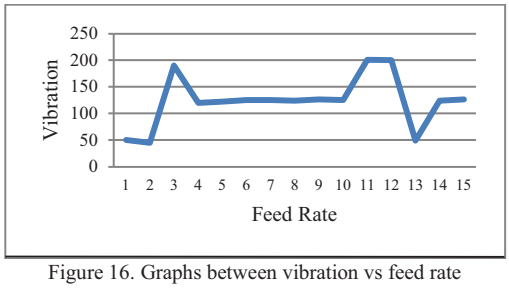

Figure 16. Graphs between vibration vs feed rate

CVR Journal of Science and Technology, Volume 21, December 2021
DOI: 10.32377/cvrjst2122

Figure 16 shows the interrelationship in between the feed rate and vibration.

As the feed rate is increased the vibration is changed in zig zag manner and the maximum is found at 11.5 mm/s feed rate for the vibration value of 200 volt.

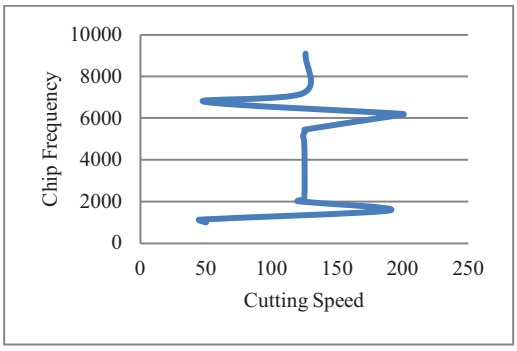

Figure 17. Graphs between chip frequency vs cutting speed

Figure 17 shows the interrelationship in between the chip frequency and cutting speed. As the feed rate is increased the chip frequency is changed in zig zag manner and the maximum is found at 125.1 mm/s cutting speed for the chip frequency value of 9000 Hz.

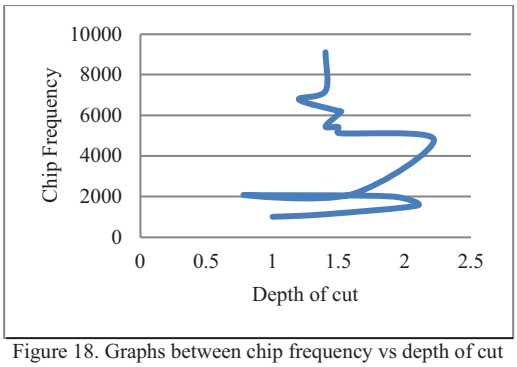

Figure 18. Graphs between chip frequency vs depth of cut

Figure 18 shows the interrelationship in between the chip frequency and depth of cut. As the depth of cut is increased the chip frequency is changed in zig zag manner and the maximum is found at 1.41 mm depth of cut for the chip frequency value of 9100 Hz.

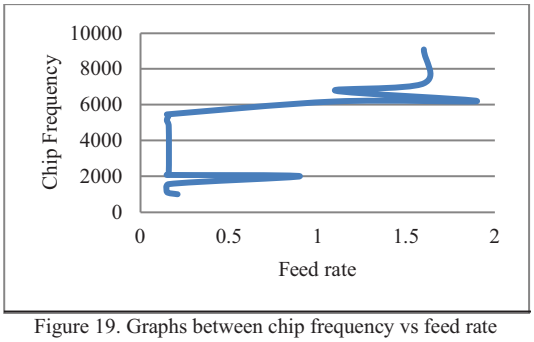

Figure 19. Graphs between chip frequency vs feed rate

Figure 19 shows the interrelationship in between the chip frequency and feed rate. As the feed rate is increased the chip frequency is changed in zig zag manner and the maximum is found at 1.691 mm/s feed rate for the chip frequency value of 9150 Hz.

IV. Conclusions

In this work, RSM based on TS & SA is solicit to forecasts the ramifications of the key process parameters, such as depth of cut, cutting speed, vibration, feed rate and frequency over surface roughness. The conclusion can be made as vibration is increased in the range of cutting speed from 50 mm/s to 200 mm/s. Similarly, the vibration is dwindled in the range from 1mm to 2mm depth of cut. The optimal conditions are observed to minimize the chip frequency and vibration are 50mm/s of cutting speed and 0.80 mm/s of feed rate and 0.795mm of depth of cut.

References

[1] Suresh, Anthati & Garikapati, Diwakar. (2021). Investigation of Effects of Working Parameters in Turning of TWIP Steel rods with Eco-Friendly Cutting Fluids using Response Surface Methodology on CNC Machines. Gazi University Journal of Science. 34. 069-078. 10.35378/gujs.691716.

[2] Suresh, Anthati & Rithika, G & Srujana, J & Pavan, Mr & Reddy, Kumar. (2020). Evaluating the Effects of Residual Stresses On CNC Turning For TWIP Steel Plates.2. 2582-5208.

[3] A. Suresh. CH. Murali, (2019), Analysis and Improvement of Testing Parameters for Mild Steel and Stainless Steel using Taguchi and ANOVA Method, International Journal for Scientific Research & Development, 7(6), 269-272, ISSN (online): 2321-0613,

[4] Mr. A. Suresh, Mr. K. Mohan Naidu, Ms. Vandavasu Pranathi, Mr. E. Moses Raj Kumar, (2020), Influence of Cutting Fluids on Residual Stresses in CNC Turning of Austenitic Stainless Steel Rods, 7(1) 1882-1885, e-ISSN: 2395-0056,

[5] Mr. A. Suresh, Ms. G. Rithika, Ms. J. Srujana, Mr. M. Pavan Kumar Reddy, (2020), Evaluating the Effects of Residual Stresses on CNC Turning for TWIP Steel Plates , International Research Journal of Modernization in Engineering Technology and Science, 2(12), 182-188, e-ISSN: 2582-5208,

[6] A. Suresh & G. Diwakar, (2018), Optimization of Process Parameters for Machining of Aluminum 6061-O alloy on Lathe and Drilling machine, International Journal of Mechanical and Production Engineering Research and Development, 8(5), 85-90, ISSN (P): 2249-6890; ISSN (E): 2249-8001.

[7] A. Suresh & G. Diwakar, (2018), Optimization of Process Parameters in Turning operation of Austenitic Stainless steel rod using Taguchi method and ANOVA, International Journal of Mechanical and Production Engineering Research and Development, 9(3), 379-386, ISSN (P): 2249-6890; ISSN (E): 2249-8001.

[8] A. Suresh, G. Diwakar (2019), Process Parameters Optimization using Kuhn-Tucker Conditions For Plasma Arc Welding Using Austenitic Stainless Steel Alloy-304l Plates, International Journal of Engineering and Advanced Technology, 8(6), 4537-4541, ISSN: 2249 – 8958,

[9] A. Suresh, G. Diwakar (2019), Optimization Of Machining Process Parameters In Turning And Drilling By using Design Of Experiments With Aluminum 6061-O Alloy And Austenitic Stainless Steel, International Journal of Innovative Technology and Exploring Engineering, 8(11), 625-633, ISSN: 2278-3075,

[10] A. Suresh , Dr. G. Diwakar, (2021), Investigation of Effects of Working Parameters in Turning of TWIP Steel rods with Eco-Friendly cutting fluids using Response Surface Methodology on CNC machines, GAZI University Journal of Science, 34(3), 68-78, ISSN: 1303-9709,

E-ISSN 2581 – 7957
P-ISSN 2277 – 3916
CVR Journal of Science and Technology, Volume 21, December 2021
DOI: 10.32377/cvrjst2123

Impact of Post Welding Heat Treatment Process on Microstructure and Mechanical Properties of TIG Welded SS-304 & SS316l Dissimilar Metals

K.L.N. Murthy[1] and A.C. Uma Maheshwar Rao[2]
[1]Asst. Prof., Sreyas Institute of Engineering and Technology/ Mechanical Engg. Department, Hyderabad, India.
murthy.kln@sreyas.ac.in
[2]Assoc. Prof., Sreyas Institute of Engineering and Technology/ Mechanical Engg. Department, Hyderabad, India
Umamaheswar.ac@sreyas.ac.in

Abstract: **The present work aims at improvising the mechanical properties of the weldments under different heating conditions. Two materials SS304 and 316L are joined under various parameters like current, gas flow rate, and root gap. The weldments are post heated to a temperature of 800^{0}C in a muffle furnace to improve the mechanical properties at fusion zone HAZ and parent materials. The microstructure of the specimens at different zones is studied under 500x magnification which revealed the formation of dendritic structure and austenitic grain boundaries with annealing twins showing elongated grains with ASTM No 7 and 8 at SS304 base material, Fusion zone, and SS316L parent material.**

Index Terms**: hardness, microstructure, welding, weldments, base metal.**

I. Introduction

Just like preheating, Post welding heat treatment process is very important as a part of welding. As the name suggest Post welding heat treatment process is done after completion of the welding of a particular component. It helps to improve welding quality and stress relief [1,2], not only the quality of the weld metal but also increases the quality of the base metal. As said earlier it also releases the stresses which are internally developed during the welding process. It is impossible to see the temperature distribution inside the weldments with our naked eye and is possible only when observed under the thermal cameras.

This temperature distribution is different at various locations for example the central area is very hot when compared with the edges of the base metal. Because of this nonlinear temperature distribution several stresses are generated which are called as Residual Stresses. Which eventually effects the weld strength.

After completion of the welding of the metals there will be heat transfer between weld metal and base metal due to conduction heat transfer. This heat transfer will take place unevenly, sometimes the thickness of the base metal will also be the reason for uneven heat transfer. Depending up on the cooling rate weldment's mechanical and microstructure properties gets changed.

II . Literature

Effects of post-weld heat treatments on the microstructure, mechanical and corrosion properties of gas metal arc welded 304 stainless steel was studied by Taiwo Ebenezer et al [3]. It was observed that there is significant improvement of microstructure, mechanical and corrosion properties of the weldment after the post welding heat treatment process. Post tempering process increased the tensile strength to 10%. At the end of the experimentation, it was concluded that post tempering heat treatment process shows the better improvements than that of post annealing because more refined grains formed during tempering process.

In a study conducted by M. R. Dodo et al [4] on effect of post-weld heat treatment on the microstructure and mechanical properties of arc welded medium carbon steel. The study comprises of detail description of effect of the three different heat treatment processes i.e., annealing, normalizing and quenching on the weldment. It was concluded that normalizing heat treatment process is the best of the three processes. Tensile strength was increased after normalizing and quenching.

III. Experimentation

The experiments are performed on TIG welded SS-304 & SS-316L dissimilar metals with SS-316LER as filler metal. Table 1 shows the chemical composition of the metals used for the experiments. Fig.1 shows the sample weldment before and after heat treatment process.

TABLE I.
Chemical Composition of the Metals

S.no	Metal	C	N	Cr	Ni	Mo	Mn	Si
1	SS-304	0.05	0.05	18.3	8.1	0.3	1.8	0.45
2	SS-316L	0.02	-	16.4	10.5	2.1	1.8	0.50
3	SS-316LER	0.02	-	18.00	12	2.75	1.50	0.50

Received on 13-04-2021, Revised on 10-05-2021, Accepted on 25-06-2021.

TABLE II.

S.No	Test	Load (Kgf)	Indenter	Time (S)	Before Normalizing RHN	Avg	After Normalizing RHN	Avg
1	SS-304	150	Diamond	30	77		85	
2	SS-304	150	Diamond	30	58	**73.3**	98	**89**
3	SS-304	150	Diamond	30	85		98	
4	BEAD	150	Diamond	30	63		67	
5	BEAD	150	Diamond	30	90	**82.66**	99	**83.6**
6	BEAD	150	Diamond	30	95		85	
7	SS-316L	150	Diamond	30	92		91	
8	SS-316L	150	Diamond	30	87	**83.3**	91	**93.6**
9	SS-316L	150	Diamond	30	72		99	

HARDNESS VALUES OF TEST WORK PIECE 1

TABLE III.

S.No	Test	Load (Kgf)	Indenter	Time (S)	Before Normalizing RHN	Avg	After Normalizing RHN	Avg
1	SS-304	150	Diamond	30	68		75	
2	SS-304	150	Diamond	30	85	**78**	94	**87**
3	SS-304	150	Diamond	30	81		92	
4	BEAD	150	Diamond	30	51		71	
5	BEAD	150	Diamond	30	71	**57.6**	71	**71**
6	BEAD	150	Diamond	30	51		71	
7	SS-316L	150	Diamond	30	73		70	
8	SS-316L	150	Diamond	30	81	**73.3**	91	**78.33**
9	SS-316L	150	Diamond	30	66		74	

HARDNESS VALUES OF TEST WORKPIECE 2

TABLE IV.

S.No	Test	Load (Kgf)	Indenter	Time (S)	Before Normalizing RHN	Avg	After Normalizing RHN	Avg
1	SS-304	150	Diamond	30	77		100	
2	SS-304	150	Diamond	30	78	**76.6**	91	**95.5**
3	SS-304	150	Diamond	30	75		95	
4	BEAD	150	Diamond	30	74		95	
5	BEAD	150	Diamond	30	65	**70**	99	**97**
6	BEAD	150	Diamond	30	71		97	
7	SS-316L	150	Diamond	30	70		89	
8	SS-316L	150	Diamond	30	61	**73**	90	**89.3**
9	SS-316L	150	Diamond	30	88		89	

HARDNESS VALUES OF TEST WORKPIECE 3

TABLE V.

S.No	Test	Load (Kgf)	Indenter	Time (S)	Before Normalizing RHN	Avg	After Normalizing RHN	Avg
1	SS-304	150	Diamond	30	93		100	
2	SS-304	150	Diamond	30	97	**94.6**	91	**95.3**
3	SS-304	150	Diamond	30	94		95	
4	BEAD	150	Diamond	30	71		87	
5	BEAD	150	Diamond	30	59	**61.6**	96	**93.6**
6	BEAD	150	Diamond	30	55		98	
7	SS-316L	150	Diamond	30	83		98	
8	SS-316L	150	Diamond	30	77	**79**	92	**91**
9	SS-316L	150	Diamond	30	77		83	

HARDNESS VALUES OF TEST WORK PIECE 4

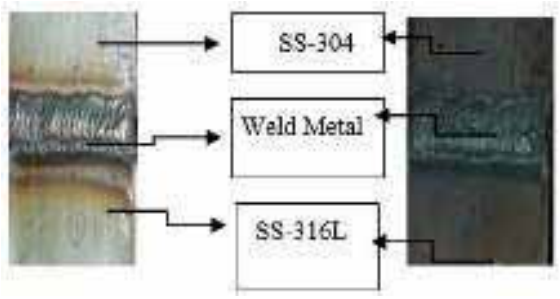

Figure.1 Weldment before and after heat treatment

Post Welding Heat Treatment (Normalizing) [6] is performed on the weldments in order to reduce the internal stress developed during the welding process. The weldments were kept inside Muffle furnace as shown in the Fig.2 and heated to 800^0C [7][8] such that recrystallization process takes place inside the weldment.

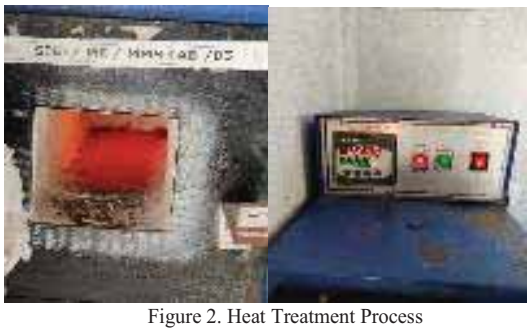

Figure 2. Heat Treatment Process

Hardness measurement was carried out on the SS-304 (HAZ), Weld zone and SS-316L (HAZ) of the weldment using Rockwell Hardness tester with Diamond indenter and with a load of 150 kg for a dwell time period of 30s. Hardness values were taken before and after Post Welding Heat Treatment Process (PWHT). The hardness values are tabulated in Tables 2, 3, 4 &5 and plotted in Graph.1&2 and compared with each other.

GRAPH I.
ROCKWELL HARDNESS NUMBER VS WORK PIECES BEFORE POST WELDING HEAT TREATMENT PROCESS

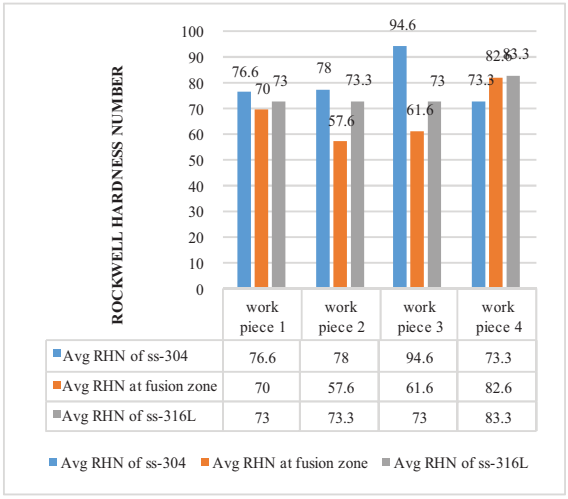

E-ISSN 2581 – 7957
P-ISSN 2277 – 3916

DOI: 10.32377/cvrjst2123

GRAPH II.
2 ROCKWELL HARDNESS NUMBER VS WORK PIECES AFTER POST WELDING HEAT TREATMENT PROCESS.

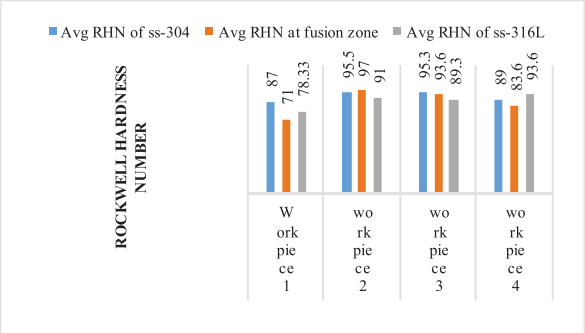

It can be observed from the above Tables and Graphs that the hardness values of the work pieces are increased after post welding heat treatment process (normalizing).

Microstructure analysis is performed under optical microscope at 500X magnifications at different location's i.e., at HAZ of 304, HAZ of 316L and fusion zone of workpiece 2 as it had performed very well when compared it with other workpieces. It is very difficult task to reveal the microstructure of the welded bimetallic joint due to the existence of the different chemical composition across the weldment. Composite region of the work piece is polished using emery sheet, which was then followed by disk polishing machine with aluminum oxide. Etchant used was modified Fry's reagent consisting of 25ml of hydrochloric acid (HCL), 1g of Cupric Chloride ($CuCl_2$), 150ml of water (H_2O) and 25ml of Nitric acid (HNO_3) [9]. The microstructure of the workpiece is shown in the fig.4. Table 6 shows the microstructure at different locations. To get the grain size according to ASTM standards Jeffries' formula (1) is used. Fig 3 shows the Jeffries' multiplier (f) values [10].

TABLE 5 Relationship Between Magnification Used and Jeffries' Multiplier, *f*, for an Area of 5000 mm² (a Circle of 79.8-mm Diameter) ($f = 0.0002\ M^2$)

Magnification Used, *M*	Jeffries' Multiplier, *f*, to Obtain Grains/mm²
1	0.0002
10	0.02
25	0.125
50	0.5
75[A]	1.125
100	2.0
150	4.5
200	8.0
250	12.5
300	18.0
500	50.0
750	112.5
1000	200.0

[A] At 75 diameters magnification, Jeffries' multiplier, *f*, becomes unity if the area used is 5625 mm² (a circle of 84.5-mm diameter).

Figure 3. Values of Jeffries' multiplier

$$N_A = f\left(N_{inside} + \frac{N_{intercept}}{2}\right) \quad \text{----------(1)}$$

N_A = number of grains per square millimeter.
N_{inside} = number of grains inside the circle.
$N_{intercept}$ = number of grains on the circumference of the circle.

Figure 4. Cross Section zoomed in image of the workpiece-2

TABLE VI.
MICROSTRUCTURE AT DIFFERENT LOCATIONS WITH DESCRIPTIONS

Microstructures	Description
 SS-304	SS-304 base material consisting of the austenitic grain boundaries with annealing twins showing elongated grains since the material7 is rolled. The grain size is ASTM No = 8.
 SS-304 HAZ	SS-304 HAZ consisting of austenitic grain boundaries with annealing twins showing Equiaxed grains since the material affected by the heat so the grains are recrystallized.
 Fusion Zone	The Fusion zone is showing the dendritic structure (Epitaxial Grain Growth).
 SS-316L HAZ	SS-316L HAZ structure consisting of austenitic grain boundaries with annealing twins.
 SS-316L	SS-316L base material structure consisting of austenitic grain boundaries with annealing twins having the grain size ASTM No = 7.

IV. RESULTS

- 22.435% increase in average hardness of SS-304.
- 68.402 % increase in average hardness of fusion zone.
- 24.657 % increase in average hardness of SS-316L.
- It can be clearly said that Post Welding Heat Treatment process (Normalizing) increases the hardness of the SS-304 and SS-316L TIG welded dissimilar metals.

V. Conclusions

In this study Post Welding Heat Treatment process (PWHT) is carried out on all the four work pieces. A change can be observed on comparing the hardness values of the weldments before and after the heat treatment process. There is a significant increase in the hardness values of workpiece-2.

Acknowledgement

The author KLN Murthy, Assistant Professor, Department of Mechanical Engineering, Sreyas Institute of Engineering and Technology, Nagole, Hyderabad is highly thankful to the Principal Dr. Suresh Akella and management of the college for their support in doing this research work.

The author Dr.A.C.UmaMaheshwar Rao, Assistant Professor, Department of Mechanical Engineering, Sreyas Institute of Engineering and Technology, Nagole, Hyderabad is highly thankful to the Principal and management of the college for their support in doing this research work.

References

[1] Effect of Post Weld Heat Treatment on Mechanical Properties and Microstructure of P11 Weld: A Review, ISSN: 2230-9845 (Online), ISSN: 2321-516X (Print) Volume 8, Issue 3 by Amit R. Patel, G.D. Acharya.

[2] Post-Weld Heat Treatment Case Studies by Khaleel Ahmed and J. Krishnan, Centre for Design and Manufacture Bhabha Atomic Research Centre.

[3] Effects of post-weld heat treatments on the microstructure, mechanical and corrosion properties of gas metal arc welded 304 stainless steels by Taiwo Ebenezer Abioye et.al.

[4] Effect of post-weld heat treatment on the microstructure and mechanical properties of arc welded medium carbon steel by M. R. Dodo1 et.al. Print ISSN: 0331-8443, Electronic ISSN: 2467-8821.

[5] Austenitic Stainless Steels Text book, Chapter 6.

[6] S.H. Avner, Introduction to Physical Metallurgy. (McGraw-Hill Inc., 1974).

[7] Effect of Post-Weld Heat Treatment on Mechanical and Electrochemical Properties of Gas Metal Arc-Welded 316L (X2CrNiMo 17-13-2) Stainless Steel JMEPEG ASM International.

[8] Designing of CK45 carbon steel and AISI 304 stainless steel dissimilar welds Print version ISSN 1516-1439 Mat. Res. vol. 17 no.1 São Carlos Jan./Feb. 2014 Epub Oct 11, 201.

[9] University of Cambridge Chemical Hazard Risk Assessment form.

[10] Standard Test Methods for Determining Average Grain Size, Designation: E112 – 10, ASTM international.

E-ISSN 2581 – 7957
P-ISSN 2277 – 3916

CVR Journal of Science and Technology, Volume 21, December 2021
DOI: 10.32377/cvrjst2124

Effect of Water Level on Mechanical Properties of Underwater Friction Stir Welded Aluminum Alloys

G. Mrudula[1], Sk. Mohammad Shareef[2], P. Bhargavi[3]
[1]Assoc. Professor, CVR College of Engineering/Mechanical Engg. Department, Hyderabad, India
Email: mrudula.gundla@gmail.com
[2]Asst. Professor, CVR College of Engineering/Mechanical Engg. Department, Hyderabad, India
Email: shareefshaik4@gmail.com
[3]Asst. Professor, CVR College of Engineering/Mechanical Engg. Department, Hyderabad, India
Email: pokalabhargavi.09@gmail.com

Abstract: **The rise of unconventional means of joining metals has given way to Friction stir welding and underwater friction stir welding (UFSW). Underwater friction stir welding is a modern technique of welding metals together that does not involve excessive amounts of heat, filler rods and shielding gases and is considered an effective 'Green Technology '. It is an upgrade on Friction stir welding in the way it uses water as a cooling medium. In this project, experiments have been conducted to determine the effect of the water level on mechanical properties of underwater friction stir welded aluminum alloys. Three sets of Aluminum slabs are welded using underwater friction Stir welding at three different water levels and then attempt to compare the variation of mechanical properties of the weld under different water levels. It is observed that the tensile strength of welded joints varies with the water level in proportion.**

Index Terms: **Friction stir welding, filler rods, Aluminum Slabs, Mechanical Properties**

I. Introduction

Welding of aluminum alloys requires different techniques and process parameters. Improper selection of welding technique and process parameters produces defective welds [1]. The conventional welding techniques are not effective to produce sound aluminum joints due to many reasons like hot cracking, porosity and distortion [2]. An advanced and innovative welding technique Friction Stir Welding was invented by The Welding Institute of UK in 1991 to produce defective free aluminum joints. This method also can be used not only for various metals but also for different materials like polymers and composites [3]. It is a solid-state joining technique which uses non consumable rotating tool. The strength of the welded joint depends on various process parameters like rotational speed, weld speed, tool pin profile, plunge depth [5]. In recent years underwater friction stir welding has come into existence which is carried out at temperatures below the melting point temperature of the material. During UFSW, the high heat absorption capacity of water reduces the transmission of heat flow to the thermo-mechanically affected zone (TMAZ) and heat affected zone (HAZ) which results in the low heat existence in the TMAZ and HAZ. Due to less heat input, the TMAZ and HAZ width is narrowed. UFSW gives improved mechanical properties by minimizing several welding defects like porosity, shrinkage, and solidification cracking. It also provides well defined variation in grain size in different zones along the joint and therefore, a high-quality weld joint is produced. This process is suitable for alloys that are sensitive to overheating during the welding process and it is widely used for aluminum alloys. It is also proved that the underwater friction stir welding improves the tensile strength of the weld joint than in air [6]. This process also requires less energy compared to conventional techniques and does not require any consumable or filler materials and shielding gases which makes this process cheaper. It is widely used in shipbuilding, submarines, oil and fuel tanks and various offshore structures involving fabrication and repair.

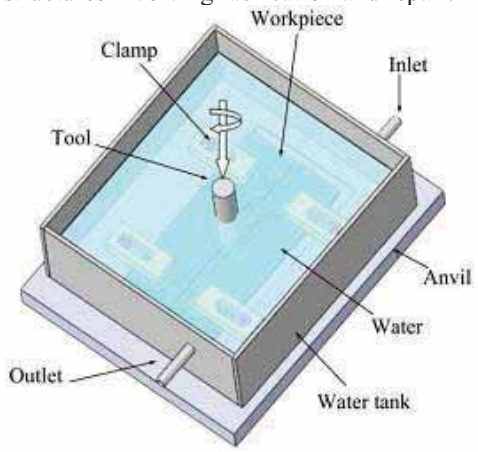

Figure 1. Under water FSW Technology

II. Literature Survey

Nandan et.al. (2008) explained the influence of different FSW process parameters on the principle of heat flow, material flow during friction stir welding of different materials.

Yong Zhao et.al. (2016) worked on underwater friction stir welding of Aluminum and Magnesium alloys and compared the tensile strength and hardness results when the same materials were welded in air. He concluded that the tensile strength of the welded joint was improved by underwater welding.

Anil Kumar et.al (2016) concluded that the rotational speed is the most significant process parameter which has the highest influence on tensile strength and hardness, followed by the weld speed or feed.

Sagar et.al. (2016) focused on the effect of tool pin length, rotational speed and feed on the mechanical

Received on 20-03-2021, Revised on 26-04-2021, Accepted on 04-05-2021.

properties of friction stir welded dissimilar Aluminum joints. The relation between the thickness of the workpiece and plunge depth was also determined.

Saravana kumar. R (2016) derived the optimum rotational speed of the FSW tool to control the rise in temperature during welding of dissimilar Aluminum alloys.

Tulika Garg and others (2014) stated that little work is done on under water friction stir welding. It is an innovative and novel technique which can be effectively used in welding of marine ships.

Lui et. al. (2010) concluded that mechanical properties of aluminum joints can be improved by cooling effect.

III. Problem Definition

From the above literature survey, it is observed that the underwater friction stir welding produces efficient joints with proper selection of process parameters like rotational speed, feed, axial force [7]. But the previous studies focused only on cooling effect and did not study the effect of depth of water level. Therefore, it is also necessary to study effect of exact depth of water level on heat flow and mechanical properties of welded joints.

A. Methodology

In this experiment, we study the effects of depth of water level in underwater friction stir welding on the weld performance of joints by conducting tensile test, Vickers hardness test and optical microscopy.

B. Description of workpiece and tool material

Workpiece: Aluminum 7075 slabs
Dimensions: 100*75*6 mm
No of pieces: 3
UFSW tool: Taper turned cylindrical tool.
Tool material: H13 tool steel

C. Welding parameters

Rotational speed: 900 rpm
Welding feed: 40mm/min
Depth of water: 30mm, 40mm and 50mm

D. Work material

7075 aluminum alloy (AA7075) is an aluminum alloy, with zinc as the primary alloying element. It has excellent mechanical properties, and exhibits good ductility, high strength, toughness, and good resistance to fatigue [8,9]. It is more susceptible to embrittlement than many other aluminum alloys because of micro segregation but has significantly better corrosion resistance than the 2000 alloys. It is one of the most used aluminum alloys for highly stressed structural applications and has been extensively utilized in aircraft structural parts.

I. Chemical composition

TABLE I.
CHEMICAL COMPOSITION OF 7075 ALUMINUM ALLOY TOOL STEEL

Element	Zn	Mg	Cu	si	Fe	Mn	Ti	Cr	Al
Composition in %	6.1	2.5	1.6	0.4	0.5	0.3	0.2	0.15	Balance

II. Mechanical properties

TABLE II.
MECHANICAL PROPERTIES OF ALUMINUM ALLOY

Tensile strength	Yield Strength	Elongation	Vickers hardness
572 Mpa	503 Mpa	11%	175 HV

E. Tool material

H13 Tool Steel is a versatile chromium-molybdenum hot work steel that is widely used in hot work and cold work tooling applications. The hot hardness (hot strength) of H13 resists thermal fatigue cracking which occurs because of cyclic heating and cooling cycles in hot work tooling applications. Because of its excellent combination of high toughness and resistance to thermal fatigue cracking (also known as heat checking) H13 is used for more hot work tooling applications than any other tool steel.

I. Chemical composition

TABLE III..
CHEMICAL COMPOSITION OF H13 TOOL STEEL

Element	C	Mn	Si	Cr	Ni	Mo	V
Composition	0.35	0.3	0.88	5	0.3	0.5	1

II. Mechanical Properties

TABLE IV.
MECHANICAL PROPERTIES OF H13 TOOL STEEL

Tensile strength	Yield Strength	Elongation	Vickers hardness	Elastic Modulus	Density
1990 Mpa	1650 Mpa	9%	549 HV	190-210 GPa	7.76 g/cm3

F. Tool Design:

Figure 2. FSW Tool

CVR Journal of Science and Technology, Volume 21, December 2021
DOI: 10.32377/cvrjst2124

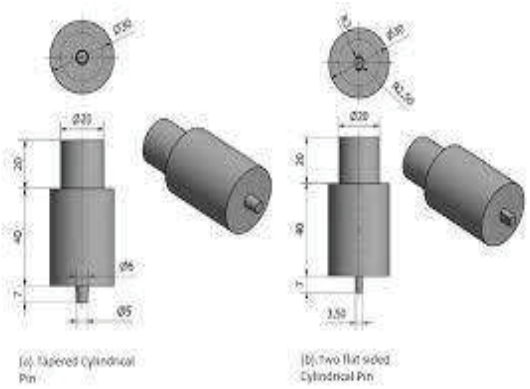

Figure 3. Design of Tool

IV. Experimental Work

In this work weld Aluminum 7075 slabs on their edges to form a butt weld. Aluminum slabs are welded by Underwater friction stir welding at a constant speed of 900 rpm. The slabs welded at 900 rpm were tested to have the best and most optimum mechanical properties such as tensile strength and hardness. H13 tool with taper threaded profile is used to weld the slabs at the feed rate of 40mm per min. Underwater friction stir welding is done at three different levels of water in the water tank. The underwater welded slabs are then tested for their strength, hardness, microstructure etc. Initially Aluminum slabs (100 * 75 mm) are made level with each other to prevent any irregularities and notches. The rough surfaces of the slabs are polished using a file to give a smoother cleaner cut. The slabs are taken together and levelled at every dimension to ease the operation of welding. Those are clamped on a surface and held against a press mechanism that levels them. Any additional metal on any of the slabs is either trimmed off by filing or cut off by a saw tooth milling cutter.

Figure 4. Aluminum slabs after levelling

Aluminum slabs after levelling are then clamped inside the water tub. The slabs are held together at one of their edges whilst the other edge is clamped by a weight that is attached to the welding board. The weights are placed on the edges of the slabs on both sides that hold the metal to the welding board. The weights are linked to the welding board by a thread screw that tightens the grip on the metal. After the process of welding, the thread screw is loosened, and the weights are removed to remove the butt-welded slab.

After clamping the slabs to the welding board in the water tub, the tool H13 taper threaded steel is taken. The tool is polished and made sharp. The tool is then fixed into the tool holder that rotates at 900 rpm. The tool rotates at a very high speed underwater to melt the metal slabs and weld them together at room temperature. After the tool is clamped to the tool holder, water is filled into the tub. Water level in the tub is seen through a scale attached on its side. The scale accounts for the depth of water involved in the welding operation. Butt welds welded at different depths have different mechanical properties.

Figure 5. Water tank arrangement

Water level on the given scale is measured. Zero level is seen as 23 mm on the scale. Zero level is the level at which the surface of the slabs touches the water without submerging in them. It is the level at which there is virtually zero depth of water. The first level or first depth is taken at 30mm or 7mm above the zero level. The second level is taken at 40mm or 17 mm above the zero level. The third and the final level of water is taken at 50mm or 27mm above the zero level.

Aluminum slabs are welded at the depths of 30, 40 and 50 mm underwater consecutively.

Figure 6. Slabs at a depth of 30 mm

In the above figure, the aluminum slabs are welded at 900 rpm at the depth of 30mm or 7mm above the zero level.

CVR Journal of Science and Technology, Volume 21, December 2021
DOI: 10.32377/cvrjst2124

Figure 7. Slabs at a depth of 30 mm

In the above figure, the slabs are welded at depth of 40mm or 17 mm above the zero level. From the figure, we can see that welding at greater depths of water causes lower turbulence in the water.

Figure 8. Slabs at a depth of 30 mm

In the above figure, slabs are welded at the depth of 50mm or 27mm above the zero level. From the figure, we see that turbulence at this depth is almost invisible.

Another observation we can see is that at lower levels of depth of water, the uncut flash thickness is substantially greater than the flash thickness of the welds at higher levels of water. Slabs welded at a higher depth have more smoothness in appearance and precision in cut.

Figure 9. Slab welded at 30 mm

The above figure shows slabs welded at 30mm depth or 7mm over zero level. The weld is not smooth and large sharp uncut flash is seen on the edges of the circular weld.

Figure 10. Slab welded at 40 mm

The above figure shows slabs welded at depth of 40mm. The weld is smooth and there is virtually no uncut flash in this case. There is negligible difference between the uncut flash of slabs welded at 40mm and 50mm.

V. Testing of Specimen

A. Visual Inspection

In the first step of inspection of the weld, several welding defects are revealed. Open surface tunnels are found in the joint due to lack of significant downward pressure. Excessive lateral flash was also observed in the first weld (at the depth of 30mm) resulting from outward flow of plasticized material from underneath of the shoulder. For welds done at higher depths, no defects were found.

Figure 11. Inspection of welded piece

B.Mechanical Testing

UFSW produces almost defect free welds that are used in almost all the industries. They are an effective 'Green Technology' that do not require excessive heating, filler rods and shielding gases. The success of the applicability of the weld is replicated in the real world through mechanical testing.

Some of the tests are.

- Vickers Hardness Test
- Tensile test

C Tensile Test

Tensile testing, also known as tension testing, is a fundamental materials science and engineering test in which

CVR Journal of Science and Technology, Volume 21, December 2021
DOI: 10.32377/cvrjst2124

a sample is subjected to a controlled tension until failure. Properties that are directly measured via a tensile test are ultimate tensile strength, breaking strength, maximum elongation, and reduction in area] From these measurements the following properties can also be determined: Young's modulus, Poisson's ratio, yield strength, and strain-hardening characteristics.

D. Hardness Test

Vickers hardness testing machine is used to determine the hardness of friction stir welded 7075 aluminum plates. It is an indentation hardness test which works on basic principle of indentation or depth of penetration caused on the material when minimum required amount load is applied. The hardness of the material is defined by Vickers hardness number and the unit of hardness is Vickers Pyramid Number (HV).

VI. Results and Discussions

In this study, three sets of Aluminum slabs of 75*100 mm dimensions were welded using Underwater friction stir welding technique. The AA slabs were welded at 900 rpm tool rotation speed and 40mm/min feed of Aluminum slabs attached to the welding table. The tool used for welding is H13 taper turned tool steel. The water level has been taken as 30mm 40 mm and 50 mm on measuring scale and they are 7 mm, 17 mm and 27 mm above the base level.

Visual Inspection: In the first step of inspection of the weld, open surface tunnels are found in the joint due to lack of significant downward pressure. Excessive lateral flash was also observed in the first weld (at the depth of 30mm) resulting from outward flow of plasticized material from underneath of the shoulder. For welds done at higher depths, no defects were found.

Tensile Test Results:

The yield strength and ultimate strength of the welded specimens were determined by using ASTM D638 universal tensile testing machine.

TABLE V.
TENSILE TEST RESULTS

S.No	Absolute Water Level(mm)	Yield strength (Mpa)	Ultimate strength (Mpa)
1	30	1655	2010
2	40	1662	2035
3	50	1660	2050

From the above results it is observed that the yield strength and ultimate strength of the welded specimens have been improved with increasing of water level. The maximum value of ultimate strength of 2050 Mpa is observed at water level of 50 mm.

Hardness Test Results:

The hardness test is conducted by using VM50 Vickers's hardness testing machine to determine the hardness of welded joints.

TABLE VI.
HARDNESS TEST RESULTS

S. No	Absolute Water Level(mm)	Vickers's Hardness (HV))
1	30	551
2	40	558
3	50	562

From the above results it is observed that there is slight increase in the hardness of aluminum joints with the increase in water level. The maximum value of 562 HV is observed at water level of 50 mm.

A. Graphs

Graphs showing Tensile test results

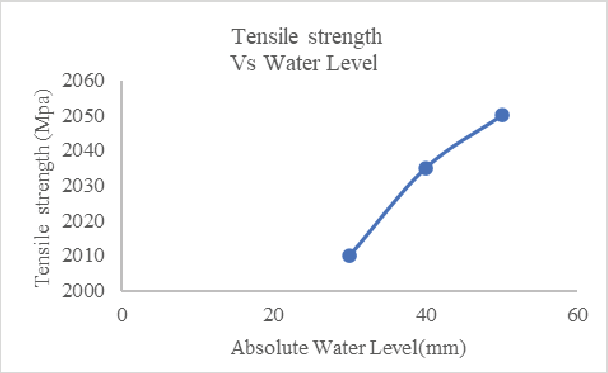

Figure 12. Variation of tensile strenth with water level

Graph showing Vickers Hardness results

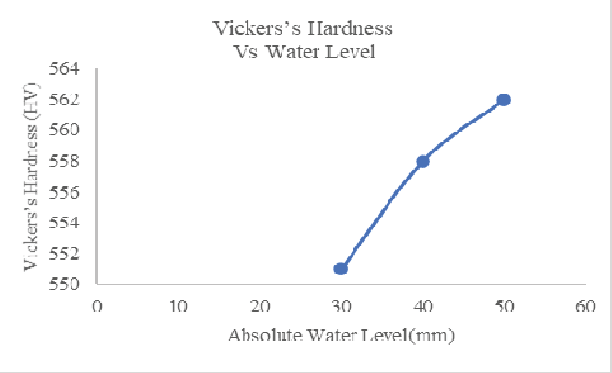

Figure 13. Variation of hardness with water level

Graph showing Yield Strength results

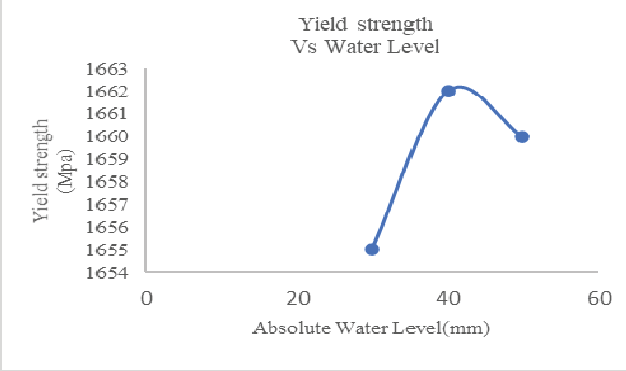

Figure 14. Variation of yield strength with water level

VII. Conclusions

The present work focused on finding out the effect of water level on tensile strength and hardness of underwater friction stir welded aluminum joints.

From the above experiment, it is observed that the effect of water level plays a prominent role on the mechanical properties of welded joints. Aluminum slabs welded at 900 rpm by H13 tool steel at different depths of water were analyzed thoroughly in detail. From the investigation, following conclusions were obtained.

UFSW uses water as a cooling medium which reduces temperature and restricts the coarsening or dissolution of the precipitates leading to enhanced mechanical properties of the joint.

The tensile strength of the welded joint increases with increase in the depth of water. The yield Strength of the welded joint increases with increase in the depth of water. The highest yield Strength is obtained at 27 mm depth as 1662 MPa and the highest ultimate tensile strength is obtained at a depth of 27 mm (50mm from the base) as 2050 MPa.

The Hardness of the welded joint increases with increase in the depth of water. The highest Vickers hardness is obtained at 27 mm depth as 562 HV.

Limitations: There are limitations like large down forces are required with heavy duty clamping, leaves a keyhole in welded specimen, high cost of initial set up and difficult to weld forgeable materials.

Applications: Underwater friction stir welding can be used successfully to weld wide variety of metals and materials. This is mainly used to produce defect free welds of aluminum alloys used for industrial, aerospace, and marine applications.

Future Scope: The metallurgical characteristics can be determined at welded zone, heat affected zone and thermo mechanically affected zone.

It is also necessary to study and understand the thermal flow of material during welding as the water is acting as cooling medium and the mechanical and metallurgical results can be compared with the results when the welding is done in air.

References

[1] Ramesh Rudrapathi: Recent advances in joining of Aluminum alloys by Using Friction Stir Welding. DOI: 10.5772/intechopen.89382

[2] P L Threadgill, A J Leonard, H R Shercliff and P J Withers: *International Materials Reviews*, vol.54. no.2. March 2009. pp. 49-93.

[3] Harish Kumar, S.V. Satish: Studies on Friction Stir Welding of Polymers- *A Review. International Journal of Engineering Research & Technology (2020)* ISSN: 2278-0181, Vol. 9 Issue 06, June-2020.

[4] W. M. Thomas, E. D. Nicholas, and J. C. Needham, "Friction stir welding", *International patent PCT/GB92102203 and Great Britain patent* 9125978.8, 1991.

[5] R Nandan, T DebRov, H.K.D.H.Bhadeshia : Recent advances in friction-stir welding-process, weldment structure and properties. *Progress in Materials Science 53* (2008) 980–1023.

[6] Yong Zha Sheng Jiang, Shaofeng Yang, Zhengping Lu1, Keng Yan: Influence of cooling conditions on joint properties and microstructures of aluminum and magnesium dissimilar alloys by friction stir welding. *International Journal of Advance Manufacturing Technology* (2016) 83:673–679.

[7] Anil Kumar Bodukuri, Rajendar Katla. Upender: Influence of Friction Stir Welding Parameters on Properties of AL-7075 Alloy. *International Journal of Scientific & Engineering Research,* Volume 7, Issue 6, June-2016 129 ISSN 2229-5518.

[8] Sagar M. Patil, Dr. P. S. Adwani: Effect of the Process Parameters of Friction Stir Welding of Dissimilar Aluminum Alloys Al 6061-T6 and Al 7075-T6 on the Weld Quality. - *International Journal for Scientific Research & Development*| Vol. 4, Issue 07, 2016 | ISSN (online): 2321-0613.

[9] Saravana kumar: Effect of process parameters on mechanical properties of friction stir welded AL6063 & AL7075, *Journal of Chemical and Pharmaceutical Sciences*, Volume 9, Issue 2, April-June-2016, ISSN: 0974-2115.

E-ISSN 2581 – 7957
P-ISSN 2277 – 3916

CVR Journal of Science and Technology, Volume 21, December 2021
DOI: 10.32377/cvrjst2125

Exploration of Multicomponent Phase Diagrams and Evaluation of Calphad Databases

Raghavendra Kulkarni[1], and K. Guruvidyathri[2]
[1]Assoc. Professor, CVR College of Engineering/H & S Dept (Physics), Hyderabad, India,
Indian Institute of Technology Madras, Chennai, India
Email: cvrphyrk@gmail.com
[2]Asst. Professor, University of Hyderabad/School of Engineering Sciences and Technology, Hyderabad, India
Email: guruvidyathri@gmail.com

Abstract: **With the emergence of modern materials such as high-entropy alloys (HEAs) and the ever-increasing demand for improvement in conventional metallic materials, it becomes essential to have multicomponent phase diagrams. The availability of such diagrams, however, is very scarce. Calphad (CALculation of PHAse Diagram) method offers a way to construct such diagrams, combining theoretical and experimental methods into appropriate computational programs. The various visualization of multicomponent diagrams, the associated advantages and compromises are reviewed in the present work with a few example calculations on CoCrFeNi and AlCoCrFeNi systems. Besides, the accuracy of the Calphad method relies mainly on the available multi-component thermodynamic databases. A few of such databases are evaluated in this work as well.**

Index Terms: **Phase diagrams, Calphad, Gibbs energy, Thermo-calc.**

I. Introduction

Research groups of Yeh and Cantor independently came up with the earliest works on HEAs [1], [2]. These alloys have recently attracted significant academic interest [3]. HEAs have a stark difference from conventional alloys in terms of composition. Conventional alloys have one major element called the base element, e.g. Fe is the base element in steel. On the other hand, HEAs have multiple principal elements, often five or more, and no single element can be called as base element [4], e.g. equiatomic CoCrFeMnNi. When such a composition occurs as a solid solution, it will have high configurational entropy. This thermodynamic factor depends on the number of elements used and not on the type of elements used. Yeh et al. [1] proposed that the high entropy may dominate the competition among various thermodynamic factors of competing phases and improve the stability of the simple solid solution over other phases. The reality, however, turned out to be more complex. Microstructures of HEAs have been observed to be heavily depending on the type of elements used. From a simple single-phase solid solution to complex multi-phase microstructures were reported in various HEAs [5]. The field, however, has opened large unexplored metallic materials for investigation.

Since possible number of HEAs are astronomically high, compositional design is a necessary step in HEA research, which involves finding useful compositions to achieve a suitable microstructure vis-à-vis properties. Investigating the multicomponent phase diagrams for HEAs is the most important activity since phase diagrams are the roadmaps for compositional design. This activity greatly reduces the experimental effort to a small set of alloys rather than doing trial and error, which requires monumental efforts due to the shear immensity of possible alloy compositions. In this regard, the biggest challenge is that multi-component phase diagrams are almost unavailable beyond ternaries and experimentally determining such phase diagrams is also extremely difficult.

The Possible number of HEAs are astronomically high. A necessary step in HEA research is to find useful compositions to achieve a suitable microstructure vis-à-vis properties. Phase diagrams are the roadmaps for composition selection. Multi-component phase diagrams are almost unavailable beyond ternaries and experimentally determining such phase diagrams is also extremely difficult.

There are simple empirical rules which are fast and quite useful to predict the likely microstructure. These rules are not very sophisticated, e.g. one alloy is predicted to have one microstructure at all temperatures. Besides, significant exceptions are reported for such rules [5]. However, none of these methods are as sophisticated as using a phase diagram for compositional design.

Apart from these simple methods, the Calphad method is robust, as it gives the phase diagram directly. The drawback is that the method requires reliable multicomponent Gibbs energy databases [6]. One reason for discrepancies is, the unavailable or inaccurate Gibbs energy databases. With such databases, the rapid screening methods for useful HEA compositions face serious accuracy issues [7].

One of the reasons is that only unary, binary and ternary Gibbs energy descriptions are usually developed and used. Data for higher order systems are obtained using extrapolation from lower order systems. In order to account for the higher-order effects, correction terms are required. Beyond ternary effects, usually, the contribution of higher order effects diminish and are usually ignored [8], which can

Received on 25-03-2021, Revised on 15-04-2021, Accepted on 12-05-2021.

cause significant issues in certain alloys. Further, developers focus on designing the Gibbs energy databases, usually, to work for specific compositional ranges. Evaluating the uncertainties associated with using the databases beyond such ranges is necessary for efficient alloy discovery.

Therefore, evaluation of the available databases is important which is attempted in the present work. However, firstly, the visualization of multicomponent phase diagrams is difficult since often it is a 2 dimensional representation. Therefore, various ways of looking at such a multicomponent composition way need to be explored. A few standard ways are revised in the present work with a few example calculations, outlining the advantages, calculation methods and compromises.

II. Modelling & Simulation Methods:

Thermo-Calc software were used for calculations. TCNI and SSOL thermodynamic databases were used in Thermo-Calc software. The databases contain Gibbs energy descriptions for the phases that are competing for stability. These descriptions are obtained through statistical curve fitting procedures, to obtain model parameters of Gibbs energy. The models are fitted to various kinds of experimental and theoretical data that are in some way related to Gibbs energy. The descriptions are compiled into databases, addressing various compatibility and higher order model parameters. For construction of isoplethal section, for example, in a four component system, the ratio between the mole fractions of three of the elements is maintained constant, as the mole fraction of the fourth element varies in x axis and temperature in y axis. For the construction of phase fraction plots, the composition is fixed at one value and the temperature is varied. It is also called as one axis diagram since only one variable is changed. The equilibrium phases are predicted in all these diagrams through the process of Gibbs energy minimization. Mathematically, it is a constrained optimization technique, where the constraints are compositions and temperature. The pressure is not varied and is kept equal to atmospheric pressure.

III. Visualizations Of Multicomponent Phase Space

Reported Calphad studies use various visualizations of phase diagrams in multicomponent space. One type is an isoplethal section, where restrictions on composition are used as conditions. Such diagrams are similar to conventional binary phase diagrams in terms of axes (T vs x) [9]–[12]. Such diagrams are made in the present study as well. Quaternary diagrams at a single temperature using a tetrahedron are reported [13]. A stack of pseudo quaternary diagrams was proposed to represent the quinary diagram. A 3D compromise representation of a 4D polytope using an isometric projection was also reported to visualize quinary diagram, preserving many details. Representations using graph theory were reported to have severe compromises [5]. Recently, parallel coordinate plots [14] were applied to HEAs [15], [16], which represent compositional relationships of phases at a single temperature. When it comes to fixed compositions, the widely considered representation is a phase fraction plot, which is made in the present study as well. In phase fraction plot, the amount of equilibrium phases is plotted against temperature [17]–[20].

IV. Results and Discussion

Isoplethal section or vertical sections or pseudo binary sections of multicomponent Co-Cr-Fe-Ni alloys are shown in Fig. 1 a-d. The Co, Cr, Fe and Ni elemental mole fractions were varied respectively. The way to visualize the diagrams, for example, Fig. 1a, is that at the left end of x axis the phases present in CrFeNi equiatomic ternary alloy are shown. As the Co content increases in the x axis, let's say to a value of 0.2, the other elements Cr, Fe and Ni maintain their equiatomic ration and occupy a cumulative mole fraction of 1 - 0.2 = 0.8. The right end of the diagram shows the phases in pure Co. Similarly, the diagrams in Fig.1 b-d can be visualized. In such diagrams mole fractions of all the four elements change in x axis. Apart from such an x axis, one can keep the mole fraction of two elements constant and allow that of the other two elements vary. Similar to Fig. 1, one can understand the five component diagrams shown in Fig. 2a and b for Al-Co-Cr-Fe-Ni alloys.

Although such diagrams are quite useful in giving familiar visualization of a phase diagram, we can sense that these diagrams show only a tiny portion of the four component phase space, i.e., these are merely four 2-dimensional slices of such a vast space. Thus, a severe compromise is present here in not showing potential compositions with combination of phases suitable for a particular application.

E-ISSN 2581 – 7957
P-ISSN 2277 – 3916

DOI: 10.32377/cvrjst2125

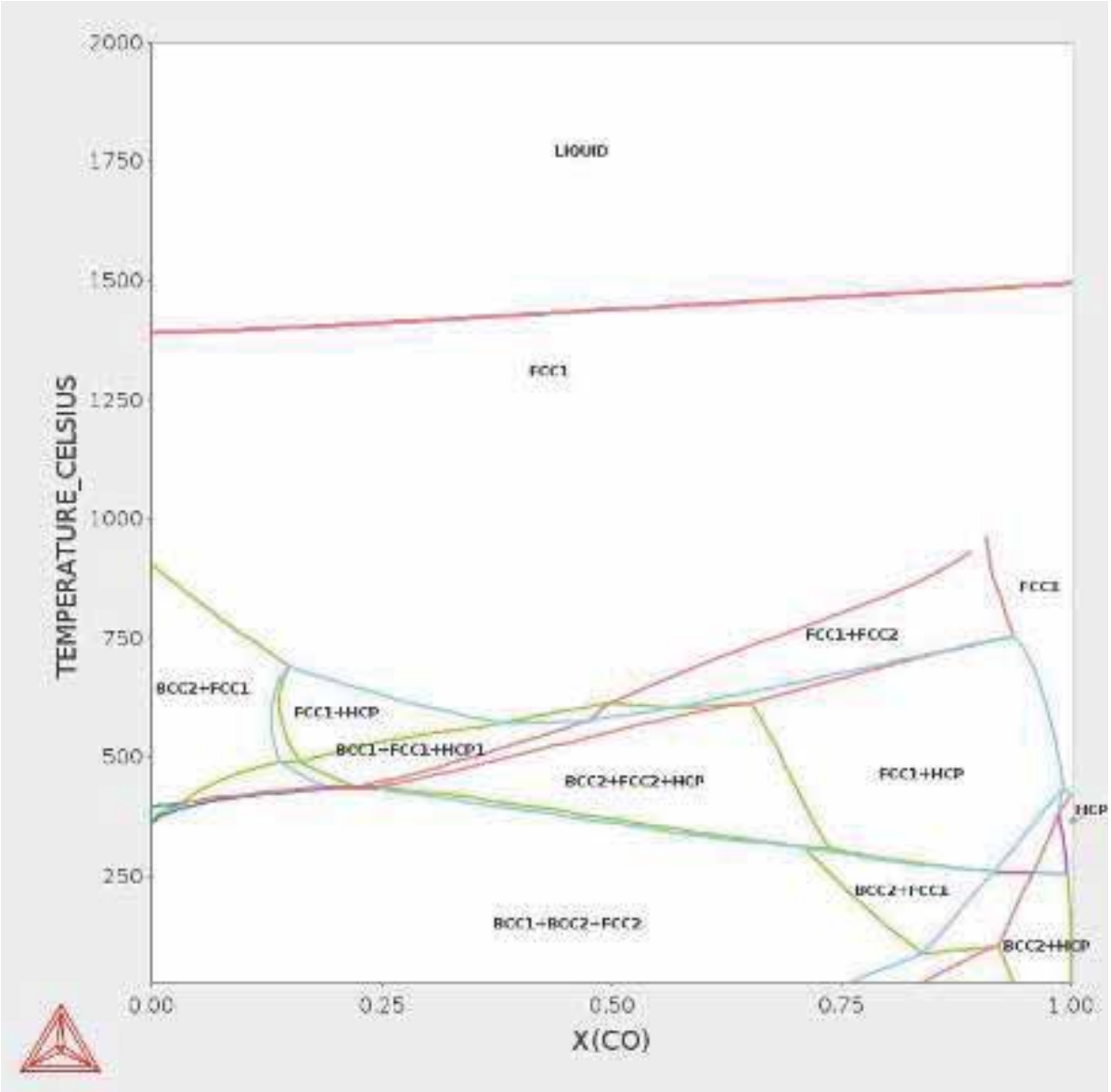

(a)

E-ISSN 2581 – 7957
P-ISSN 2277 – 3916

DOI: 10.32377/cvrjst2125

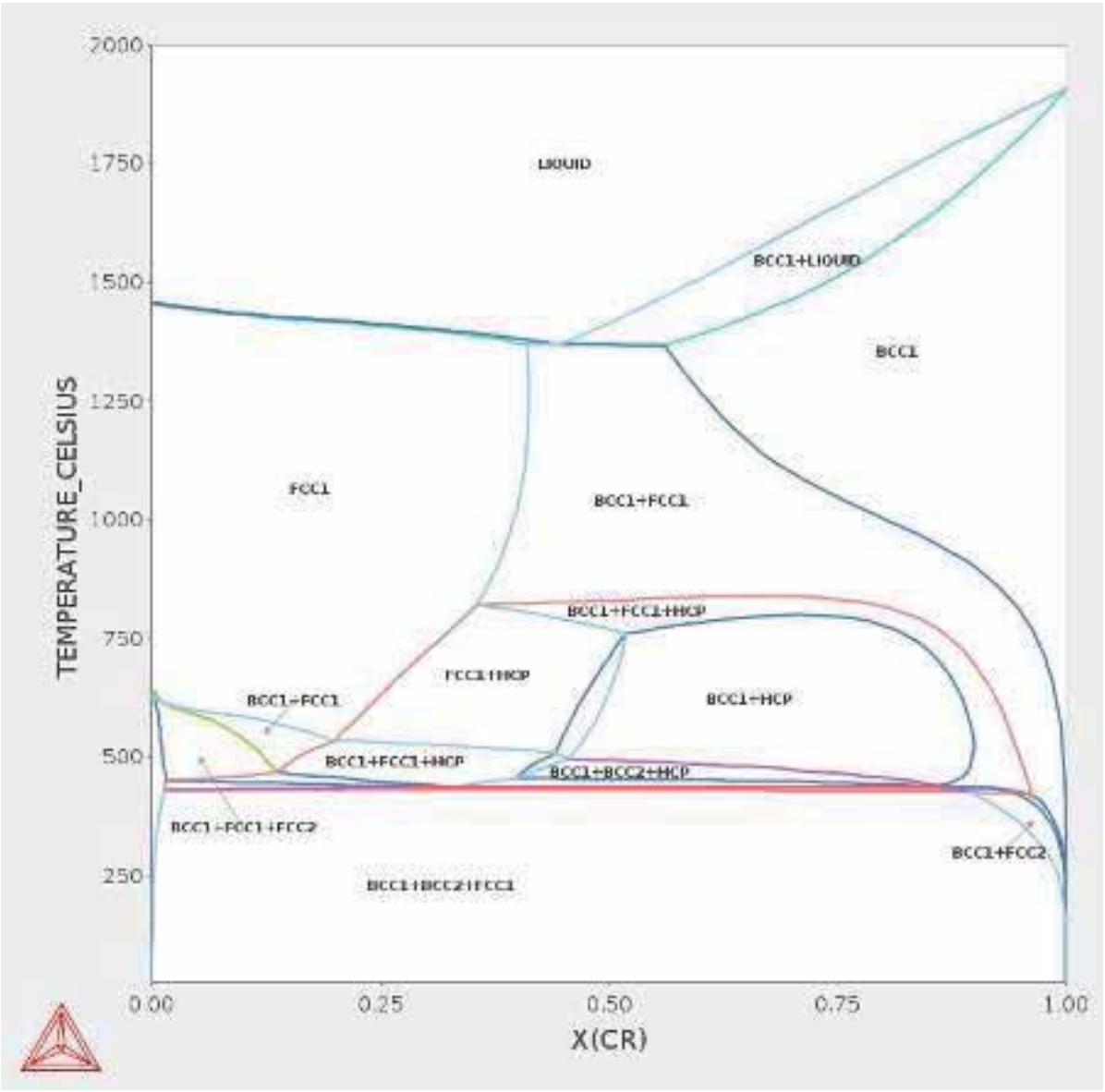

(b)

E-ISSN 2581 – 7957
P-ISSN 2277 – 3916

DOI: 10.32377/cvrjst2125

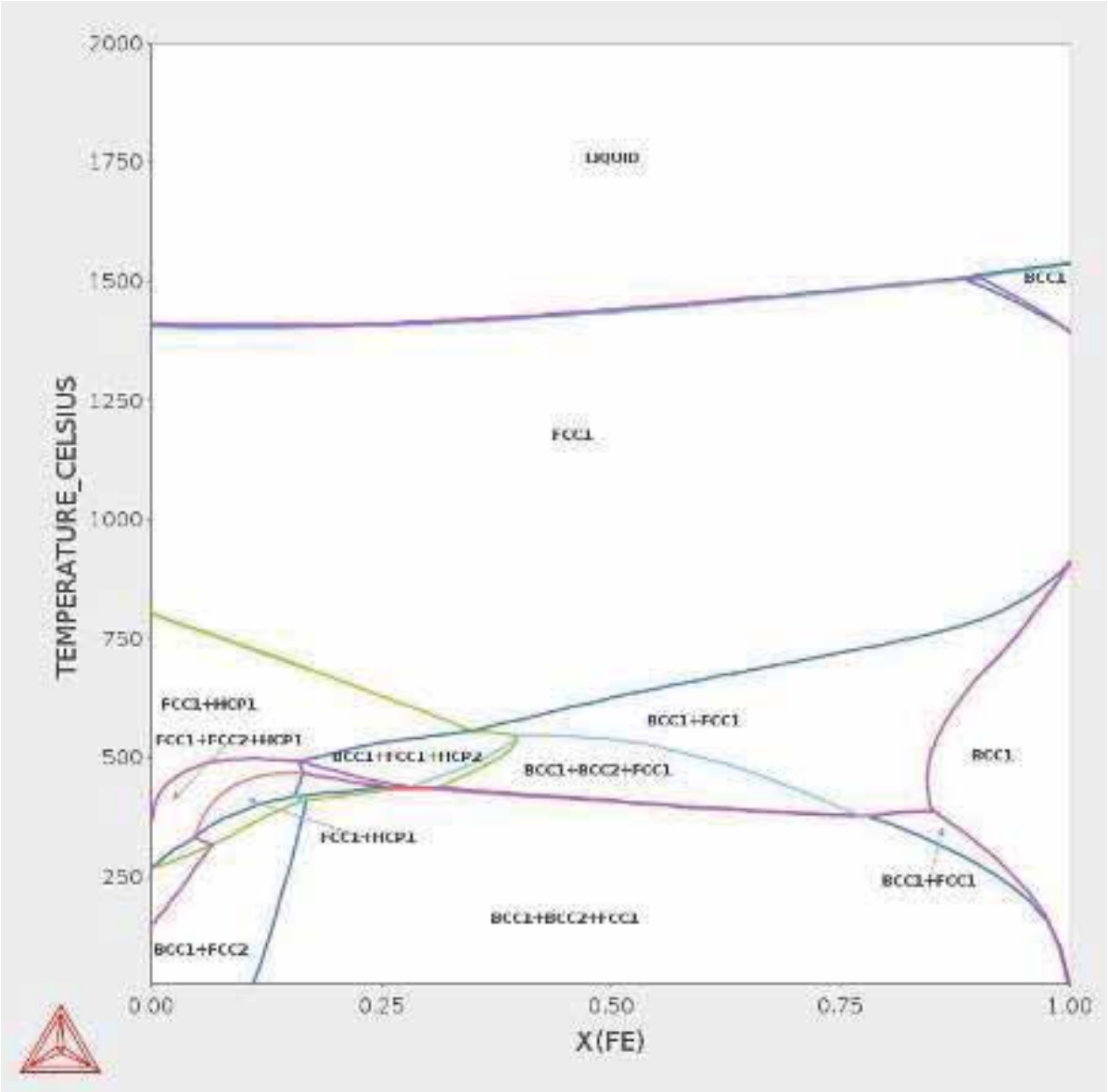

(c)

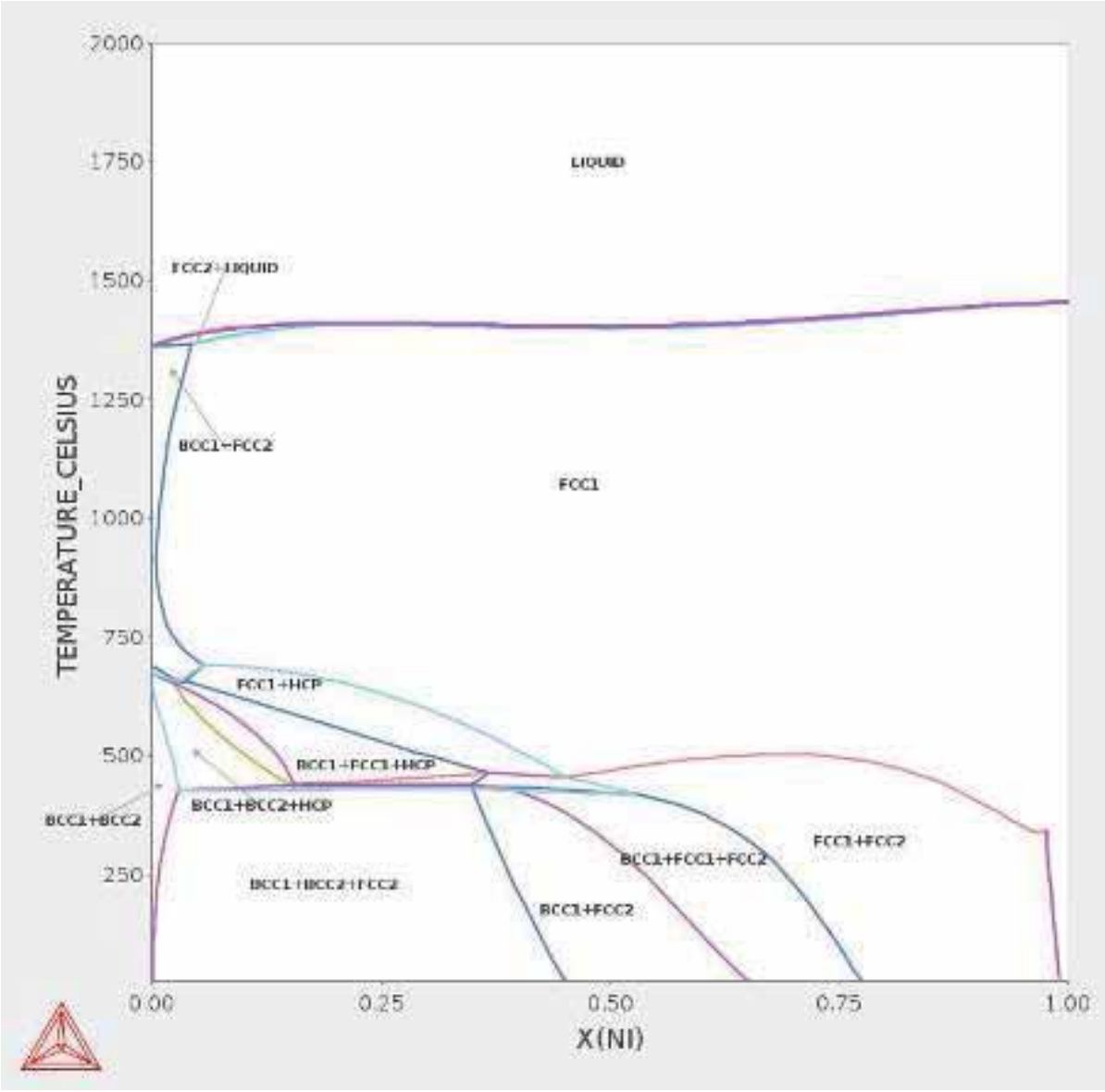

(d)

Figure 1. Co-Cr-Fe-Ni isoplethal sections with varying amounts of a) Co, b) Cr, c) Fe and d) Ni in x axis.

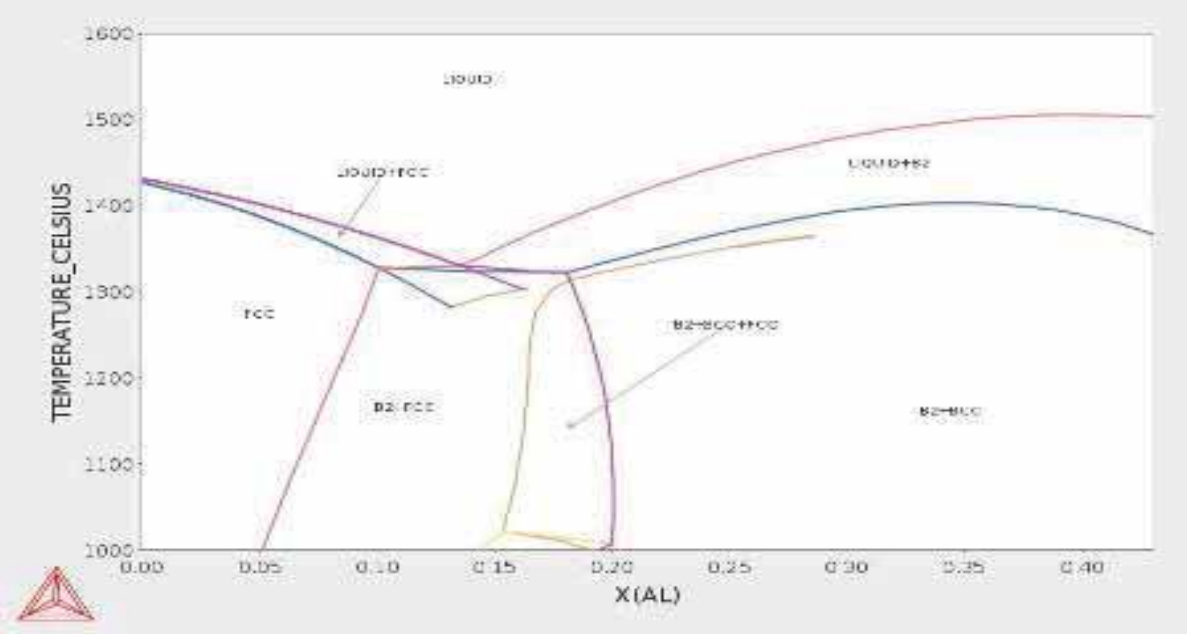

(a)

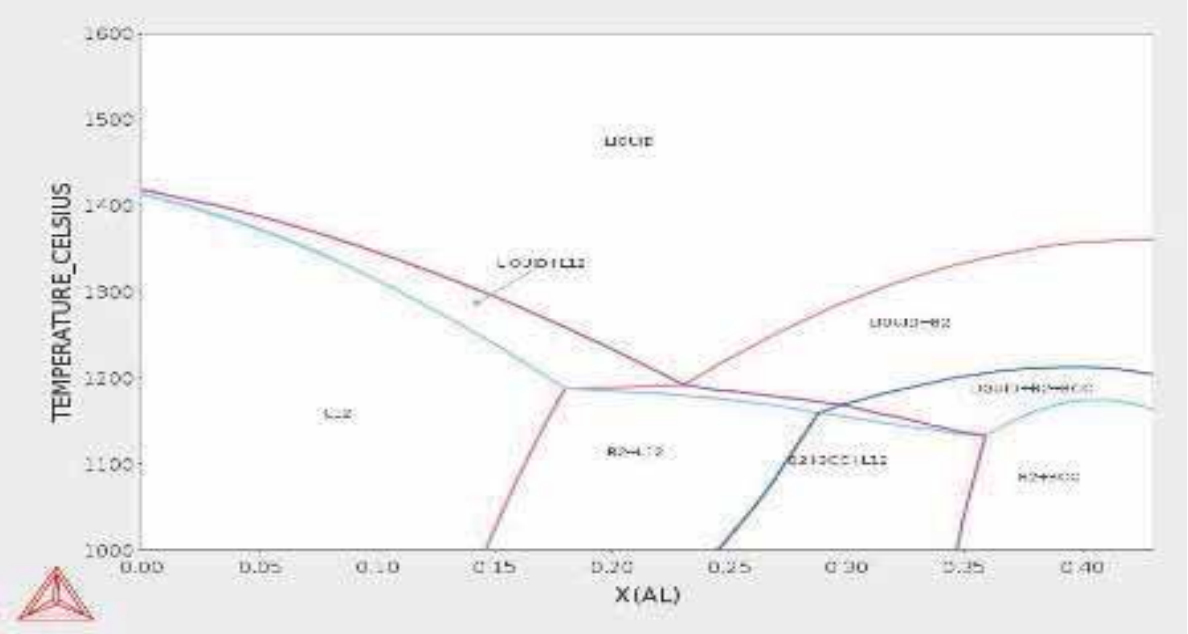

(b)

Figure 2. Al-Co-Cr-Fe-Ni isoplethal sections plotted using the data bases a) TCNI and b) SSOL with variation of Al mole fraction in x axis.

In Fig.2, a comparison between two different databases are made, TCNI and SSOL. When the experimental results reported in literature [3] are compared with these diagrams, the melting points, primary solidifying phases, etc. match reasonably well with the Fig. 2a compared to Fig. 2b. The prime reason for such a difference is mainly due to the included assessed data of binary and ternary subsytems in each database. In Al-Co-Cr-Fe-Ni system, there are 10 binary and 10 ternary subsystems. Both the databases have all the ten binary subsystems included. When it comes to ternary SSOL5 hardly has data for only one system whereas TCNI has data for about 7 systems. Therefore, the better accuracy is achieved with TCNI database.

Phase fraction plots or the one axis diagrams are given in Fig.3a and b for the single fixed composition of AlCoCrFeNi equiatomic alloy. The advantage in such diagrams is that the phase fraction information can be directly obtained whereas, in a conventional T-x diagram, it has to be calculated by applying lever rule separately at each temperature. The compromise however is, phases at any other composition cannot be seen.

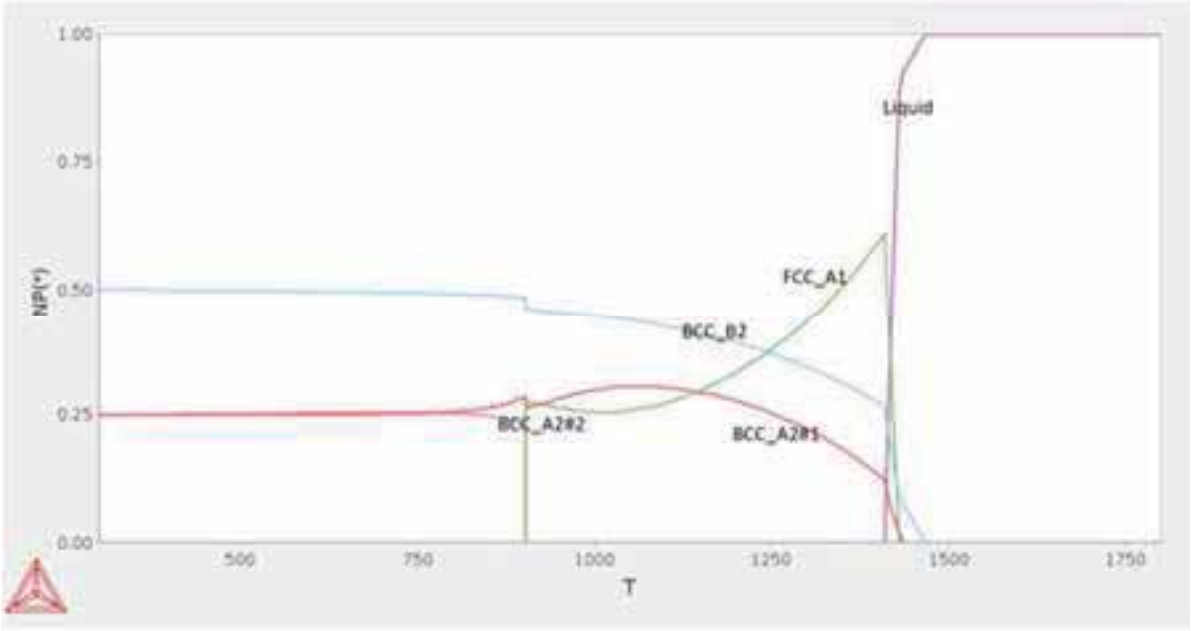

(a)

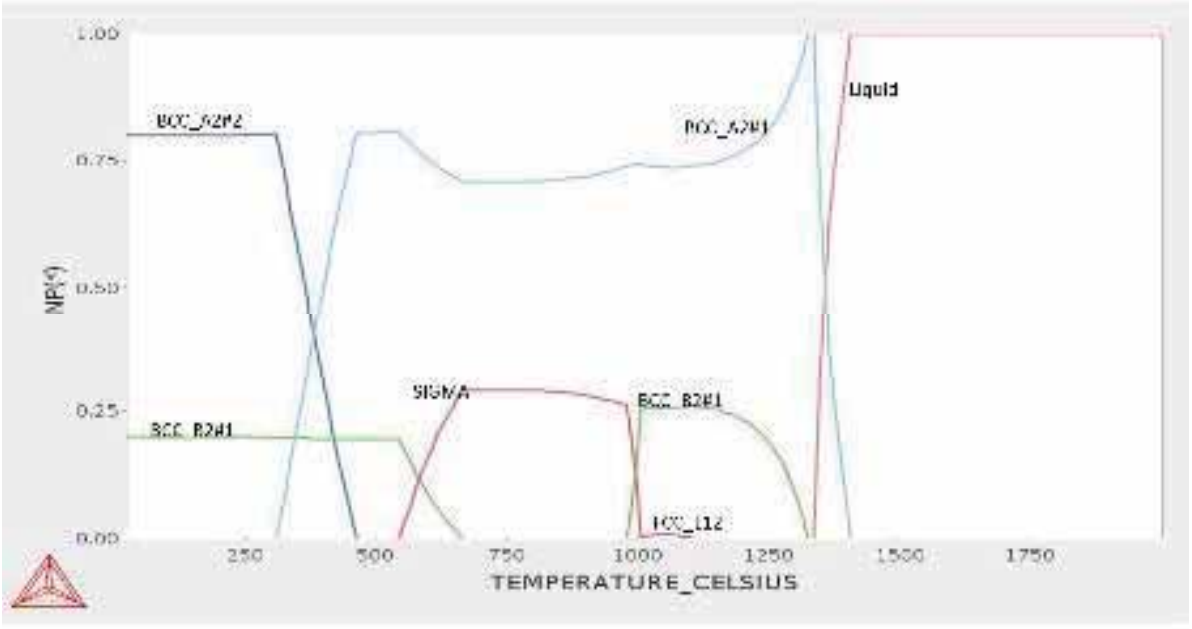

(b)

Figure 3. a) AlCoCrFeNi phase fraction plots drawn using the databases a) SSOL b) TCNI. (NP- Mole fraction of phases).

Again, severe differences are seen and the TCNI database gives better results compared to reported experimental data in terms of melting point and primary solidifying phases. However, when it comes to solid state, the FCC_A1 phase is experimentally observed at a higher fraction compared to what is predicted using TCNI. The SSOL database on the other hand, shows the FCC phase content to be higher, matching closely with the experiment. However, with SSOL

database, FCC appears as a primary solidifying phase which is not matching with the experimental reports.

Another aspect of difference is the appearance of sigma phase. It is experimentally reported to appear at intermediate temperatures, which is predicted using TCNI database. However, the exact range of its stability and the phase content have certain inaccuracies [21]. SSOL database was not capable to predict the sigma phase since the solution phases are given focus in it on top of missing ternary data.

V. Conclusions

Isoplethal or vertical or pseudo binary sections for Co-Cr-Fe-Ni and Al-Co-Cr-Fe-Ni systems are calculated. Such diagrams are a useful way to visualize the multicomponent phase space, although there are compromises since these are only 2-dimensional slices thus, such a vast phase space. One axis or phase fraction plots are useful in obtaining equilibrium phase fraction data along with the stable phases for a fixed multicomponent compositions.

The evaluation of Calphad databases SSOL and TCNI are made. TCNI calculations are, in general, better than SSOL. The reason is found to be mainly the included number of ternary descriptions. TCNI has 7 ternary systems of Al-Co-Cr-Fe-Ni system, whereas the SSOL has only one.

When it comes to predicting topologically close packed phases such as σ-phase, TCNI is better, although the stability range and the phase fraction have significant inaccuracies compared to experiments. There is a scope to improve such databases with more ternary data and possibly higher order data, Revisiting models may be one of the ways to improve the databases, however, in the present work it was not explored.

References

[1] J. W. Yeh et al., “Nanostructured High- EntropyAlloys with Multiple Principal Elements: Novel Alloy Design Concepts and Outcomes,” Adv. Eng. Mater., vol. 6, no. 5, pp. 299–303, May 2004,doi: 10.1002/adem.200300567.

[2] B. Cantor, I. T. H. Chang, P. Knight, and A. J. B. Vincent, “Microstructural development in equiatomic multicomponent alloys,” Mater. Sci. Eng. A, vol. 375–377, no. 1-2 SPEC. ISS., pp. 213–218, Jul. 2004, doi: 10.1016/j.msea.2003.10.257.

[3] B.S . Murty, J. W. Yeh, and S. Ranganathan, High Entropy Alloys. London: Butterworth- Heinemann, 2014.

[4] S. Ranganathan, “Alloyed pleasures: Multimetallic cocktails,” Curr. Sci., vol. 85, no. 10, pp. 1404–1406, 2003.

[5] D. B. Miracle and O. N. Senkov, “A critical review of high entropy alloys and related concepts,” Acta Mater., vol. 122, pp. 448–511, Jan. 2017, doi: 10.1016/j.actamat.2016.08.081.

[6] M. C. Gao, J. W. Yeh, P. K. Liaw, and Y. Zhang, High-Entropy Alloys: Fundamentals and Applications. Cham: Springer International Publishing, 2016.

[7] O. N. Senkov, J. D. Miller, D. B. Miracle, and C. Woodward, “Accelerated exploration of multi-principal element alloys with solid solution phases,” Nat. Commun., vol. 6, no. 1, p. 6529, Dec. 2015, doi: 10.1038/ncomms7529.

[8] N. Saunders and A. P. Miodownik, CALPHAD (Calculation of Phase Diagrams): A Comprehensive Guide. Pergamon, 1998.

[9] K. C. Hsieh et al., “The microstructure and phase equilibrium of new high performance high-entropy alloys,” J. Alloys Compd., vol. 483, no. 1–2, pp. 209–212, Aug. 2009, doi: 10.1016/j.jallcom.2008.08.118.

[10] C. Zhang, F. Zhang, S. Chen, and W. Cao, “Computational thermodynamics aided high- entropy alloy design,” JOM, vol. 64, no. 7, pp. 839–845, Jul. 2012, doi: 10.1007/s11837-012- 0365-6.

[11] F. Zhang, C. Zhang, S. L. Chen, J. Zhu, W. S. Cao, and U. R. Kattner, “An understanding of high entropy alloys from phase diagram calculations,” Calphad Comput. Coupling Phase Diagrams Thermochem., vol. 45, pp. 1– 10, 2014, doi: 10.1016/j.calphad.2013.10.006.

[12] G. Bracq, M. Laurent-Brocq, L. Perrière, R. Pirès, J. M. Joubert, and I. Guillot, “The fcc solid solution stability in the Co-Cr-Fe-Mn-Ni multi-component system,” Acta Mater., vol. 128, pp. 327–336, 2017, doi: 10.1016/j.actamat.2017.02.017.

[13] F. He et al., “Solid solution island of the Co-Cr- Fe-Ni high entropy alloy system,” Scr. Mater., vol. 131, pp. 42–46, 2017, doi: 10.1016/j.scriptamat.2016.12.033.

[14] A. Inselberg, “The plane with parallel coordinates,” Vis. Comput., vol. 1, no. 2, pp. 69– 91, Aug. 1985, doi: 10.1007/BF01898350.

[15] S. Gorsse and F. Tancret, “Current and emerging practices of CALPHAD toward the development of high entropy alloys and complex concentrated alloys,” J. Mater. Res., vol. 33, no. 19, pp. 2899–2923, Oct. 2018, doi: 10.1557/jmr.2018.152.

[16] S. Gorsse and O. Senkov, “About the Reliability of CALPHAD Predictions in Multicomponent Systems,” Entropy, vol. 20, pp. 1–9, 2018, doi: 10.3390/e20120899.

[17] C. Huang, Y. Zhang, J. Shen, and R. Vilar, “Thermal stability and oxidation resistance of laser clad TiVCrAlSi high entropy alloy coatings on Ti-6Al-4V alloy,” Surf. Coatings Technol., vol. 206, no. 6, pp. 1389–1395, Dec. 2011, doi: 10.1016/j.surfcoat.2011.08.063.

[18] C. Ng, S. Guo, J. Luan, S. Shi, and C. T. Liu, “Entropy-driven phase stability and slow diffusion kinetics in an Al0.5CoCrCuFeNi high entropy alloy,” Intermetallics, vol. 31, pp. 165– 172, Dec. 2012, doi: 10.1016/j.intermet.2012.07.001.

[19] O. N. Senkov, S. V. Senkova, C. Woodward, and D. B. Miracle, “Low-density, refractory multi-principal element alloys of the Cr-Nb-Ti- V-Zr system: Microstructure and phase analysis,” Acta Mater., vol. 61, no. 5, pp. 1545– 1557, Mar. 2013, doi: 10.1016/j.actamat.2012.11.032.

[20] A. Manzoni et al., “Investigation of phases in Al23Co15Cr23Cu8Fe15Ni16 and Al8Co17Cr17Cu8Fe17Ni33 high entropy alloys and comparison with equil,” J. Alloys Compd., vol. 552, pp. 430–436, 2013, doi: 10.1016/j.jallcom.2012.11.074.

[21] K. Guruvidyathri, K. C. Hari Kumar, J. W. Yeh, and B. S. Murty, “Topologically Close-packed Phase Formation in High Entropy Alloys: A Review of Calphad and Experimental Results,” JOM, vol. 69, no. 11, 2017, doi: 10.1007/s11837-017-2566-5.

In the next issue (Vol. 22, June 2022)

1.	*A Scheme for Verifying Integrity of SQL Query Processing on Encrypted Databases*	*Dr. K. Srinivasa Reddy and Dr. K. Pranitha Kumari*
2.	*Supervised Learning for COVID Mortality Span Prediction*	*Dr. A. Srinivasa Reddy*
3.	*Development of a System for the Detection of Leukemia in Blood Cells based on Image Processing*	*Dr. Narendra B Mustare*
4.	*Predicting Diabetic Retinopathy using Deep Learning*	*P. Prathyusha and A. Mallareddy*
5.	*Investigation on the Hysteresis Characteristics of Vibration Isolation Devices using Bouc-Wen Model*	*Dr. K. Karthik Selva Kumar and Rajesh Kumar*
6.	*Experimental Investigation and Study the Influence of Turning Parameters by Taguchi and Anova Analysis*	*Sarat Kumar Sahoo, S. T. Ahmed Nizami, Shaik Wahajuddin, and Gampa Smruthi*
7.	*Optimization of Turning Parameters of Inconel 718 Alloy Using ANOVA in PYTHON*	*M. Ravi Kumar and P. Lava Kumar*

E-ISSN 2581 – 7957
P-ISSN 2277 – 3916

CVR Journal of Science and Technology, Volume 22, June 2022
DOI: 10.32377/cvrjstxxxx

Template for the Preparation of Papers for Publication in CVR Journal of Science and Technology

First A. Author[1] and Second B. Author[2]
[1]Designation, Name of Institution/Department, City, Country
Email: first.author@hostname1.org
[2]Designation, Name of Institution/Department, City, Country
Email: second.author@hostname2.org

Abstract: **These instructions give you basic guidelines for preparing camera-ready papers for CVR College journal Publications. Your cooperation in this matter will help in producing a high-quality journal.**

Index Terms: **first term, second term, third term, fourth term, fifth term, sixth term**

I. Introduction

Your goal is to simulate the usual appearance of papers in a Journal Publication of the CVR College. We are requesting that you follow these guidelines as closely as possible. It should be original work. Format must be done as per the template specified. Diagrams with good clarity with relevant reference within the text are to be given. References are to be cited within the body of the paper. Number of pages must not be less than five with minimum number of 4000 words and not exceeding eight pages. The journal is published in colour. Colours used for headings, subheadings and other captions must be strictly as per the template given in colour.

A. Full-Sized Camera-Ready (CR) Copy

Prepare your CR paper in full-size format, on A4 paper (210 x 297 mm or 8.27 x 11.69 in). No header or footer, no page number.

Type sizes and typefaces: Follow the type sizes specified in Table I. As an aid in gauging type size, 1 point is about 0.35 mm. The size of the lowercase letter "j" will give the point size. Times New Roman has to be the font for main text. Paper should be single spaced.

Margins: Top and Bottom = 24.9mm (0.98 in), Left and Right = 16 mm (0.63 in). The column width is 86mm (3.39 in). The space between the two columns is 6mm (0.24 in). Paragraph indentation is 3.7 mm (0.15 in).

Left- and right-justify your columns. Use tables and figures to adjust column length. On the last page of your paper, adjust the lengths of the columns so that they are equal. Use automatic hyphenation and check spelling. Digitize or paste down figures.

For the Title use 24-point Times New Roman font, an initial capital letter for each word. Its paragraph description should be set so that the line spacing is single with 6-point spacing before and 6-point spacing after. Use two additional line spacings of 10 points before the beginning of the double column section, as shown above.

TABLE I.
TYPE SIZES FOR CAMERA-READY PAPERS

Type size (pts.)	Appearance		
	Regular	Bold	Italic
6	Table caption, table superscripts		
8	Tables, table names, f irst letters in table captions, figure captions, footnotes, text subscripts, and superscripts		
9	References, authors' biographies	Abstra ct	
10	Section titles ,Authors' affiliations, main text, equations, first letters in section titles		Subheading
11	Authors' names		
24	Paper title		

Each major section begins with a Heading in 10 point Times New Roman font centered within the column and numbered using Roman numerals (except for REFERENCES), followed by a period, two spaces, and the title using an initial capital letter for each word. The remaining letters are in SMALL CAPITALS (8 point). The paragraph description of the section heading line should be set for 12 points before and 6 points after.

Subheadings should be 10 point, italic, left justified, and numbered with letters (A, B, …), followed by a period, two spaces, and the title using an initial capital letter for each word. The paragraph description of the subheading line should be set for 6 points before and 3 points after.

For main text, paragraph spacing should be single spaced, no space between paragraphs. Paragraph indentation should be 3.7mm/0.21in, but no indentation for abstract & index terms.

II. Helpful Hints

A. Figures And Tables

Position figures and tables at the tops and bottoms of columns. Avoid placing them in the middle of columns. Large figures and tables may span across both columns. Leave sufficient room between the figures/tables and the main text. Figure captions should be centered below the figures; table captions should be centered above. Avoid placing figures and tables before their first mention in the

Received on xx-xx-2022, Revised on xx-xx-2022, Accepted on xx-xx-2022.

CVR Journal of Science and Technology, Volume 22, June 2022
DOI: 10.32377/cvrjstxxxx

text. Use the abbreviation "Fig. 1," even at the beginning of a sentence.

To figure axis labels, use words rather than symbols. Do not label axes only with units. Do not label axes with a ratio

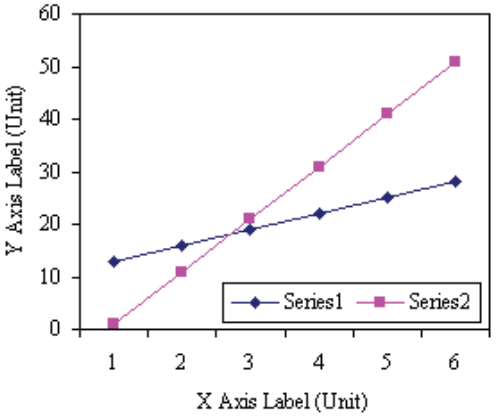

Figure 2. Note how the caption is centered in the column.

of quantities and units. Figure labels should be legible, about 8-point type.

All figures, tables and references must be cited in the text.

Please indicate the broad area/specializations into which the research paper falls, in the covering letter/mail to the Editor, so that reviewers with those specializations may be identified.

B. References

Number citations consecutively in square brackets [1]. Punctuation follows the bracket [2]. Use "Ref. [3]" or "Reference [3]" at the beginning of a sentence:

Give all authors' names; use "et al." if there are six authors or more. Papers that have not been published, even if they have been submitted for publication, should be cited as "unpublished" [4]. Papers that have been accepted for publication should be cited as "in press" [5]. In a paper title, capitalize the first word and all other words except for conjunctions, prepositions less than seven letters, and prepositional phrases. Good number of references must be given.

Latest references in the area must be included and every refence must be cited in the text of the research article.

C. Footnotes

Number footnotes separately in superscripts [1, 2, ...]. Place the actual footnote at the bottom of the column in which it was cited, as in this column. See first page footnote as an example.

D. Abbreviations and Acronyms

Define abbreviations and acronyms the first time they are used in the text, even after they have been defined in the abstract. Do not use abbreviations in the title unless they are unavoidable.

E. Equations

Equations should be left justified in the column. The paragraph description of the line containing the equation should be set for 6 points before and 6 points after. Number equations consecutively with equation numbers in parentheses flush with the right margin, as in (1). Italicize Roman symbols for quantities and variables, but not Greek symbols. Punctuate equations with commas or periods when they are part of a sentence, as in

$$a + b = c \ . \qquad (1)$$

Symbols in your equation should be defined before the equation appears or immediately following. Use "(1)," not "Eq. (1)" or "equation (1)," except at the beginning of a sentence: "Equation (1) is ..."

F. Other Recommendations

Use either SI (MKS) or CGS as primary units. (SI units are encouraged.) If your native language is not English, try to get a native English-speaking colleague to proofread your paper. Do not add page numbers.

III. Conclusions

The authors can conclude on the topic discussed and proposed, future enhancement of research work can also be briefed here.

References

[1] G. Eason, B. Noble, and I. N. Sneddon, "On certain integrals of Lipschitz-Hankel type involving products of Bessel functions," Phil. Trans. Roy. Soc. London, vol. A247, pp. 529–551, April 1955.

[2] J. Clerk Maxwell, *A Treatise on Electricity and Magnetism*, 3rd ed., vol. 2. Oxford: Clarendon, 1892, pp.68–73.

[3] I. S. Jacobs and C. P. Bean, "Fine particles, thin films and exchange anisotropy," in *Magnetism*, vol. III, G. T. Rado and H. Suhl, Eds. New York: Academic, 1963, pp. 271–350.

[4] K. Elissa, "Title of paper if known," unpublished.

[5] R. Nicole, "Title of paper with only first word capitalized", *J. Name Stand. Abbrev.*, in press.

[6] Y. Yorozu, M. Hirano, K. Oka, and Y. Tagawa, "Electron spectroscopy studies on magneto-optical media and plastic substrate interface," *IEEE Transl. J. Magn. Japan*, vol. 2, pp. 740–741, August 1987 [Digests 9th Annual Conf. Magnetics Japan, p. 301, 1982].

[7] M. Young, *The Technical Writer's Handbook*. Mill Valley, CA: University Science, 1989.

[8] T. Ali, B.K. Subhash and R.C. Biradar, "A Miniaturized Decagonal Sierpinski UWB Fractal Antenna", PIERS C, vol. 84, pp. 161-174, 2018.

ABOUT THE COLLEGE

CVR College of Engineering (An UGC Autonomous Institution) was established in the year 2001, and its Seventeenth batch of students graduated from the College. This college has been ranked **155** by **NIRF** among the Engineering institutions of the country.

The College was the **first** college in Telangana that was promoted by NRI technology professionals resident in the US. The NRI promoters are associated with cutting-edge technologies of the computer and electronics industry. They also have strong associations with other leading NRI professionals working for world-renowned companies like IBM, Intel, Cisco, Facebook, AT&T, Google and Apple who have agreed to associate with the College with a vision and passion to make the College a state-of-the-art engineering institution.

An Expert Committee of the UGC visited the college in January 2021 and extended the Autonomous status from 2020-2021 to 2024-2025.

The college has many accomplishments and to name a few, it obtained **NBA Tier 1 accreditation for all eligible UG Programs, NAAC 'A' grade**, **UGC autonomous status**, **National Employability Award** for seventh year in a row and received a very high rating by several ranking agencies including the most recent Education World ranking of third best college in Telangana and Outlook magazine, rating CVRCE, one among the **top 100 colleges in the country**, and **AAAA grade** from Careers 360.

The college has been sanctioned Rs.2.87 Crores from NEWGEN IEDC from the Department of Science and Technology. NEWGEN centre has been established to enable the staff and students to work on NEWGEN projects. 20 projects are lined up for 2021-22.

Publications by faculty have increased considerably. These publications can be found at: http://cvr.ac.in/research. Consultancy work has been taken up by the departments of CE and ME. The number of faculty with doctorates has increased to 125.

Dr. K. Lal Kishore, Dean – Research was honoured with the Lifetime Achievement Award by the ISTE in April 2021 for a meritorious career in the field of education.

The departments ECE, EEE and EIE are organizing an Online International Conference "Recent Trends in Electrical, Electronics, Communications and Instrumentation" (ICRTEECT 21) in December 2021.

Faculty members are working on Rupees One crore worth projects with funding from AICTE, UGC and ISRO. 30 Projects worth Rs. 2.54 Crores have been completed thus far. The current number of patents published is 29.

The AICTE sanctioned Rs. 2 lakhs to students and faculty of CE and ME for a study tour of ATAL tunnel and Ra. 1 lakh towards activities under scheme for Promoting Interests, Creativity and Ethics among Students (SPICES).

The College Conducted a COVID -19 Vaccination drive for students and faculty to safeguard them from the pandemic.

The students have brought home laurels by winning prizes in competitions outside the college.

The college has been creating records year after year. With more than 100 companies visiting CVR and 1000+ placements for the 2020 - 2021 academic year, it is the highest among the peer group of colleges. The highest offer of **Rs. 30.25 Lakhs PA** was bagged by 8 students and close to 20 students got offers higher than **Rs. 10 Lakhs PA**. About 300 offers are higher than Rs. 5 Lakhs PA and another 60 offers are higher than Rs. 8 Lakhs PA. With this, CVR became the leading college in entire Telangana in terms of the offers with higher salaries. CVR has made huge progress in a short span of time and was preferred by the students and parents during the EAMCET counseling this year and is among the **top 3 colleges** in the state.

In keeping with the current global emphasis on green and eco-friendly energy generation, 360kW Solar PV plant has been installed on the campus to meet the power requirements of the college to a significant extent.

CALL FOR PAPERS:

Papers in Engineering, Science and Management disciplines are invited for Publication in our Journal. Authors are requested to mail their contributions to Editor, CVR Journal of Science and Technology (Email Id: journal@cvr.ac.in). Authors can also submit their papers through our online open journal system(OJS) www.ojs.cvr.ac.in or www.cvr.ac.in/ojs. Papers are to be written using a Standard Template, which may be obtained on request from the Editor. It is also available on the college website www.cvr.ac.in.

CVR JOURNAL OF SCIENCE AND TECHNOLOGY

CVR COLLEGE OF ENGINEERING

(UGC Autonomous- Affiliated to JNTU Hyderabad)
Mangalpalli (V), Ibrahimpatnam (M),
R.R. District, Telangana - 501510
http://cvr.ac.in